YOUNG STELLAR OBJECTS AROUND SUPERNOVA REMNANTS IN THE LARGE MAGELLANIC CLOUD

Bachelorarbeit aus der Physik

Vorgelegt von

Jurk Katharina

October 27, 2022

Dr.Karl-Remeis-Sternwarte

Erlangen Centre for Astroparticle Physics

Friedrich-Alexander-Universität Erlangen-Nürnberg

Betreut von: Prof. Dr. Manami Sasaki

Eigenständigkeitserklärung

Hiermit versichere ich, Jurk Katharina, dass ich diese Arbeit selbstständig und nur mit den im Literaturverzeichnis angegebenen Quellen angefertigt habe. Alle wörtlichen Zitate oder sinngemäß übernommenen Aussagen wurden als solche gekennzeichnet. Ich erkläre weiterhin, dass diese Arbeit bisher nicht Gegenstand eines anderen Prüfungsverfahrens gewesen ist und nicht bereits veröffentlicht wurde.

October 27, 2022 Jurk Katharina

Table of Contents

1 Introduction and Project Outline

The Large Magellanic Cloud (LMC) is an irregular galaxy at a distance of 50 kpc from the Milky Way Galaxy. The LMC provides an advantageous position to study the 'life-cycle of matter' from the interstellar medium and star formation through the life of stars on the main-sequence until the stellar material is eventually returned to the interstellar medium [Carlson et al., 2012].

Due to its proximity and low inclination angle (30°, [Gruendl & Chu, 2009]) the LMC allows to investigate individual objects which are still in the process of forming stars as well as resolve supernova remnants changing the interstellar medium surrounding them.

As supernova remnants (SNRs) have a shorter lifetime than young stellar objects (YSOs) when they are found in the vicinity of star forming regions, it can be expected that SNRs have a physical impact on the evolution of YSOs and thus on the star formation process itself [Heim, 2017].

Chapter 2 of this thesis gives an overview of the star formation process, describes the properties of YSOs and introduces terminology and physical parameters of stars that are vital in order to grasp the photometric analysis following in chapter 6. The subsequent chapter 3 elaborates on the nature of supernovae and supernova remnants and stresses the consequences of such events on star formation regions. Chapter 4 and 5 will provide an overview of the science instruments and observation surveys through which source catalogs for both YSOs and SNRs were obtained.

This work then proceeds to investigate possible associations between SNRs and YSOs. Firstly, YSOs are grouped according to their distance to the SNRs (6.1). In the following step, a comparison of their brightness in various infrared bands is performed through color-magnitude and color-color diagrams (6.2.1). Lastly, the spectral energy distribution and the infrared spectral index are calculated separately for each group (6.4).

2 Young Stellar Objects

In astrophysical terms a star is defined as a selfgravitating sphere of gas mainly consisting of hydrogen and helium whose core temperature is high enough to produce energy through thermonuclear fusion.

Star birth is a two-step process in which a star-forming system gradually evolves into the necessary equilibrium states for it to be called a *star*:

1. *Hydrostatic Equilibrium*: the internal pressure, i.e., the internal thermal motion, of the gas cloud and the gravity are in balance, so there is no contraction or expansion of the cloud.

2. *Thermal Equilibrium*: the energy radiated away by the star (*luminosity*) is made up for by the nuclear fusion in the stars core.

The next section on star formation follows the text in [Stahler & Palla, 2008] and [Karttunen et al., 2007].

2.1 Star Formation

Stars form in *giant molecular clouds*, structures which are solely stabilized due to their own gravity. These clouds have mean temperatures of about 15 K with masses in the range of hundred thousand solar masses ($M_\odot$). They mostly consist of molecular hydrogen H_2.

The distribution of giant molecular clouds and thus the main star forming regions across the galaxy can be established by observations in the 2.6 mm line of $^{12}C^{16}O$. In spiral galaxies such as our Milky Way the molecular clouds mostly form the prominent spiral arms.

Observations and theoretical calculations confirm that stars are not formed individually, but in larger groups containing a few hundred stars. Therefore, young stellar objects are often observed in clusters.

In the 1920's James Jeans calculated the limiting mass for a cloud with a temperature T and a density n to gravitationally contract. If the stars' mass is larger than the *Jeans mass*, the potential energy exceeds the kinetic energy. Therefore, the mass is high enough for gravity to overcome the pressure of the gas. As a result, the cloud will start to collapse. Under its own gravity a giant cloud contracts and fragments into smaller individual clouds.

$$M_{\text{Jeans}} \approx 3 \cdot 10^4 \sqrt{\frac{T^3}{n}} M_\odot \tag{2.1}$$

The individual clouds themselves fragment into smaller high-density entities, the *dense cores*, which are eventually the sites that become *protostars*. Table 2.1 compares key characteristics such as mass M, density n, diameter D and temperature T of the three cloud types mentioned.

TABLE 2.1: Comparison of physical properties of giant molecular clouds and dense cores [Stahler & Palla, 2008], [Karttunen et al., 2007]. The values describing density and temperature of the Sun are mean values, since they vary with the distance to the core.

Type	n [cm^{-3}]	D [pc]	T [K]	M [$M_{\odot}$]
Giant Molecular Clouds	100	50	15	10^5
Individual dark clouds	10^3	2	10	30
Dense Cores	10^4	0.1 – 1	10	0.3 – 10

As the contraction begins, gravitational energy is liberated and transformed into thermal energy of the gas molecules. This released energy subsequently escapes as radiation, since the density is still low and the gas is optically thin. The temperature remains constant. As the contraction proceeds, the density increases while the Jeans mass decreases (2.1). As a result, the cloud *fragments*: separate entities are formed which continue to contract independently. These are referred to as individual dark clouds in table 2.1. Eventually, the density increases to such an extent that the individual fragments become optically thick. The energy that was liberated through the contraction process is no longer carried away but is turned into heat and the temperature rises.

During the contraction process the gas falls freely towards the center of the cloud. Consequently, the pressure as well as the density increase the fastest near the clouds' center. The increasing pressure starts acting as a resistance to the free-falling gas. The contraction in the centre slows down. However, the gas from outer regions continues to free-fall. Now, the cloud can be considered a *protostar*.

The initial giant molecular clouds consisted of mostly molecular hydrogen H_2. Due to the increasing temperature the molecules are first dissociated into hydrogen atoms H ($T \approx 1800\,\mathrm{K}$). Afterwards, the hydrogen atoms are ionized at roughly $1 \times 10^4\,\mathrm{K}$. The contraction of a protostar ceases when the gas is fully ionized. The gas is now described as a *plasma*. The young star is considered to have reached hydrostatic equilibrium. The radius of the young star shrinks during this process from about 100 AU to 1/4 AU.

While still embedded in a gas cloud, the protostar starts accreting matter from its surroundings forming an *accretion disk*. The increasing mass of the star results in a higher density and temperature in the stars' centre. In this phase, material can be ejected in a *jet* or a *wind* - suspected to be associated with the presence of a magnetic field (see figure 2.1).

Reasons for a cloud to begin contracting include supernova explosions, expanding HII regions as well as compression of the gas while passing through the spiral arms of the galaxy. The details of these processes go beyond the scope of this work.

The star formation process starting with the contraction of the giant molecular clouds described above was highly simplified. Other important aspects such as the roll of rotation or magnetic fields will not be discussed.

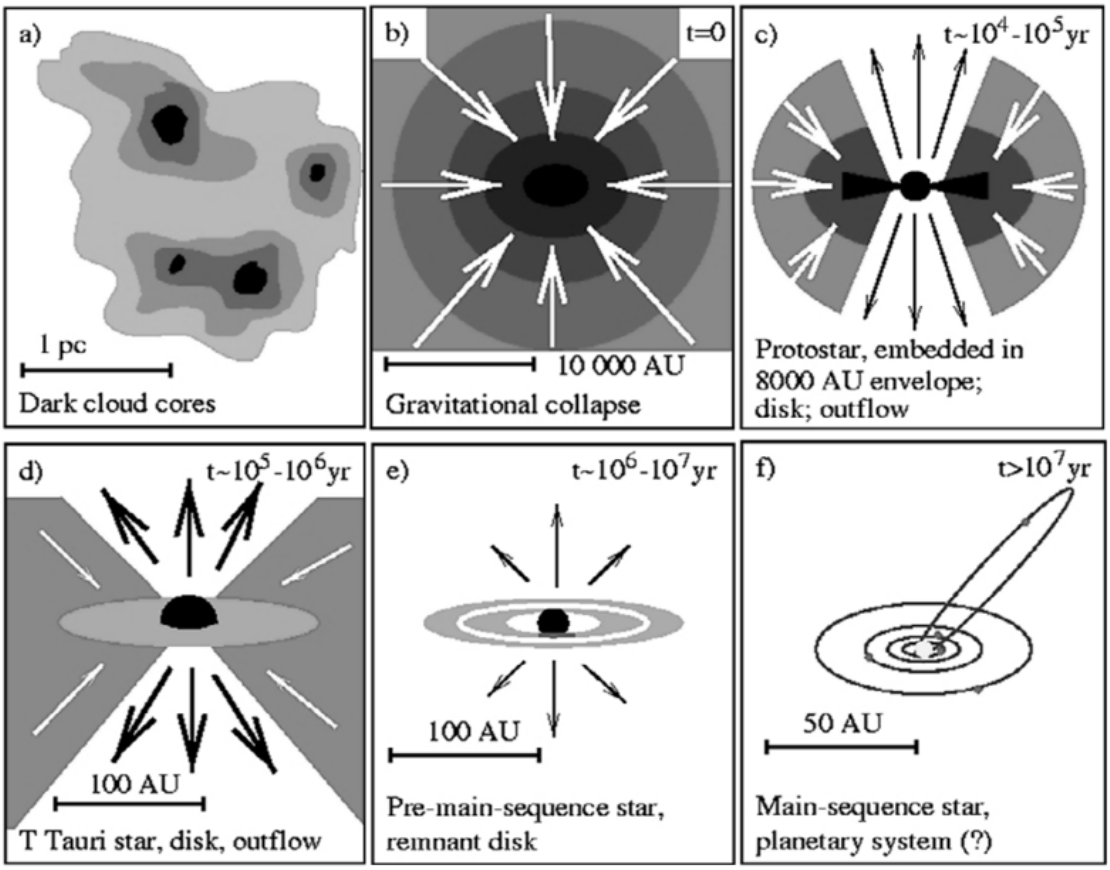

FIGURE 2.1: The various steps of star formation. Within a giant molecular cloud, matter gathers into dense cores (a) which form protostars due to gravitational collapse (b). The protostars are surrounded by infalling envelopes and accretion disks (c). Eventually the protostar becomes hot enough to ignite nuclear fusion. Outflowing jets are formed and the accretion rate decreases (d). When the accretion phase ends, a young star surrounded by a disk is left (e). Adopted from [Tielens, 2021].

2.2 Young Stellar Objects

Protostars have two prominent sources of energy:

1. Gravitational potential energy is released as the protostar contracts and material is accreted.
2. Stellar energy is released as soon as the central temperature is high enough for the protostar to be able to ignite nuclear fusion reactions in its core.

The young stars' luminosity will now have a significant increase allowing it to be detected as a point-like source [Draine, 2010].

Following the star formation in the previous section, young stars are surrounded by disks and envelopes composed of dust. The dust grains are formed as the gas of the interstellar clouds condenses (just as water condenses to ice). They are usually smaller than one micrometer [Karttunen et al., 2007]. In the early stages of evolution, the disks are opaque and absorb most of the short-wavelength stellar radiation. The absorbed photons are then re-emitted with energies corresponding to the temperature of the dust [Shu et al., 1987]. Young stars and their gas envelopes have temperatures of a few 100 K or 1000 K [Karttunen et al., 2007]. According to Wien's displacement law the corresponding wavelength range at maximum emission for the stated temperatures is 30 µm – 3 µm which falls into the infrared regime of the electromagnetic spectrum. As the stars evolve, the disks and envelopes disperse and become optically thin. They become fainter in the infrared, as they emit less infrared radiation [Whitney et al., 2008].

It is difficult to observe star formation during the contraction phase as the stars are embedded in the dense environment of gas and dust. By using suitable instruments which can detect the infrared radiation escaping the dense environment around protostars, observations are made accessible.

Protostars and Young Stellar Objects (YSOs) can empirically be divided into four classes based on the shape of their infrared spectrum which is determined by the (infrared) *spectral index* α [Draine, 2010]. It is derived from the slope of the infrared spectral energy distribution:

$$\alpha \equiv \frac{d \log \lambda F_\lambda}{d \log \lambda}, \tag{2.2}$$

where λF_λ is the specific flux at the wavelength λ.

The classes correspond to evolutionary stages of the young stars characterized by the opacity of their dusty envelopes and disks. While class I stars are hidden among infalling envelopes, class II stars have already developed opaque disks and class III stars are surrounded by optically thin disks [Whitney et al., 2008]. Class 0 protostars are objects whose radiation is deeply absorbed by dust. They can be invisible even in the infrared spectral range. Therefore, the spectral index α is not a suitable parameter to characterize their spectrum [Draine, 2010]. Exemplary spectra of the four evolutionary stages with the contribution of the envelope, disk and the stellar photosphere are depicted in figure 2.3.

The spectrum of low-mass protostars ($M \lesssim 3M_\odot$), often referred to as *T-Tauri stars*, has been observed to display an excess in infrared radiation. This excess is caused by the process of absorption and re-emission of photons described above. Adjacent to the example in [Draine, 2010] for T-Tauri stars, the spectral index α yields the following evolutionary stages (figure 2.2):

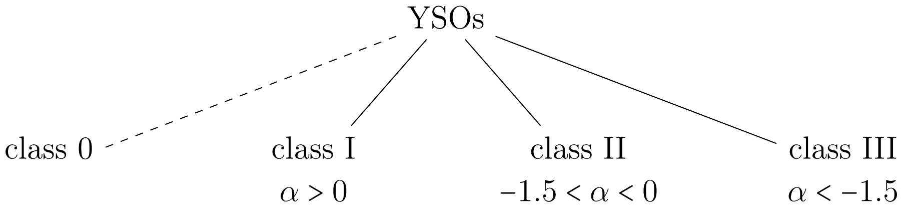

FIGURE 2.2: Tree diagram depicting the classification of low-mass Young Stellar Objects (YSOs) by using the spectral index.

It is to be noted that the absolute values of the spectral index α may change depending on the calculation methods and the available flux measurements. Generally, the trend towards a decreasing spectral index α with increasing class is maintained. This relates to stars of higher class III in the sense that they depict less infrared excess than stars of class I/II due to their fading disks.

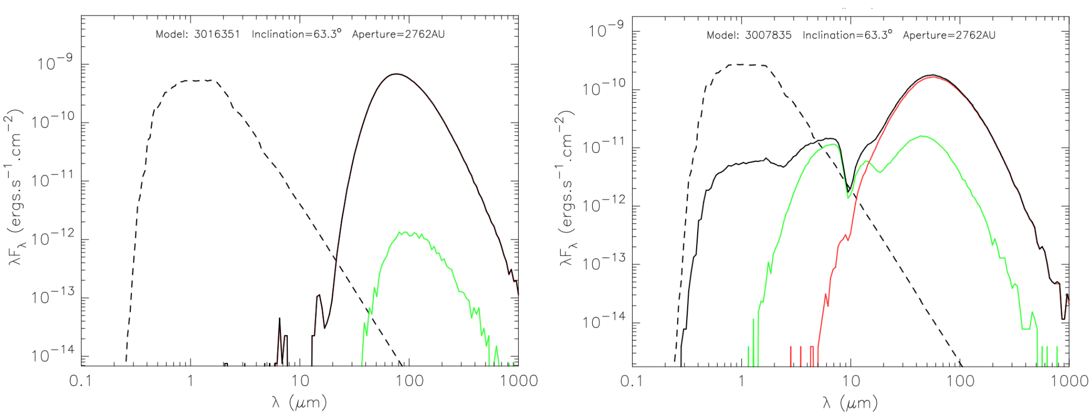

(A) class 0 (B) class I

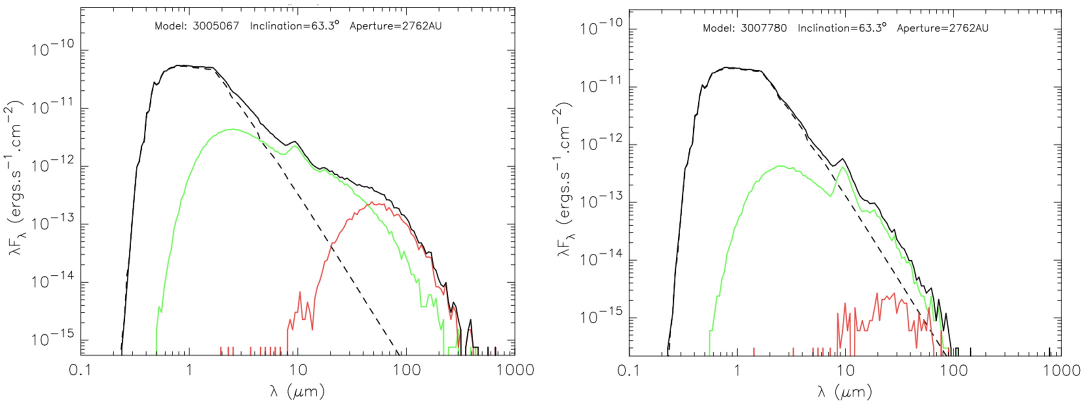

(C) class II (D) class III

FIGURE 2.3: Spectral Energy Distribution for low-mass YSOs in different evolutionary stages. The $x-$axis displays the wavelength λ [µm] and the $y-$axis the specific flux λF_λ [$\mathrm{erg\,s^{-1}\,cm^{-2}}$]. The solid black line depicts the complete spectrum. The contribution from the envelope is shown in red, the one from the disk in green. The dashed line displays the blackbody radiation spectrum. Since Class 0 sources (A) are completely obscured by dust, the maximum of their spectrum lies in the infrared. For class I (B) and class II YSOs (C) the infrared excess is evident. The spectrum of class III stars (D) resembles the blackbody spectrum with almost no infrared excess. Adapted from [Knies, 2015].

2.3 Properties of Stars

Stars which are in both hydrostatic and thermal equilibrium and are powered by hydrogen fusion in their core are called *main-sequence* stars. The following sections introduce important quantities utilized to describe and classify the observed stars. The following summary is based on selected chapters in [Karttunen et al., 2007].

2.3.1 Flux Density, Luminosity and Effective Temperature

The *photosphere* is an optically thin layer that is a few hundred kilometers thick in which roughly 99.9% of all radiation is emitted. The interior of a star is extremely dense and optically thick for photons, meaning they are absorbed by atoms before they can leave the star. Therefore, electromagnetic radiation is detected from the star due to photons escaping the photosphere.

When a radiation source such as a star is observed, the radiation collected by a detector is documented over a certain period of time. An important quantity to characterize this energy is described by the *radiant flux* F. It depicts the total amount of the radiation in all wavelengths per unit area and per unit time received by the detector. The *luminosity* L is the power (energy per unit time) traversing a closed sphere enclosing the source. Under the assumption that the star radiates isotropically, the luminosity at a distance r is given by

$$L = 4\pi r^2 F \quad [\mathrm{W}]. \tag{2.3}$$

The spectrum of the detected radiation from a star approximately equals a blackbody radiation spectrum. For a blackbody of temperature T, this spectrum is continuous with a peak at a certain wavelength λ_{max}. The relation between temperature T and λ_{max} is known as *Wien's displacement law*:

$$\lambda_{\mathrm{max}} T = 2.8978 \cdot 10^{-3}\ \mathrm{K\,m}. \tag{2.4}$$

Furthermore, the *Stefan-Boltzmann law* describes a relation between temperature T and flux F:

$$F = \sigma T^4 \quad [\mathrm{W\,m^{-2}}], \tag{2.5}$$

where σ is the *Stefan-Boltzmann constant*. This relation can be inserted into equation (2.3):

$$L = 4\pi\sigma R^2 T_{\mathrm{eff}}^4 \quad [\mathrm{W}], \tag{2.6}$$

where R is the radius of the star and $4\pi R^2$ its surface area.

This new definition for the luminosity defines the *effective temperature* T_{eff}, a quantity characterizing the surface temperature of a star. The effective temperature is made use of in order to classify stars based on lines in their spectra which are sensitive to the temperature. Mainly, seven spectral types can be distinguished with decreasing temperature towards the right: O - B - A - F - G - K - M. For a more subtle differentiation each spectral type is additionally given a number from 0 to 9 dividing it into several subclasses.

2.3.2 Magnitude and Color Index

The luminosity L is not a directly accessible parameter in experimental measurements. As indicated in the last section, the luminosity is not a suitable quantity to describe young stellar objects, since they are not main-sequence stars and their primary energy source is not hydrogen fusion yet.

The monochromatic flux density F_λ observed at a wavelength λ can be employed to define the *apparent magnitude* m_λ an estimate for the brightness of the star as viewed from earth:

$$m_\lambda - m_{0,\lambda} = -2.5 \log_{10} \frac{F_\lambda(r)}{F_{0,\lambda}} \quad [\mathrm{mag}]. \tag{2.7}$$

The zero-point flux density $F_{0,\lambda}$ is a reference value and corresponds to $m_{0,\lambda} = 0$.

Magnitudes are advantageous as they can be utilized to portray any astronomical object's brightness. A difference of 5 magnitudes in brightness translates to the higher-magnitude object being 100 times fainter than the lower-magnitude one. By using modern detectors apparent magnitudes can be measured with an accuracy of 0.01 magnitudes [Carroll & Ostlie, 2017].

In order to compare the brightness of two objects independent of their distance to earth, the *absolute magnitude* M_λ needs to be introduced. It is defined as the apparent magnitude m_λ of an object if it were located at a distance of 10 pc. Equation (2.7) now becomes:

$$m_{\lambda,1} - m_{\lambda,2} = -2.5 \log_{10} \frac{F_{\lambda,1}}{F_{\lambda,2}} \quad [\mathrm{mag}]. \tag{2.8}$$

The connection between a star's absolute and apparent magnitudes and its distance d (in parsec) is illustrated by the *distance modulus*:

$$m_\lambda - M_\lambda = 5 \log_{10} d\ [\mathrm{pc}] - 5. \tag{2.9}$$

The color index (CI) is a measure for the *color* of a star. It is defined as the difference between magnitudes at the two wavelengths λ_1 and λ_2 or equivalently as the ratio of the fluxes at the two involved wavelengths:

$$\mathrm{CI} = m_{\lambda_1} - m_{\lambda_2} = M_{\lambda_1} - M_{\lambda_2} \tag{2.10}$$

It is to be noted that using equation (2.9) for the magnitudes in the above definition (2.10) implies that the color index is independent of distance d.

It is crucial to consider that the magnitudes, whether apparent or absolute, and thus also their color indices are instrument dependent. The percentage of incident stellar radiation measured, depends both on the wavelength band as well as the particular components of the detector. Therefore, care needs to be applied in comparing such measurement values from different instruments [Zeilik & Gregory, 1998].

3 Supernovae and Supernova Remnants

To discuss supernova remnants, first, their origin has to be understood: stellar explosions or short supernovae (SNe), the most energetic stellar events known. Stellar material is ejected into the interstellar medium (ISM) with velocities of up to $15\,000\,\mathrm{km\,s^{-1}}$ and heated to temperatures of millions of Kelvin. A powerful shock wave forms and propagates into the ISM. SNe are extremely luminous and cause a burst of radiation which can outshine an entire galaxy in some cases. The energy of motion initially stored in the stellar debris after the explosion is around 10^{51}erg (10^{44}J). As the debris expands, this energy is converted to radiation energy which is mainly released in form of X-ray and radio radiation. The resulting structure that is observed is then referred to as the supernova remnant (SNR).

Observations of SN1987A, a core-collapse SN, in the Large Magellanic Cloud revealed that the majority of the energy is released through a burst of neutrinos marking the exact time of the explosion. This detection also confirmed theories on which processes are occurring in the core of a collapsing star [Vink, 2020].

The study of events after a supernova or the observation of SNRs can reveal why such an outbreak occurred and what type of progenitor star exploded. SNe are considered one of the most important mechanisms in the universe, since they enrich the ISM with heavy elements, out of which new stars and planetary systems can be formed [Seward & Charles, 2010].

3.1 Classification of supernovae

Late stages of stellar evolution need to be considered to understand observations of SNRs. In general, two main explosion mechanisms exist that lead to a SN: firstly, the thermonuclear explosion of accreting white dwarfs which occurs when the mass of the white dwarf exceeds the Chandrasekhar limit (1.44 $M_{\odot}$). The accreted material from the companion star raises the temperature of the white dwarf and ignites runaway nuclear fusion of carbon and oxygen which disrupts the white dwarf completely. Secondly, the core-collapse of a massive star ($> 8 M_{\odot}$) due to its own gravitation. The fusion of ^{56}Fe requires more energy than it releases, so the nuclear fusion chain breaks off. The radiation pressure decreases and the star is no longer in the state of hydrostatic equilibrium. The following gravitational core-collapse leaves behind a neutron star or a black hole. Which compact object actually forms, is indicated by the initial mass of the star.

SNe are classified based on their optical light curves, i.e., the evolution of the luminosity after the explosion, and optical spectra, i.e., the absence and presence of emission lines of certain elements. A first distinction is the presence (type I) and absence (type II) of Hydrogen (H) in optical spectra (see figure 3.1). Silicon (Si) is prominent in the spectra of Ia SNe. It is assumed that all white dwarf explosions result in this type of SN. Since white dwarf progenitor stars are old and not particularly massive, they are observed in all kinds of galaxies, so, for example, in the halos of spiral or in elliptical galaxies. Both Ib/c and II are core-collapse SNe. In type Ib spectra Helium (He) is present, while those of Ic show neither Si nor He. Therefore, it is supposed that some progenitor stars could have been Wolf-Rayet stars which have already lost their H and He envelopes. Regarding type II explosions, a variety of characteristics exist involving the shape of light curves. A classification is not as simple and will not be further elaborated on (see [Seward & Charles, 2010] or [Vink, 2020] for more details). All three mentioned SNe are associated with young objects (Population I stars) in galaxies and are hence found in the spiral arms of spiral or irregular galaxies where star formation takes place.

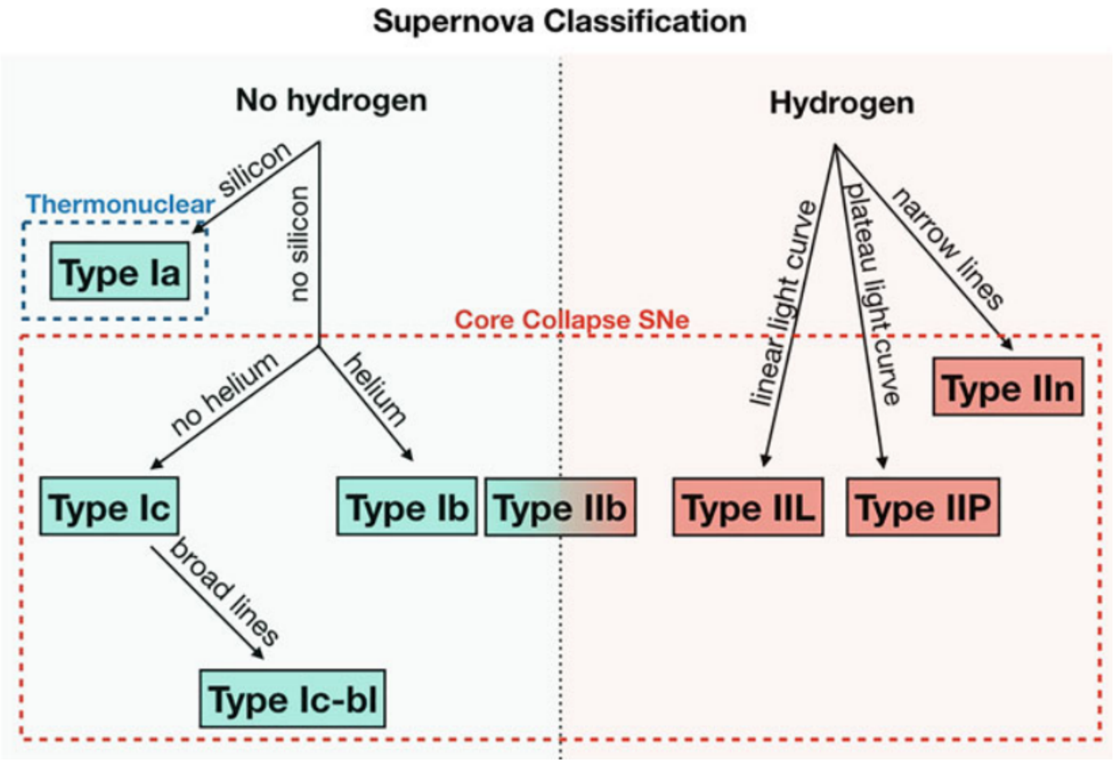

FIGURE 3.1: Supernova classification scheme based on presence and absence of emission lines in optical spectra and shape of light curves [Vink, 2020].

3.2 Types of supernova remnants

Supernova remnants are grouped by their morphology, i.e., form and shape, in the X-ray and radio energy band. Four categories are distinguished following the argumentation in [Seward & Charles, 2010]:

- *shell-like*. The shock wave propagating from the SN explosion into the ISM heats interstellar gas, producing a shell of hot plasma. Radio and X-ray are limb-brightened, i.e., the shell appears bright at the edges and thus ring-like[1].

- *plerionic*. Radio and X-ray images are the brightest in the center. Limb-brightening is not observed or quite weak. A pulsar in the middle of the SNR is surrounded by relativistic electrons which interact with the magnetic field and emit synchrotron radiation. A diffuse wind nebula (pulsar wind nebula) is formed.

- *(plerionic) composite*. Images in the X-ray and radio band show both limb-brightening and bright centers. Emission lines in the X-ray spectrum indicate a hot thermal plasma. Referring to a thermal plasma means that the electron velocity distribution is described by Maxwell-Boltzmann function.

- *mixed morphology/thermal composite*. These remnants have filled centers in the X-ray band and the spectra include lines indicative of a hot gas. However, in the radio waveband they appear shell-like suggesting relativistic particles are present that emit synchrotron radiation.

3.3 Supernova remnant evolution

After the SN, the supersonically traveling ejecta interacts with the ISM and results in the formation of a shock wave that heats the gas resulting in a shell of plasma. This forward shock sweeps up more and more material and expands rapidly. The shell's energy is spread over more mass and thus the shock decelerates and the remnant cools down. Additionally, the shell loses energy through radiation [Vink, 2020]. The expansion rate is determined by the initial energy of the SN explosion and the density of the ISM [Seward & Charles, 2010]. The evolution of SNRs can be divided into four phases (see figure 3.2):

---

[1] `https://www.oxfordreference.com/view/10.1093/oi/authority.20110803100105987`, accessed on 13.10.2022.

1. *Free expansion phase*: mass of the ejecta M_{ej} is sufficiently larger than the mass of swept up material M_{sw}. Therefore, the majority of the energy is contained in the expanding ejecta. It is assumed that the blast wave expands at nearly uniform velocity. This phase lasts a few hundred years until $M_{\mathrm{sw}} \approx M_{\mathrm{ej}}$ [Vink, 2020].

2. *Sedov-Taylor/Blast wave phase* ($\approx 10^4$ years): Since the ISM is surrounding the SNR, it prevents the stellar ejecta to continue expanding freely. The interaction of the blast wave, the forward shock, with the ISM forms an additional shock wave, the reverse shock, that ultimately propagates inwards when $M_{\mathrm{sw}} > M_{\mathrm{ej}}$ [Vink, 2020]. Only the matter between the two shock waves is hot, since it has been compressed and heated by the rapidly moving ejecta. The shocked ejecta is the prime reason for the observation of X-ray emission which result in the bright shells, especially visible in young remnants. The radiation from the shell is still negligible compared to its internal energy of the hot material, hence the expansion is considered to be adiabatic [Seward & Charles, 2010]. This phase is called Sedov-Taylor phase since the SN explosion (assumed to happen in a homogeneous medium) can be described by an analytic solution independently derived by Sedov and Taylor in the fifties.

3. *Radiative phase* ($\approx 10^5$ years): The material behind the blast wave cools down to about 10^{5-6} K. The rate of radiation increases and the gas loses energy efficiently through UV line emission [Seward & Charles, 2010].

4. *Merging phase*: The shock wave will slowly disappear as the blast wave velocity becomes similar to the speed of sound and the shell will expand subsonically [Vink, 2020]. The majority of the energy has been lost due to radiation, the remnant becomes fainter until it is indistinguishable from the ISM.

It is to be noted that the four-phase SNR evolution elaborated above can only partially be applied to reality. The development of the shocks depend strongly on the density as well as the density gradient of the ISM and does not have to be homogeneous around the SNR. In some cases, the phases can portray the evolution of one part of a SNR, but fail to in another part.

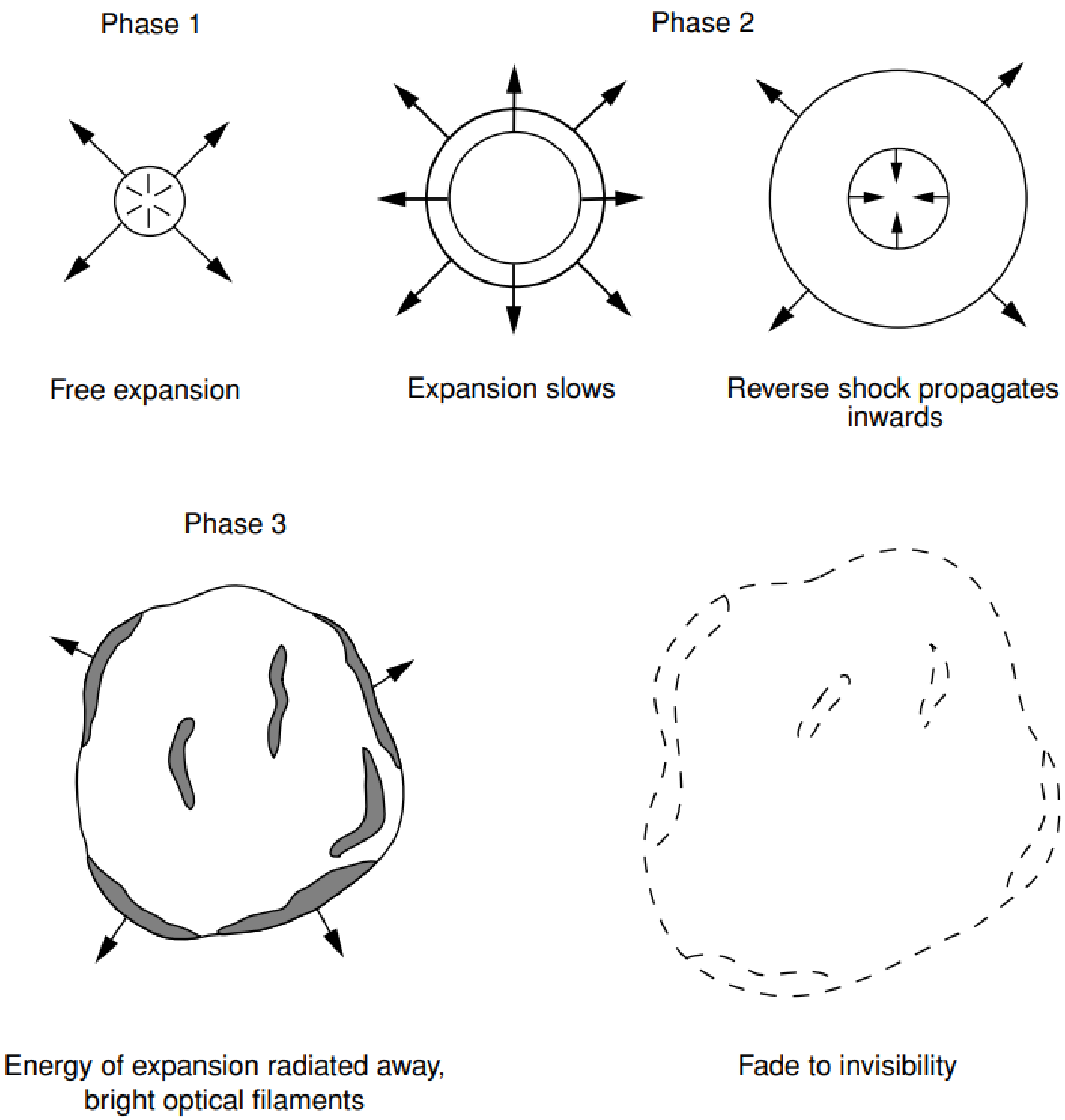

FIGURE 3.2: Evolution of a SNR. In the first phase, the remnant expands freely into the ISM. It incorporates an increasing amount of matter, thus cooling down. The reverse shock wave forms which finally travels inward. The Sedov-Taylor phase leads into the radiation phase in which the remnant loses an extensive amount of energy through radiation. Eventually, the SNR cannot be distinguished from the surrounding ISM [Seward & Charles, 2010].

4 Instruments and Observation Surveys

This section gives a short overview of the instruments utilized to detect and identify objects such as YSOs and SNRs. Given the distinct physical nature of these two objects, different types of telescopes are required to detect YSOs and SNRs.

4.1 Infrared Observations

As argued in section 2.2, Young Stellar Objects (YSOs) exhibit an infrared excess and are thus observed in the infrared range of the electromagnetic spectrum which roughly spans from $\lambda \approx 700\,\mathrm{nm}$ to $\lambda \approx 1\,\mathrm{mm}$.

An infrared observatory can be ground-based, air-borne or it may be launched into space. Whichever type of observatory is selected, its instrument is equipped with an infrared camera containing a specially designed infrared detector which has to be cooled down to and operated at cryogenic temperatures, meaning temperatures below 120 K (−153.15 °C)[2].

All lists of confirmed YSOs and YSO candidates utilized in this work (see the following section 5) utilized data from the *Spitzer Space Telescope* (see 4.1.1) or ground-based observatories (see 4.1.2).

4.1.1 Spitzer Space Telescope

The *Spitzer Space Telescope* is one of the four space telescopes in NASA's Great Observatories Program. Each of the observatories was constructed to observe the universe in a different wavelength range. *Spitzer* was in charge of observing at infrared wavelengths from $\lambda \approx 3.6\,\mu\mathrm{m}$ to $\lambda \approx 160\,\mu\mathrm{m}$.

The payload consisted of a 0.85 m telescope and three science instruments: two cameras for taking images, the Infrared Array Camera (IRAC) and the Multiband Infrared Photometer for *Spitzer* (MIPS), as well as a spectrograph, the Infrared Spectrograph (IRS). IRAC operated at four wavelengths ($3.6\,\mu\mathrm{m}, 4.5\,\mu\mathrm{m}, 5.8\,\mu\mathrm{m}, 8.0\,\mu\mathrm{m}$) and MIPS at three additional ones in the mid-/far-infrared range ($24.0\,\mu\mathrm{m}$, $70.0\,\mu\mathrm{m}$, $160.0\,\mu\mathrm{m}$).

The telescope was launched in 2003 and placed into a - at that time - novel heliocentric orbit in which the spacecraft trails the earth. Such an orbit is advantageous for an infrared telescope as it is not affected by the heat radiated by the

---

[2] `https://dictionary.iifiir.org/index.php?inputLang=en&truncPos=right&srchTerm=cryogenic&outputLang=xx&defnLang=en&submit=View+results`, accessed on 30.09.2022.

earth.

The cryogenic coolant, liquid helium, necessary to operate the far-infrared instruments lasted until 2009. The telescope continued operating while only the IRAC camera remained collecting data at 3.6 µm and 4.5 µm for eleven more years. In January 2020 *Spitzer* was officially decommissioned. The James Webb Space Telescope can be named its successor [Werner et al., 2004].

The Surveying the Agents of a Galaxy's Evolution (SAGE) survey was a Legacy project to image the Large Magellanic Cloud (LMC). In total an area of $7^\circ \times 7^\circ$ was mapped using the IRAC and MIPS cameras on board the *Spitzer Space Telescope*. The science drivers for this program include the detection of the population of infrared point sources as well as diffuse and molecular clouds and HII regions. Through such observation star formation, properties of evolved stars and the interstellar medium (ISM) could be investigated [Meixner et al., 2006].

The relevance for this work lies in one of the products of this survey, the SAGE IRAC and MIPS point-source catalogs which contain photometric data in various wavelengths for about three million point sources. Through this catalog YSOs and YSO candidates could be identified.

4.1.2 Two-Micron All Sky Survey

The Two Micron All Sky Survey (2MASS) is an all-sky near-infrared survey. Over the span of four years (1997 – 2001) two ground-based 1.3 m telescopes mapped the entire celestial sphere in three bands: J (1.25 µm), H (1.65 µm), and K_s (2.16 µm). The 2MASS project improved the sensitivity in these bands a 80.000-fold. The Whipple Observatory on Mount Hopkins in Arizona covered the northern sky, while the southern one was observed from the Cerro Tololo Inter-American Observatory (CTIO) in Chile [Skrutskie et al., 2006].

As one of the results, a point-source catalog was established which documented the positions and flux densities for 471 million stars and other unresolved objects [California Institute of Technology, 2006]. Further, the mission identified 1.6 million objects in an extended source catalog and produced millions of images depicting the infrared sky [Skrutskie et al., 2006].

4.1.3 InfraRed Survey Facility

The InfraRed Survey Facility (IRSF) is a collaboration project between Japan and South Africa which started its observations of the Magellanic Clouds at the end of 2000. The observatory consisted of a 1.4 m telescope equipped with a newly developed camera. The survey was carried out in three near-infrared bands JHK_s with a finer resolution and higher sensitivity than that of previous instruments (also those of 2MASS). The resulting point source catalog consisted of 14.8 million sources for the LMC [Kato et al., 2007].

4.2 Multiwavelength observations of supernova remnants

Supernova remnants are multiwavelength sources. The radiation processes that provide information on their properties involve photons with wavelengths in all parts of the electromagnetic spectrum. The detection of photons in different wavelength bands and thus different energies requires separate instruments. Radio and optical observations can be performed from earth, whereas X-ray observatories have to be placed in space since X-ray radiation is absorbed by the earth's atmosphere.

In radio astronomy, the parameter used to describe electromagnetic waves is the frequency ν [Hz] instead of wavelength λ [m]. The radio band spans over seven orders of magnitude in energy (or frequency ν or wavelength λ). The most scientific observations are performed between $\nu = 3\,\mathrm{kHz}$ ($\lambda = 100\,\mathrm{km}$) and $\nu = 900\,\mathrm{GHz}$ ($\lambda < 1\,\mathrm{mm}$)[3]. Radio telescopes are located all over the world (and in space) and can be connected to perform interferometry to enlarge the angular and therefore the spatial resolution. Ground-based radio observations can be performed during the day, at night as well as on (slightly) cloudy days.

Optical observations of supernova remnants outside our own Galaxy are difficult due to interstellar absorption. However, the Large Magellanic Cloud provides an unique environment for such a task due to its proximity and low foreground absorption [Smith & the MCELS Team, 1998]. Foreground absorption describes the presence of absorbing matter between the astronomical source and the observer. The Magellanic Cloud Emission-Line Survey (MCELS) is a project aiming for the investigation of the Magellanic Clouds in multiple optical emission lines. The three narrow-band filters utilized in the survey depict the distribution of doubly-ionized oxygen [O III], singly-ionized sulfur [S II] and neutral hydrogen Hα (see table 4.1). The Hα spectral line encodes the energy of a photon which is emitted when an electron changes its energy level from the third ($n = 3$) to the second lowest ($n = 2$) level. Observations were performed with the Curtis Schmidt telescope at the Cerro Tololo Inter-American Observatory (CTIO) in Chile [Smith & the MCELS Team, 1998].

---

[3] `https://public.nrao.edu/radio-astronomy/the-science-of-radio-astronomy/`, accessed on: 12.10.2022

TABLE 4.1: Narrow-band filters, their central wavelengths λ and bandwidths $\Delta\lambda$ utilized at the UM/CTIO telescope during the MCELS survey [Smith & the MCELS Team, 1998]. The colors red, green and blue are utilized to distinguish between the filters in a three-color composite image (see section 6.1).

Filter	O III	Hα	S II
Color	red	green	blue
λ [nm]	500.7	656.3	672.4
$\Delta\lambda$ [nm]	4	3	5

Most radiation processes in supernova remnants involve electrons changing their energy levels. Especially for young remnants, these transitions cause bright X-ray emission. XMM-Newton (Xray Multi-Mirror Mission) is a X-ray space observatory launched in 1999 by the European Space Agency and still being operated to this date. It is the largest satellite that has ever been built for science purposes in Europe[4]. The XMM-Newton spacecraft carries three identical X-ray telescopes, each consisting of 58 nested mirrors[4]. Further instruments include spectrometers and the so called optical monitor allowing to make simultaneous observations in both X-ray (which is the primary mission goal) as well as optical and ultraviolet bands. XMM-Newton has performed about 200 observations of the Large Magellanic Cloud in which specific objects were investigated. Through the telescopes' data products, up to 20 sources were either newly discovered as supernova remnants or their remnant nature was confirmed [Maggi et al., 2016].

---

[4] `https://www.esa.int/Science_Exploration/Space_Science/XMM-Newton_overview`, accessed on: 13.10.2022.

5 Data Catalogs

This section describes the data catalogs which provide samples of SNRs and YSOs for the analysis in this work.

5.1 Young Stellar Objects

This subsection introduces three papers in which YSOs and YSO candidates were identified using various data sets and selection criteria. The YSOs in the respective catalogs will be visually displayed. Figure 5.1 reveals a reference map of the LMC, depicting the distribution of the Hα spectral line. The ICRS coordinates (ep=J2000) of the LMC are R.A. = 05:23:34.6000, Dec = -69:45:22.000 [Smith et al., 2004].

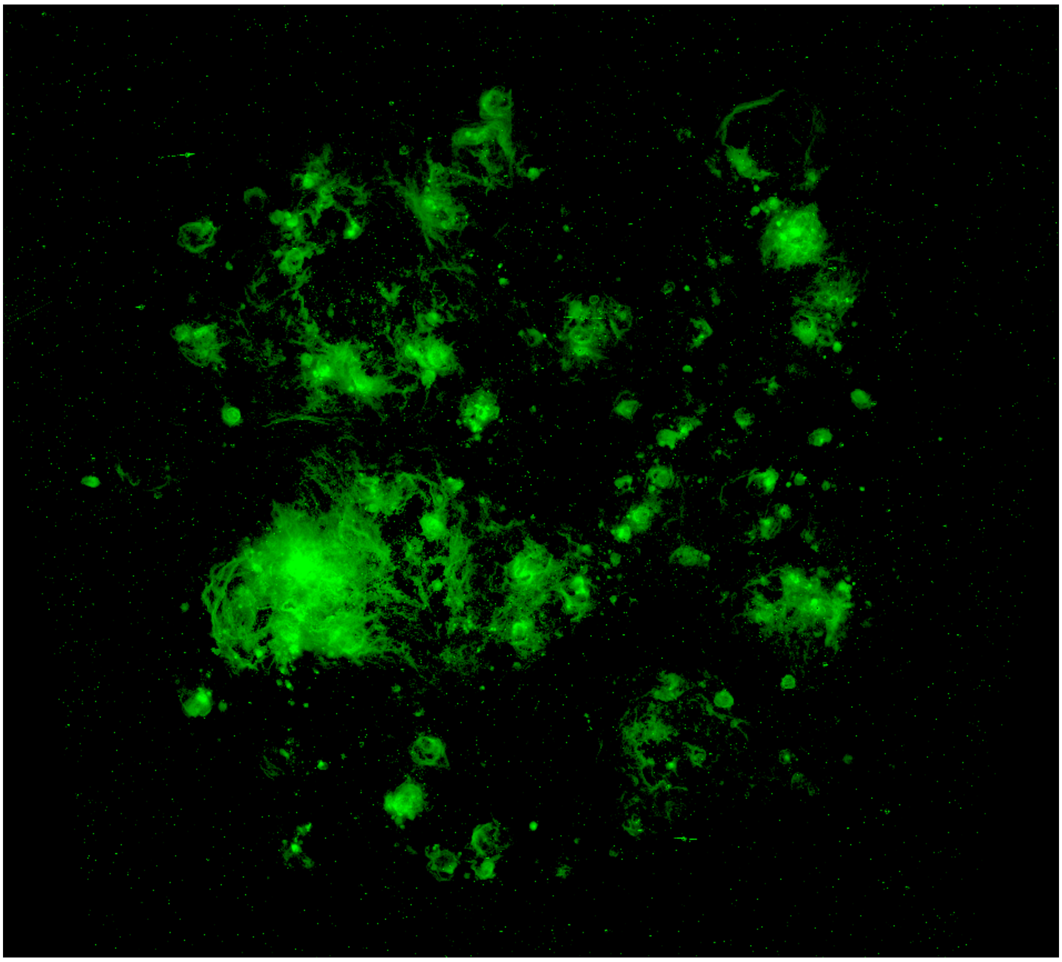

FIGURE 5.1: The LMC is depicted through the distribution of the Hα line obtained from MCELS.

5.1.1 Catalog 1: Whitney et al., 2008

[Whitney et al., 2008] analyzed *Spitzer Space Telescope* data and presented 1197 new YSOs candidates. These were selected from the SAGE Point Source Catalog of IRAC and MIPS 24.0 µm and the 2MASS JHK_s catalog based on their colors and magnitudes.

The approach is as follows: with the knowledge of star formation and evolution models of spectral energy distributions (SEDs) can be generated. Then, predictions of the stars' locations in various combinations of color-magnitude (CMDs) and color-color diagrams (CCDs) can be made. These theoretical calculations can be compared with observations and utilized to determine the evolutionary stages of YSOs.

To prevent their candidate list from being largely contaminated by other bright infrared sources such as galaxies, evolved stars and planetary nebulae, only selected regions of color-magnitude space were considered. As a result, the list is biased towards *intermediate*- and *high-mass* stars in *young* evolutionary stages (*class I*).

Figure 5.2 depicts the location of the identified YSOs in the LMC.

5.1.2 Catalog 2: Gruendl & Chu, 2009

In addition to the identical data sets from the SAGE and 2MASS surveys as in catalog 1, data products of a previous *Spitzer* survey[5] were made use of for finding YSOs.

However, a varied approach was selected for the analysis in order to carry out an independent search: Firstly, inspecting infrared images revealed groups associated with YSO candidates. Through color-magnitude diagrams candidates were further selected and separated from contaminants. Secondly, each candidate was investigated in more detail through their spectral energy distribution and other characteristics.

The final catalog consists of three subgroups: 855 definite and 317 probable YSOs as well as 213 possible sources for which a YSO nature could neither be confirmed nor refuted. It is stated that the lists are expected to be biased towards *class I and II intermediate*- and *high-mass* sources, though there was no calculations done to determine the evolutionary stages of the YSOs.

---

[5] `https://ui.adsabs.harvard.edu/abs/2004sptz.prop..142L/abstract`

In this work the distinction in three groups (definite, probable, possible) was maintained. Figure 5.3 distinguishes between the sets by using dissimilar colors (see table 5.1).

TABLE 5.1: Documentation of the colors utilized to distinguish the three classification groups in catalog 2.

Catalog	Subcategory	Color	Reference
2	definite probable possible	yellow cyan white	[Gruendl & Chu, 2009]

5.1.3 Catalog 3: Carlson et al., 2012

Infrared data from the SAGE program and near-infrared photometry from the IRSF was combined with optical (photometric) measurements from surveys of the Magellanic Clouds[6].

[Carlson et al., 2012] employed similar methods to [Gruendl & Chu, 2009] in identifying YSOs, but introduced new selection criteria (which will not be discussed here). Instead of searching the entire LMC, the team focused on nine HII regions (figure 5.4) as well as on finding *lower-mass* YSOs.

The final YSO candidate list contained 918 previously unknown sources and increased the number of known YSOs in the nine HII regions by a factor of 3. As more evolved YSOs which are less embedded in dust are fainter in the infrared regime, the resulting catalog consisted of more class I than II/III YSOs.

---

[6] `https://ui.adsabs.harvard.edu/abs/1999IAUS..190..320Z/abstract`

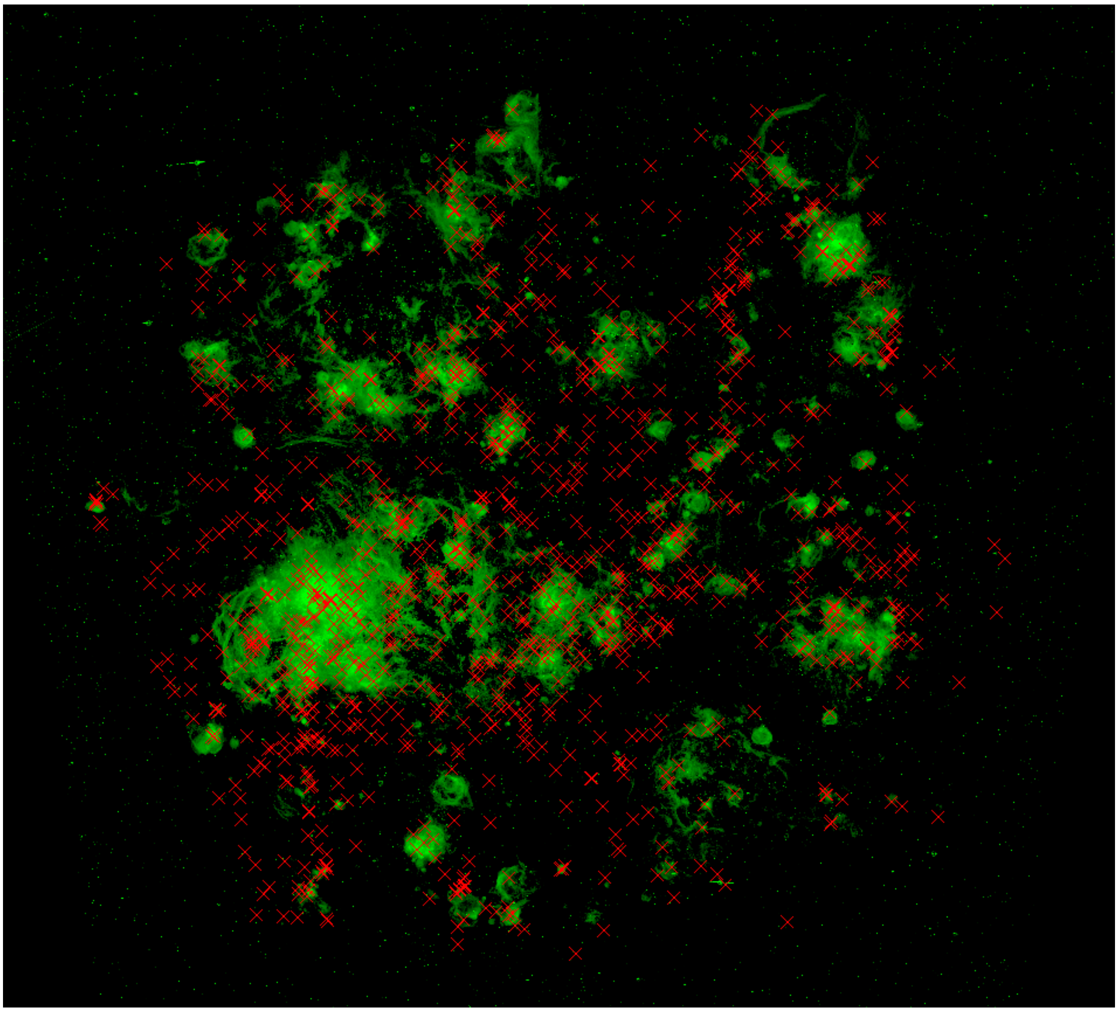

FIGURE 5.2: The location of YSOs from catalog 1 [Whitney et al., 2008]. The LMC is depicted through the distribution of the Hα spectral line obtained from MCELS [Smith et al., 2004].

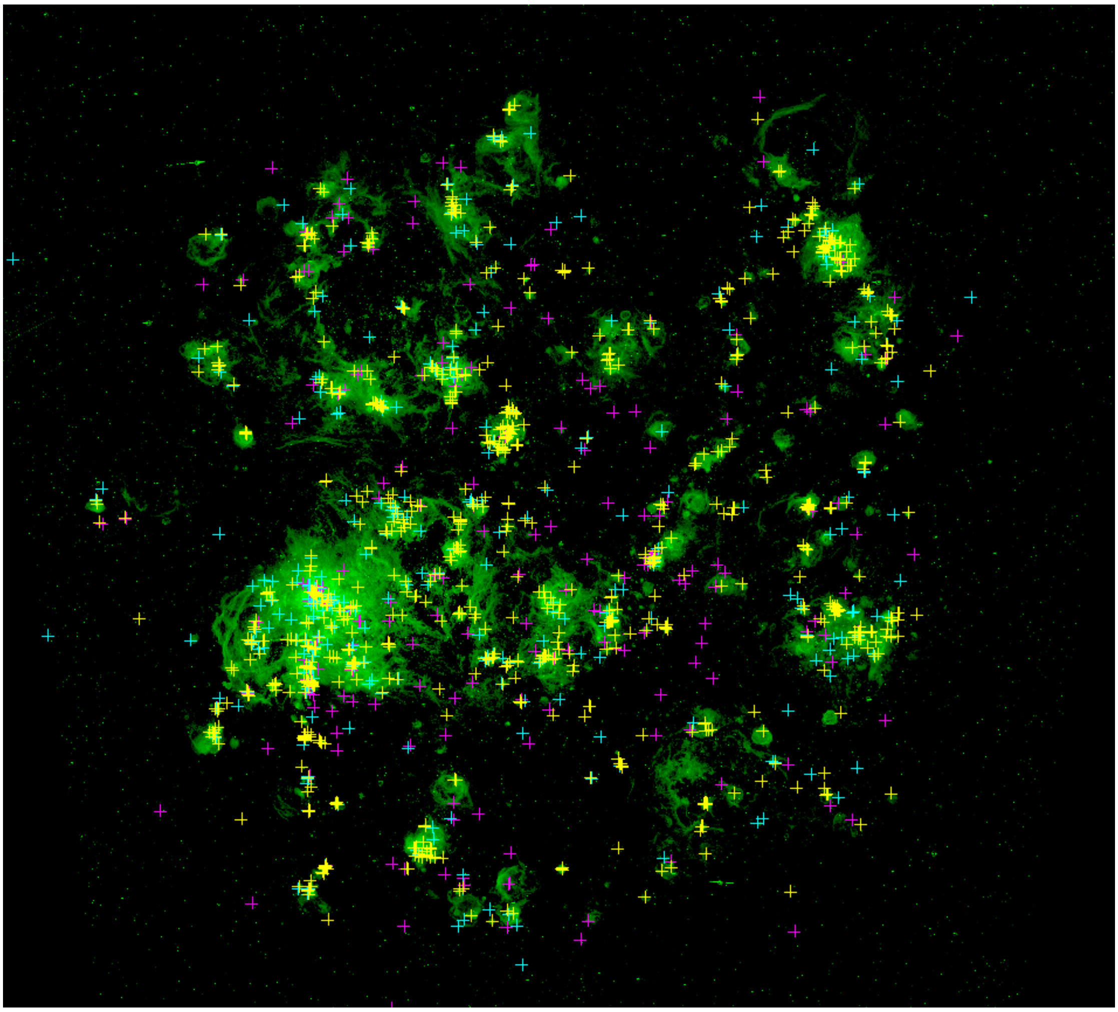

FIGURE 5.3: The location of YSOs from catalog 2 [Gruendl & Chu, 2009]. The colors distinguish sources classified as definite (yellow), probable (cyan) and possible (white) YSOs. The LMC is depicted through the distribution of the Hα line obtained from MCELS [Smith et al., 2004].

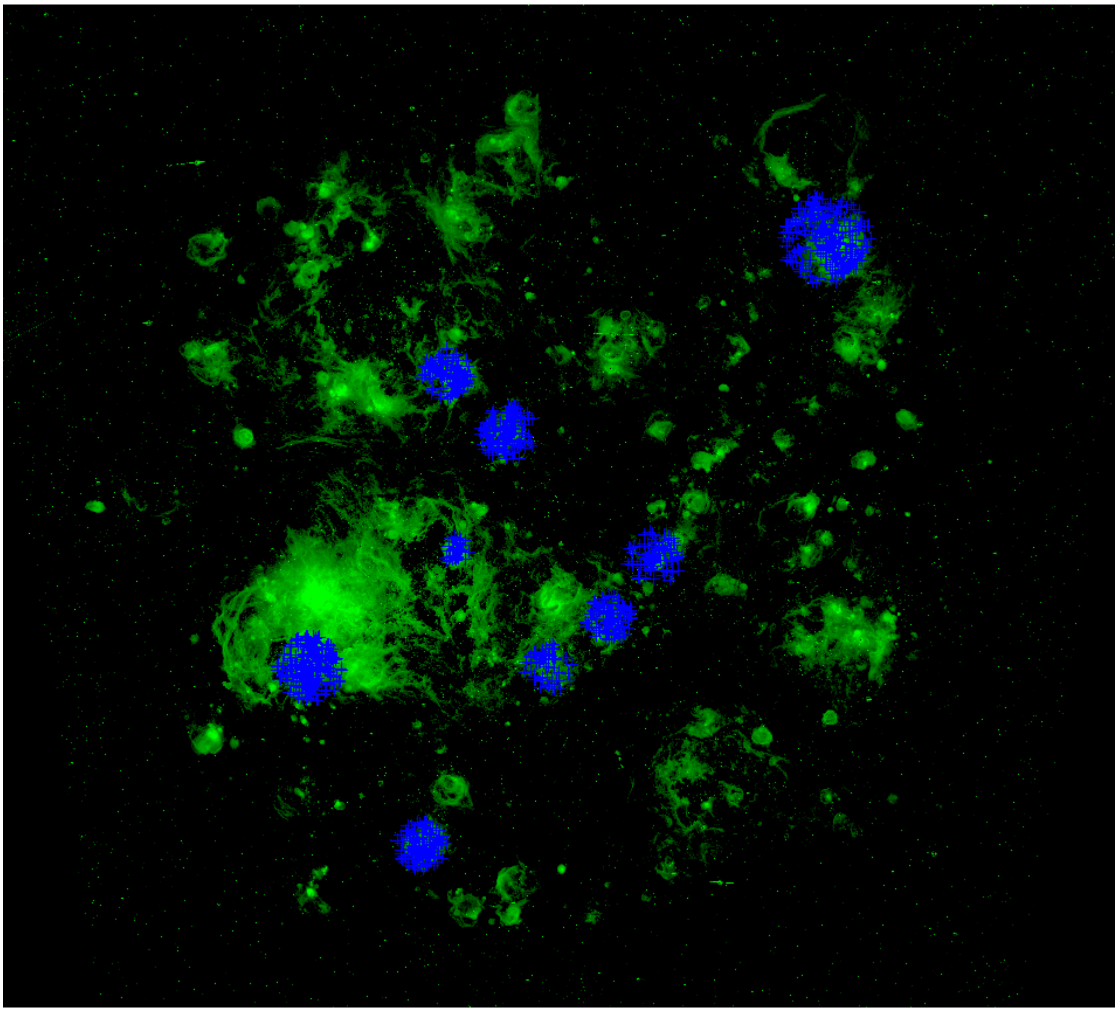

Figure 5.4: The location of YSOs in the nine HII regions from catalog 3 [Carlson et al., 2012]. The LMC is depicted through the distribution of the Hα spectral line obtained from MCELS [Smith et al., 2004].

5.2 Supernova Remnants

The following subsection shortly introduces three catalogs of SNRs and SNR candidates in the LMC that were utilized in this work. Each catalog lists SNRs as well as candidates which were selected as such in different wavelength bands. There was no distinction made between remnants and remnant candidates in this analysis. They were treated on equal footing. In the following, they are differentiated for correctness.

[Maggi et al., 2016] present a list of 59 definite SNRs. XMM-Newton data are available for the majority of these sources (see section 4.2). If this was not the case, data from other X-ray telescopes (Chandra, ROSAT) was employed to examine the objects.

[Bozzetto et al., 2017] report a sample consisting of 74 objects from which 59 are already confirmed SNRs which coincide with the objects from [Maggi et al., 2016]. The remaining 15 are classified as candidates. Seven were presented for the first time. The candidates from this sample were not subject of this analysis. The remnants were studied in the radio domain of the electromagnetic spectrum.

[Yew et al., 2021] compiled a list of three SNRs and 16 SNR candidates through optical images from the MCELS survey (see section 4.2).

The following images depict the distribution of SNRs throughout the LMC separately for all three catalogs (figures 5.5, 5.6, 5.7). Figure 5.8 combines all sources into one image. The overlap in samples from the X-ray and radio observations for 59 of the confirmed SNRs is evident.

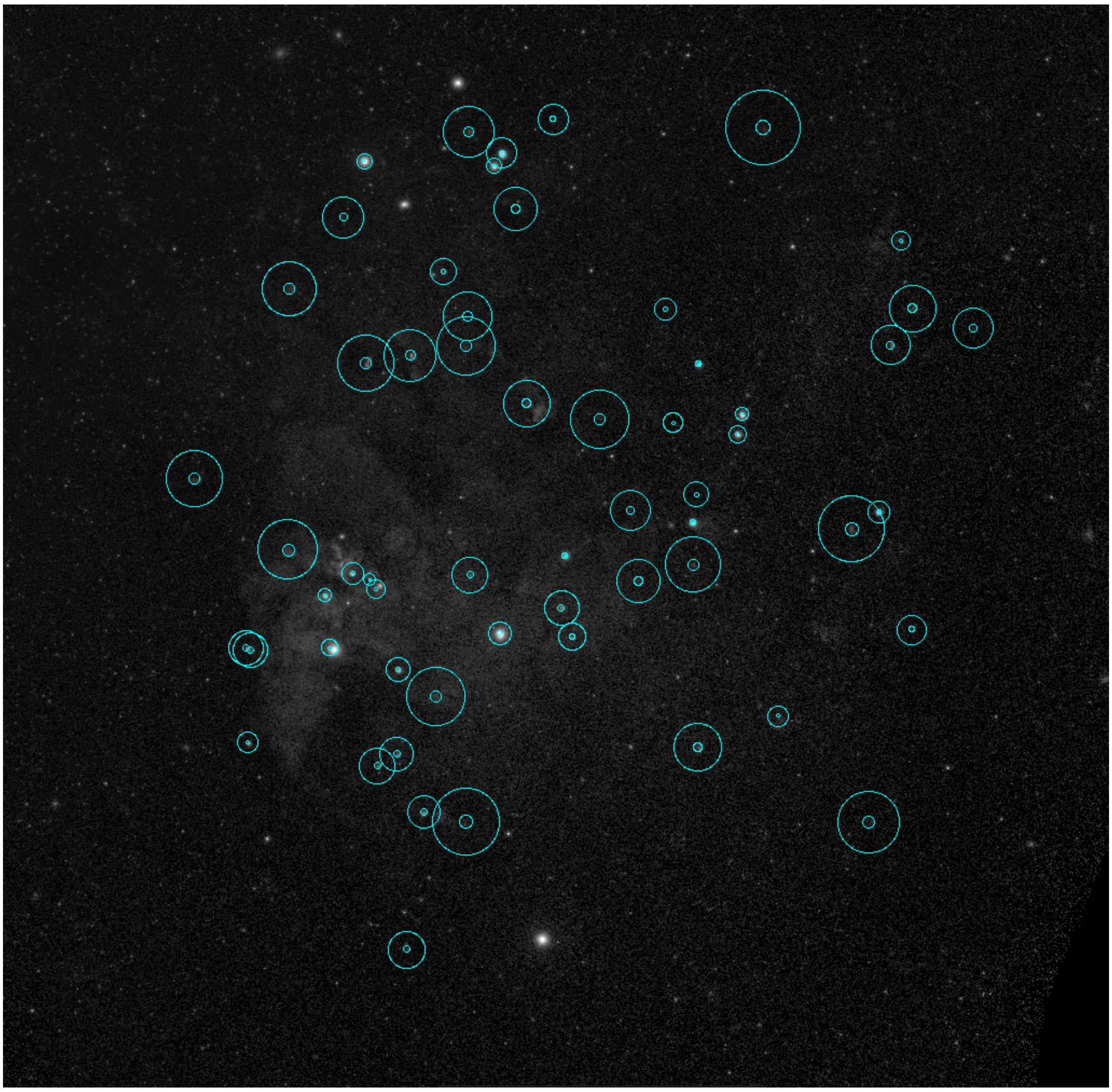

FIGURE 5.5: The distribution of SNRs in the X-ray band [Maggi et al., 2016]. Each SNR is depicted as two circles. The smaller circle represents its true size. The second circle is five times larger and is shown to make the SNRs easier to identify. The X-ray image (0.2 – 4.5 keV) of the LMC was obtained by the X-ray telescope eROSITA (see section 6.1).

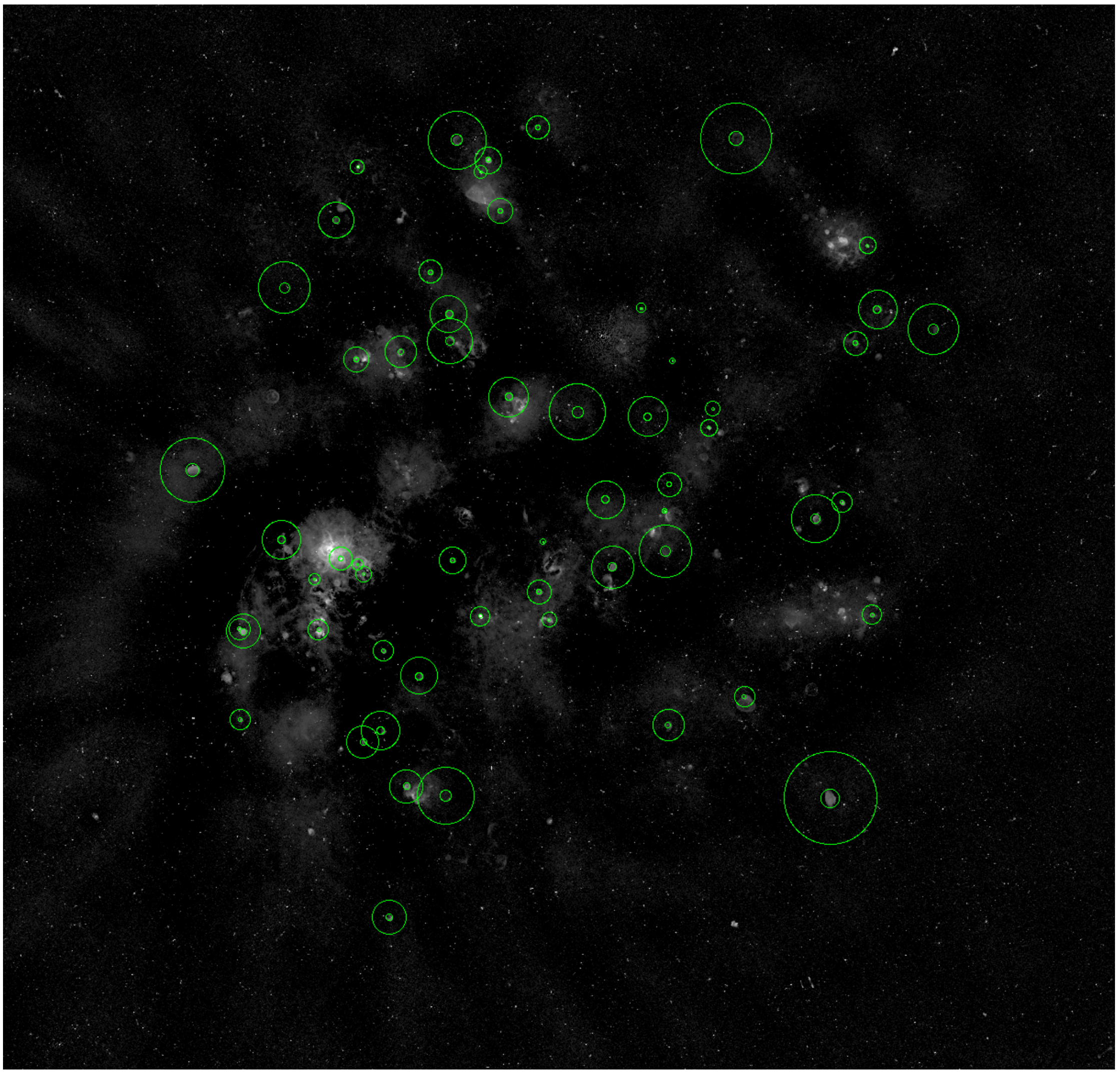

Figure 5.6: The distribution of SNRs in the radio band [Bozzetto et al., 2017]. Each SNR is depicted as two circles. The smaller circle represents its true size. The second circle is five times larger and is shown to make the SNRs easier to identify. The radio image of the LMC was obtained by the Australian observatory ASKAP (see section 6.1) [Pennock et al., 2021].

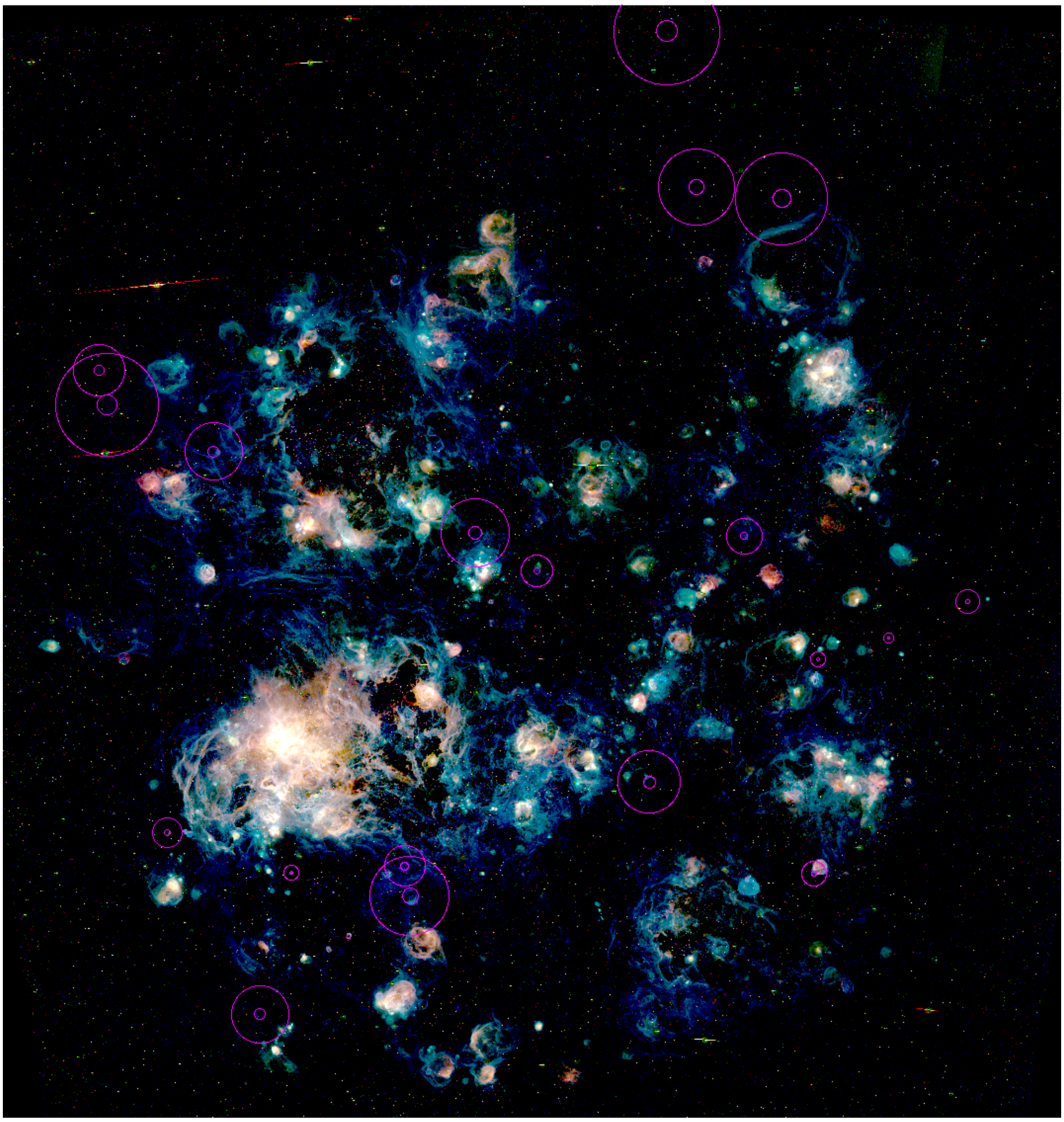

FIGURE 5.7: The distribution of 19 SNRs in the optical band [Yew et al., 2021]. Each SNR is depicted as two circles. The smaller circle represents its true size. The second circle is five times larger and is shown to make the SNRs easier to identify. The optical image of the LMC is a three-color composite and was obtained by a ground-based telescope in Chile and was processed for this work (see section 6.1) [Smith et al., 2004].

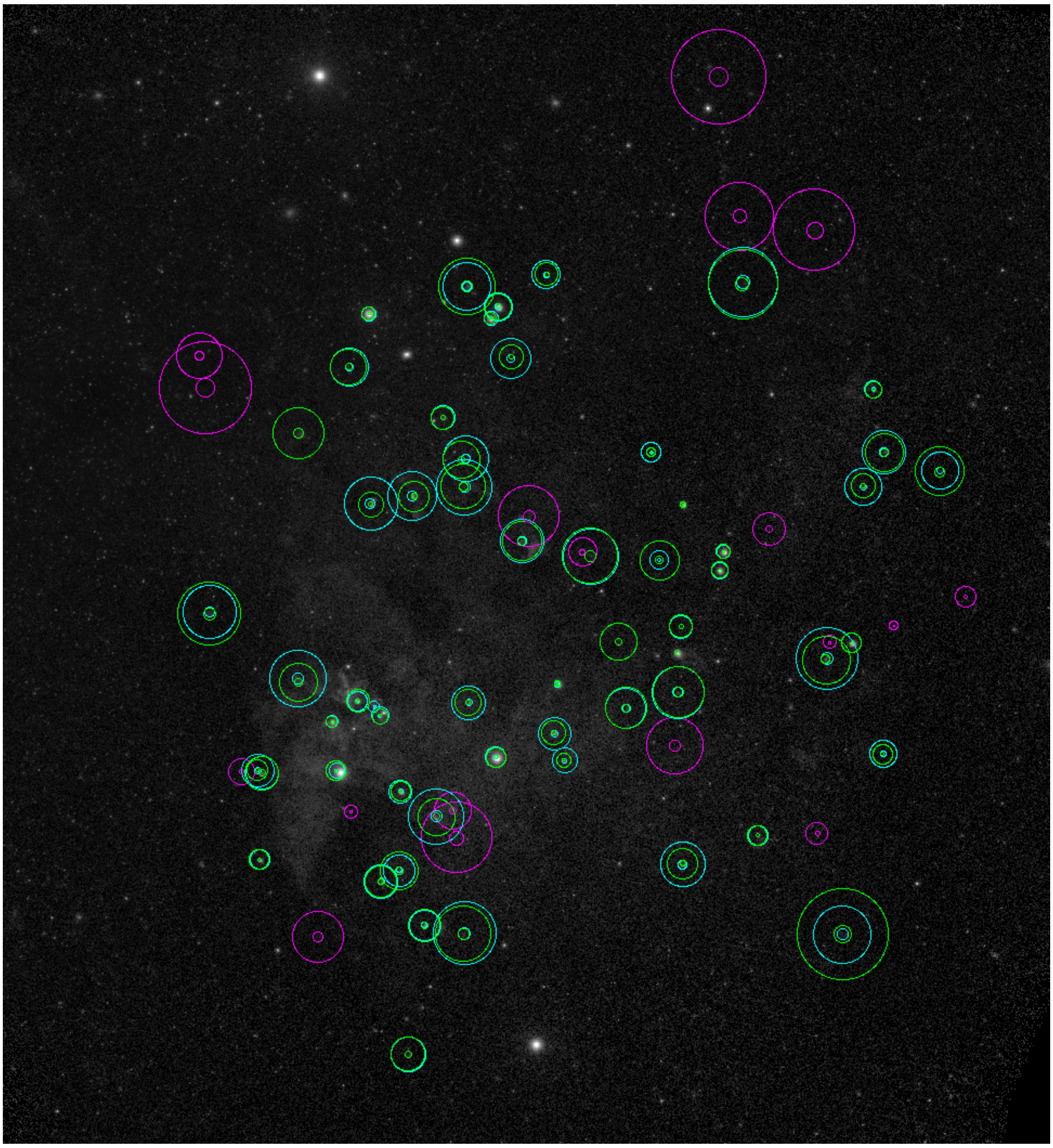

FIGURE 5.8: The LMC in the X-ray band (see section 6.1) and all SNRs. The colors distinguish between the three SNR catalogs: cyan [Maggi et al., 2016], green [Bozzetto et al., 2017], magenta [Yew et al., 2021]. The overlap in remnant samples from [Maggi et al., 2016] and [Bozzetto et al., 2017] is apparent.

6 Photometric Analysis

Photometry is a technique in astronomy that measures the flux radiated by any astronomical object such as stars, supernova remnants or even entire galaxies. Magnitudes and color indices are defined to determine various properties of objects. The luminosity can be calculated if the distance to the radiation source can be established. Subsequently, variations in brightness can be studied so that extrasolar planets can be detected in example. Furthermore, temperature and chemical composition can be determined using photometric methods.

This work intends to investigate Young Stellar Objects (YSOs) around Supernova Remnants (SNRs) in the Large Magellanic Cloud (LMC); in particular, whether SNRs have an effect on the evolution of YSOs in their vicinity.

In a first step, various regions are defined around a SNR to group the YSOs by their distance to the SNRs. Therefore, the definition relies on the 2D projection of positions of YSOs and SNRs in the LMC. In a second step, the positions of YSOs in the different regions were examined in color-magnitude (CMD) and color-color diagrams (CCD) in order to compare the brightness of the YSOs. In the last step, the Spectral Energy Distribution (SED) is plotted and calculated the spectral index α (see chapter 6.4) for the YSOs separately for each defined region and catalog.

6.1 Regions

To assess the effects of SNRs on star forming regions and explicitly on YSOs in their proximity, three regions around a SNR were specified and the YSOs were grouped according to their distance to the remnants. The size of the regions was selected upon empirically studying the relative positions of SNRs and YSOs in the LMC. Table 6.1 specifies the exact extent as well as the names which the regions will be addressed by in the following.

TABLE 6.1: Definition of three regions around a SNR.

Region	inner	edge	outer	none
Definition	$< 1R$	$1R - 3R$	$3R - 5R$	$> 5R$

A YSO is classified as belonging to the *inner* region with the highest priority. This implies that if two SNRs are close to each other (see figure 6.1) and one YSO would be identified as being in the *inner* region of one SNR and in the *edge* region of the other, the YSO is assigned to the *inner* region. The same principle applies to the *edge* and *outer* regions: the *edge* region is prioritized over the *outer* region and the *outer* region over the *none* region.

The number of YSOs associated with each group decreases in the following way: none - outer - edge - inner. Consequently, the *inner* region consists of the lowest number of YSOs, the *none* region consists of the highest number.

Figure 6.1 depicts one SNR with YSOs in the selected regions used in the analysis. All other SNRs are documented in the same way in appendix C.

A supernova remnant is depicted through a circle with the radius given in the data catalogs (see section 5.2). If the supernova remnant was not of spherical symmetry, but of elliptical shape, it was approximated by a circle nevertheless. Its radius was then the value of the semi-major axis. Due to the overlap in the samples for SNRs identified in the radio [Bozzetto et al., 2017] and X-ray bands [Maggi et al., 2016], the larger of the two radii was selected.

For each SNR three images are displayed which depict the SNR in the three wavelength bands. Green circles represent SNRs which were identified in radio, cyan circles in X-ray and magenta circles in optical observations. The center of the image is placed at the coordinates of the corresponding SNR. All images have the same size (unless stated otherwise in the caption) and span an area of $(x, y) = (\text{R.A.}, \text{Dec}) = (8', 45')$. The radius of the smallest circle $(1R)$ - the actual size of the SNR or its semi-major axis - is given in the caption of the image for the corresponding SNR. YSOs are represented by a + sign and the colors differentiate between the different catalogs (table 6.2).

TABLE 6.2: Documentation of the colors for the three YSO-catalogs.

Catalog	Subcategory	Color	Reference
1		red	[Whitney et al., 2008], section 5.1.1
	definite	yellow	
2	probable	cyan	[Gruendl & Chu, 2009], section 5.1.2
	possible	white	
3		blue	[Carlson et al., 2012], section 5.1.3

The X-ray image was obtained by the first telescope module of the X-ray telescope eROSITA (extended ROentgen Survey with an Imaging Telescope Array) during the first survey eRASS1 in the 0.2 – 4.5 keV regime. The Australian Square Kilometre Array Pathfinder (ASKAP) telescope mapped the LMC at the radio frequency 888 MHz [Pennock et al., 2021]. The optical image is a three-color composite in which the color red depicts the distribution of the doubly-ionized oxygen [O III], the color green depicts the detection of the hydrogen spectral line Hα and the color blue depicts the distribution of the singly-ionized sulfur [S II] (see table 4.1) [Smith et al., 2004]. All three raw images were obtained as part of the MCELS survey (see section 4.2) and processed for this work.

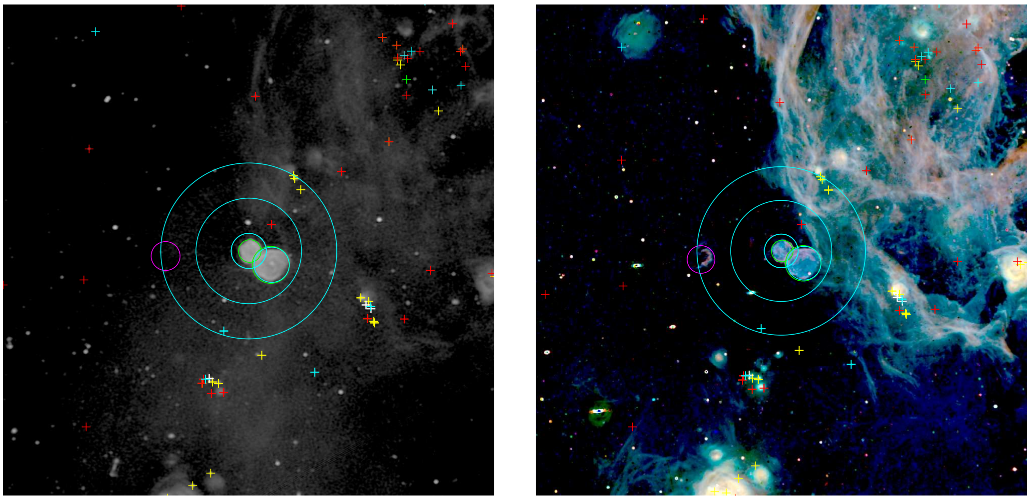

(A) Radio (B) Optical

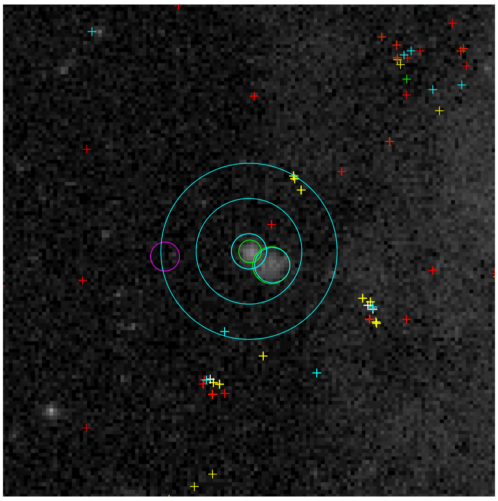

(C) X-ray

Figure 6.1: MCSNR J0547−7024, LHG 89
ICRS coordinates (ep=J2000): R.A. = 05:47:48.8, Dec = −70:24:52.0
$R = 60''$

6.2 Color-Magnitude and Color-Color Diagrams

To analyze the brightness of the YSOs in the four groups (inner, edge, outer, none) defined in the previous section, the magnitudes and color indices are plotted in color-magnitude (CMD) and color-color diagrams (CCD).

The YSOs of the three catalogs are depicted in separate diagrams, since it became apparent that not every data set was calibrated in the same way.

6.2.1 Color-Magnitude Diagrams

Starting with color-magnitude diagrams, the color index of two neighbouring wavelengths (e.g., [3.6 – 4.5]) is plotted against the magnitude of the shorter wavelength (e.g., [3.6]). Following the discussion in section 2.3.2 the plot shows the relation between temperature (from the color index) and luminosity (from the magnitude) for main-sequence stars. It is to be noted that for YSOs which are obscured by dust these parameters rather reflect the properties of the dust surrounding the star than its surface [Stahler & Palla, 2008]. The diagrams are utilized to determine spectral types of stars and evolutionary stages of YSOs.

In total, diagrams for six wavelength pairs were plotted, resulting in six diagrams for each catalog ($[J-H]$ vs $[\mathrm{m}_J]$, $[H-K]$ vs $[\mathrm{m}_H]$, $[K-3.6]$ vs $[\mathrm{m}_K]$, $[3.6-4.5]$ vs $[\mathrm{m}_{3.6}]$, $[4.5-5.8]$ vs $[\mathrm{m}_{4.5}]$, $[5.8-8.0]$ vs $[\mathrm{m}_{5.8}]$, $[8.0-24]$ vs $[\mathrm{m}_{8.0}]$). Since magnitudes were used in the diagram, both the $x-$ and $y-$axis are logarithmic. Larger magnitude values correspond to lower brightness in the respective band. Higher color indices indicate redder, meaning younger, stars.

For each CMD the total number N_{tot} of YSOs in the catalog and the number N_{mag} of YSOs for which values for the respective magnitude combinations were available are given. In example, considering the $[\mathrm{m}_J]$ versus $[J-H]$ plot, magnitudes in both the J-band and the H-band need to be documented in the catalog to create the CMD. Not all YSOs had magnitudes obtainable for each wavelength. N_{mag} is always smaller than N_{tot}. In addition, the number of YSOs assigned to the four regions is pointed out in brackets after the name of the region.

An example of the result is figure 6.2 depicting data from catalog 3 (section 5.1.3) [Carlson et al., 2012]. The general trend consistent in all CMDs indicates that the color indices of *inner* region YSOs extend less to higher, redder values. The CMDs for catalog 1 and 2 can be viewed in the appendix A, figures A.1 and A.2–A.4. The statement above is accurate for catalog 1 except for the $[K-3.6]$ vs $[\mathrm{m}_K]$ and $[8.0-24]$ vs $[\mathrm{m}_{8.0}]$ combinations. In the former, *inner*, *edge* and *outer* region YSOs exhibit no noticeably different extent in $[K-3.6]$, only YSOs in the *none* region are redder. In the latter, *inner* region YSOs are less blue (lower $[8.0-24]$) than the rest of the sources. For catalog 2 YSOs (group *definite*), the statement above can only be confirmed for the $[J-H]$ vs $[\mathrm{m}_J]$ and $[8.0-24]$ vs $[\mathrm{m}_{8.0}]$ combinations. For the $[K-3.6]$ vs $[\mathrm{m}_K]$ it is to be noted that *edge*, *outer* and *none* region YSOs are bluer (lower $[K-3.6]$) than *inner* region sources. The *inner* region YSO candidates for catalog 2 (group *probable* and *possible*) have a small sample size (see the following paragraph) and no statements such as the one above are made.

To be able to compare the positions of YSOs in the four regions in each diagram in more detail, a density function estimation was performed using the method `scipy.stats.gaussian_kde()` in Python[7]. The four regions (table 6.1) are now shown with the contours of the density function in different diagrams. The width of the $x-$ and $y-$axis is identical in each CMD, respectively. That way it is straightforward to compare the distribution of the YSOs. The respective positions of YSOs in the four regions were evaluated by comparing the location of the maximum of the density functions, the broadness and the overall shape of the distribution. If the *inner* region consisted of less than 10 YSOs, the sample size was considered too small and no comparison between the *inner* and the other three regions was conducted. Nevertheless, the CMDs were plotted and can be viewed in appendix A. In the following, the CMDs which showed the most significant differences in the distribution of the *inner* and remaining regions are discussed.

Figure 6.3 depicts the $[4.5-5.8]$ vs $[\mathrm{m}_{4.5}]$ diagram for catalog 1 (section 5.1.1). The YSOs in the *inner* region have a lower limit for $[\mathrm{m}_{4.5}]$ at ~ 8.5 mag, while YSOs in the *edge*, *outer* and *none* regions also have lower magnitudes. *Inner* region YSOs exhibit an upper limit at about 14.5 mag, whereas YSOs in other regions have even higher $[\mathrm{m}_{4.5}]$ values, especially towards larger $[4.5-5.8]$ between 2 mag and 3 mag. A higher color index $[4.5-5.8]$ above $[\mathrm{m}_{4.5}] = 15$ mag (faint sources) is associated with redder, younger YSOs, meaning class 0/I (figure 1a, [Whitney et al., 2008]).

In contrast to the $[4.5-5.8]$ vs $[\mathrm{m}_{4.5}]$ diagram for catalog 1, the YSOs in the *inner* region for catalog 3 (figure 6.4) are slightly more populated towards higher $[4.5-5.8]$ and younger stars (class 0/I). The *edge*, *outer* and *none* YSOs have a higher density towards lower $[4.5-5.8]$ and older stars (class II). Although this seems to be contradictory at first, one should be careful in drawing conclusions on the evolutionary stages in the different regions from just one CMD.

---

[7] `https://docs.scipy.org/doc/scipy/reference/generated/scipy.stats.gaussian_kde.html`, accessed on: 15.10.2022.

Considering the $[8.0-24]$ vs $[m_{8.0}]$ diagram for catalog 3 (figure 6.5), the *inner* region YSOs are more confined in $3\,\mathrm{mag} < [8.0-24] < 5.5\,\mathrm{mag}$. Other region YSOs extend towards the red $[8.0-24] > 5.5\,\mathrm{mag}$. That *inner* region YSOs have a lower magnitude $[m_{8.0}]$ (brighter sources), whereas YSOs in the remaining regions are clumped around a higher magnitude $[m_{8.0}] \sim 13-14\,\mathrm{mag}$ (fainter sources) seems to be apparent.

The shape of the density function for catalog 2 group *definite inner* region YSOs in the $[8.0-24]$ vs $[m_{8.0}]$ diagram (figure 6.6) is more narrow in color ($3\,\mathrm{mag} < [8.0-24] < 5.5\,\mathrm{mag}$) and more broad in magnitude ($5\,\mathrm{mag} < [m_{8.0}] < 11\,\mathrm{mag}$) than for other regions. The maximum of the distribution is located at a higher magnitude ($[m_{8.0}] \sim 7.7\,\mathrm{mag}$) and a higher color index ($[8.0-24] \sim 4.3\,\mathrm{mag}$). Such sources can be associated with class I/II YSOs.

The discussion of the CMDs is concluded by stating that due to the low sample size of the *inner* region YSOs with respect to the *edge*, *outer* and *none* regions and therefore low statistical significance identifying definite differences in the properties of *inner* region and remaining region YSOs is difficult. However, after examining CMDs in figures 6.3 to 6.6, YSOs in the *inner* region tend to exhibit higher magnitudes in the [8.0] wavelength band which are related to higher mass sources (figure 1b, [Whitney et al., 2008]) and colors that would identify them rather as class I/II than class 0/III.

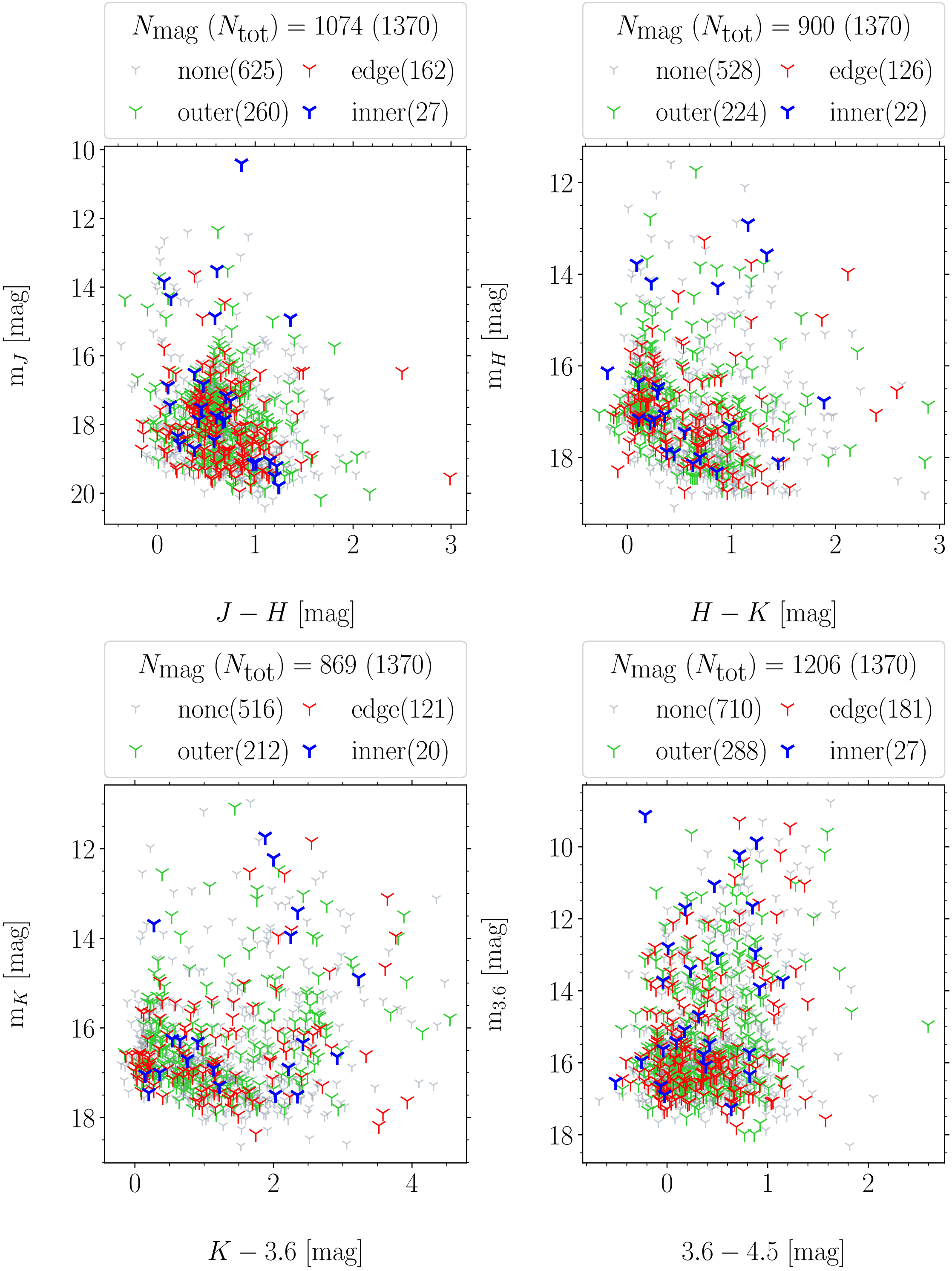

FIGURE 6.2: CMDs for all six magnitude combinations for catalog 3 (section 5.1.3) [Carlson et al., 2012].

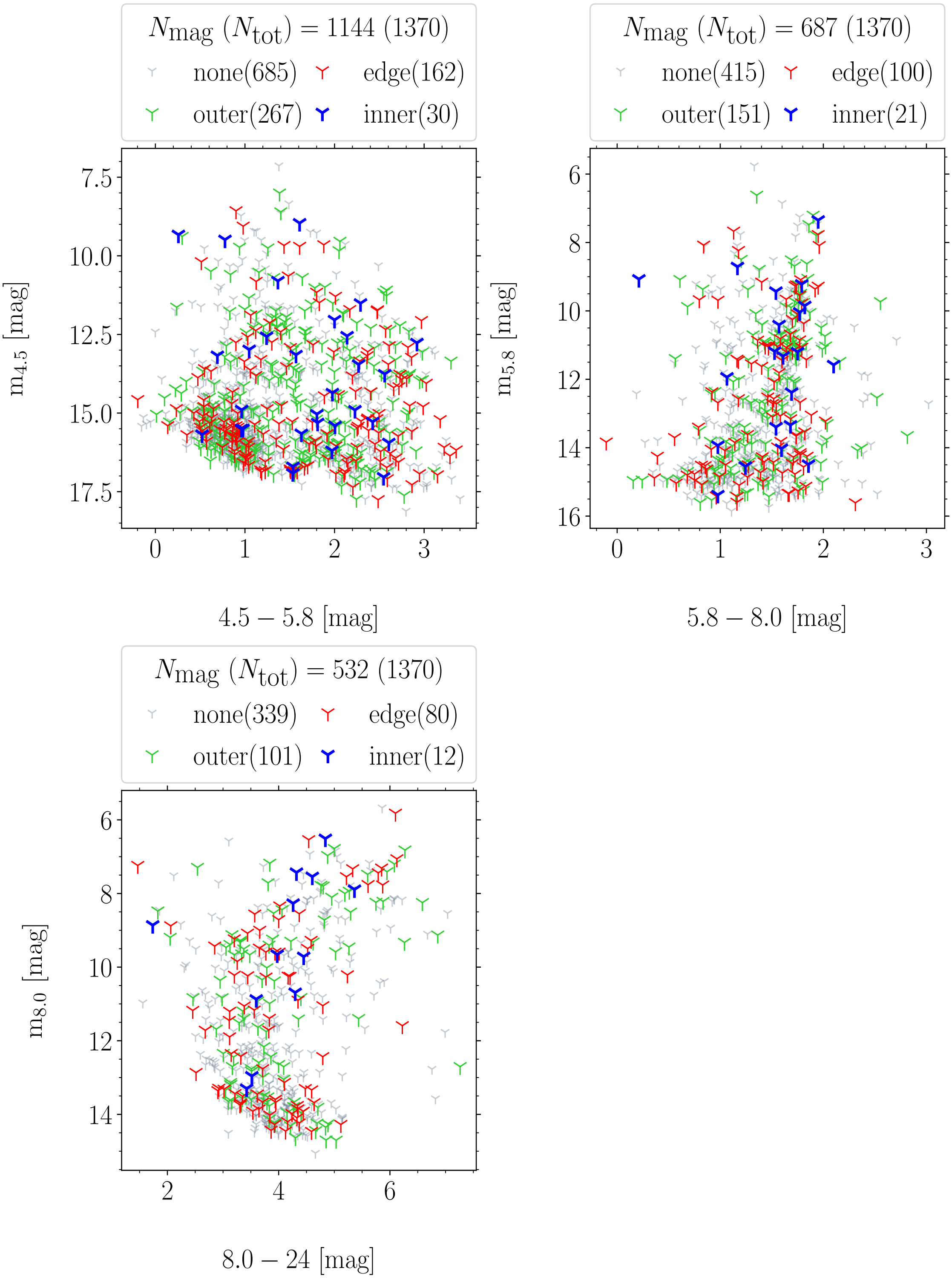

FIGURE 6.2: *Continued.* The *inner* regions YSOs are enhanced to make their relative positions to other region YSOs apparent.

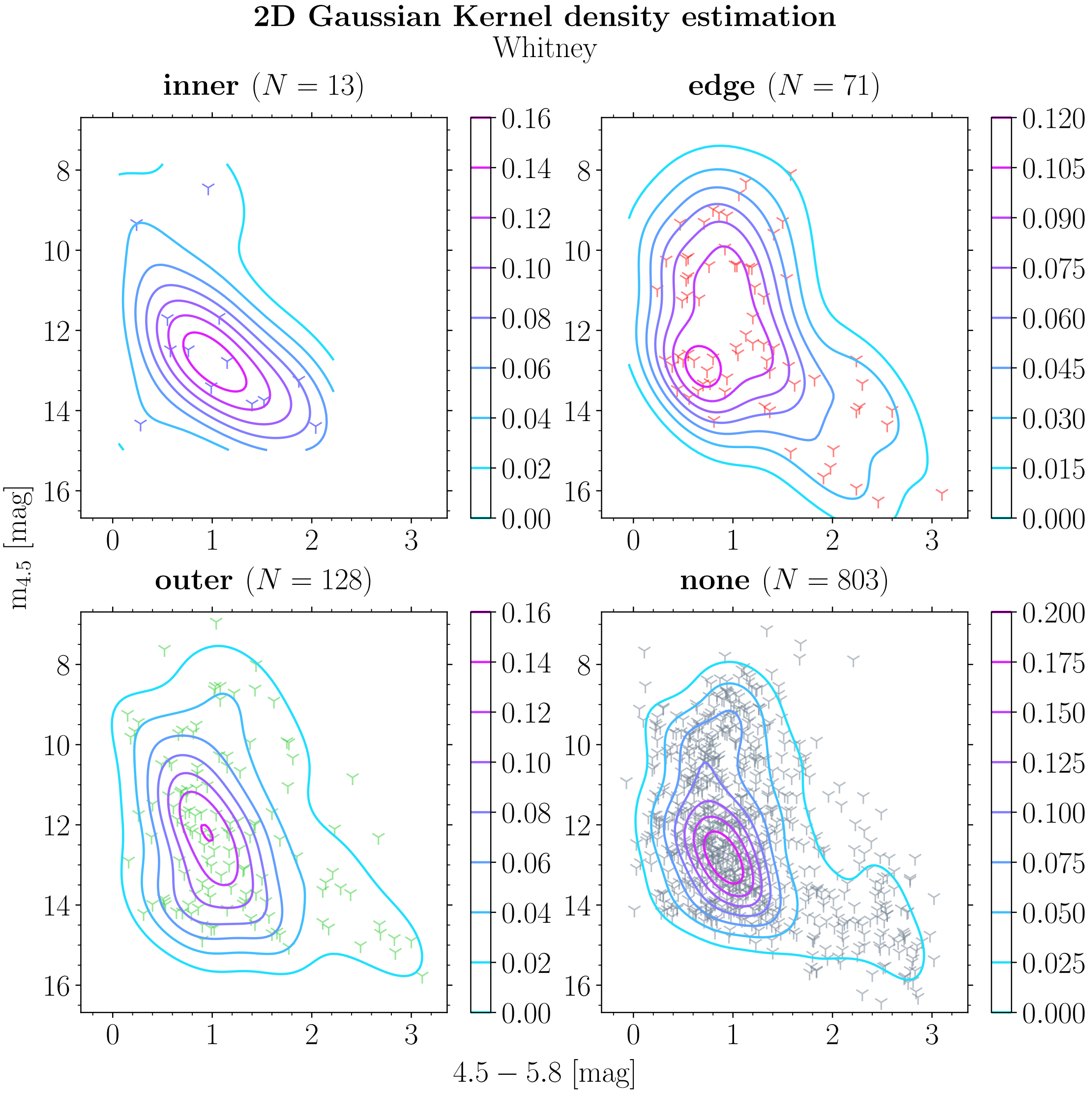

FIGURE 6.3: The [4.5 − 5.8] vs [m$_{4.5}$] diagram for catalog 1 YSOs with contours indicating the distribution (section 5.1.1).

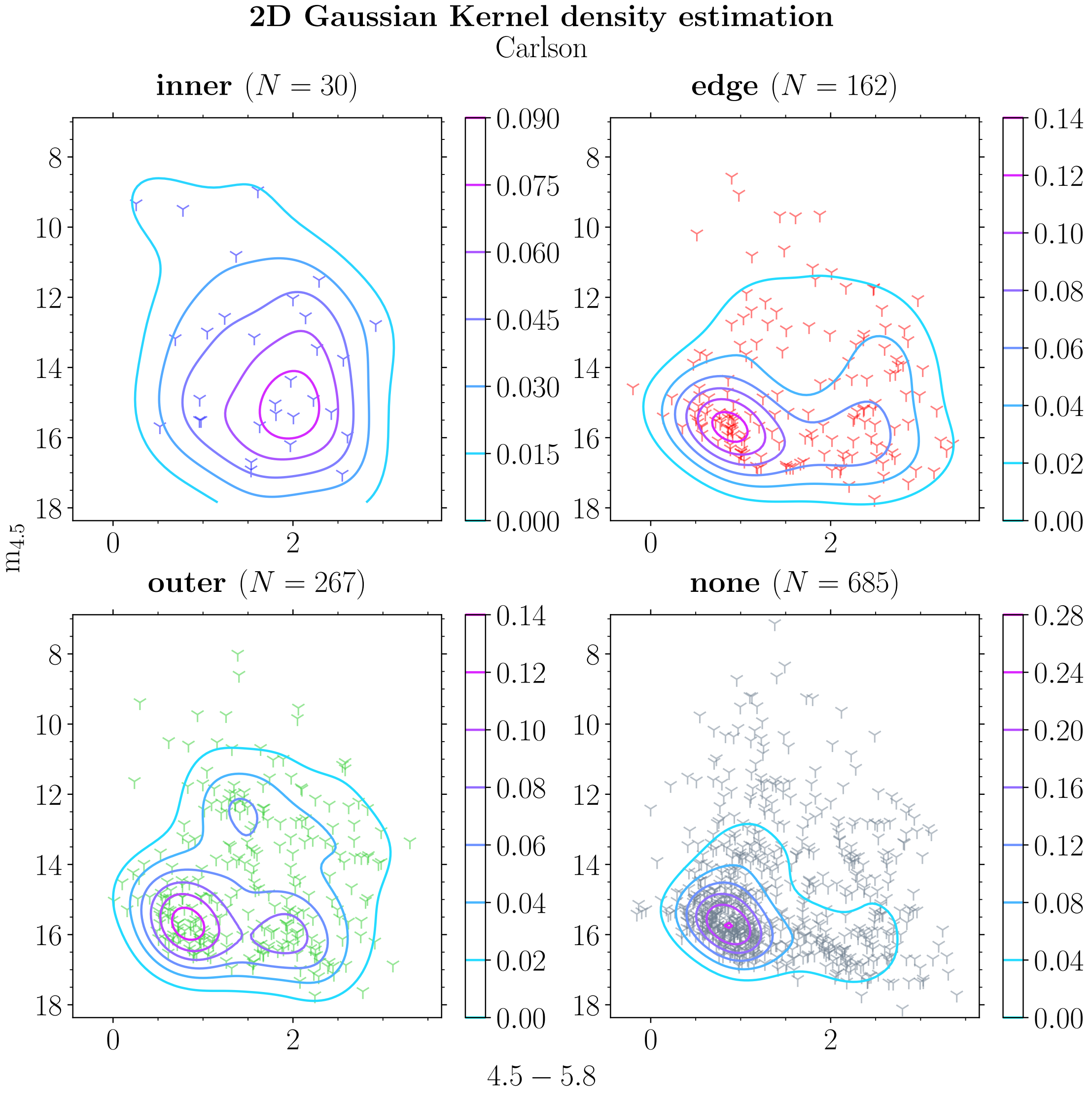

FIGURE 6.4: The $[4.5 - 5.8]$ vs $[m_{4.5}]$ diagram for catalog 3 YSOs with contours indicating the distribution (section 5.1.3).

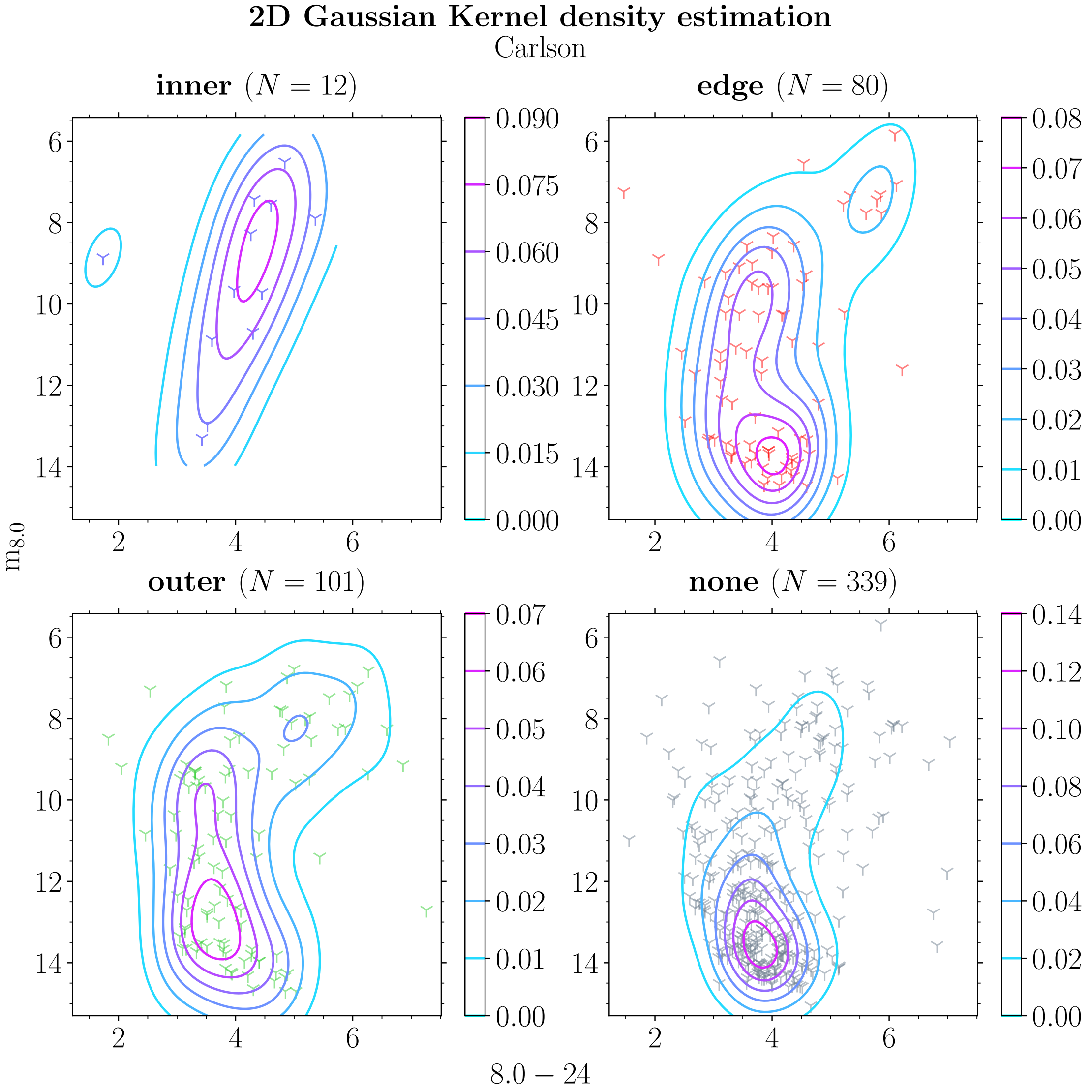

FIGURE 6.5: The [8.0 − 24] vs [$m_{8.0}$] diagram for catalog 3 YSOs with contours indicating the distribution (section 5.1.3).

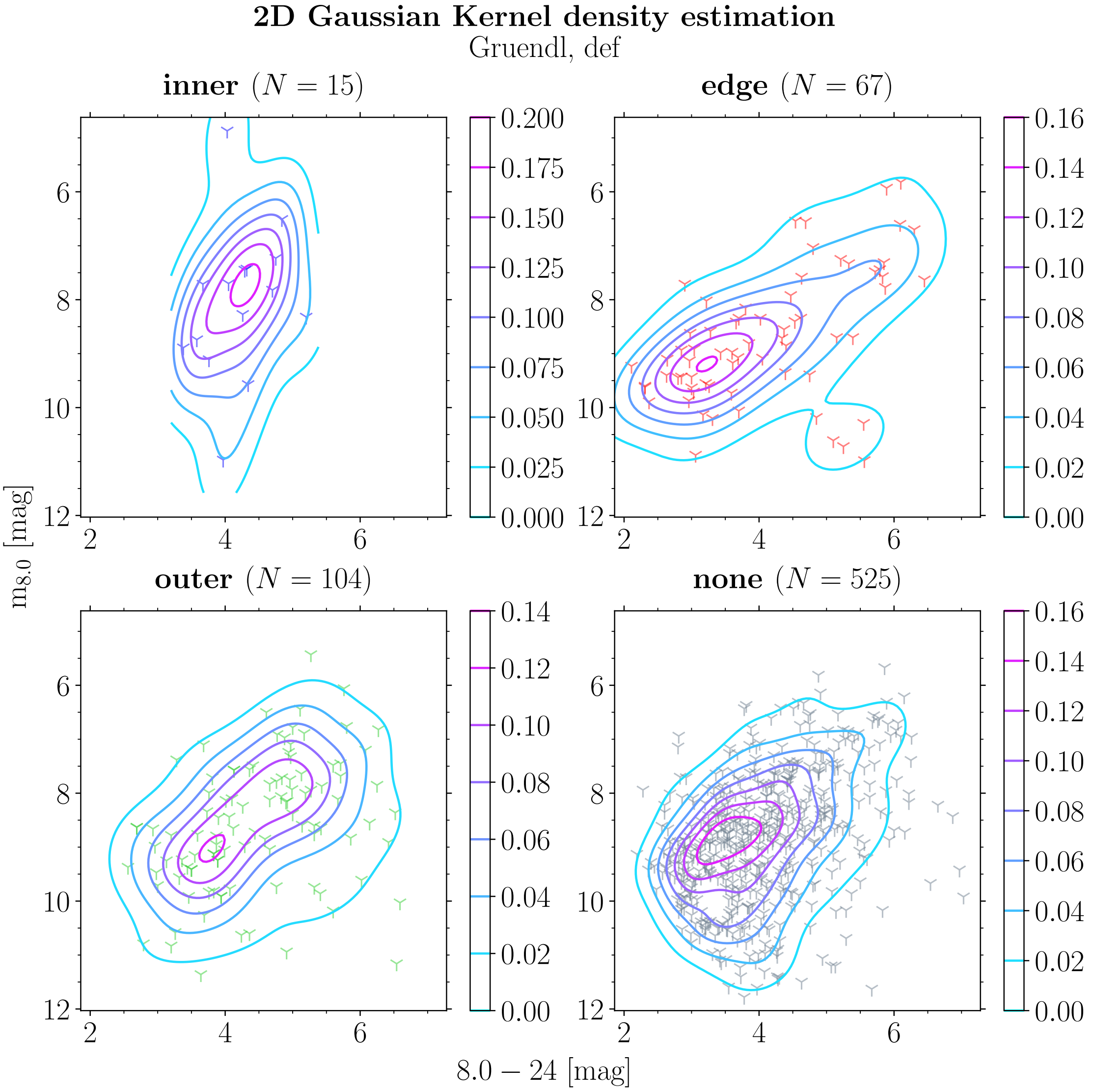

FIGURE 6.6: The $[8.0-24]$ vs $[m_{8.0}]$ diagram for catalog 2 group *definite* YSOs with contours indicating the distribution (section 5.1.2).

6.2.2 Color-Color Diagrams

In CCDs the x−axis as well as the y−axis display the color index. Therefore, it is possible to study sources in more than two wavelength bands simultaneously in one diagram. Following the definition of color indices in section 2.3.2, higher values on each axis correspond to a redder color, thus a cooler temperature and younger stars. In contrast to CMDs, sources with unknown distances can be studied (section 2.3.2).

Upon reviewing the CMDs, four color index combinations were selected to generate CCDs: [4.5 – 8.0] vs [3.6 – 4.5], [5.8 – 8.0] vs [3.6 – 4.5], [8.0 – 24] vs [3.6 – 4.5], [8.0 – 24] vs [3.6 – 5.8]. The CCDs are documented identically to CMDs in the previous section 6.2.1.

After studying catalog 1 CCDs and their respective contour diagrams, no noticeable differences in the positions of YSOs in the four regions were discovered. The diagrams are documented in appendix A in figures A.29 and A.30.

Catalog 2 group *probable* and *possible* CCDs have sample sizes for *inner* region YSOs that are less than 10. These are not discussed. The diagrams can be viewed in figures A.34, A.35 and A.39 in appendix A. In the following, group *definite* YSOs will be only addressed as catalog 2 ones.

When inspecting the CCDs for catalog 2 and 3 in figures 6.7, 6.8, it is noticed that the YSOs have higher color indices for the longer wavelength combinations (x−axis) than for the shorter ones (y−axis). This is particularly apparent for the [8.0 – 24] vs [3.6 – 4.5] and [8.0 – 24] vs [3.6 – 5.8] diagrams. Therefore, it is confirmed that the YSOs are biased towards class I/II sources (figure 8 and 9 [Dunham et al., 2015]).

In the diagrams involving the color index [8.0 – 24], the *inner* region YSOs (catalog 2, figure 6.7) are populated in the 'central' area of the plot (3 mag < [8.0 – 24] < 5.5 mag). This can also be stated for catalog 3 YSOs if one source at [8.0 – 24] ~ 1.9 mag is excluded which is separated from the rest of the *inner* region YSOs (figure 6.8). The location in the diagram relates to younger class I/II sources. The observation is further investigated by utilizing contour diagrams reflecting the density of the YSOs in the CCDs. Figures 6.9 and 6.10 depict such diagrams for catalog 2 sources. Comparing the CCDs for the defined regions in figure 6.9, the maximum of the distribution is shifted towards higher values on both axes. In figure 6.10, the maximum of the *inner* region does not differ from the remaining regions. What does stand out is the confinement to a less extended region as stated above.

The respective CCDs for catalog 3 (figures 6.11, A.42) do not allow any conclusive comments on the values of the color indices in the regions. The maximum of the density function in figure 6.11 seems to be at a slightly higher color index [3.6 – 4.5].

Catalogs 1 (5.1.1) and 3 (section 5.1.3) provide information on the evolutionary stages on the individual YSOs. The CCDs are generated a second time including this data (figures 6.12, 6.13). It is evident that *inner* region YSOs are exclusively classified as class I/II sources. Whereas, the *edge* region population has an increased number of YSOs classified as class III sources. These two figures emphasize that the different evolutionary stages of YSOs overlap in CCDs and it is difficult to clearly separate class 0/I/II/III sources.

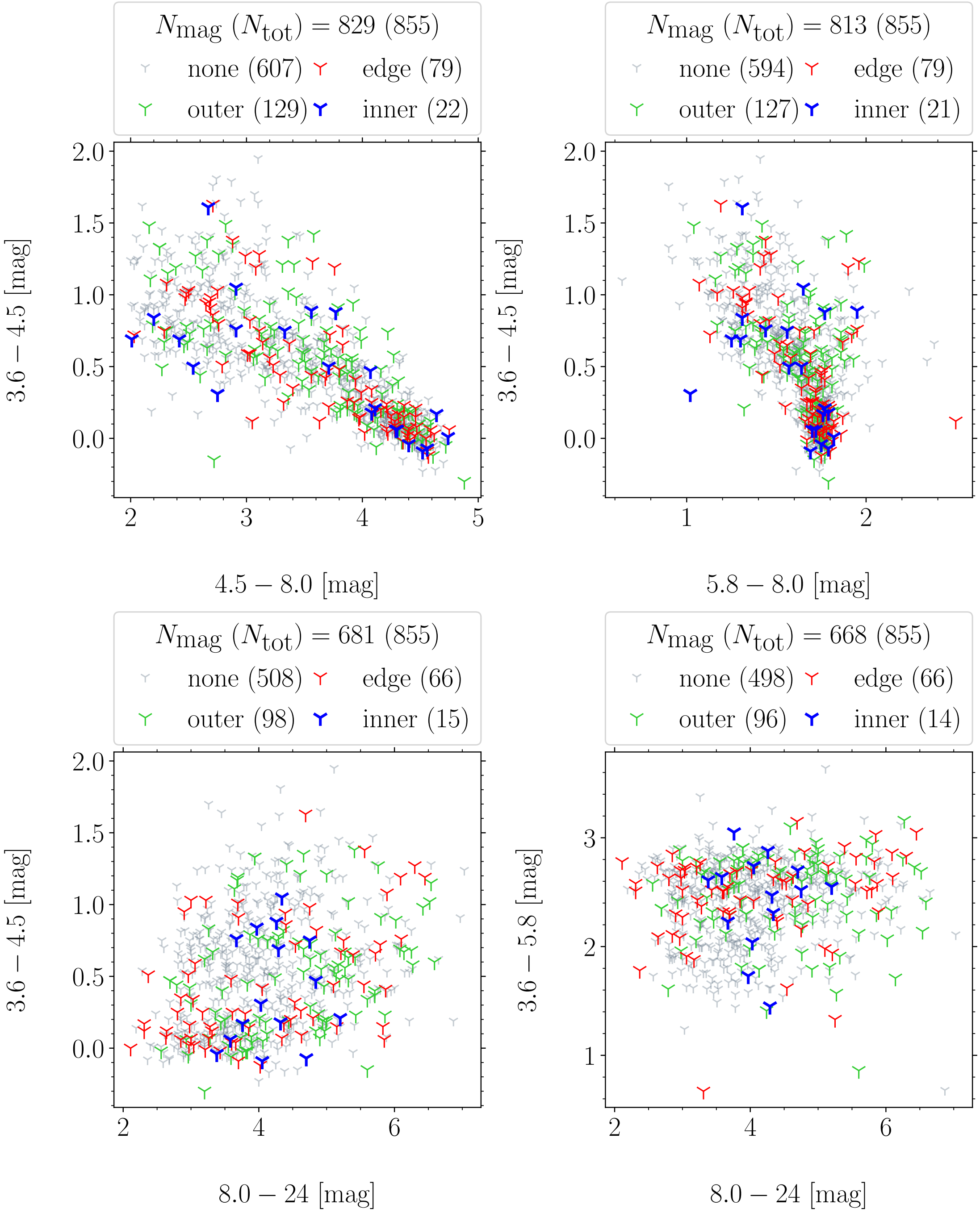

FIGURE 6.7: CCDs for four magnitude combinations for catalog 2 group *definite* (section 5.1.2) [Gruendl & Chu, 2009].

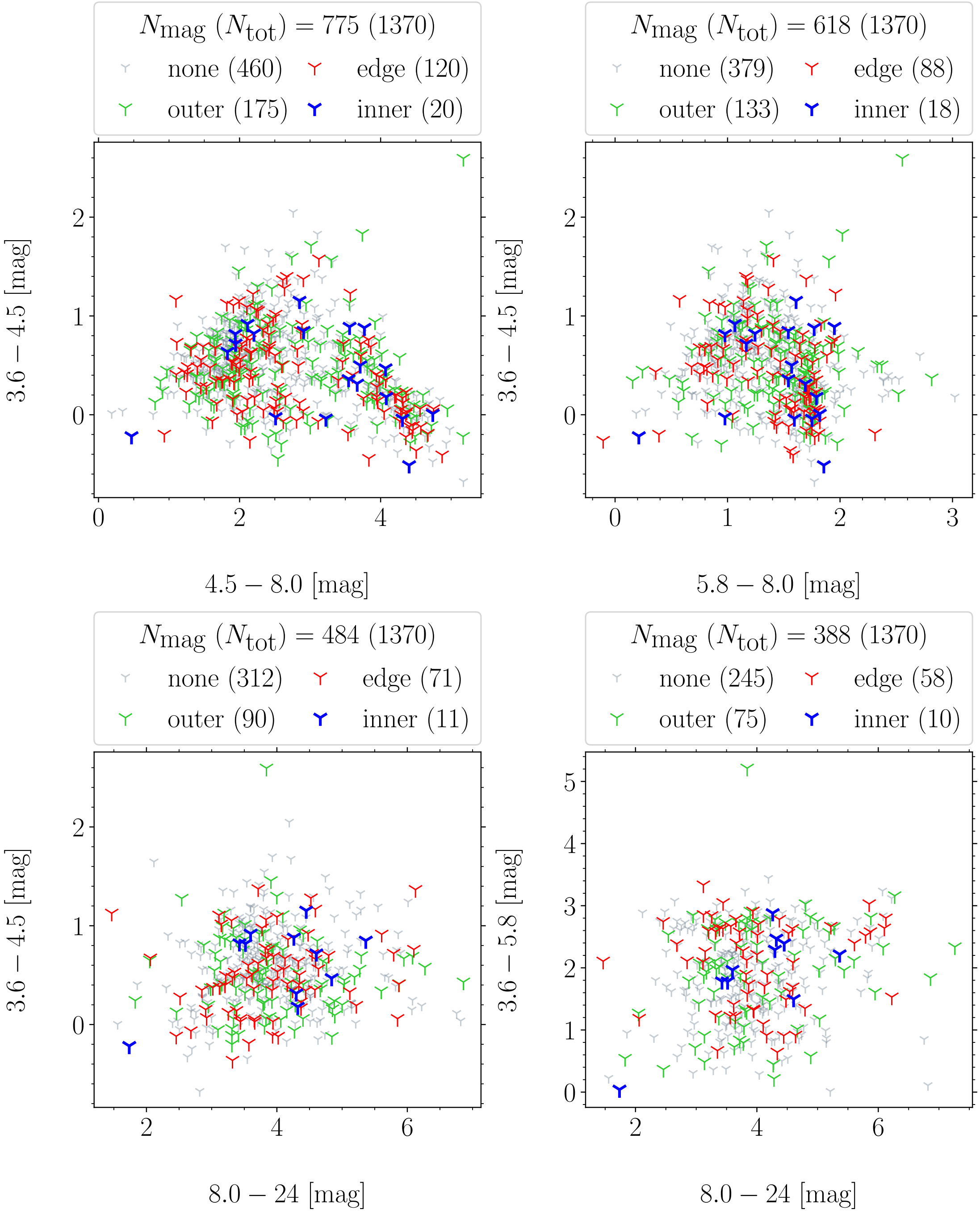

FIGURE 6.8: CCDs for four magnitude combinations for catalog 3 (section 5.1.3) [Carlson et al., 2012].

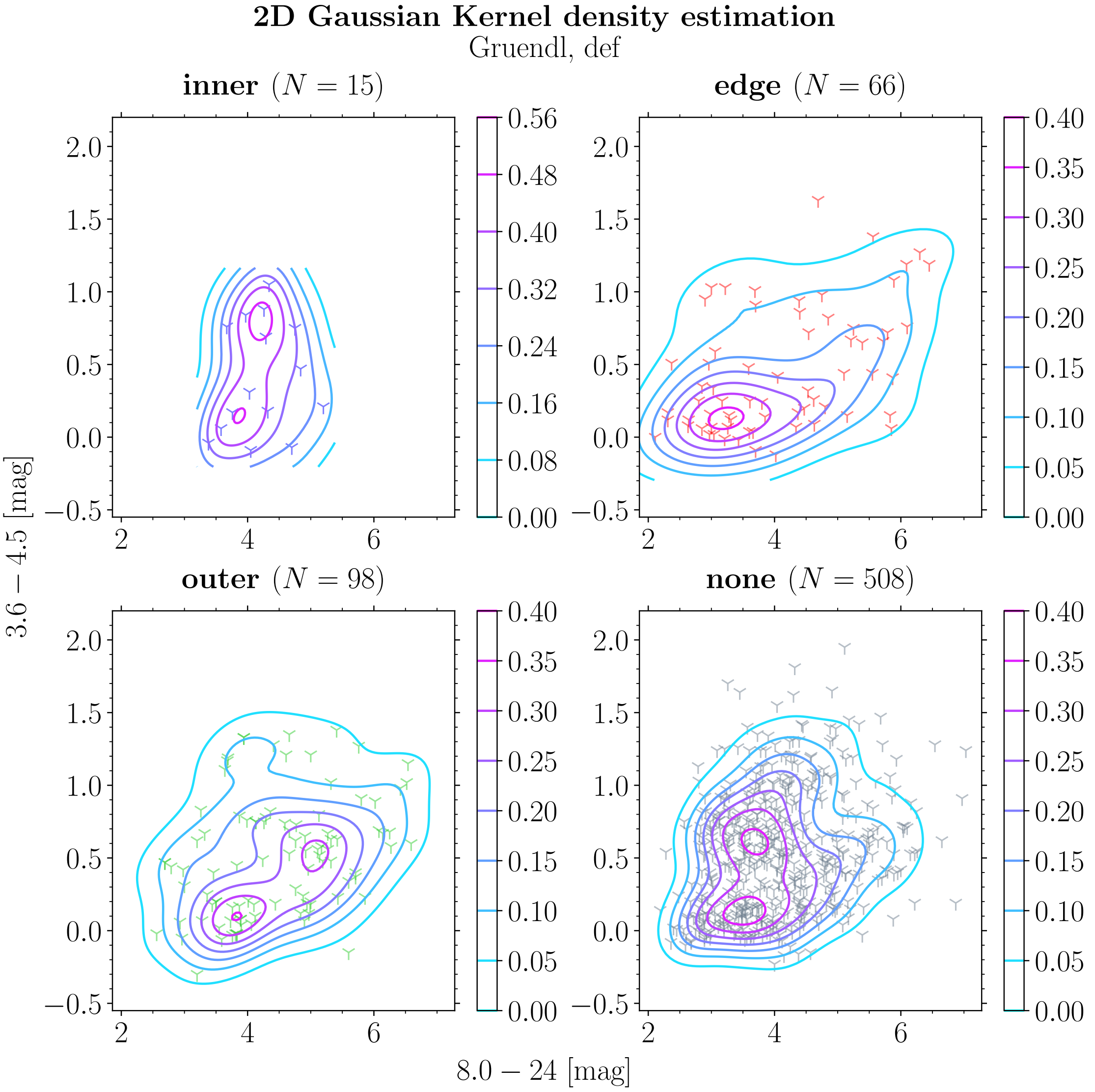

FIGURE 6.9: [8.0−24] vs [3.6−4.5] CCD with contours for catalog 2 group *definite* YSOs (section 5.1.2) [Gruendl & Chu, 2009].

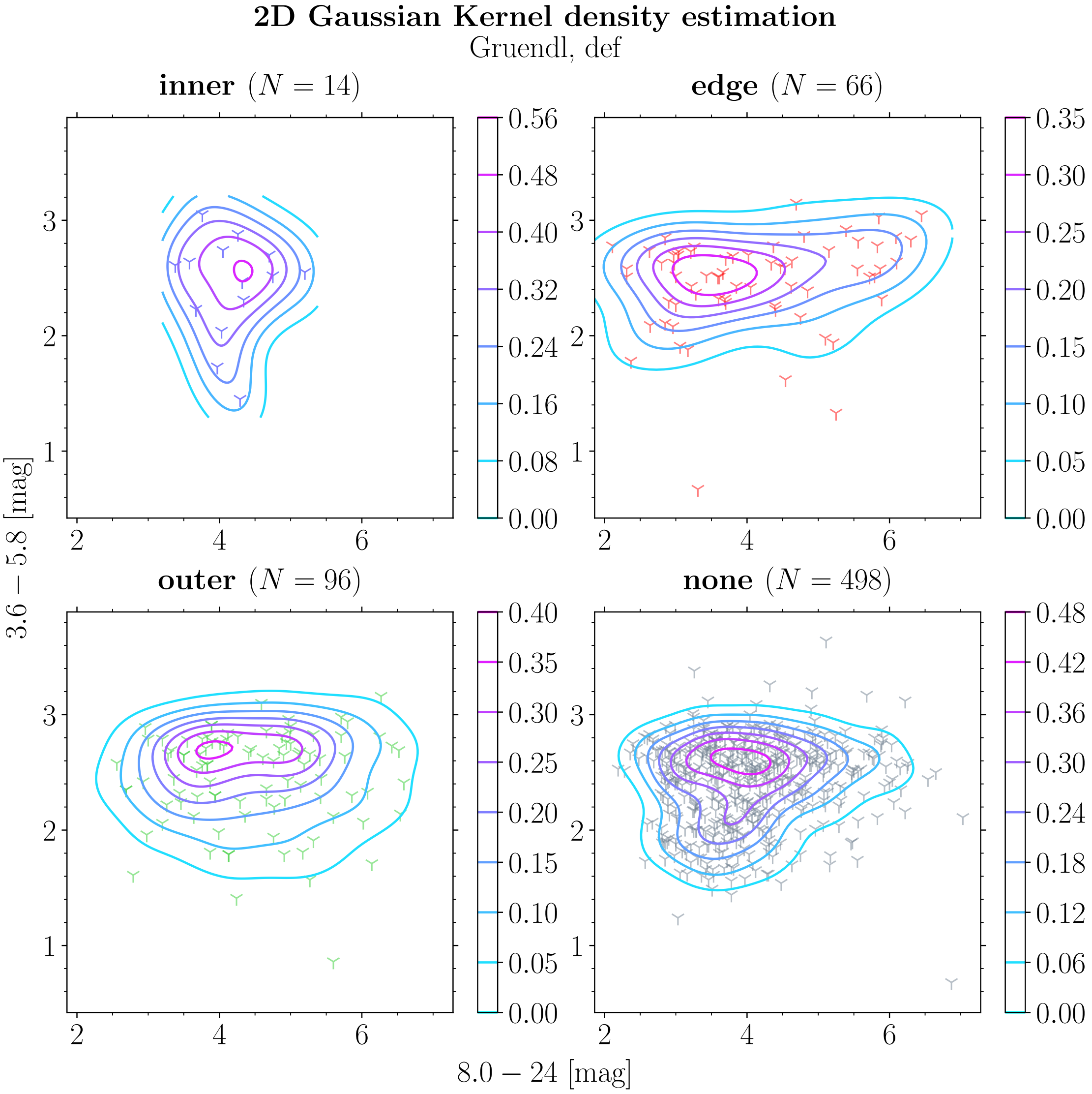

FIGURE 6.10: [8.0 – 24] vs [3.6 – 5.8] CCD with contours for catalog 2 group *definite* YSOs (section 5.1.2) [Gruendl & Chu, 2009].

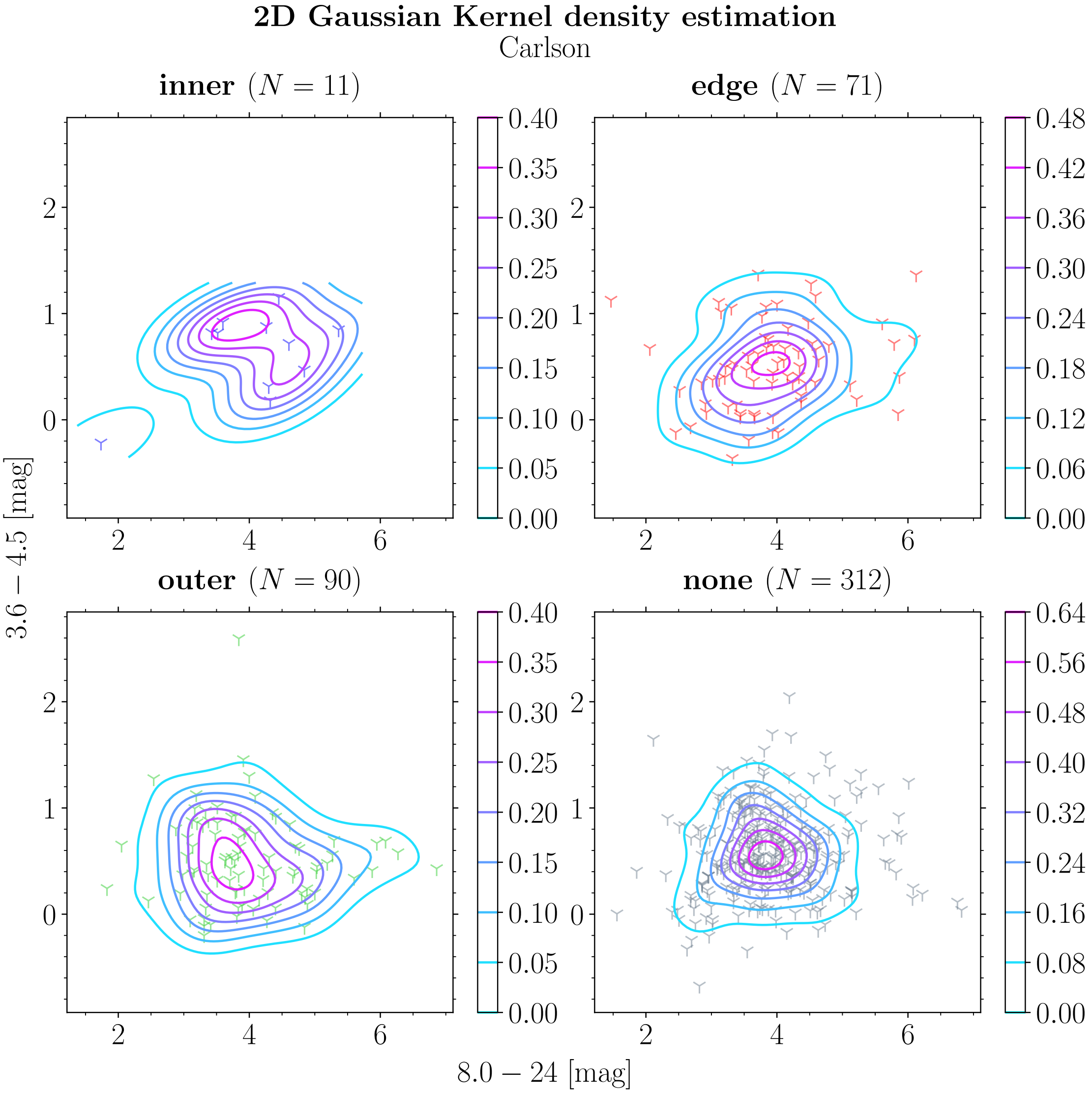

FIGURE 6.11: [8.0 – 24] vs [3.6 – 4.5] CCD with contours for catalog 3 YSOs (section 5.1.3) [Carlson et al., 2012].

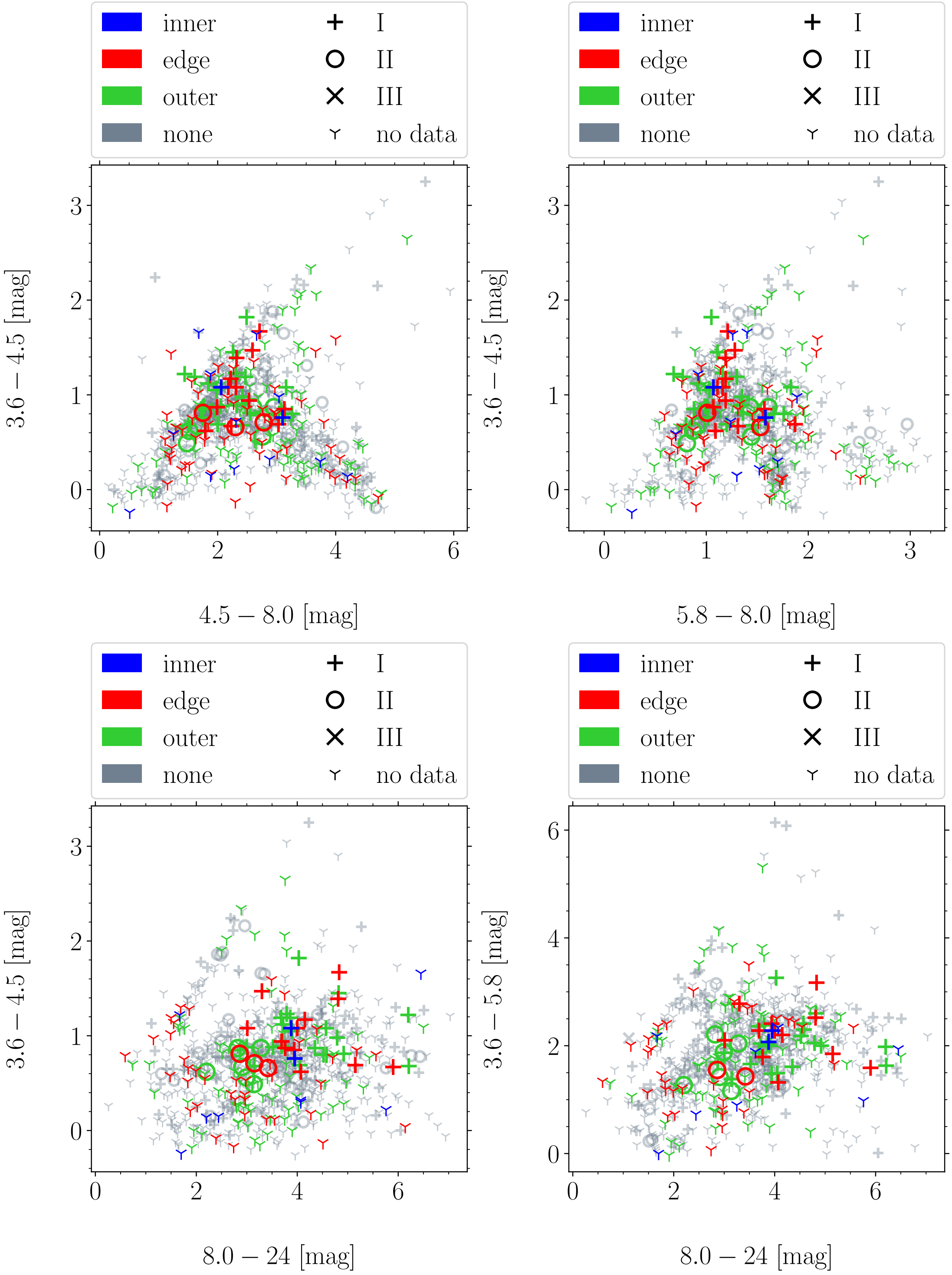

FIGURE 6.12: CCDs for four magnitude combinations for catalog 1 (section 5.1.1) with the differentiation of evolutionary stages [Whitney et al., 2008].

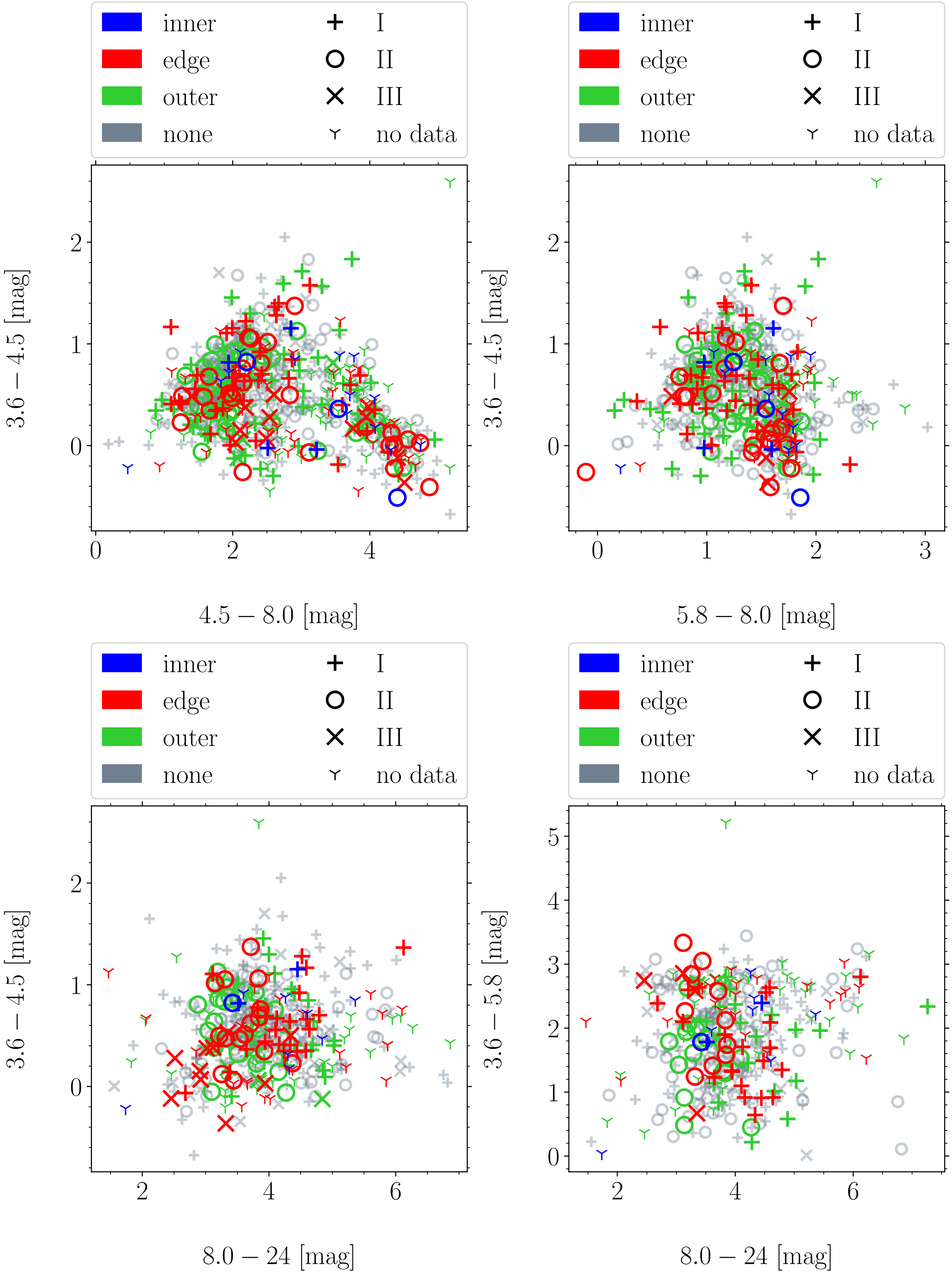

FIGURE 6.13: CCDs for four magnitude combinations for catalog 3 (section 5.1.3) with the differentiation of evolutionary stages [Carlson et al., 2012].

6.3 Kolmogorov-Smirnov test

To provide a more quantitative analysis of the distributions of YSOs, a one-dimensional two-sample Kolmogorov-Smirnov (KS) test is performed.

6.3.1 One-dimensional

For each color index, the data set of the *inner* region is compared with the set of each remaining region by using the Python method `scipy.stats.ks_2samp()`[8]. The following null hypothesis is tested: the two data samples are drawn from the same distribution.

The KS-statistic is the 'maximum value of the absolute difference' between the two empirical distribution functions of the data sets[8]. Per definition, the empirical distributions are of cumulative nature [Press et al., 2007]. If the KS-statistic is large (i.e., the $p-$value small), the samples will most likely not to be drawn from the same distribution. The $p-$value threshold is set to 10%. Below this value it is acknowledged that the samples follow different distributions, meaning the null hypothesis is rejected. The results of the tests are listed in table 6.3.

The $p-$value is smaller than 0.1 in fifteen numbers of cases (see table 6.3). Three such test results are reported for catalog 2 group *possible*. Due to low sample size for the *inner* region, these results should be treated with care. It is to be noted that $p < 0.1$ is only observed for catalog 2 and 3.

In some cases, the $p-$value decreases for *edge*, *outer* and *none* region, meaning the further the YSOs are from the SNR the smaller the $p-$value (catalog 1: [3.6–5.8], catalog 2 group *definite*: [4.5 – 8.0], [5.8 – 8.0], group *probable*: [5.8 – 8.0], [8.0 – 24], group *possible*: [3.6 – 4.5], catalog 3: [3.6 – 5.8]). In other cases, the $p-$value is lower for the *none* region than for the *edge* or *outer* region (catalog 2 *definite*: [3.6 – 5.8], catalog 3: [4.5 – 8.0], [5.8 – 8.0], [8.0 – 24]). The $p-$value is also observed to be lowest for the *edge* or the *outer* region and higher for the *none* region.

In conclusion, it cannot be stated for certain that *inner* region YSOs follow a different distribution than *edge*, *outer* or *none* region YSOs. There is no color index which stands out in all catalogs for showing $p < 0.1$. Therefore, a two-dimensional (two-sample) KS test is conducted instead in order to compare the distributions of YSOs in the CCDs and CMDs (section 6.3.2).

---

[8] `https://docs.scipy.org/doc/scipy/reference/generated/scipy.stats.ks_2samp.html`, accessed on 21.10.2022.

Table 6.3: KS-test statistic and $p-$value for comparing the distribution of values for various color indices for YSOs in the *inner* and remaining regions. The sample size for the *inner* (N_{inner}) and remaining regions (N_{mag}) is given. Here, sample size means the number of YSOs assigned to a specific region with available magnitude measurements at the two respective wavelengths. Catalog 1: [Whitney et al., 2008], catalog 2: [Gruendl & Chu, 2009], catalog 3: [Carlson et al., 2012].

Catalog		Color	N_{inner}	Region (N_{mag})	KS-statistic	$p-$value
1		[3.6 – 4.5]	14	edge (75)	0.130	0.611
				outer (126)	0.0714	0.849
				none (829)	0.107	0.684
		[3.6 – 5.8]	14	edge (69)	0.0342	0.942
				outer (119)	0.0546	0.899
				none (777)	0.107	0.682
		[4.5 – 8.0]	15	edge (75)	0.107	0.722
				outer (130)	0.0615	0.870
				none (844)	0.0725	0.815
		[5.8 – 8.0]	15	edge (72)	0.139	0.568
				outer (125)	0.0720	0.828
				none (814)	0.0979	0.710
		[8.0 – 24]	12	edge (64)	0.177	0.473
				outer (118)	0.169	0.481
				none (847)	0.127	0.634
2	definite	[3.6 – 4.5]	22	edge (79)	0.128	0.517
				outer (129)	0.0835	0.723
				none (607)	0.0631	0.810
		[3.6 – 5.8]	21	edge (79)	0.127	0.533
				outer (127)	0.0919	0.691
				none (594)	0.140	0.414
		[4.5 – 8.0]	22	edge (80)	0.107	0.623
				outer (136)	0.146	0.405
				none (625)	0.147	0.361

Table 6.3: *Continued.* KS-test statistic and $p-$value for various color indices.

Catalog		Color	N_{inner}	Region (N_{mag})	KS-statistic	$p-$value
2	definite	[5.8 – 8.0]	21	edge (80)	0.0232	0.963
				outer (134)	0.0768	0.762
				none (610)	0.101	0.621
		[8.0 – 24]	15	edge (67)	0.358	**0.0328**
				outer (104)	0.144	0.528
				none (525)	0.276	**0.0904**
2	probable	[3.6 – 4.5]	8	edge (28)	0.0536	0.926
				outer (55)	0.0523	0.929
				none (212)	0.00	1.00
		[3.6 – 5.8]	8	edge (26)	0.0865	0.858
				outer (52)	0.183	0.566
				none (199)	0.0251	0.970
		[4.5 – 8.0]	8	edge (28)	0.143	0.718
				outer (58)	0.181	0.567
				none (226)	0.133	0.696
		[5.8 – 8.0]	8	edge (26)	0.106	0.818
				outer (55)	0.139	0.691
				none (211)	0.159	0.613
		[8.0 – 24]	5	edge (17)	0.529	**0.0851**
				outer (41)	0.634	**0.0153**
				none (166)	0.681	**0.00486**
2	possible	[3.6 – 4.5]	2	edge (15)	0.0667	0.934
				outer (35)	0.0857	0.910
				none (153)	0.144	0.837
		[3.6 – 5.8]	2	edge (15)	0.533	0.265
				outer (35)	0.371	0.512
				none (147)	0.391	0.461

Table 6.3: *Continued.* KS-test statistic and p–value for various color indices.

Catalog		Color	N_{inner}	Region (N_{mag})	KS-statistic	p–value
2	possible	[4.5 – 8.0]	3	edge (15)	0.8	**0.0245**
				outer (36)	0.750	**0.0241**
				none (161)	0.553	0.117
		[5.8 – 8.0]	3	edge (15)	0.667	**0.0809**
				outer (36)	0.472	0.235
				none (154)	0.442	0.247
		[8.0 – 24]	0	–	–	–
3		[3.6 – 4.5]	27	edge (181)	0.105	0.556
				outer (288)	0.110	0.513
				none (710)	0.100	0.556
		[3.6 – 5.8]	27	edge (152)	0.192	0.162
				outer (247)	0.213	**0.0944**
				none (650)	0.290	**0.00984**
		[4.5 – 8.0]	23	edge (125)	0.280	**0.0384**
				outer (187)	0.271	**0.0399**
				none (485)	0.366	**0.00194**
		[5.8 – 8.0]	21	edge (100)	0.234	0.125
				outer (151)	0.211	0.167
				none (415)	0.312	**0.0158**
		[8.0 – 24]	12	edge (80)	0.246	0.243
				outer (101)	0.231	0.272
				none (339)	0.285	0.125

6.3.2 Two-dimensional

The two-dimensional KS test is performed both for color-color and color-magnitude combinations which were previously plotted in CCDs and CMDs (section 6.2). In contrast to the visual inspection of the diagrams, tests are conducted for $N_{\text{inner}} > 5$. Catalog 2 group *possible* YSOs do not meet this criterion for any CCDs or CMDs.

The calculation of the KS-statistic and the p−value in the two-dimensional case is similar to the one-dimensional case. The details can be reviewed in [Press et al., 2007]. Here, a python implementation of the code provided by [Press et al., 2007] is utilized[9].

The same null hypothesis as in the one-dimensional case (section 6.3) is tested: the two data samples follow identical distributions. Again, if the p−value is small, the two data sets are drawn from different distributions. In general, the threshold for rejecting the null hypothesis is set to $p < 0.1$.

In general, tests for the CCDs yielded p−values larger than 0.1. The few exceptions involving mostly the comparison between *inner* and *none* regions are printed in bold in table 6.4. It is noticed that the p−value is smaller than 0.1 for CCDs involving the color index $[8.0 - 24]$ (except for catalog 3) and $[3.6 - 4.5]$. Catalog 1 as well as catalog 2 CCDs employ p−values which are lower for $[8.0 - 24]$ vs $[3.6 - 4.5]$ and $[8.0 - 24]$ vs $[3.6 - 5.8]$ combinations than for the remaining two. For catalog 3, the lowest p−values are observed for the former CCD $[8.0 - 24]$ vs $[3.6 - 4.5]$ and $[4.5 - 8.0]$ vs $[3.6 - 4.5]$.

Reviewing the test results for the CMDs in table 6.5, it becomes apparent that for the $[8.0 - 24]$ vs $\mathrm{m}_{8.0}$ diagram the p−value is consistently smaller than 0.1. For catalog 2 group *probable* and catalog 3, $p < 0.1$ applies for the *edge*, *outer* as well as *none* region. For some diagrams which were discussed to display a different distribution for the *inner* region than for the remaining regions (section 6.2.1), this selection is confirmed through the KS test: catalog 3 $[4.5 - 5.8]$ vs $\mathrm{m}_{4.5}$ (figure 6.4), $[8.0 - 24]$ vs $\mathrm{m}_{8.0}$ (figure 6.5) and catalog 2 group *definite* $[8.0 - 24]$ vs $\mathrm{m}_{8.0}$ (figure 6.6). For other CMDs, the separate distributions only became evident through the KS test, particularly for shorter wavelengths (and diagrams which were not discussed due to low sample size in the *inner* region): catalog 1 $[H - K]$ vs m_H (figure A.6), $[8.0 - 24]$ vs $\mathrm{m}_{8.0}$ (figure A.10), catalog 2 group *definite* $[J - H]$ vs m_J (figure A.16), catalog 2 group *probable* $[8.0 - 24]$ vs $\mathrm{m}_{8.0}$ (figure A.25) and catalog 3 $[K - 3.6]$ vs m_K (figure A.13), $[3.6 - 4.5]$ vs $\mathrm{m}_{3.6}$ (figure A.14), $[5.8 - 8.0]$ vs $m_{5.8}$ (figure A.15).

---

[9] `https://github.com/Gabinou/2DKS`

TABLE 6.4: KS-statistic and $p-$value for comparing the empirical distributions of YSOs in CCDs between the *inner* and remaining regions. The sample size for the *inner* (N_{inner}) and remaining regions (N_{mag}) is given. Catalog 1: [Whitney et al., 2008], catalog 2: [Gruendl & Chu, 2009], catalog 3: [Carlson et al., 2012].

Catalog		CCD	N_{inner}	Region (N_{mag})	KS-statistic	$p-$value
1		[4.5 – 8.0]	14	edge (69)	0.196	0.795
		vs		outer (118)	0.194	0.776
		[3.6 – 4.5]		none (786)	0.220	0.582
		[5.8 – 8.0]	12	edge (61)	0.178	0.915
		vs		outer (111)	0.216	0.717
		[3.6 – 4.5]		none (709)	0.177	0.879
		[8.0 – 24]	10	edge (54)	0.304	0.408
		vs		outer (104)	0.392	0.122
		[3.6 – 4.5]		none (733)	0.409	**0.0790**
		[8.0 – 24]	10	edge (48)	0.335	0.298
		vs		outer (97)	0.355	0.205
		[3.6 – 5.8]		none (690)	0.339	0.217
2	definite	[4.5 – 8.0]	22	edge (79)	0.170	0.752
		vs		outer (129)	0.187	0.590
		[3.6 – 4.5]		none (607)	0.155	0.753
		[5.8 – 8.0]	21	edge (79)	0.181	0.718
		vs		outer (127)	0.229	0.378
		[3.6 – 4.5]		none (594)	0.160	0.754
		[8.0 – 24]	15	edge (66)	0.364	**0.0969**
		vs		outer (98)	0.286	0.281
		[3.6 – 4.5]		none (508)	0.313	0.151
		[8.0 – 24]	14	edge (66)	0.317	0.223
		vs		outer (96)	0.252	0.463
		[3.6 – 5.8]		none (498)	0.223	0.564

Table 6.4: *Continued.* KS-statistic and p–value for four CCDs for each catalog.

Catalog	CCD	N_{inner}	Region (N_{mag})	KS-statistic	p–value
2 probable	[4.5 – 8.0]		edge (28)	0.339	0.423
	vs	8	outer (55)	0.293	0.550
	[3.6 – 4.5]		none (212)	0.349	0.288
	[5.8 – 8.0]		edge (26)	0.293	0.610
	vs	8	outer (52)	0.337	0.374
	[3.6 – 4.5]		none (199)	0.330	0.349
	[8.0 – 24]		edge (17)	0.488	0.202
	vs	5	outer (40)	0.513	0.125
	[3.6 – 4.5]		none (161)	0.561	**0.0566**
	[8.0 – 24]		edge (15)	0.500	0.213
	vs	5	outer (38)	0.403	0.368
	[3.6 – 5.8]		none (154)	0.568	**0.0554**
3	[4.5 – 8.0]		edge (120)	0.263	0.249
	vs	20	outer (175)	0.253	0.270
	[3.6 – 4.5]		none (460)	0.367	**0.0228**
	[5.8 – 8.0]		edge (88)	0.194	0.695
	vs	18	outer (133)	0.204	0.604
	[3.6 – 4.5]		none (379)	0.280	0.187
	[8.0 – 24]		edge (71)	0.396	0.104
	vs	11	outer (90)	0.327	0.255
	[3.6 – 4.5]		none (312)	0.336	0.197
	[8.0 – 24]		edge (58)	0.295	0.441
	vs	10	outer (75)	0.297	0.417
	[3.6 – 5.8]		none (245)	0.324	0.271

Table 6.5: KS-statistic and $p-$value for comparing the empirical distributions of YSOs in CMDs between the *inner* and remaining regions. The sample size for the *inner* (N_{inner}) and remaining regions (N_{mag}) is given. Catalog 1: [Whitney et al., 2008], catalog 2: [Gruendl & Chu, 2009], catalog 3: [Carlson et al., 2012].

Catalog	CMD	N_{inner}	Region (N_{mag})	KS-statistic	$p-$value
1	$[J-H]$ vs $[\text{m}_J]$	5	edge (31)	0.400	0.349
			outer (50)	0.390	0.362
			none (349)	0.462	0.162
	$[H-K]$ vs $[\text{m}_H]$	5	edge (36)	0.619	**0.0312**
			outer (56)	0.586	**0.0435**
			none (381)	0.598	**0.0310**
	$[K-3.6]$ vs $[\text{m}_K]$	7	edge (36)	0.359	0.363
			outer (59)	0.340	0.402
			none (410)	0.367	0.275
	$[3.6-4.5]$ vs $[\text{m}_{3.6}]$	14	edge (75)	0.276	0.365
			outer (126)	0.242	0.499
			none (829)	0.279	0.281
	$[4.5-5.8]$ vs $[\text{m}_{4.5}]$	13	edge (71)	0.235	0.608
			outer (128)	0.265	0.413
			none (803)	0.254	0.426
	$[5.8-8.0]$ vs $[\text{m}_{5.8}]$	15	edge (72)	0.306	0.227
			outer (125)	0.305	0.198
			none (814)	0.285	0.227
	$[8.0-24]$ vs $[\text{m}_{8.0}]$	12	edge (64)	0.385	0.107
			outer (118)	0.455	**0.0263**
			none (847)	0.400	**0.0558**

Table 6.5: *Continued.* KS-statistic and p–value for CMDs for each catalog.

Catalog	CMD	N_{inner}	Region (N_{mag})	KS-statistic	p–value
2 definite	$[J-H]$ vs $[\mathrm{m}_J]$	7	edge (14)	0.679	**0.0107**
			outer (28)	0.661	**0.00747**
			none (139)	0.658	**0.00389**
	$[H-K]$ vs $[\mathrm{m}_H]$	9	edge (17)	0.353	0.381
			outer (34)	0.343	0.334
			none (147)	0.327	0.318
	$[K-3.6]$ vs $[\mathrm{m}_K]$	10	edge (24)	0.254	0.715
			outer (48)	0.296	0.450
			none (188)	0.309	0.332
	$[3.6-4.5]$ vs $[\mathrm{m}_{3.6}]$	22	edge (79)	0.210	0.518
			outer (129)	0.222	0.399
			none (607)	0.237	0.265
	$[4.5-5.8]$ vs $[\mathrm{m}_{4.5}]$	21	edge (80)	0.206	0.561
			outer (134)	0.179	0.692
			none (610)	0.174	0.664
	$[5.8-8.0]$ vs $[\mathrm{m}_{5.8}]$	21	edge (80)	0.231	0.417
			outer (134)	0.174	0.728
			none (610)	0.178	0.641
	$[8.0-24]$ vs $[\mathrm{m}_{8.0}]$	15	edge (67)	0.439	**0.0237**
			outer (104)	0.336	0.130
			none (525)	0.378	**0.0459**
2 probable	$[3.6-4.5]$ vs $[\mathrm{m}_{3.6}]$	8	edge (28)	0.348	0.376
			outer (55)	0.297	0.529
			none (212)	0.313	0.414
	$[4.5-5.8]$ vs $[\mathrm{m}_{4.5}]$	8	edge (26)	0.274	0.689
			outer (55)	0.245	0.761
			none (211)	0.245	0.721
	$[5.8-8.0]$ vs $[\mathrm{m}_{5.8}]$	8	edge (26)	0.226	0.881
			outer (55)	0.202	0.921
			none (211)	0.255	0.676

Table 6.5: *Continued.* KS-statistic and p–value for CMDs for each catalog.

Catalog		CMD	N_{inner}	Region (N_{mag})	KS-statistic	p–value
2	probable	[8.0 – 24] vs [$\text{m}_{8.0}$]	5	edge (17)	0.594	**0.0541**
				outer (41)	0.559	**0.0625**
				none (166)	0.602	**0.0284**
3		[J – H] vs [m_J]	27	edge (162)	0.213	0.342
				outer (260)	0.214	0.309
				none (625)	0.229	0.211
		[H – K] vs [m_H]	22	edge (126)	0.185	0.637
				outer (224)	0.158	0.789
				none (528)	0.175	0.641
		[K–3.6] vs [m_K]	20	edge (121)	0.289	0.160
				outer (212)	0.254	0.257
				none (516)	0.305	**0.0914**
		[3.6 – 4.5] vs [$\text{m}_{3.6}$]	27	edge (181)	0.305	**0.0509**
				outer (288)	0.251	0.151
				none (710)	0.354	**0.00918**
		[4.5 – 5.8] vs [$\text{m}_{4.5}$]	30	edge (162)	0.251	0.144
				outer (267)	0.217	0.246
				none (685)	0.378	**0.00250**
		[5.8 – 8.0] vs [$\text{m}_{5.8}$]	21	edge (100)	0.258	0.264
				outer (151)	0.231	0.357
				none (415)	0.348	**0.0319**
		[8.0 – 24] vs [$\text{m}_{8.0}$]	12	edge (80)	0.412	**0.0644**
				outer (101)	0.386	**0.0929**
				none (339)	0.465	**0.0174**

6.4 Spectral Energy Distribution

The spectral energy distribution (SED) is generated by plotting the wavelength λ on the x−axis and the specific flux νF_ν on the y−axis. Both axes are displayed in logarithmic scale.

The data catalogs were again inspected separately. For catalog 1 (section 5.1.1) and 3 (5.1.3), flux measurements were available, whereas for catalog 2 only magnitudes were provided. Thus, it was necessary to convert the magnitude values to flux values to proceed with plotting SEDs. Appendix B goes through the calculation.

Catalog 1 and 3 determined evolutionary stages for a large fraction of YSOs in the catalogs which are differentiated in the SEDs by using colors. Catalog 2 SEDs are displayed in a separate color to stress that no information on the classes of single YSOs is available. Since the shape of SEDs is essential for the study of evolutionary stages of YSOs, the single flux measurements are connected in the diagrams.

Firstly, the SED for every YSO in each group was plotted. Secondly, a mean SED was determined for each evolutionary stage. For the mean SED the infrared spectral index α was calculated.

The following discussion always refers to the plots of the mean SEDs on the right hand side of the diagrams.

In the SEDs of catalog 1 sources (figure 6.14) the contribution of disk, envelope and stellar surface cannot be separated. Only a slight increase in flux towards longer wavelengths is observed for class I sources and a decrease for class III sources (see the *none* region plot). Class II sources are - here - characterized by a flat spectrum.

The situation changes for catalog 3 (figure 6.15). Class I SEDs increase for wavelengths $\lambda > 4.5\,\mu\text{m}$ due to the presence of an envelope. For class II sources the emission from the star can be clearly distinguished from the envelope at $\sim 4.5\,\mu\text{m}$ (e.g., *inner* and *edge* region). The spectrum of class III YSOs resembles that of class II YSOs. The contribution from the envelope is still strongly present at longer wavelengths ($> 4.5\,\mu\text{m}$).

The shape of the SEDs for catalog 2 YSOs seems similar to class I/II sources. Considering the similarity in SEDs for class II/III YSOs in catalog 2 (the previous paragraph), class III sources cannot be excluded.

Catalog 1 and 2 YSOs exhibit a larger flux ($\nu F_\nu \sim 10^{-9} - 10^{-12}$) at $\lambda = 1.25\,\mu\text{m}$ (figure 6.14, 6.16 – 6.18), the shortest wavelength in this analysis, than catalog 3 sources ($\nu F_\nu \sim 10^{-12} - 10^{-13}$) (figure 6.15).

By inspecting *inner* region SEDs in figures 6.14 and 6.15, it is evident that only class I/II source are present. The contribution from the envelope seems to be larger than for other regions, although the increase in νF_ν at longer wavelengths is not substantial.

In the frame of this work the spectral index α is calculated using the observed flux of the YSOs at the lowest $\lambda_{\text{min}} = 1.25\,\mu\text{m}$ and largest wavelength $\lambda_{\text{max}} = 24\,\mu\text{m}$ in the following way:

$$\alpha = \frac{\ln\left[(\nu \cdot F_\nu)_{\lambda_{\text{max}}}\right] - \ln\left[(\nu \cdot F_\nu)_{\lambda_{\text{min}}}\right]}{\ln \lambda_{\text{max}}/\lambda_{\text{min}}} \tag{6.1}$$

Notice that not for all regions and classes flux measurements for λ_{min} and λ_{max} are available. In these cases, the spectral index α was calculated for the largest possible interval (although smaller than $[1.25, 24]\,\mu\text{m}$) in wavelength.

For nearly every catalog as well as the three regions (*inner*, *edge*, *outer*) the spectral index α decreases as expected (see section 2.2). For catalog 2 group *probable inner* region YSOs the index α is negative. The mean SED in figure 6.17 makes apparent that the flux for shorter wavelengths ($< 4.5\,\mu\text{m}$) is higher than would be expected for class I/II YSOs (see section 2.2).

Catalog 2 and 3 exhibit a higher and even positive spectral index α for *none* region sources, meaning more YSOs are at early stages in their evolution. For catalog 1 the respective values are generally lower. However, note the index α in the *outer* region falling out of this observation.

The spectral index α for class III YSOs is higher than expected. However, it is consistent with the previous study of SEDs above that the spectrum of class III sources resembles that of class II YSOs.

YSOs in the *inner* region do not differentiate themselves from sources in the remaining regions.

Table 6.6: Spectral index α calculated according to (6.1).
Catalog 1: [Whitney et al., 2008], catalog 2: [Gruendl & Chu, 2009], catalog 3: [Carlson et al., 2012].

Catalog	Region	Class	Spectral index α			
			λ_{min} [µm]	λ_{max} [µm]	μ_α	σ_α
1	inner	I	3.6	24	0.70	0.13
		II	–	–	–	–
		III	–	–	–	–
		no data	1.25	24	−0.96	0.28
	edge	I	1.25	24	0.81	0.16
		II	3.6	24	0.11	0.12
		III	–	–	–	–
		no data	1.25	24	−0.26	0.15
	outer	I	1.25	24	0.67	0.14
		II	1.25	24	0.17	0.096
		III	–	–	–	–
		no data	1.25	24	−0.075	0.17
	none	I	1.25	24	0.21	0.15
		II	1.25	24	−0.25	0.19
		III	1.25	24	−0.71	0.27
		no data	1.25	24	−0.20	0.096
2	inner	definite	1.25	24	0.73	0.17
	edge		1.25	24	0.67	0.089
	outer		1.25	24	0.80	0.075
	none		1.25	24	0.56	0.33
	inner	probable	1.25	24	−0.13	0.25
	edge		1.25	24	0.27	0.14
	outer		1.25	24	−0.061	0.10
	none		1.25	24	0.040	0.054
	inner	possible	3.6	8.0	1.36	0.30
	edge		1.25	24	−0.11	0.20
	outer		1.25	24	−0.33	0.12
	none		1.25	24	−0.12	0.056

Table 6.6: *Continued.* Spectral index α.

Catalog	Region	Class	Spectral index α			
			λ_{min} [µm]	λ_{max} [µm]	μ_α	σ_α
3	inner	I	1.25	24	0.72	0.24
		II	1.25	24	−0.28	0.14
		III	–	–	–	–
	edge	I	1.25	24	1.33	0.27
		II	1.25	24	0.26	0.15
		III	1.25	24	−0.018	0.097
	outer	I	1.25	24	0.92	0.16
		II	1.25	24	0.82	0.30
		III	1.25	24	0.29	0.14
	none	I	1.25	24	0.88	0.10
		II	1.25	24	0.098	0.083
		III	1.25	24	0.50	0.18

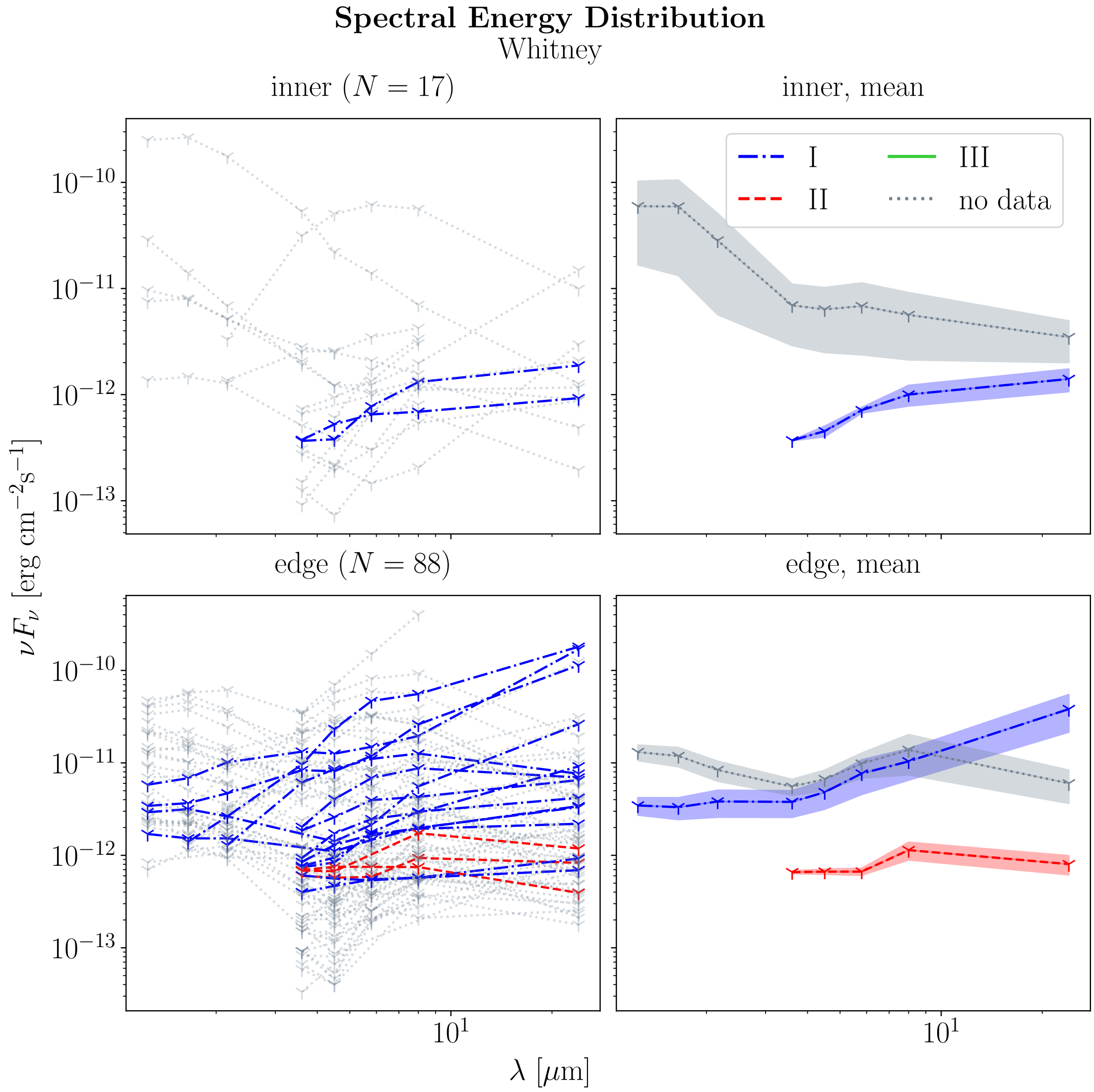

FIGURE 6.14: SEDs for the four different regions for catalog 1 YSOs (section 5.1.1) [Whitney et al., 2008].

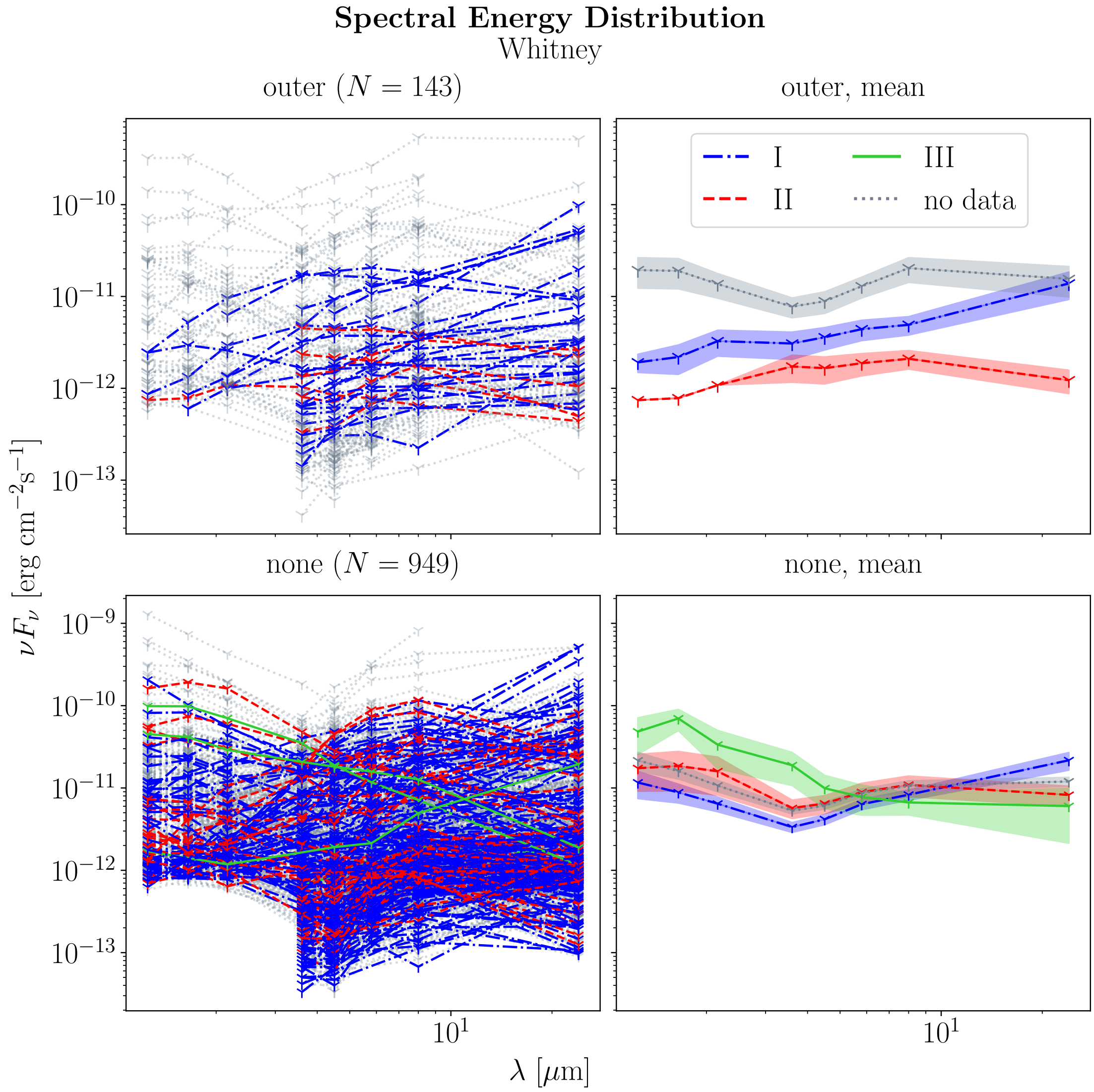

FIGURE 6.14: *Continued.*

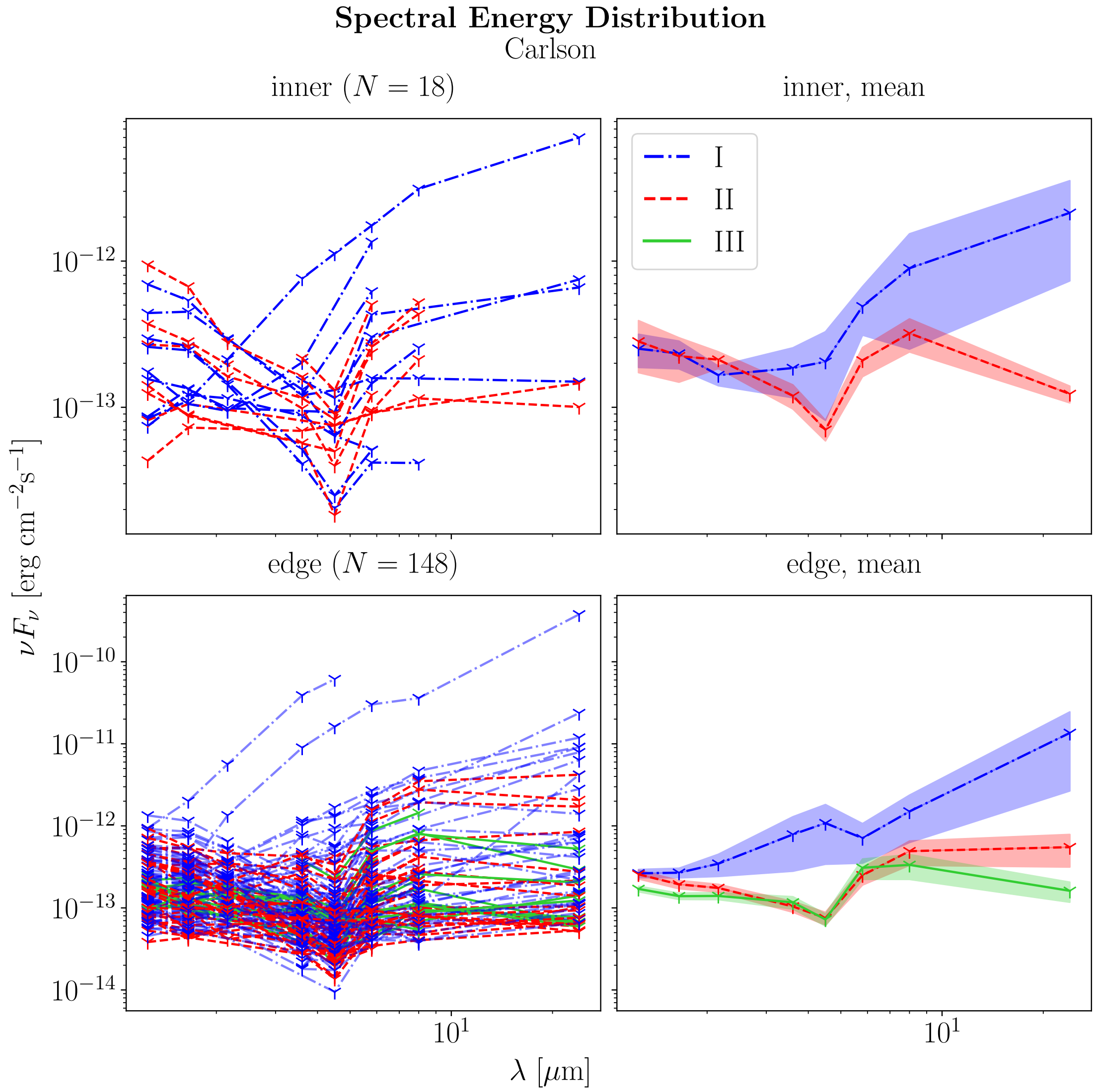

FIGURE 6.15: SEDs for the four different regions for catalog 3 YSOs (section 5.1.3) [Carlson et al., 2012].

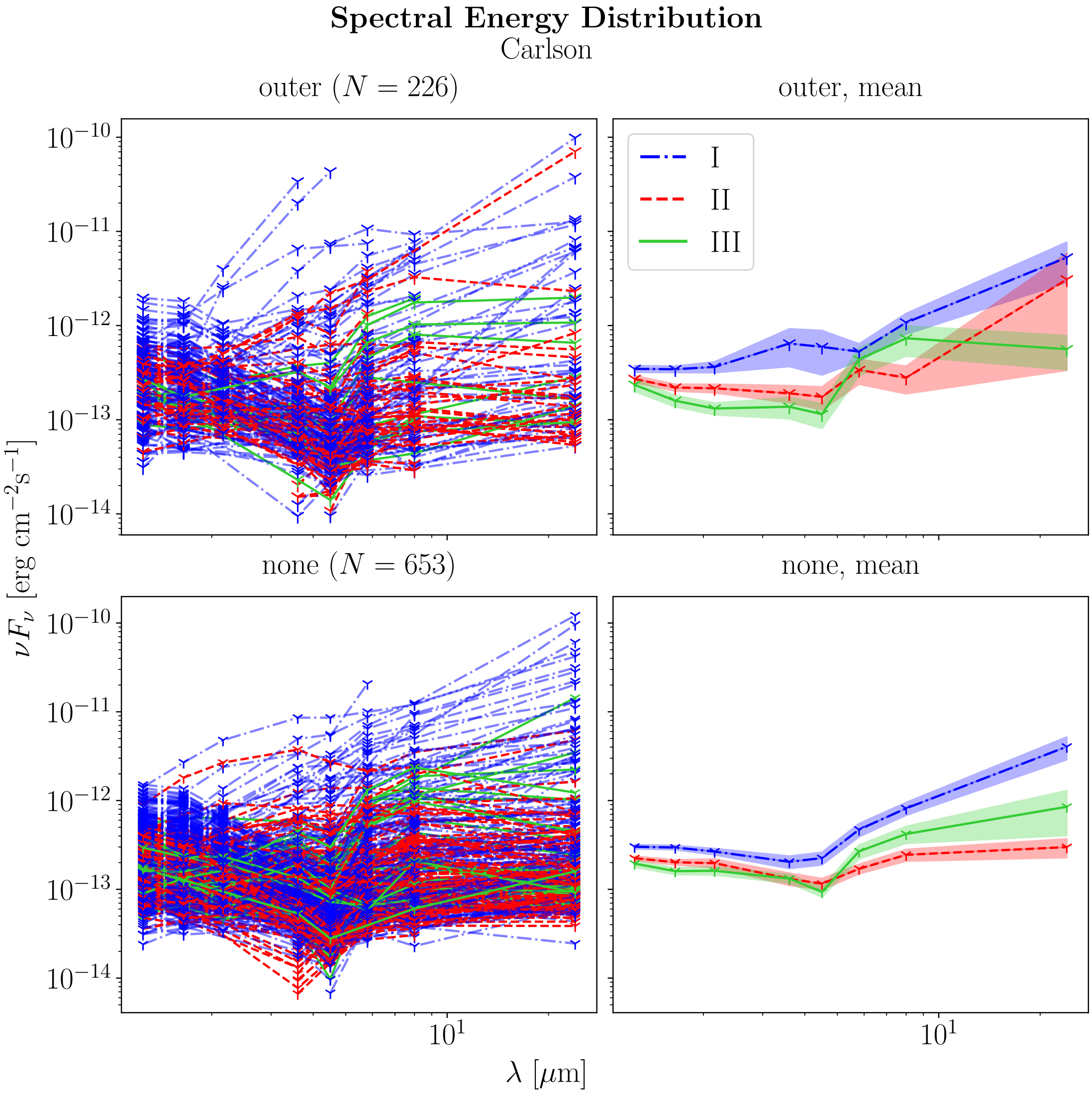

Figure 6.15: *Continued.*

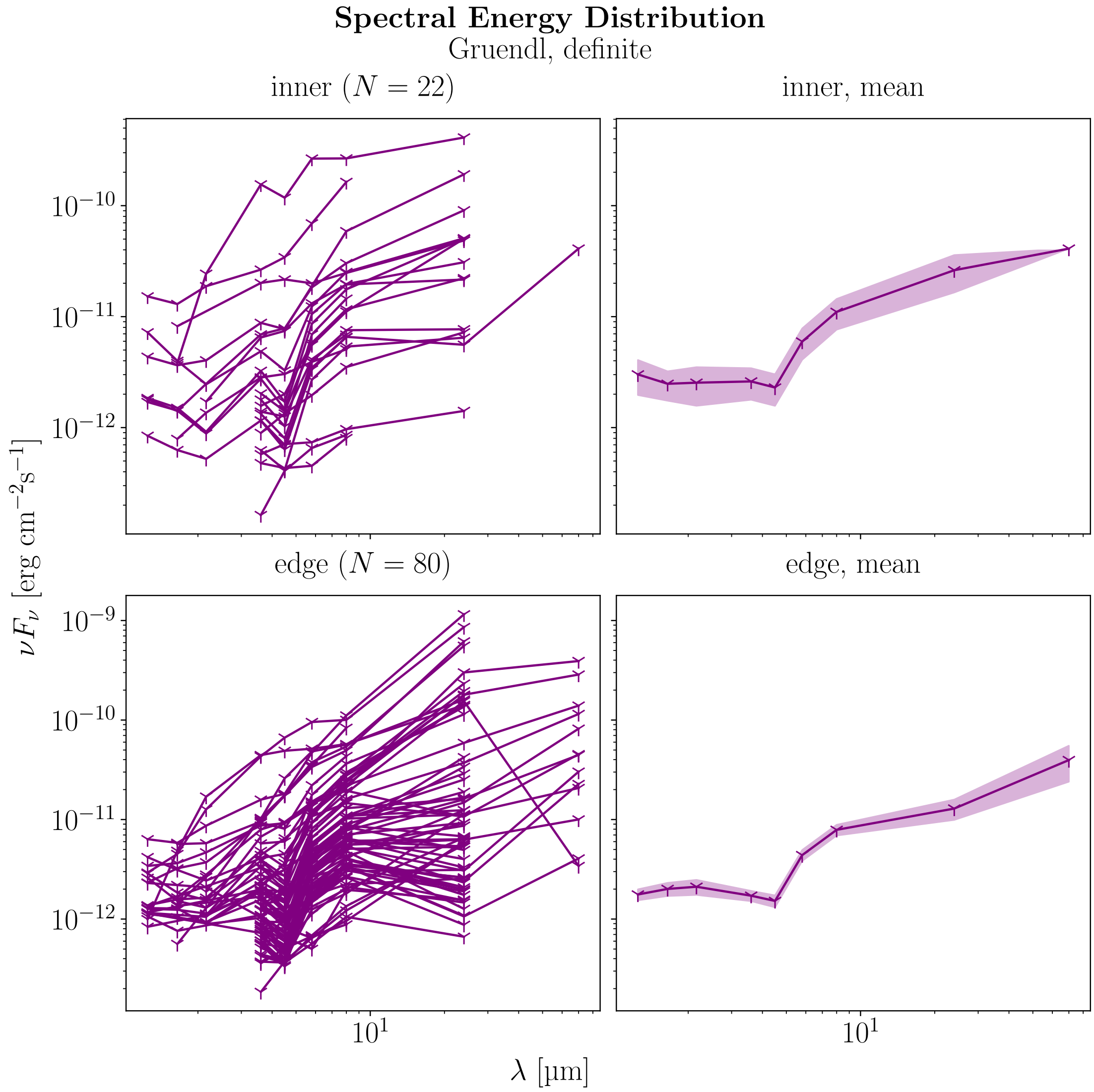

FIGURE 6.16: SEDs for the four different regions for catalog 2 group *definite* YSOs (section 5.1.2) [Gruendl & Chu, 2009].

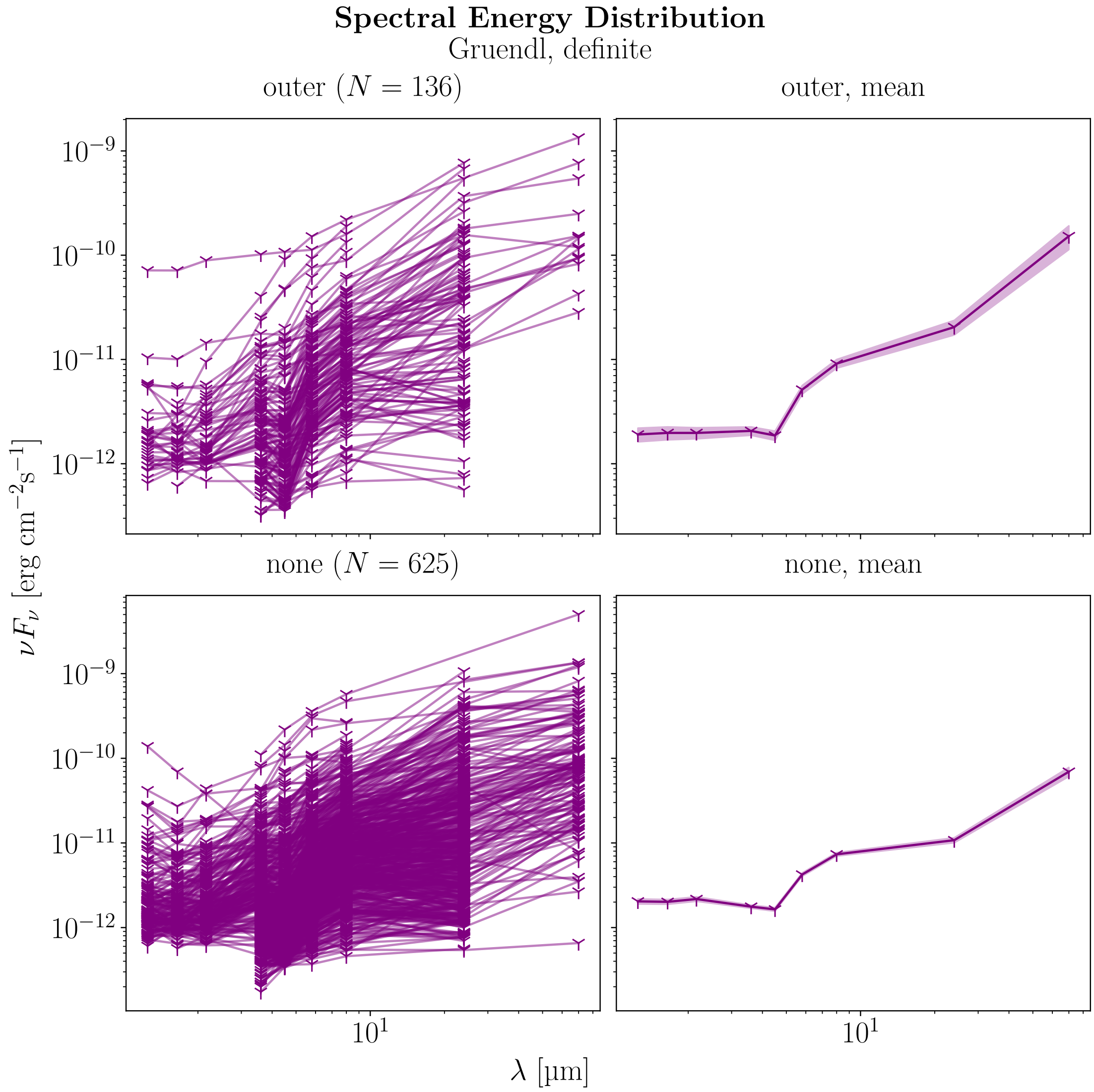

FIGURE 6.16: *Continued.*

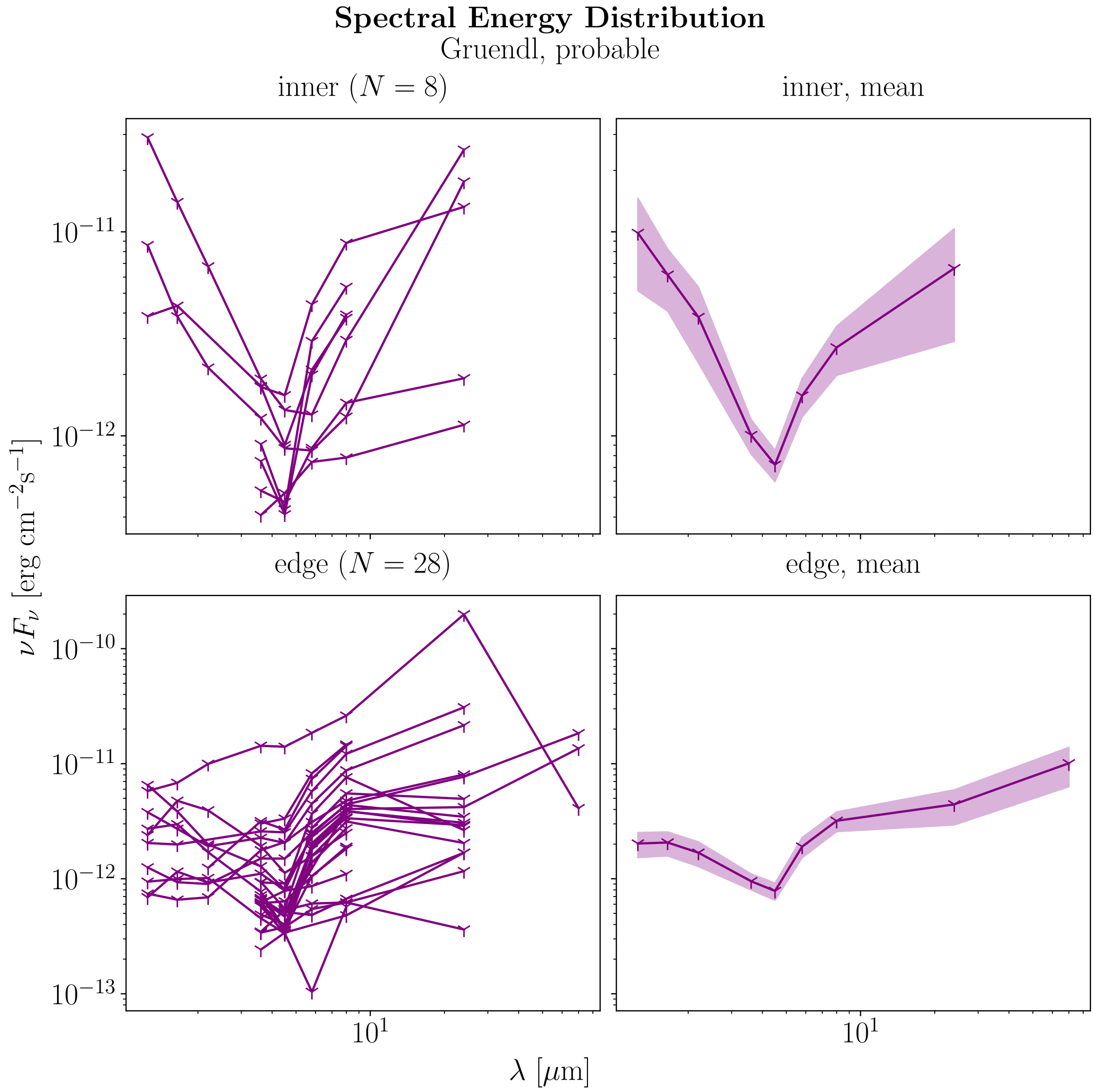

FIGURE 6.17: SEDs for the four different regions for catalog 2 group *probable* YSOs (section 5.1.2) [Gruendl & Chu, 2009].

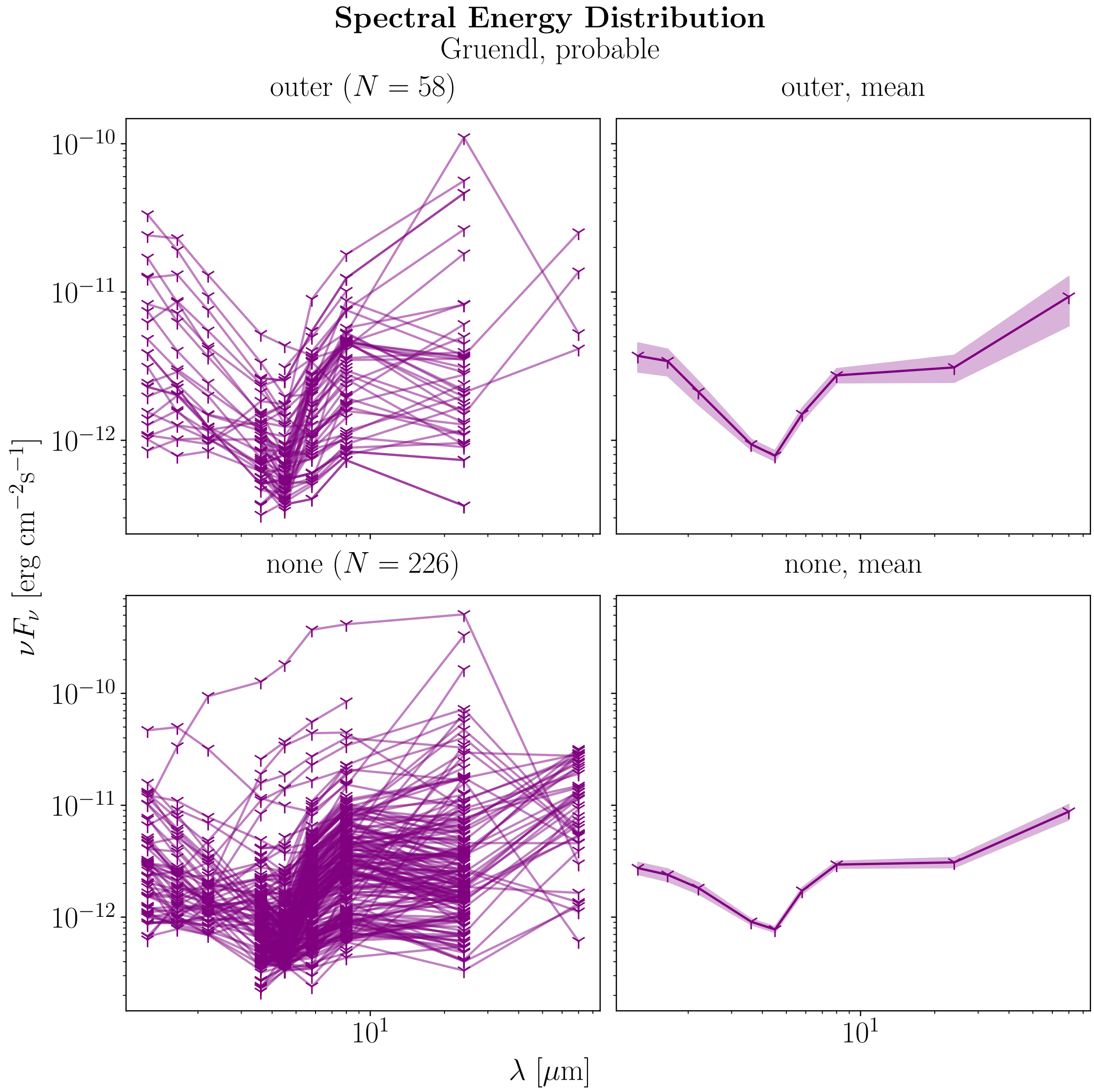

FIGURE 6.17: *Continued.*

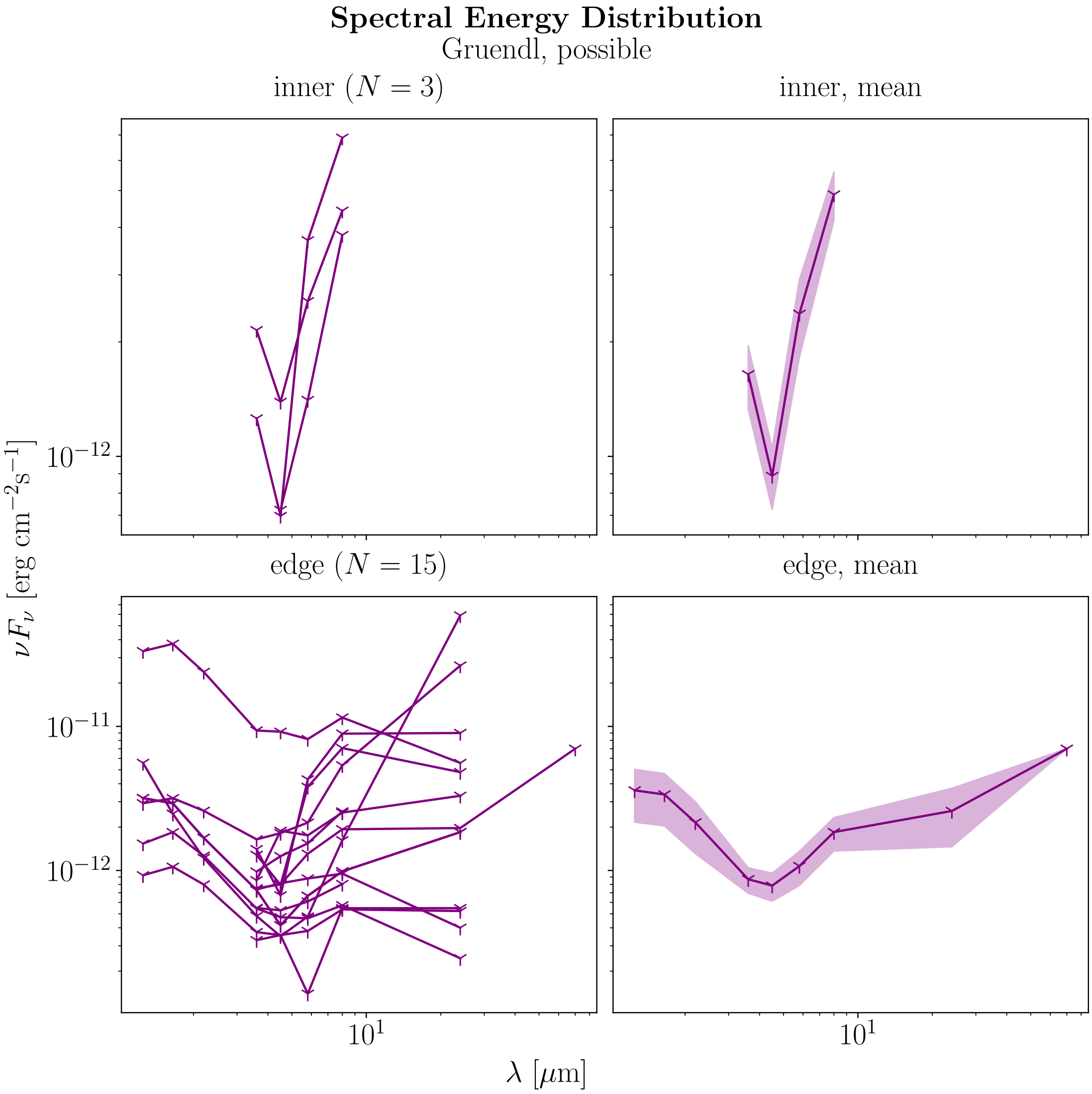

FIGURE 6.18: SEDs for the four different regions for catalog 2 group *possible* YSOs (section 5.1.2) [Gruendl & Chu, 2009].

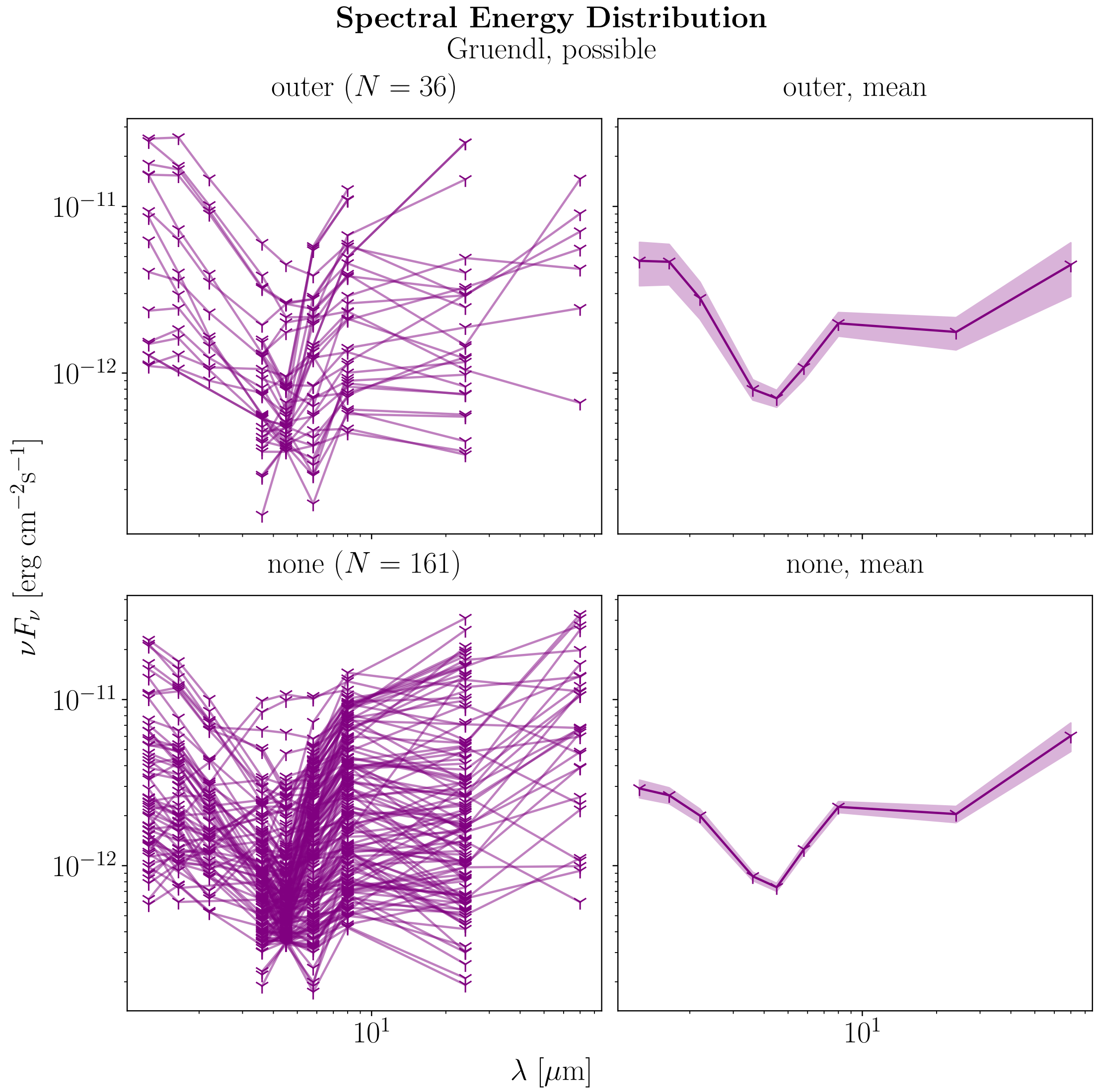

FIGURE 6.18: *Continued.*

7 Summary and Outlook

In this work, young stellar objects in and around supernova remnants in the Large Magellanic Cloud were investigated through color-magnitude and color-color diagrams. Furthermore, spectral energy distributions were plotted and the infrared spectral index was calculated. For the analysis, the YSOs were assigned to four different regions depending on their distance to supernova remnants. The young stellar objects closest to the remnants were found to be associated with class I/II sources rather than class 0/III YSOs. However, it is to be noted that the original data catalogs for YSOs are biased towards younger stars in class I/II. Kolmogorov-Smirnov tests were conducted in order to assess the similarity of distributions of YSOs in CMDs and CCDs between the *inner* and *edge* , *outer* , *none* regions. The samples in CCDs could not be established to follow different distributions. The positions of YSOs in the [8.0 – 24] vs $m_{8.0}$ CMD, on the other hand, vary in the *inner* and remaining regions. Spectral energy distributions at $\lambda \sim 10\,\mu m$ for YSOs are characterized by the contribution from the envelope and disk.

To find more conclusive evidence of the above statement, correlations between the positions of YSOs in CMDs and CCDs belonging to one specific region and to different regions can be investigated. To calculate the spectral index, a linear least squares fit to the SEDs can be performed. The results from this work will become more statistically significant if more YSOs are assigned to the *inner* region of SNRs. Therefore, further samples of YSOs or SNRs have to be included in the analysis.

References

[Bozzetto et al., 2017] Bozzetto, L. M., Filipović, M. D., Vukotić, B., Pavlović, M. Z., Urošević, D., Kavanagh, P. J., Arbutina, B., Maggi, P., Sasaki, M., Haberl, F., et al. (2017). Statistical analysis of supernova remnants in the Large Magellanic Cloud. *The Astrophysical Journal Supplement Series*, 230(1):2.

[California Institute of Technology, 2006] California Institute of Technology (2006). A Brief Explanation of 2MASS. `https://www.ipac.caltech.edu/2mass/overview/about2mass.html`.

[California Institute of Technology, 2022] California Institute of Technology (2022). NASA IPAC Teacher Archive Research Program. `https://coolwiki.ipac.caltech.edu/index.php/Central_wavelengths_and_zero_points`.

[Carlson et al., 2012] Carlson, L., Sewiło, M., Meixner, M., Romita, K., and Lawton, B. (2012). Identifying young stellar objects in nine Large Magellanic Cloud star-forming regions. *Astronomy & Astrophysics*, 542:A66.

[Carroll & Ostlie, 2017] Carroll & Ostlie (2017). *An introduction to modern astrophysics*. Cambridge University Press.

[Draine, 2010] Draine, B. T. (2010). *Physics of the interstellar and intergalactic medium*, volume 19. Princeton University Press.

[Dunham et al., 2015] Dunham, M. M., Allen, L. E., Evans II, N. J., Broekhoven-Fiene, H., Cieza, L. A., Di Francesco, J., Gutermuth, R. A., Harvey, P. M., Hatchell, J., Heiderman, A., et al. (2015). Young stellar objects in the Gould Belt. *The Astrophysical Journal Supplement Series*, 220(1):11.

[Gruendl & Chu, 2009] Gruendl & Chu (2009). High- and intermediate-mass young stellar objects in the Large Magellanic Cloud. *The Astrophysical Journal Supplement Series*, 184(1):172.

[Heim, 2017] Heim, M. (2017). Young stellar object candidates in the vicinity of Supernova Remnants. M.sc.-thesis, Friedrich-Alexander Universität Erlangen-Nürnberg und Eberhard-Karls Universität Tübingen.

[Karttunen et al., 2007] Karttunen et al. (2007). *Fundamental Astronomy*. Springer.

[Kato et al., 2007] Kato, D., Nagashima, C., Nagayama, T., Kurita, M., Koerwer, J. F., Kawai, T., Yamamuro, T., Zenno, T., Nishiyama, S., Baba, D., et al. (2007). The IRSF Magellanic Clouds point source catalog. *Publications of the Astronomical Society of Japan*, 59(3):615–641.

[Knies, 2015] Knies, J. (2015). Characterizing the Young Stars in the Vicinity of IRAS 23004+5841. B.sc.-thesis, Eberhard Karls Universität Tübingen.

[Maggi et al., 2016] Maggi, P., Haberl, F., Kavanagh, P. J., Sasaki, M., Bozzetto, L. M., Filipović, M., Vasilopoulos, G., Pietsch, W., Points, S. D., Chu, Y.-H., et al. (2016). The population of X-ray supernova remnants in the Large Magellanic Cloud. *Astronomy & Astrophysics*, 585:A162.

[Meixner et al., 2006] Meixner, M., Gordon, K. D., Indebetouw, R., Hora, J. L., Whitney, B., Blum, R., Reach, W., Bernard, J.-P., Meade, M., Babler, B., et al. (2006). Spitzer survey of the Large Magellanic Cloud: Surveying the Agents of a Galaxy's Evolution (SAGE). I. Overview and initial results. *The Astronomical Journal*, 132(6):2268.

[Pennock et al., 2021] Pennock, C. M., Van Loon, J. T., Filipović, M. D., Andernach, H., Haberl, F., Kothes, R., Lenc, E., Rudnick, L., White, S. V., Agliozzo, C., et al. (2021). The ASKAP-EMU Early Science Project: 888 MHz radio continuum survey of the Large Magellanic Cloud. *Monthly Notices of the Royal Astronomical Society*, 506(3):3540–3559.

[Press et al., 2007] Press, W. H., Teukolsky, S. A., and Vetterling, W. T. & Flannery, B. P. (2007). *Numerical recipes 3rd edition: The art of scientific computing.* Cambridge university press.

[Seward & Charles, 2010] Seward & Charles (2010). *Exploring the X-ray Universe.* Cambridge University Press.

[Shu et al., 1987] Shu, F. H., Adams, F. C., Lizano, S., et al. (1987). Star formation in molecular clouds - Observation and theory. *Annual review of astronomy and astrophysics*, 25:23–81.

[Skrutskie et al., 2006] Skrutskie, M., Cutri, R., Stiening, R., Weinberg, M., Schneider, S., Carpenter, J., Beichman, C., Capps, R., Chester, T., Elias, J., et al. (2006). The Two Micron All Sky Survey (2MASS). *The Astronomical Journal*, 131(2):1163.

[Smith et al., 2004] Smith, R., Points, S., Aguilera, C., Leiton, R., Chu, Y.-H., Winkler, P., et al. (2004). The MCELS Survey: Transition from Data to Science. In *American Astronomical Society Meeting Abstracts*, volume 205, page 101.08.

[Smith & the MCELS Team, 1998] Smith & the MCELS Team (1998). The UM/CTIO Magellanic Cloud emission-line survey. *Publications of the Astronomical Society of Australia*, 15(1):163–164.

[Stahler & Palla, 2008] Stahler & Palla (2008). *The formation of stars.* John Wiley & Sons.

[Tielens, 2021] Tielens, A. (2021). *Molecular Astrophysics*, chapter 11, section 1, pages 452–454. Cambridge University Press.

[Vink, 2020] Vink, J. (2020). *Physics and Evolution of Supernova Remnants.* Springer.

[Werner et al., 2004] Werner, M. W., Roellig, T., Low, F., Rieke, G. H., Rieke, M., Hoffmann, W., Young, E., Houck, J., Brandl, B., Fazio, G., et al. (2004). The Spitzer space telescope mission. *The Astrophysical Journal Supplement Series*, 154(1):1.

[Whitney et al., 2008] Whitney, B., Sewilo, M., Indebetouw, R., Robitaille, T., Meixner, M., Gordon, K., Meade, M., Babler, B., Harris, J., Hora, J., et al. (2008). Spitzer Sage Survey of the Large Magellanic Cloud. III. Star formation and 1000 new candidate young stellar objects. *The Astronomical Journal*, 136(1):18.

[Yew et al., 2021] Yew, M., Filipović, M. D., Stupar, M., Points, S. D., Sasaki, M., Maggi, P., Haberl, F., Kavanagh, P. J., Parker, Q. A., Crawford, E. J., et al. (2021). New optically identified supernova remnants in the Large Magellanic Cloud. *Monthly Notices of the Royal Astronomical Society*, 500(2):2336–2358.

[Zeilik & Gregory, 1998] Zeilik & Gregory (1998). *Introductory Astronomy and Astrophysics.* Thomson Learning.

Appendix

A Color-Magnitude and Color-Color Diagrams

Color-Magnitude Diagrams. The following figures document CMDs generated for catalog 1 (section 5.1.1), figure A.1, and for all three groups in catalog 2 (section 5.1.2), figure A.2, A.3, A.4.

Figures following A.5 report CMDs including contours for the density functions.

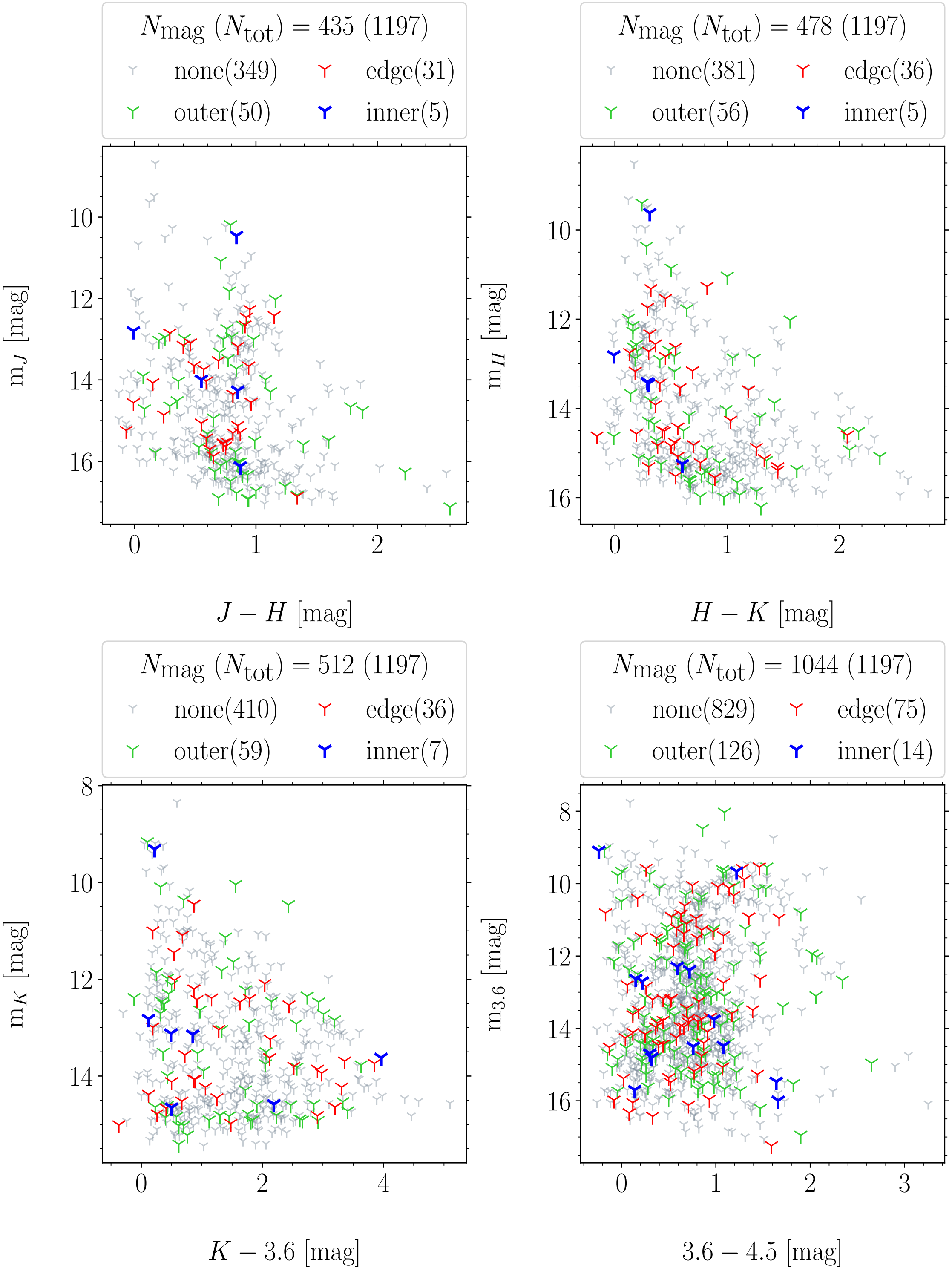

FIGURE A.1: CMDs for all six magnitude combinations for catalog 1 (section 5.1.1) [Whitney et al., 2008].

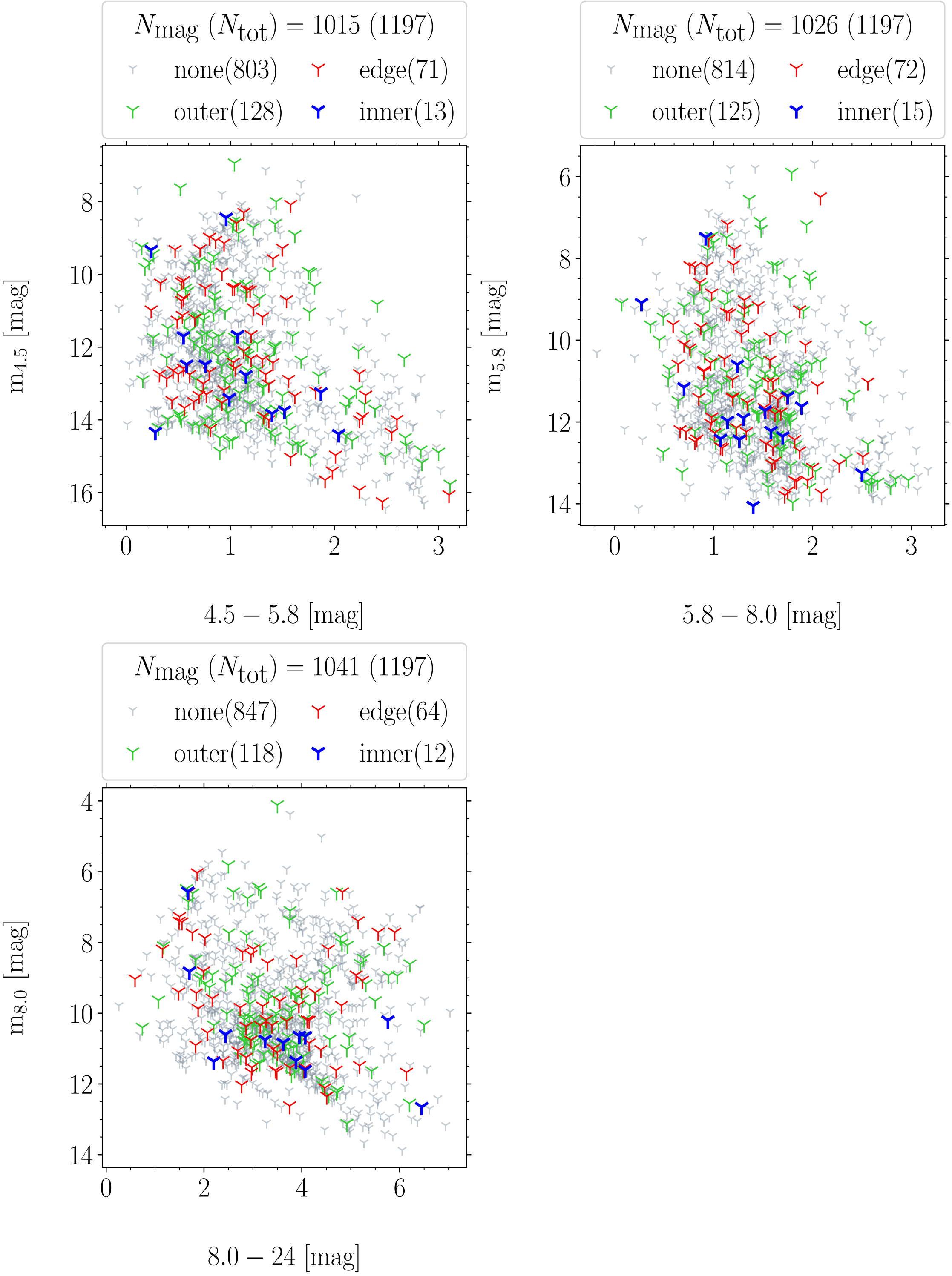

FIGURE A.1: *Continued.*

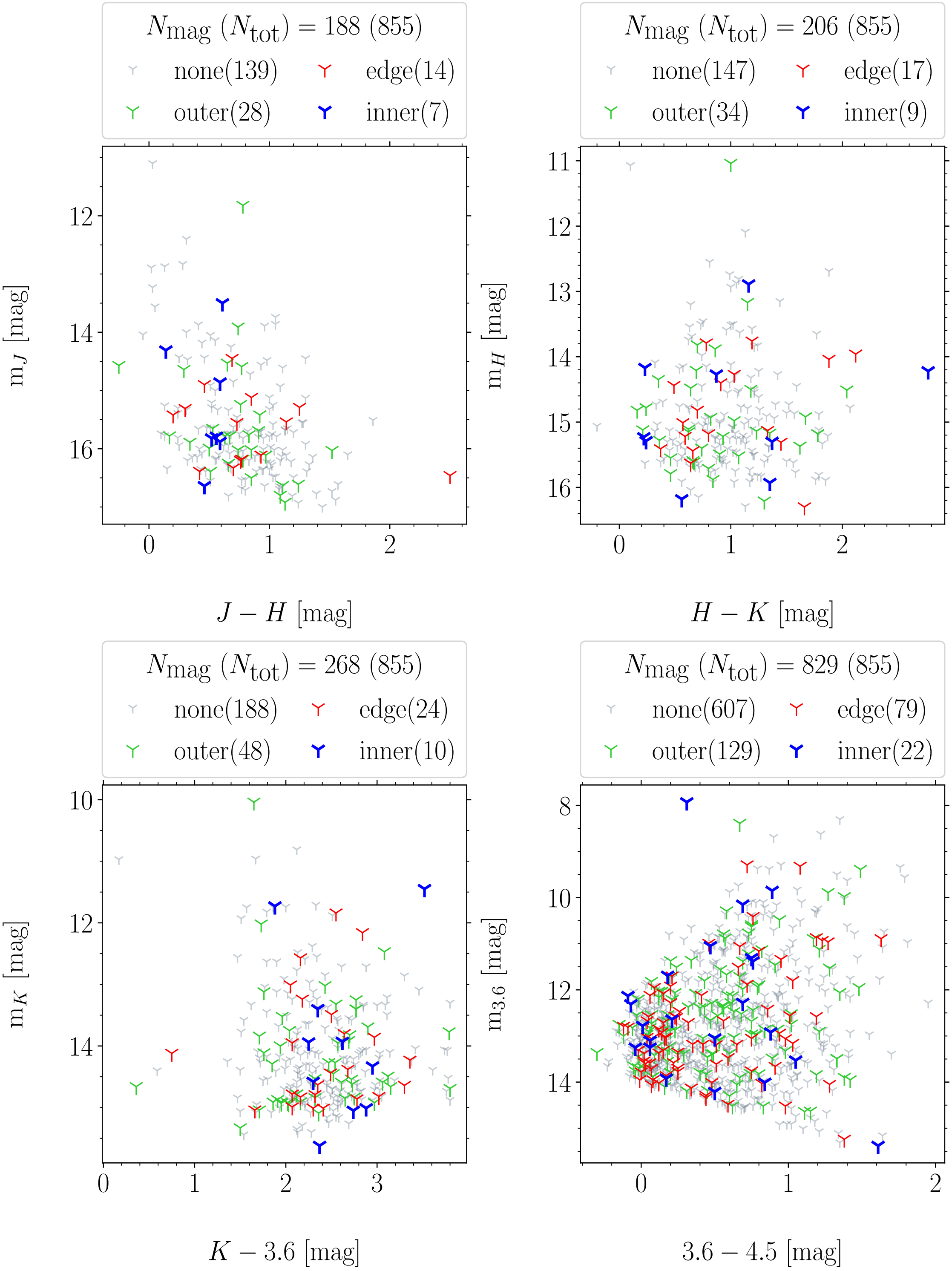

FIGURE A.2: CMDs for all six magnitude combinations for catalog 2 and group *definite* (section 5.1.2) [Gruendl & Chu, 2009].

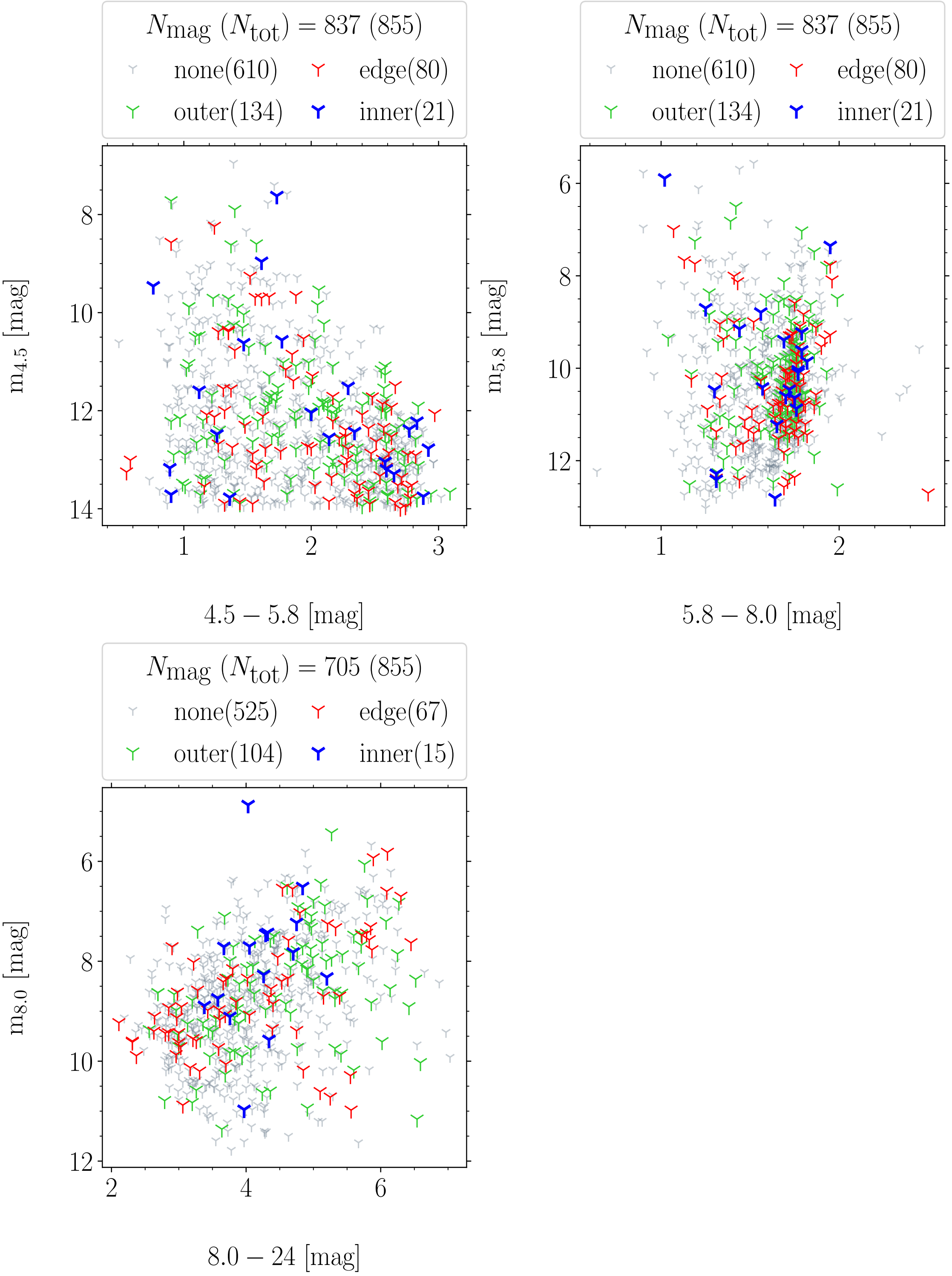

FIGURE A.2: *Continued.*

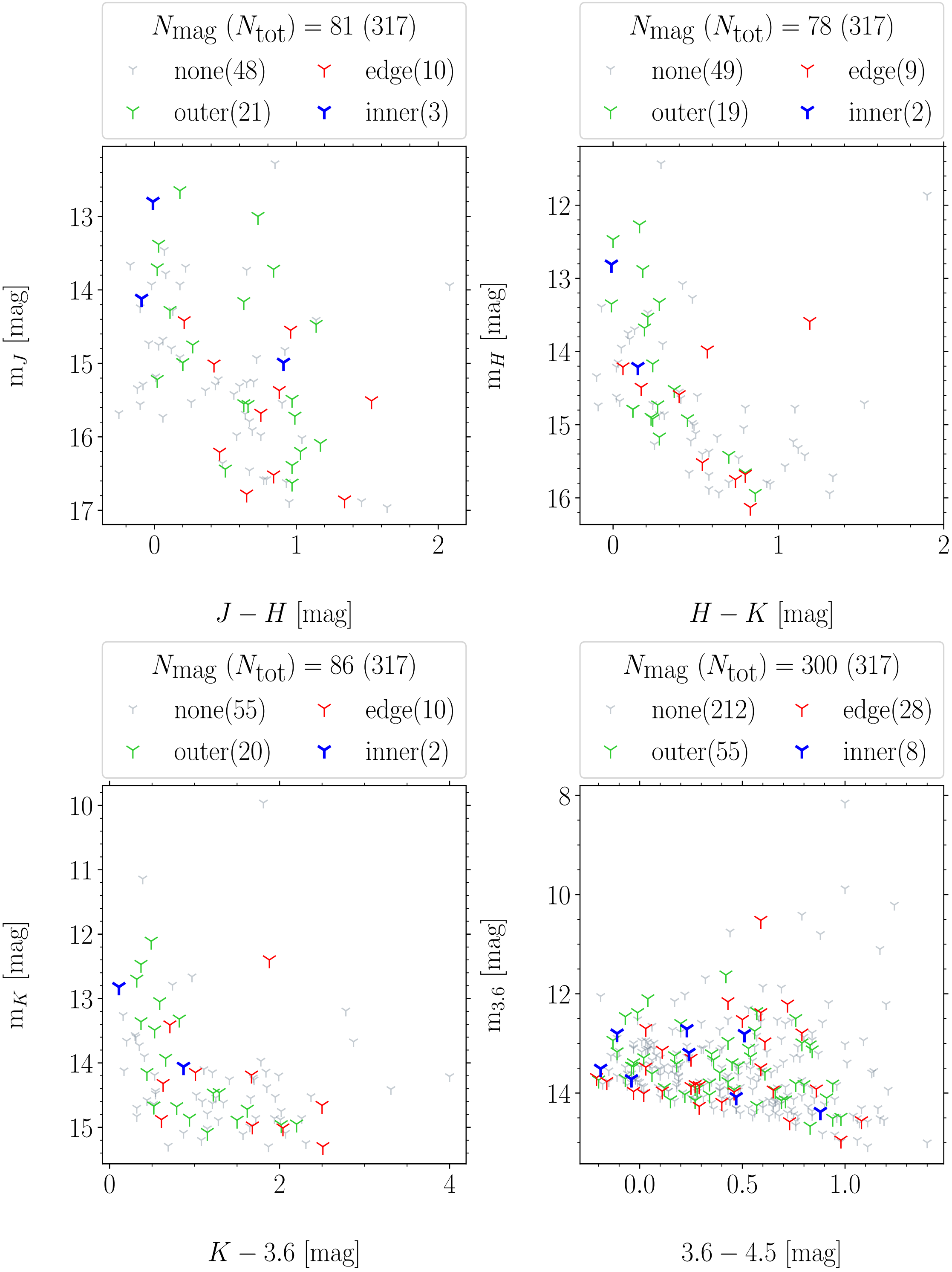

FIGURE A.3: CMDs for all six magnitude combinations for catalog 2 and group *probable* (section 5.1.2) [Gruendl & Chu, 2009].

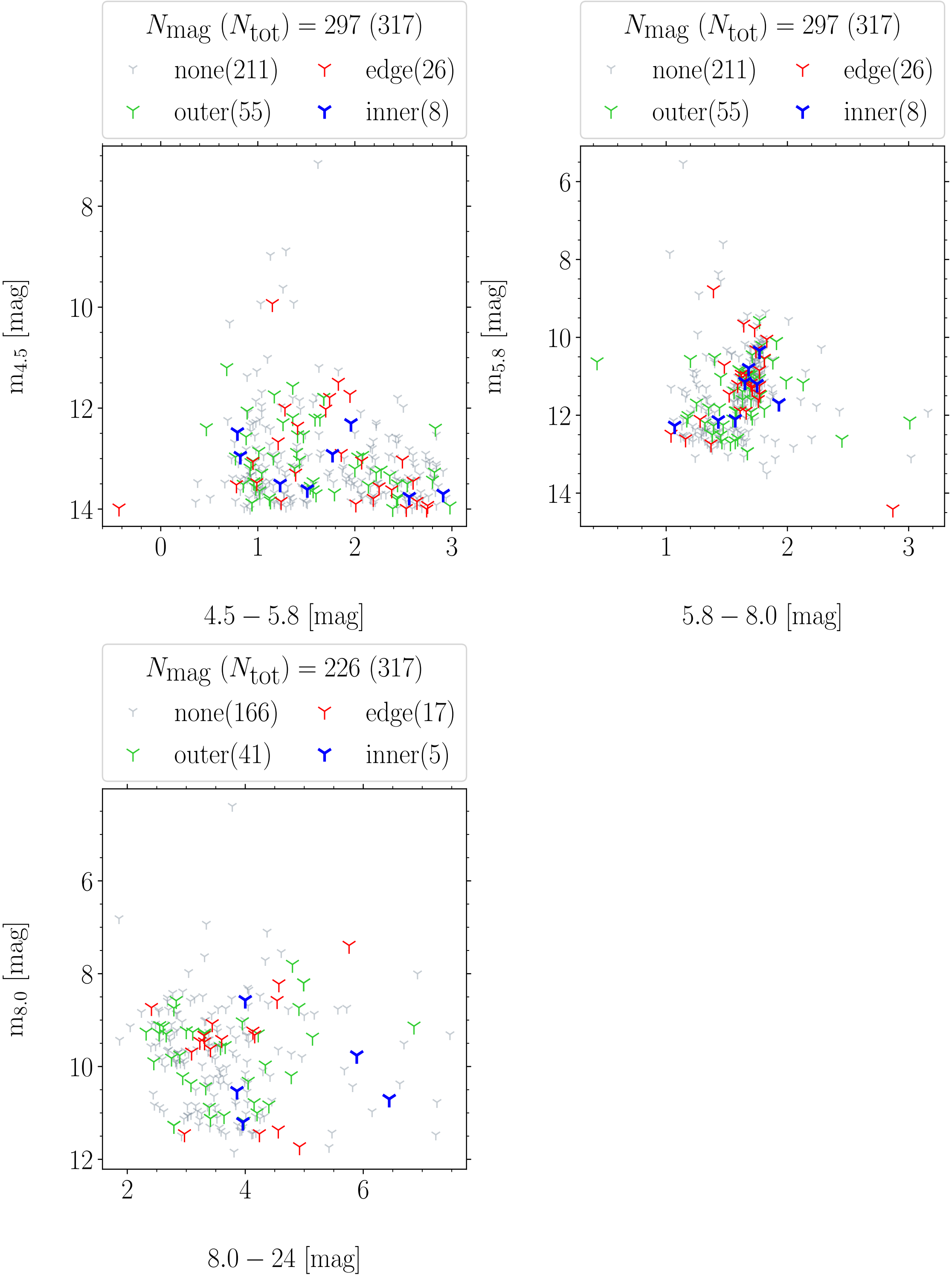

FIGURE A.3: *Continued.*

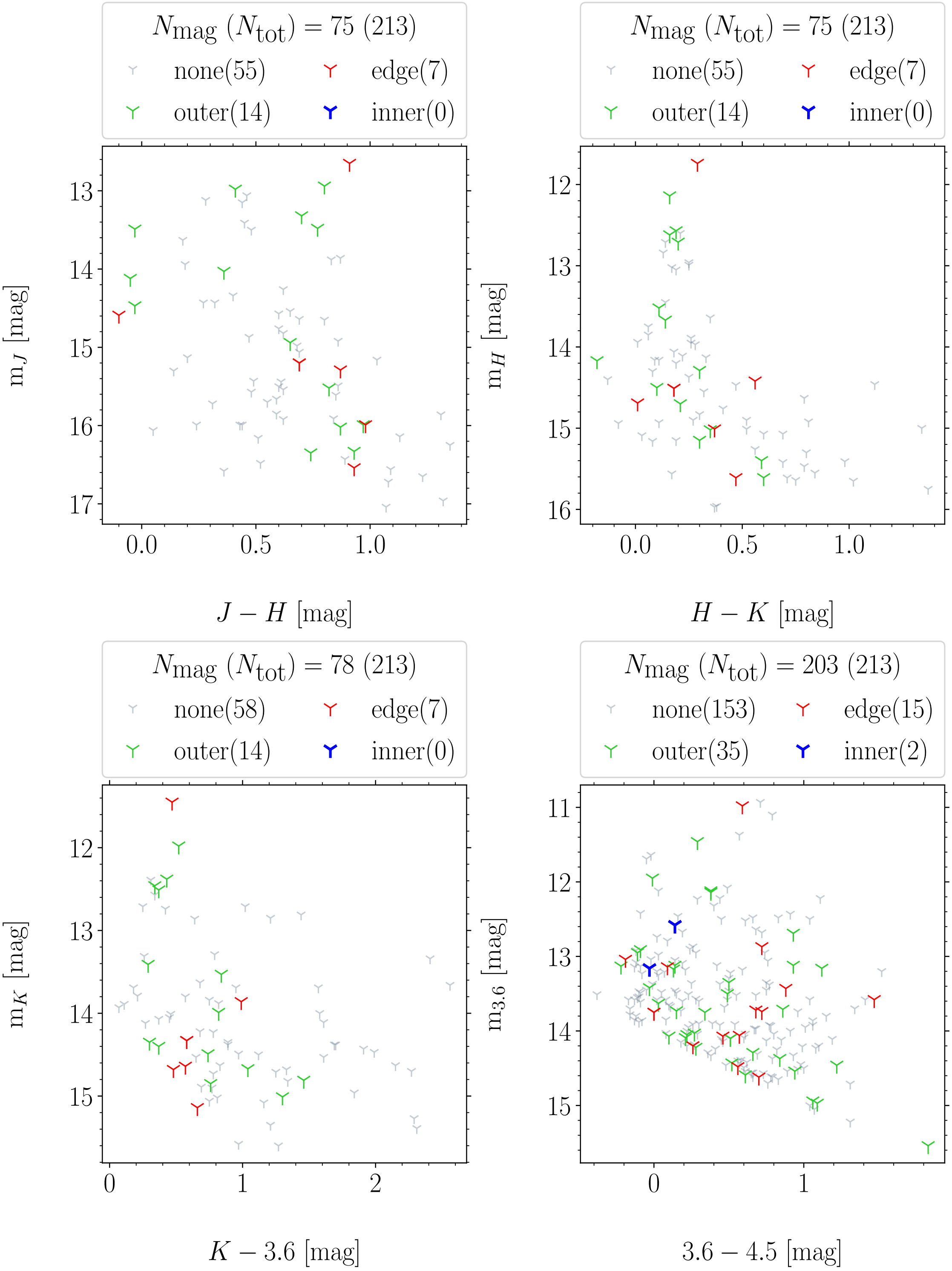

Figure A.4: CMDs for all six magnitude combinations for catalog 2 and group *possible* (section 5.1.2) [Gruendl & Chu, 2009].

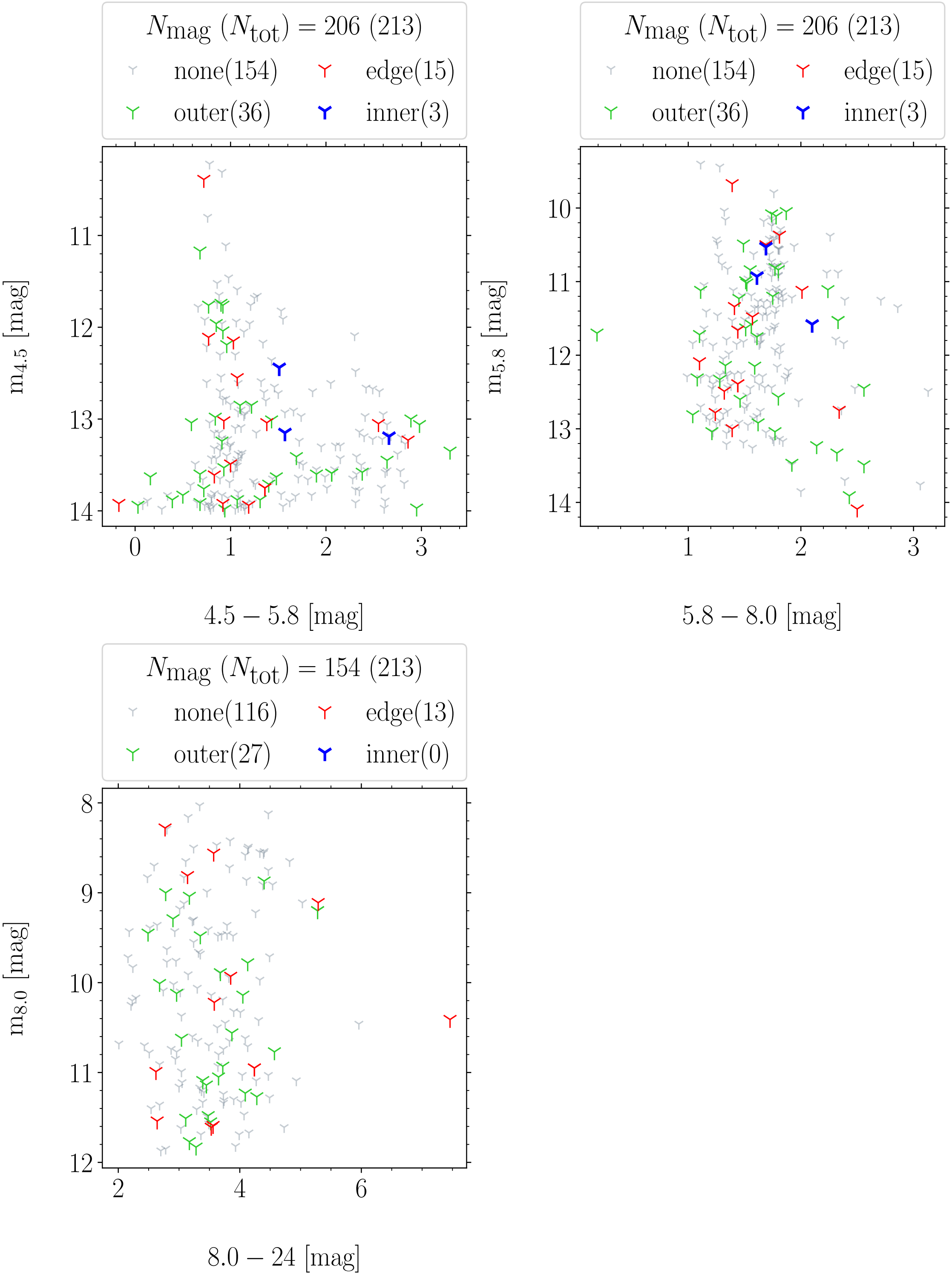

FIGURE A.4: *Continued.*

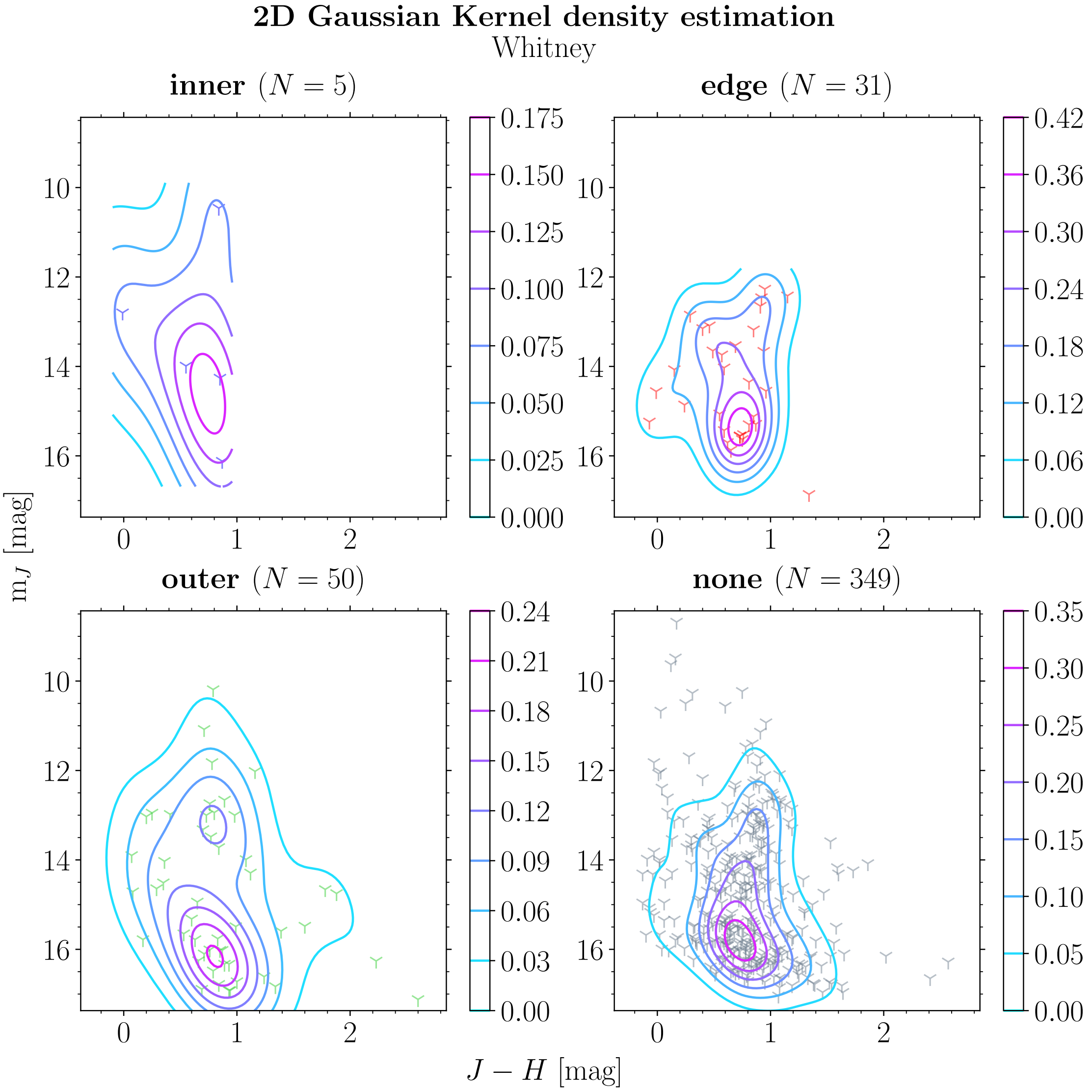

FIGURE A.5: The $[J - H]$ vs $[\mathrm{m}_J]$ diagram for catalog 1 YSOs (section 5.1.1) with contours indicating the distribution [Whitney et al., 2008].

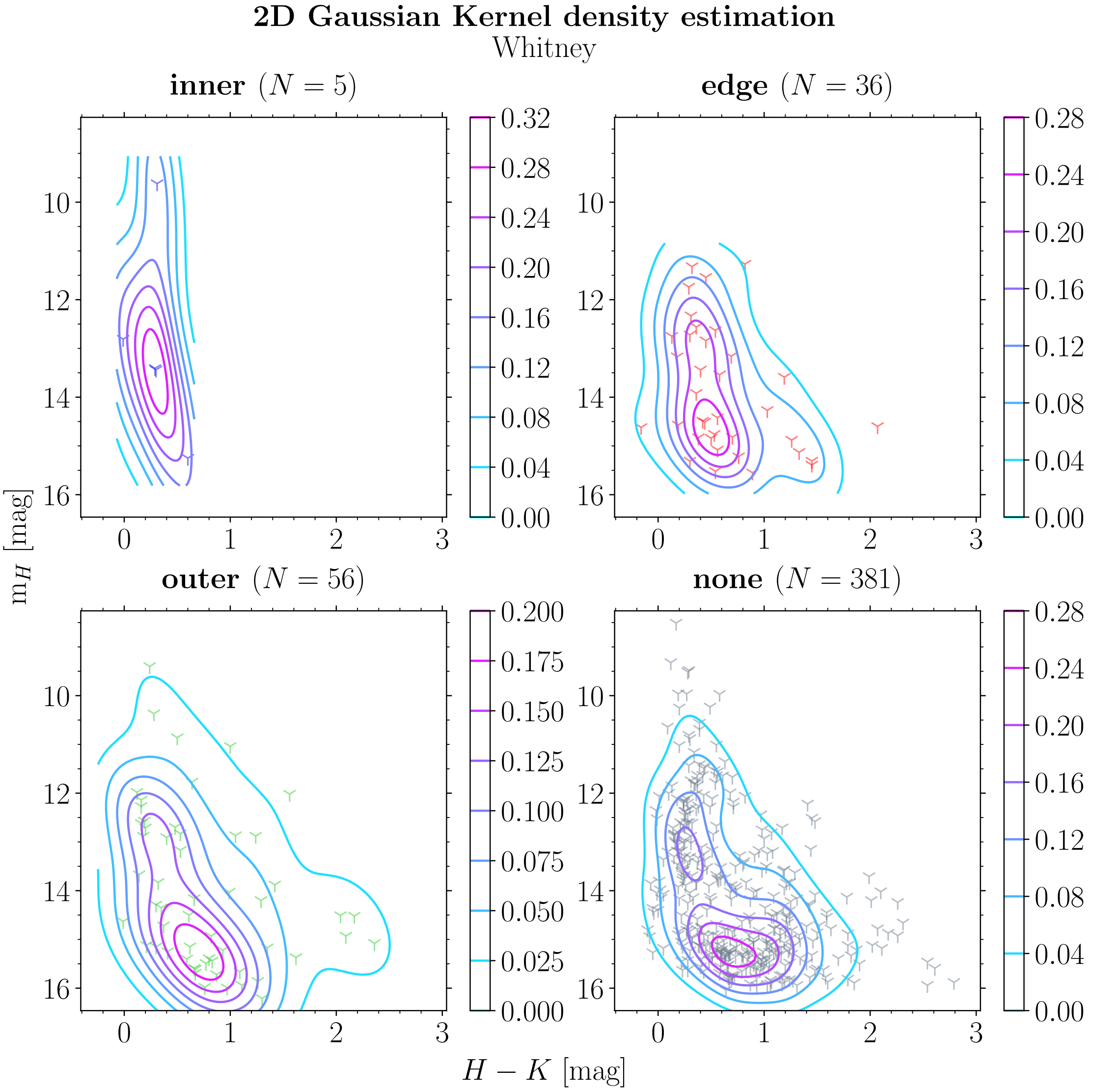

FIGURE A.6: The $[H - K]$ vs $[m_H]$ diagram for catalog 1 YSOs (section 5.1.1) with contours indicating the distribution [Whitney et al., 2008].

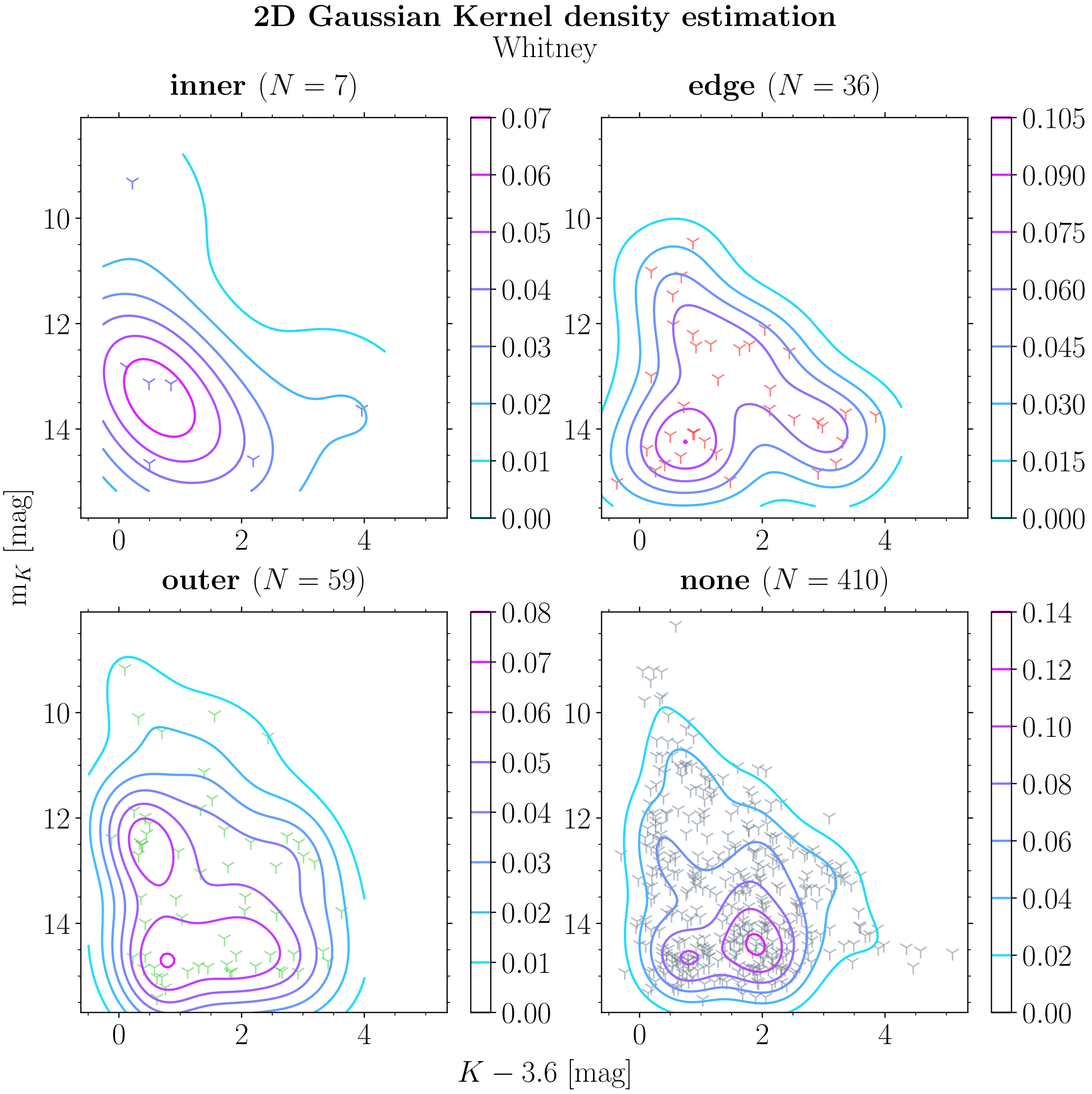

FIGURE A.7: The $[K - 3.6]$ vs $[m_K]$ diagram for catalog 1 YSOs (section 5.1.1) with contours indicating the distribution [Whitney et al., 2008].

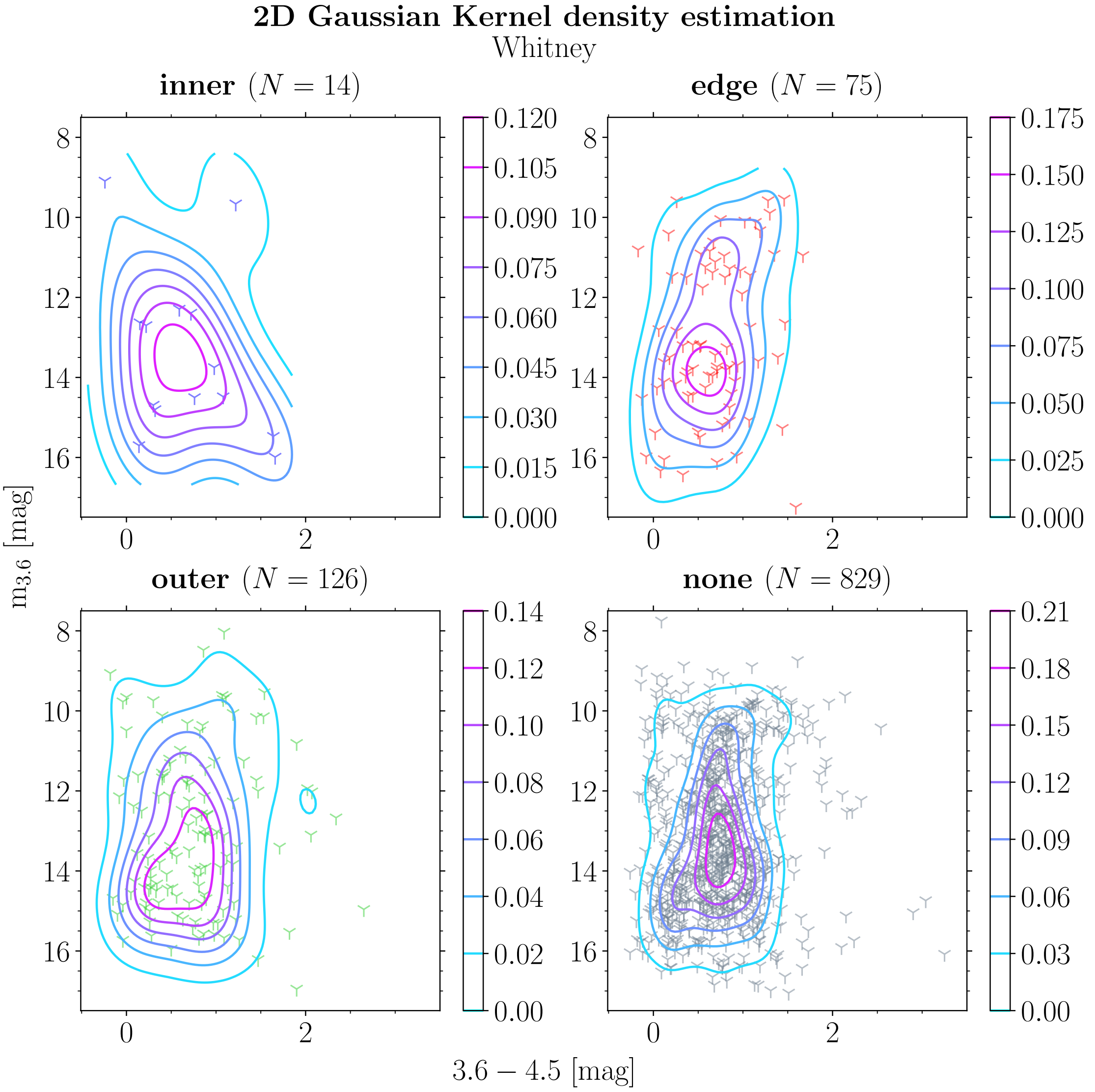

FIGURE A.8: The [3.6 − 4.5] vs [$m_{3.6}$] diagram for catalog 1 YSOs (section 5.1.1) with contours indicating the distribution [Whitney et al., 2008].

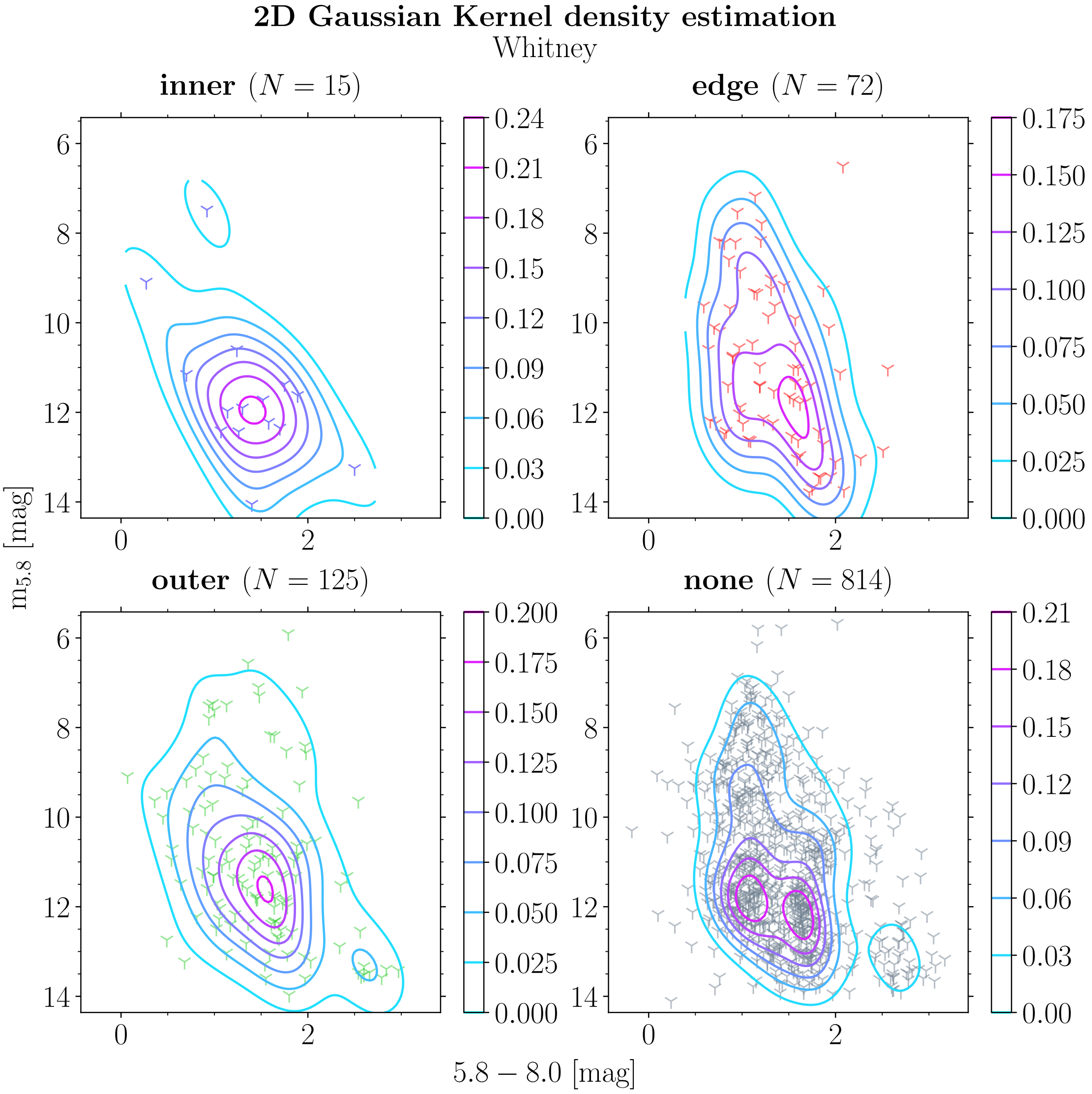

FIGURE A.9: The [5.8 − 8.0] vs [$m_{5.8}$] diagram for catalog 1 YSOs (section 5.1.1) with contours indicating the distribution [Whitney et al., 2008].

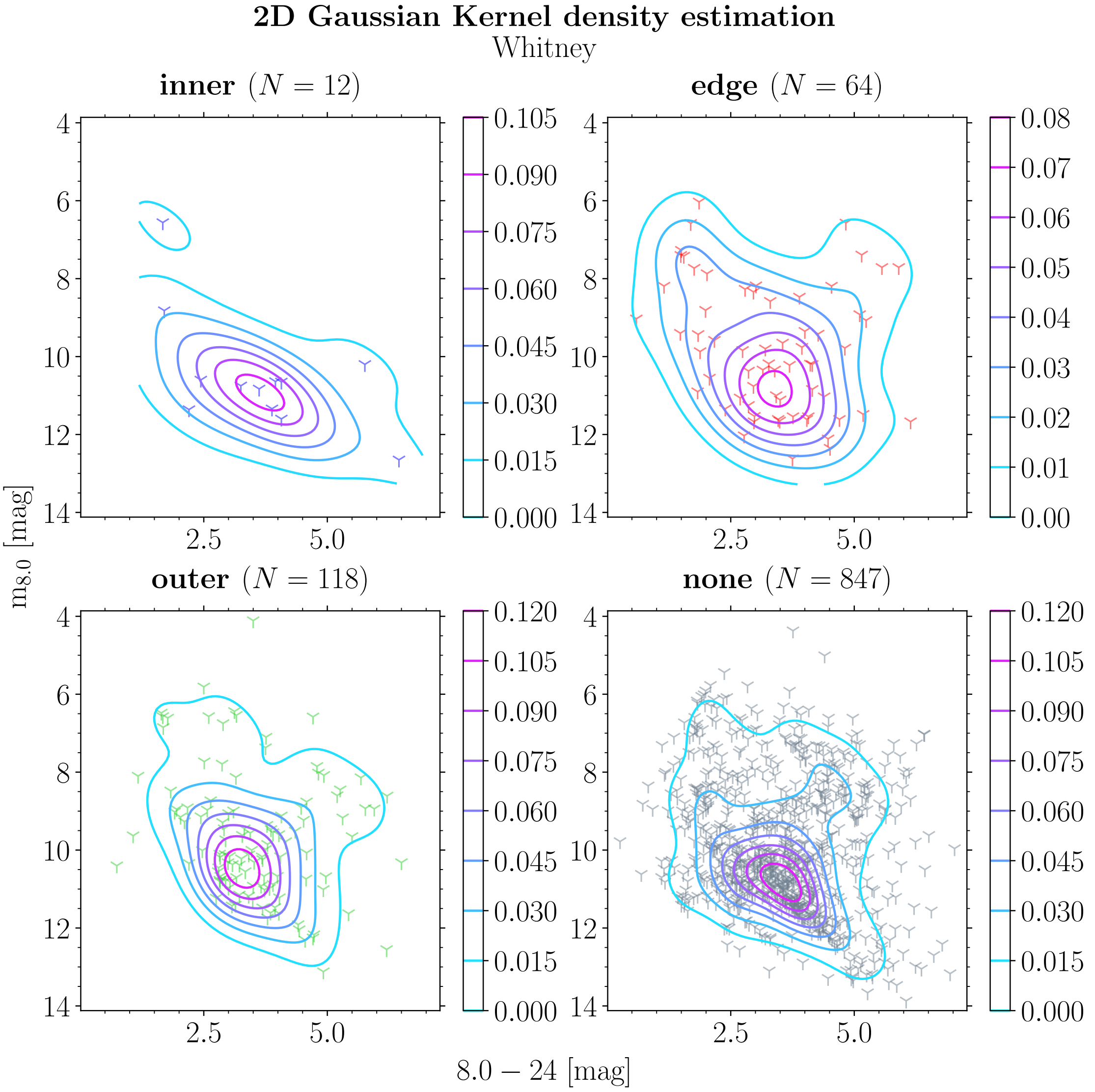

FIGURE A.10: The [8.0 − 24] vs [$m_{8.0}$] diagram for catalog 1 YSOs (section 5.1.1) with contours indicating the distribution [Whitney et al., 2008].

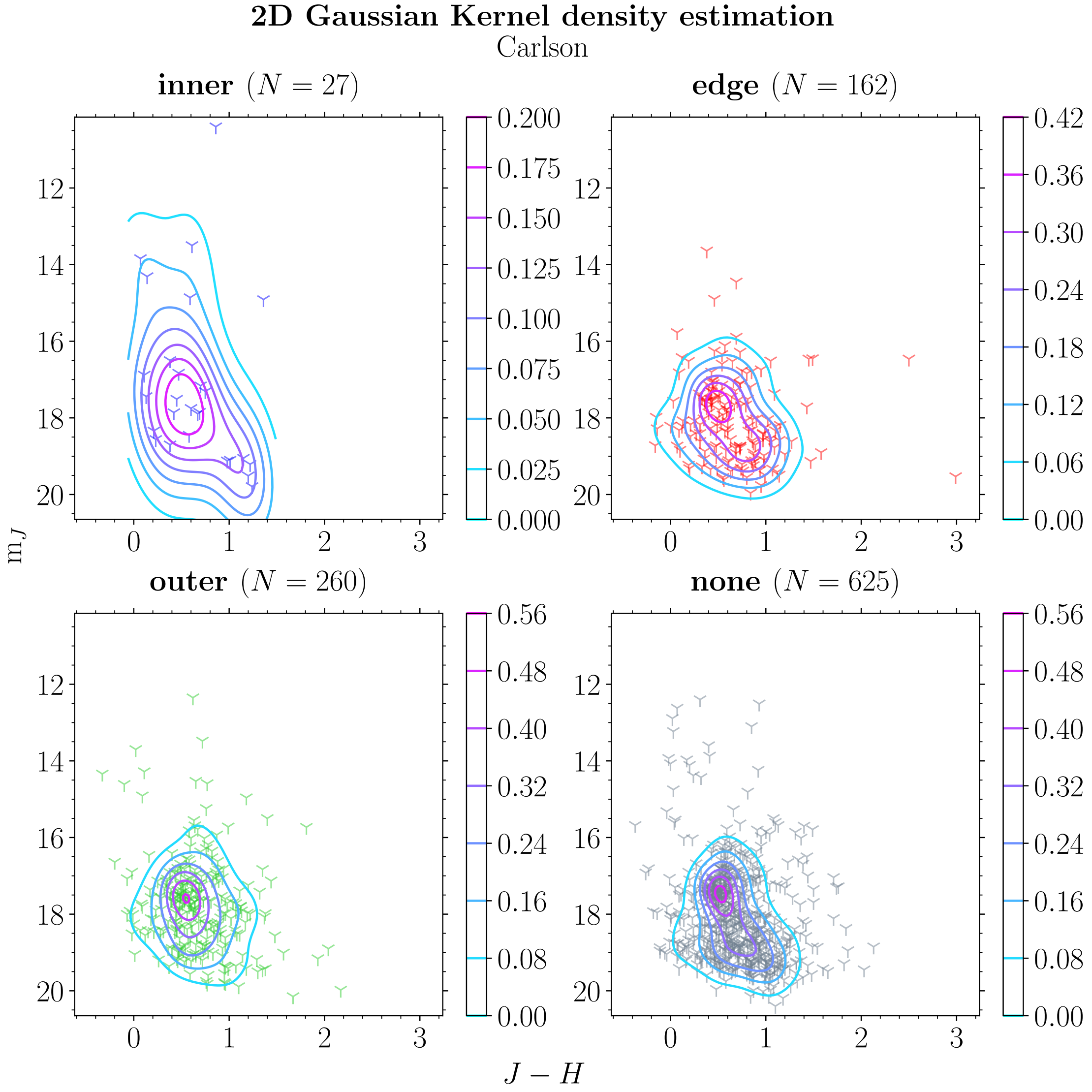

FIGURE A.11: The $[J-H]$ vs $[\mathrm{m}_J]$ diagram for catalog 3 YSOs with contours indicating the distribution (section 5.1.3).

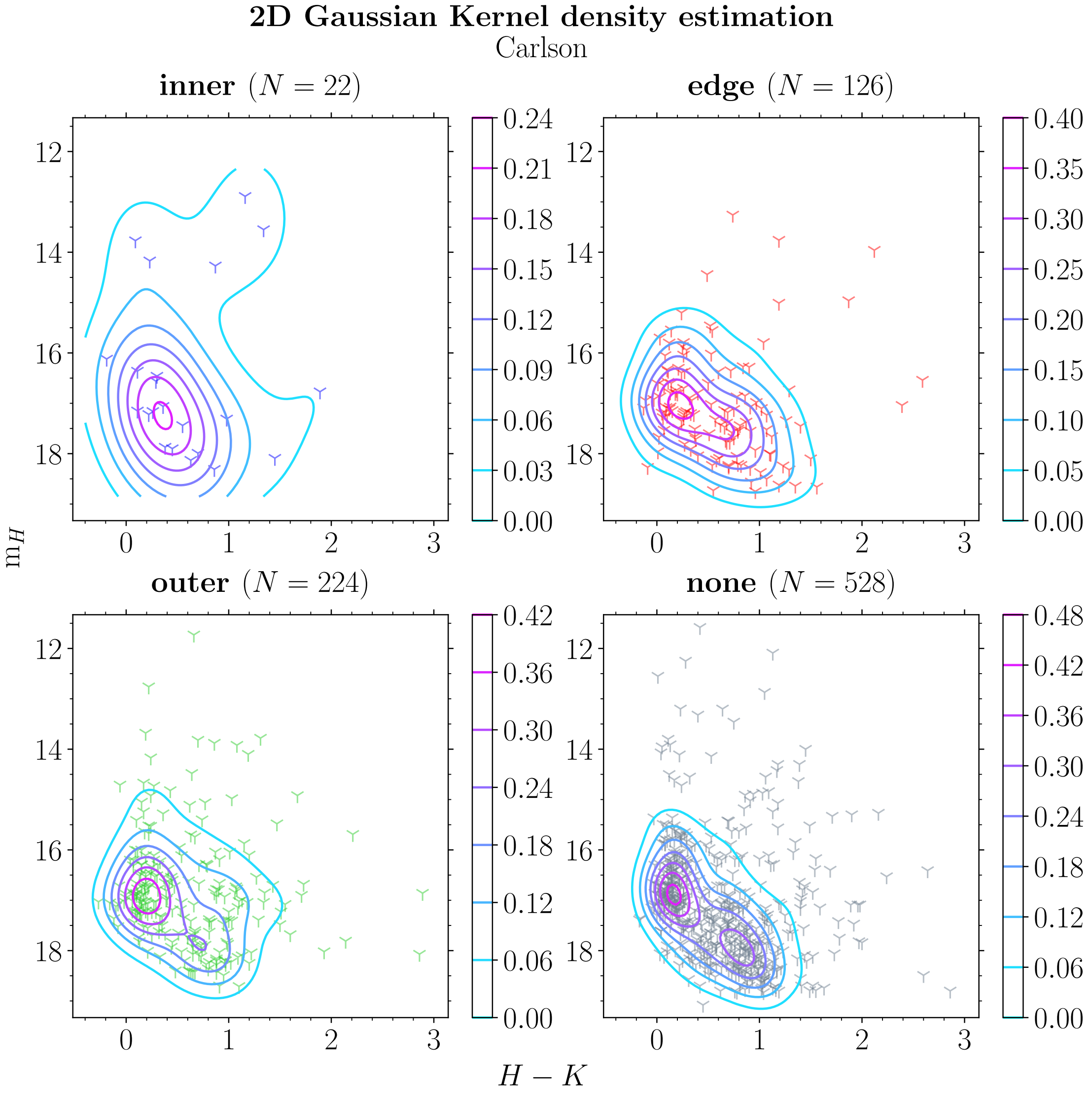

FIGURE A.12: The $[H - K]$ vs $[\mathrm{m}_H]$ diagram for catalog 3 YSOs with contours indicating the distribution (section 5.1.3).

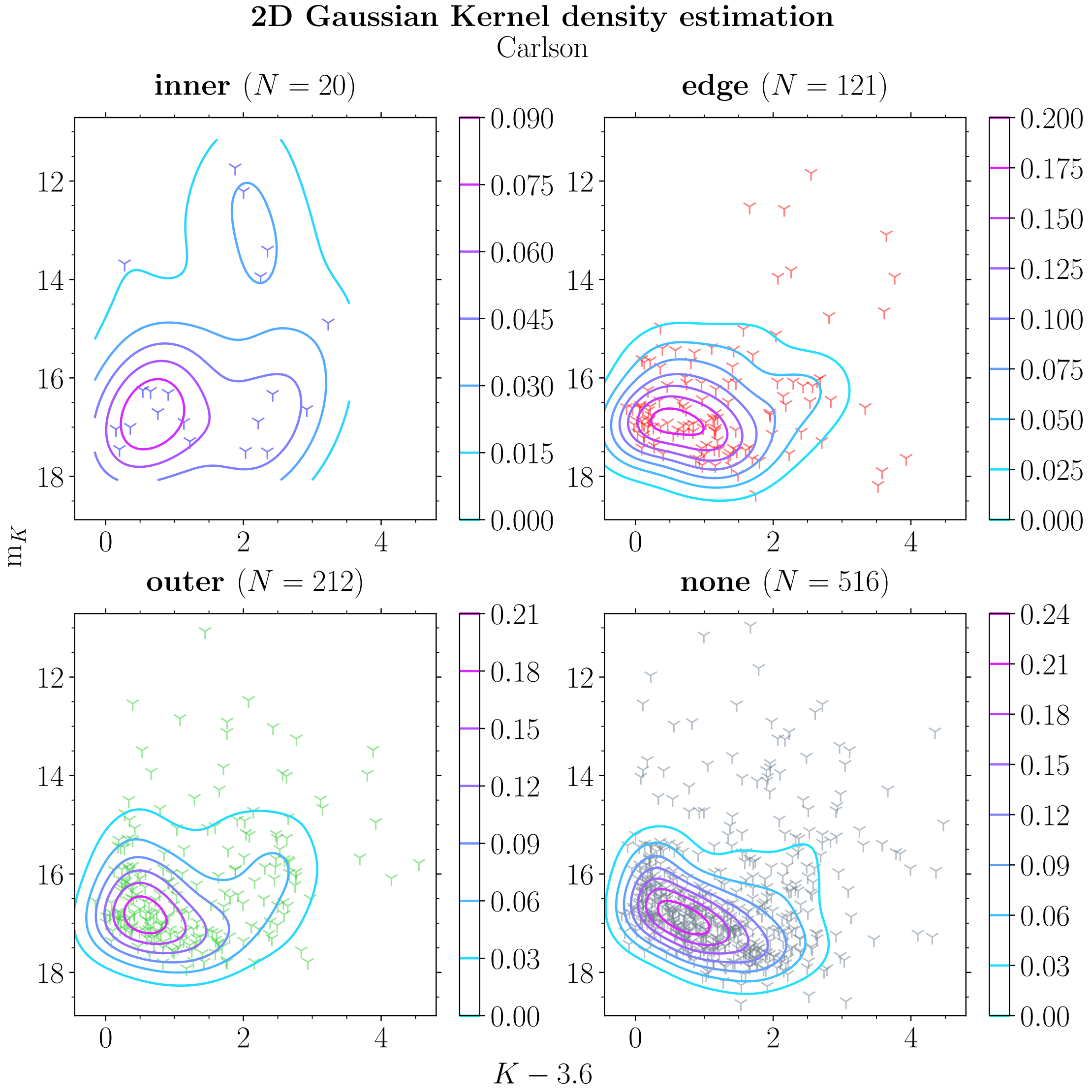

FIGURE A.13: The $[K - 3.6]$ vs $[\mathrm{m}_K]$ diagram for catalog 3 YSOs with contours indicating the distribution (section 5.1.3).

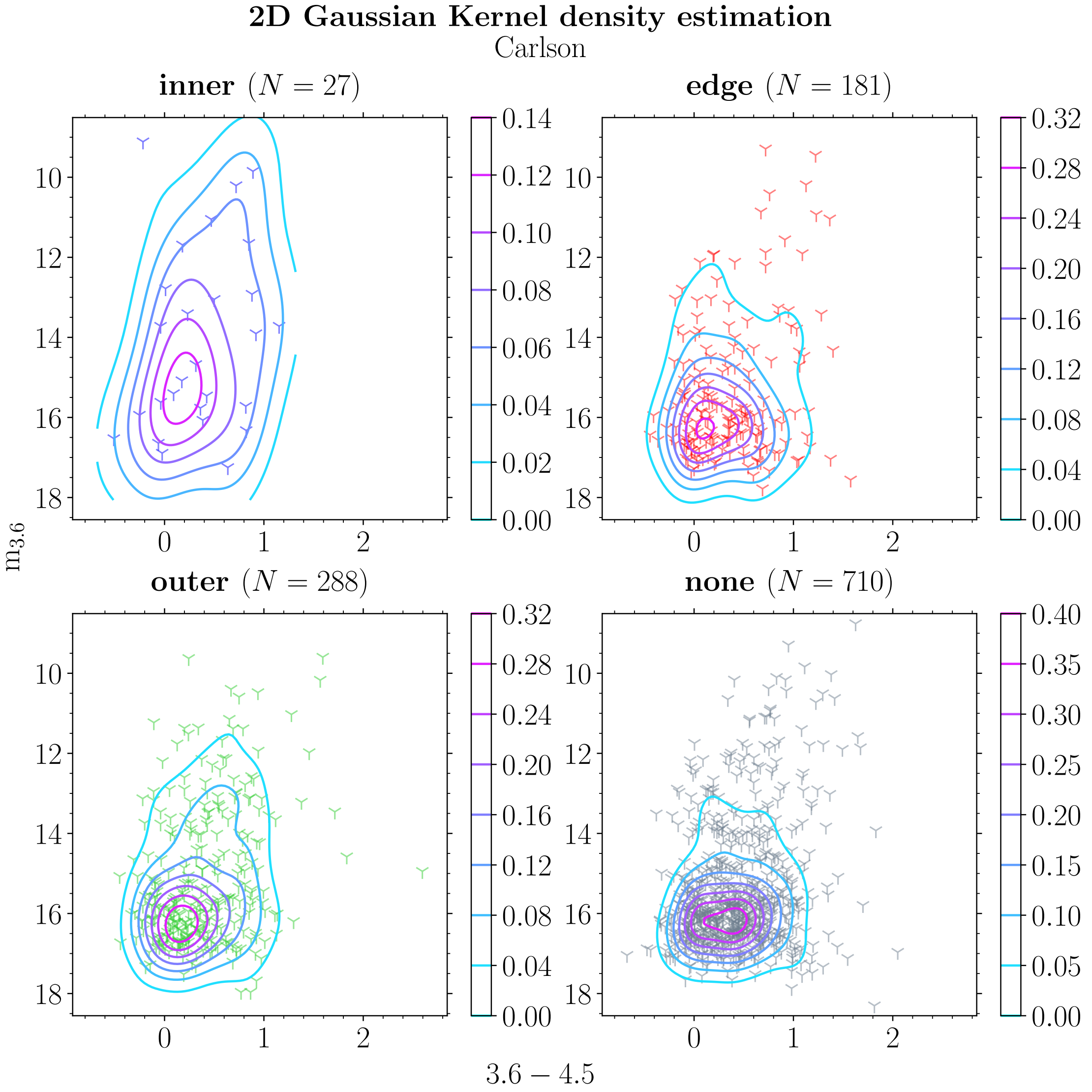

FIGURE A.14: The [3.6 – 4.5] vs [$m_{3.6}$] diagram for catalog 3 YSOs with contours indicating the distribution (section 5.1.3).

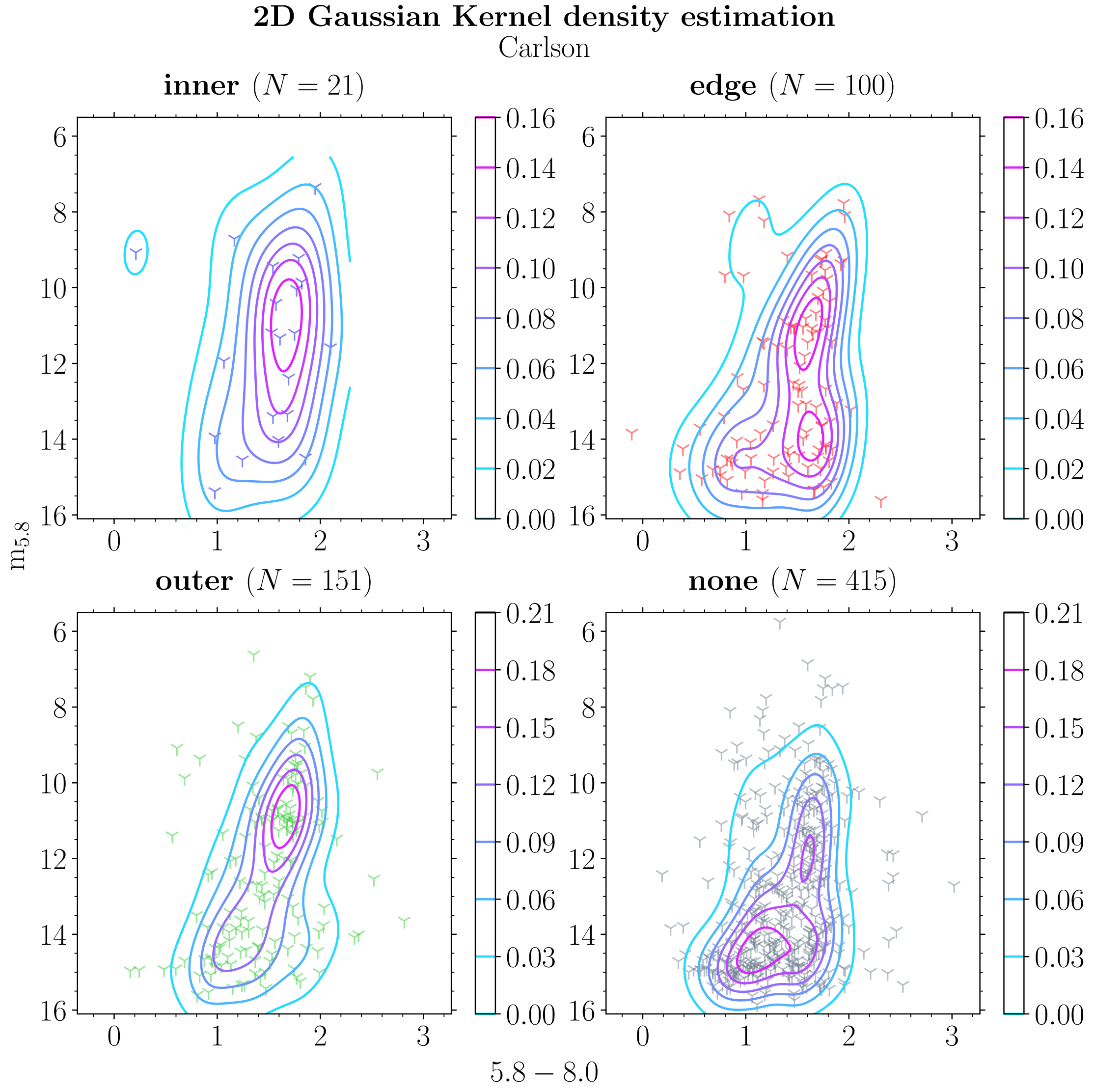

FIGURE A.15: The [5.8 − 8.0] vs [$m_{5.8}$] diagram for catalog 3 YSOs with contours indicating the distribution (section 5.1.3).

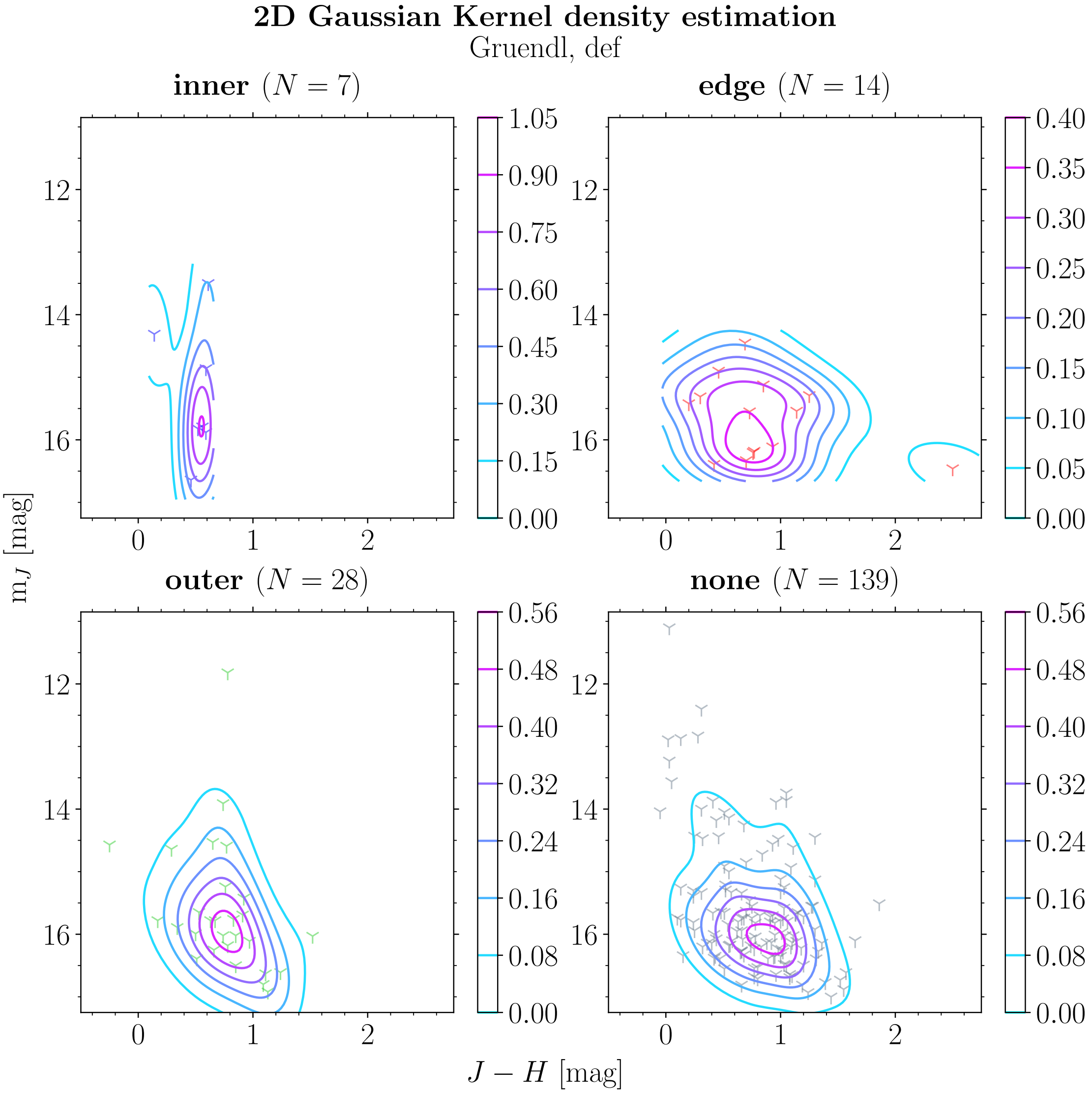

FIGURE A.16: The $[J - H]$ vs $[m_J]$ diagram for catalog 2 group *definite* YSOs (section 5.1.2) with contours indicating the distribution [Gruendl & Chu, 2009].

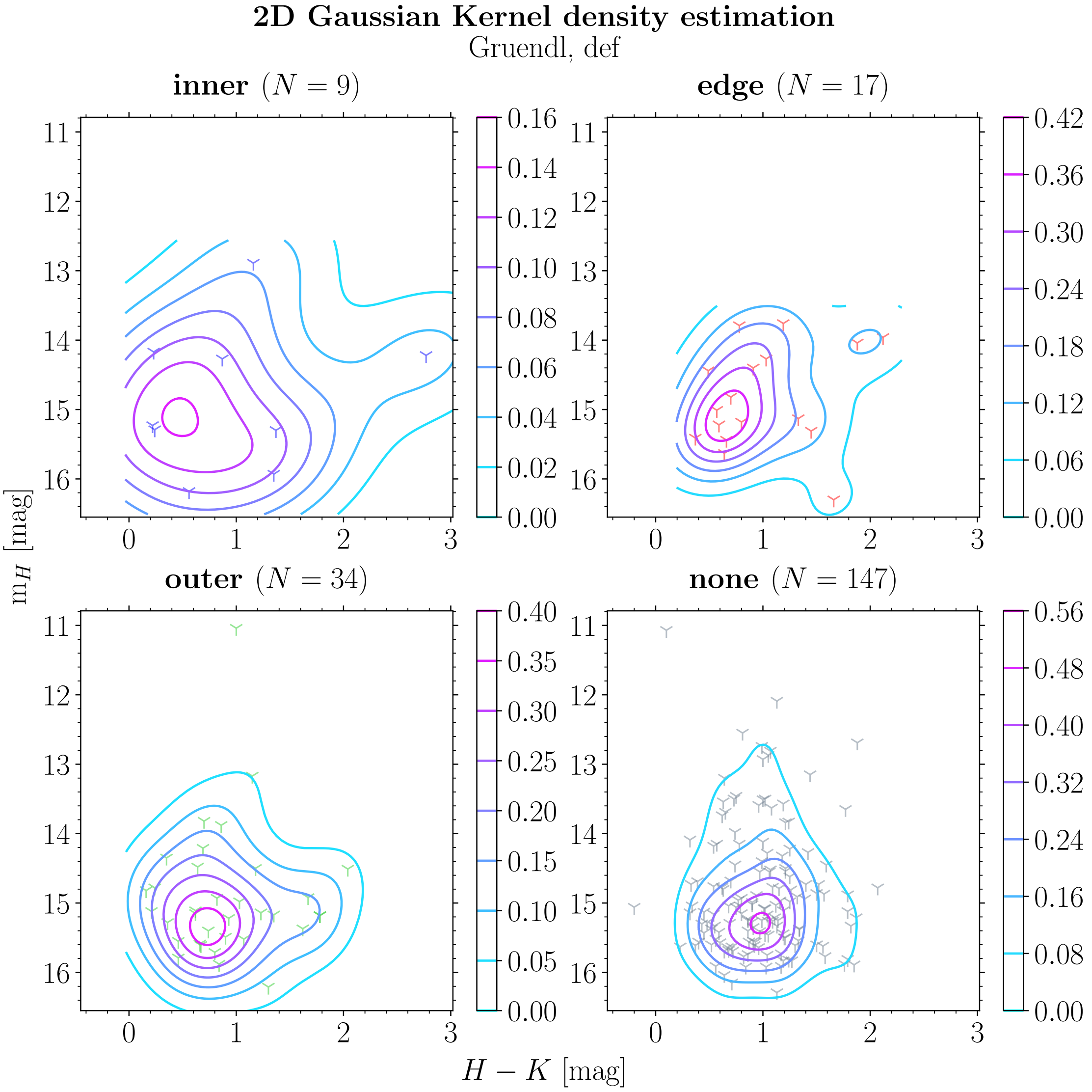

FIGURE A.17: The $[H - K]$ vs $[m_H]$ diagram for catalog 2 group *definite* YSOs (section 5.1.2) with contours indicating the distribution [Gruendl & Chu, 2009].

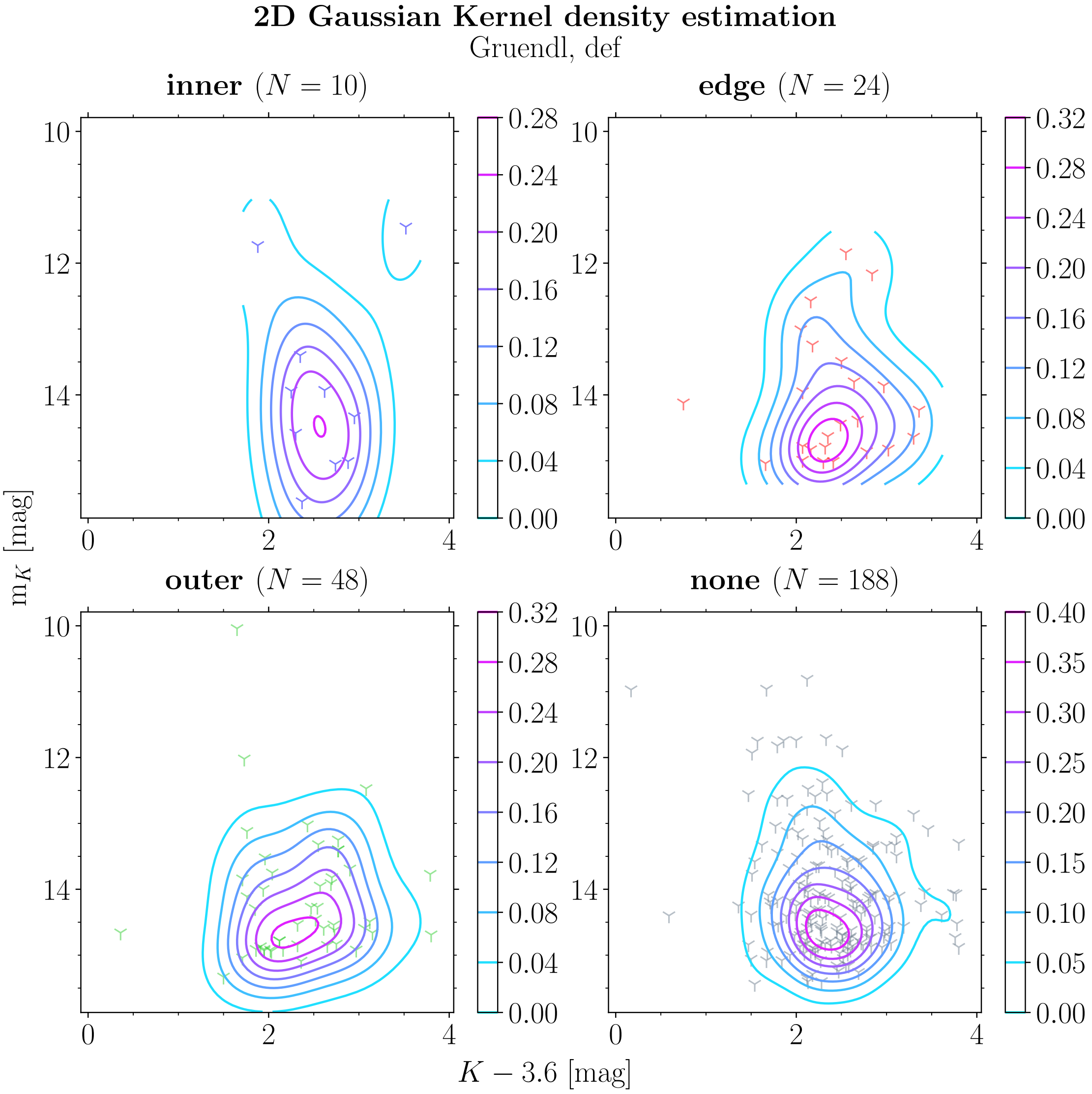

FIGURE A.18: The [K – 3.6] vs [m$_K$] diagram for catalog 2 group *definite* YSOs (section 5.1.2) with contours indicating the distribution [Gruendl & Chu, 2009].

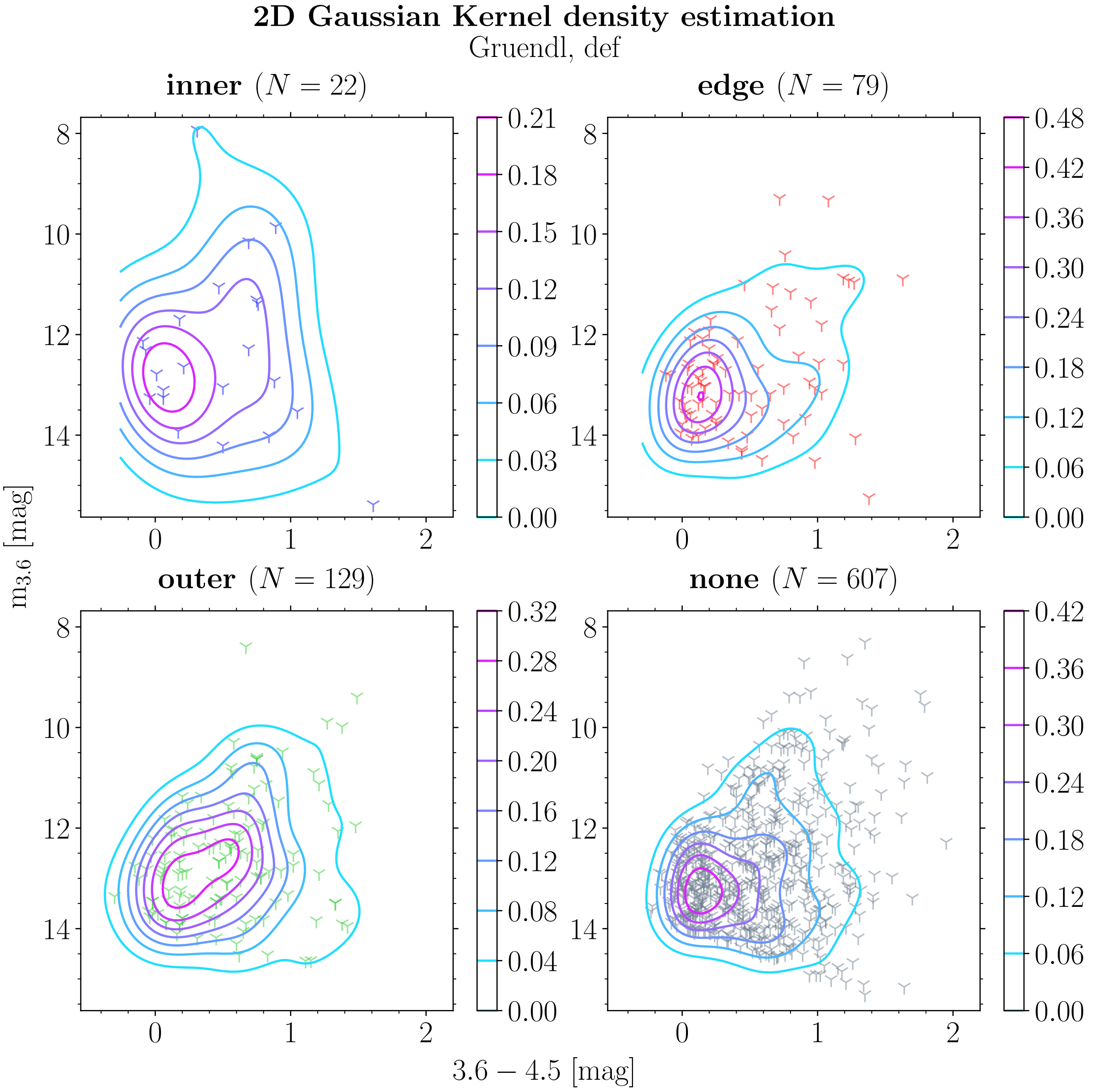

FIGURE A.19: The [3.6 – 4.5] vs [$m_{3.6}$] diagram for catalog 2 group *definite* YSOs (section 5.1.2) with contours indicating the distribution [Gruendl & Chu, 2009].

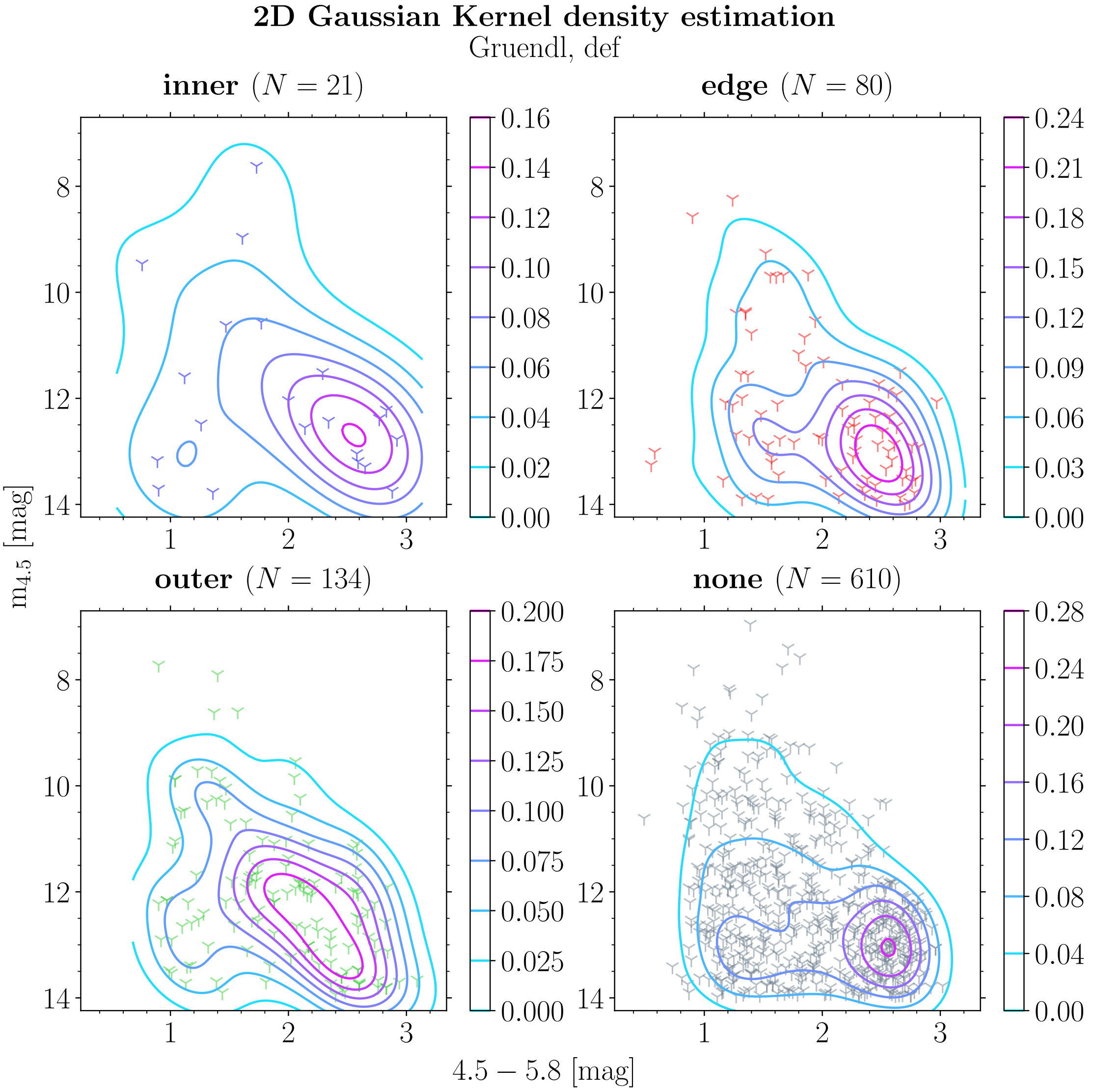

FIGURE A.20: The [4.5 – 5.8] vs [$m_{4.5}$] diagram for catalog 2 group *definite* YSOs (section 5.1.2) with contours indicating the distribution [Gruendl & Chu, 2009].

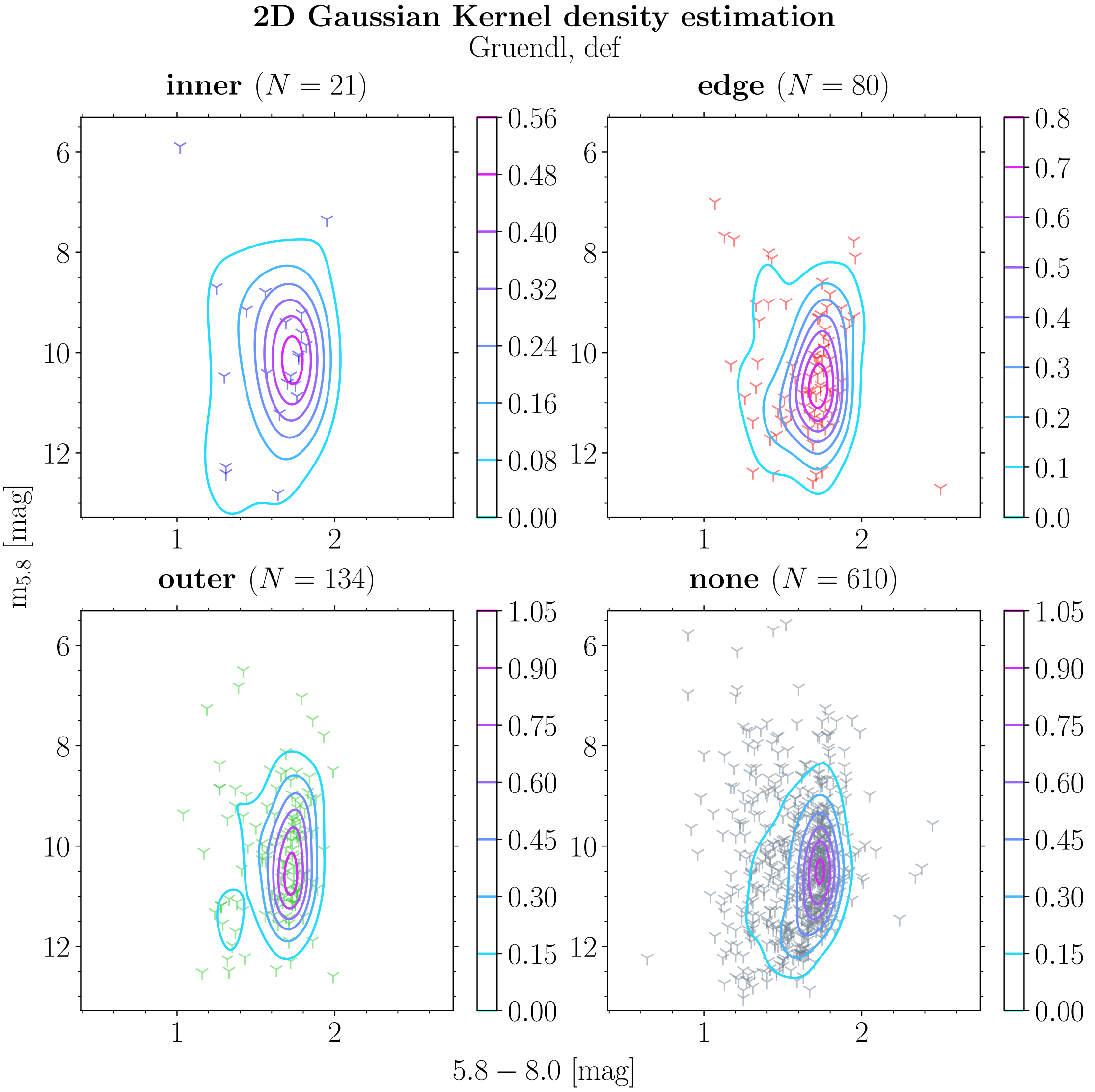

FIGURE A.21: The [5.8 – 8.0] vs [$m_{5.8}$] diagram for catalog 2 group *definite* YSOs (section 5.1.2) with contours indicating the distribution [Gruendl & Chu, 2009].

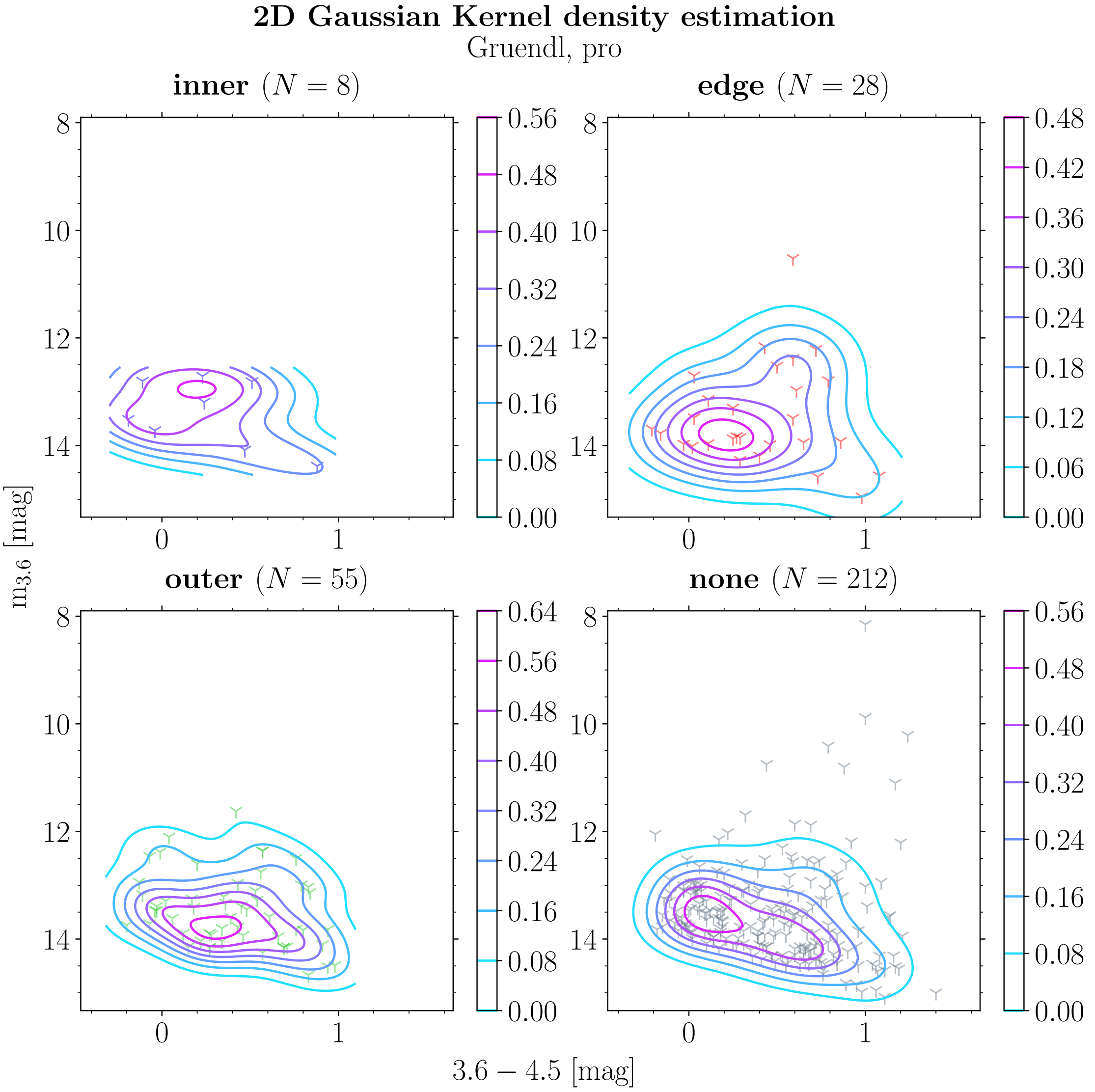

FIGURE A.22: The [3.6 – 4.5] vs [$m_{3.6}$] diagram for catalog 2 group *probable* YSOs (section 5.1.2) with contours indicating the distribution [Gruendl & Chu, 2009].

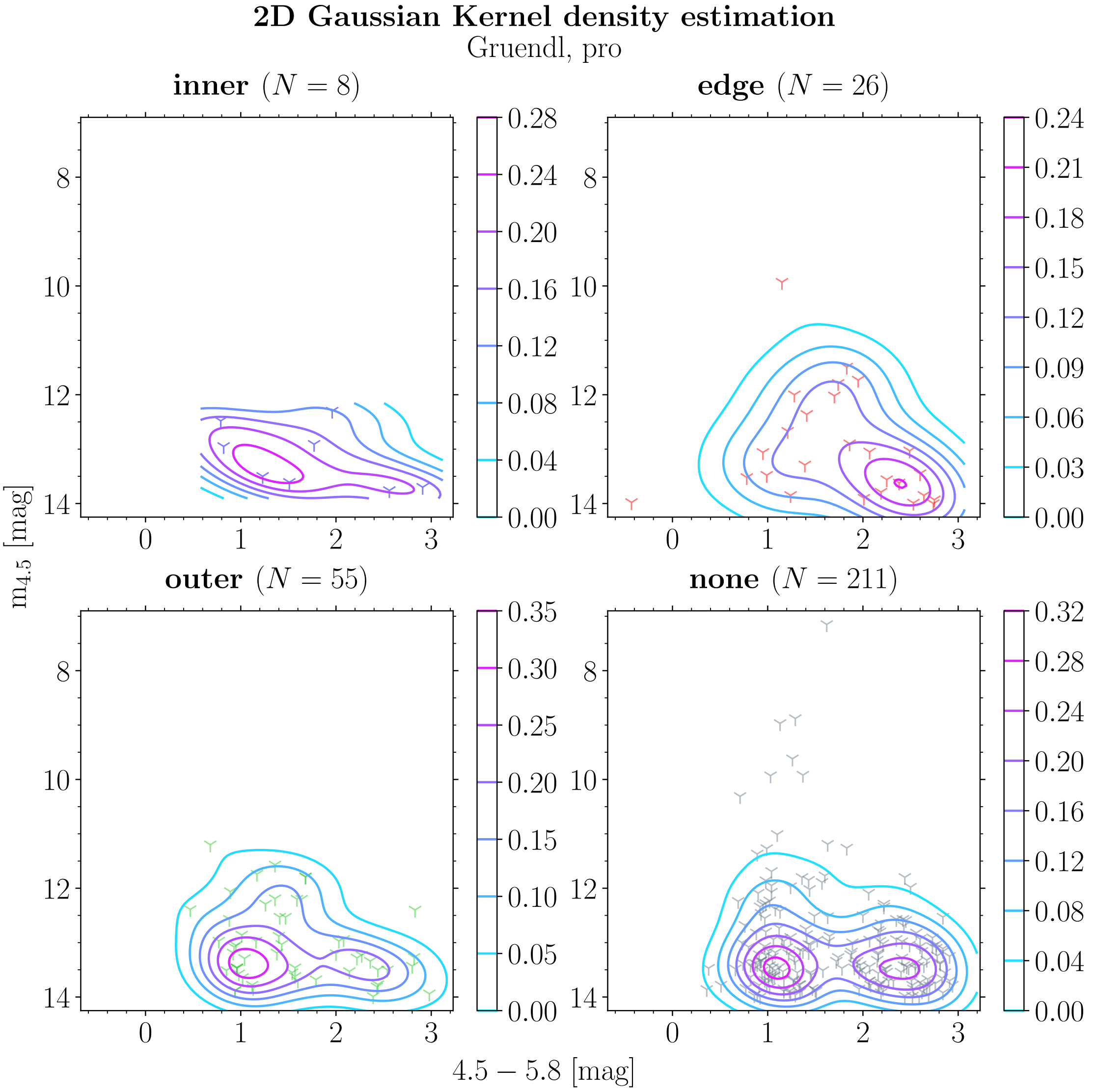

FIGURE A.23: The [4.5 – 5.8] vs [$m_{4.5}$] diagram for catalog 2 group *probable* YSOs (section 5.1.2) with contours indicating the distribution [Gruendl & Chu, 2009].

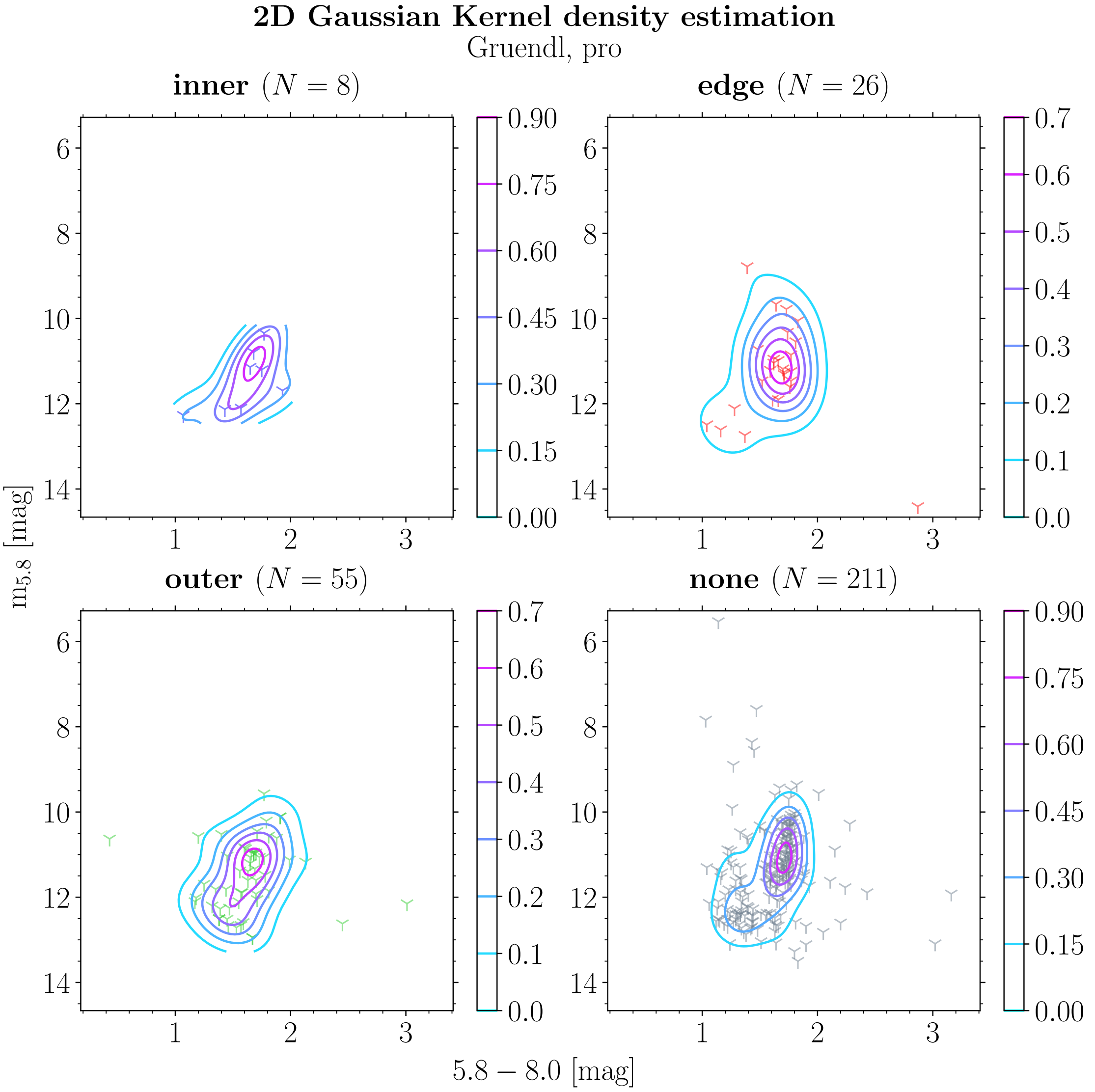

FIGURE A.24: The [5.8 – 8.0] vs [$m_{5.8}$] diagram for catalog 2 group *probable* YSOs (section 5.1.2) with contours indicating the distribution [Gruendl & Chu, 2009].

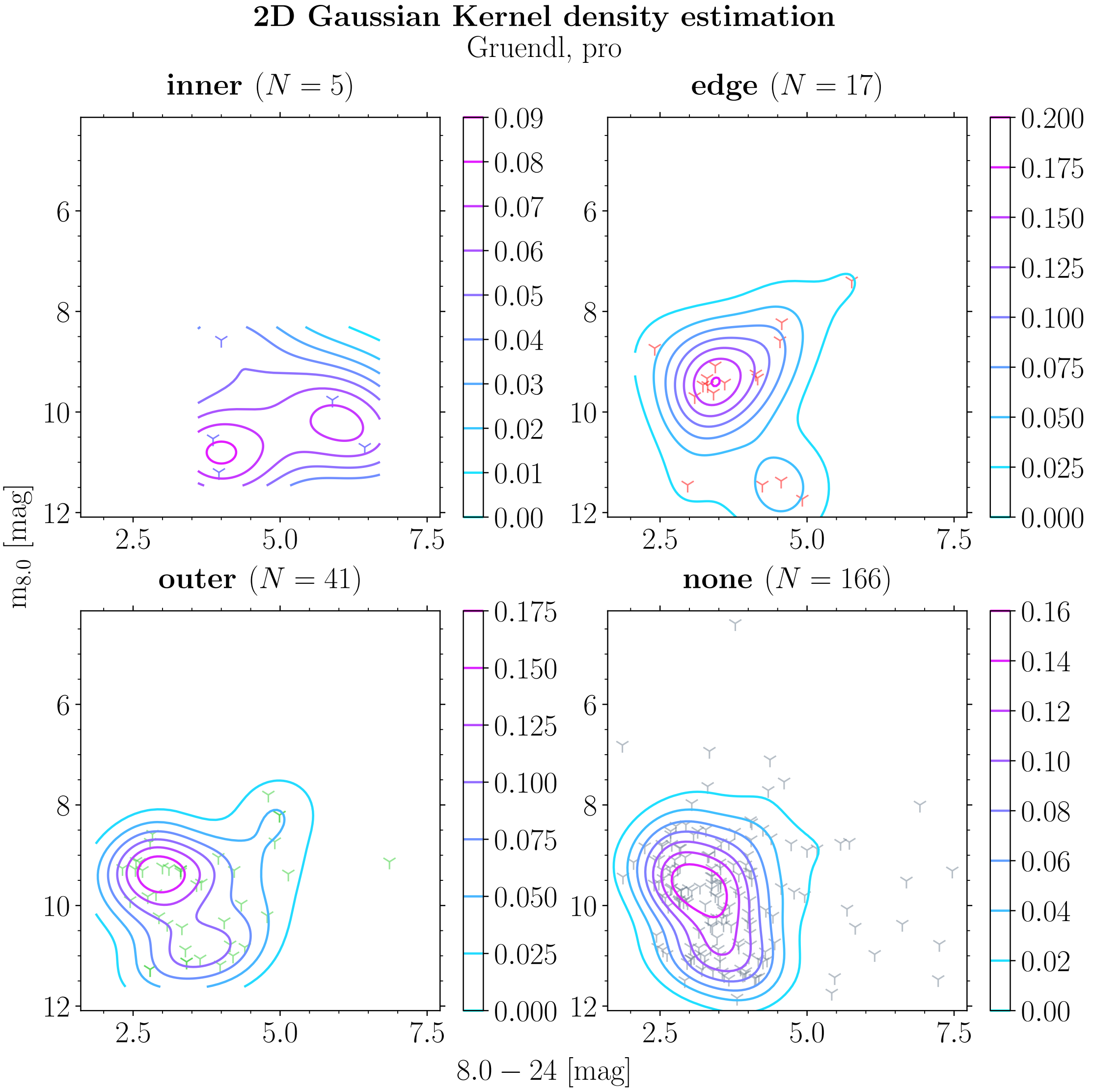

FIGURE A.25: The [8.0 – 24] vs [$m_{8.0}$] diagram for catalog 2 group *probable* YSOs (section 5.1.2) with contours indicating the distribution [Gruendl & Chu, 2009].

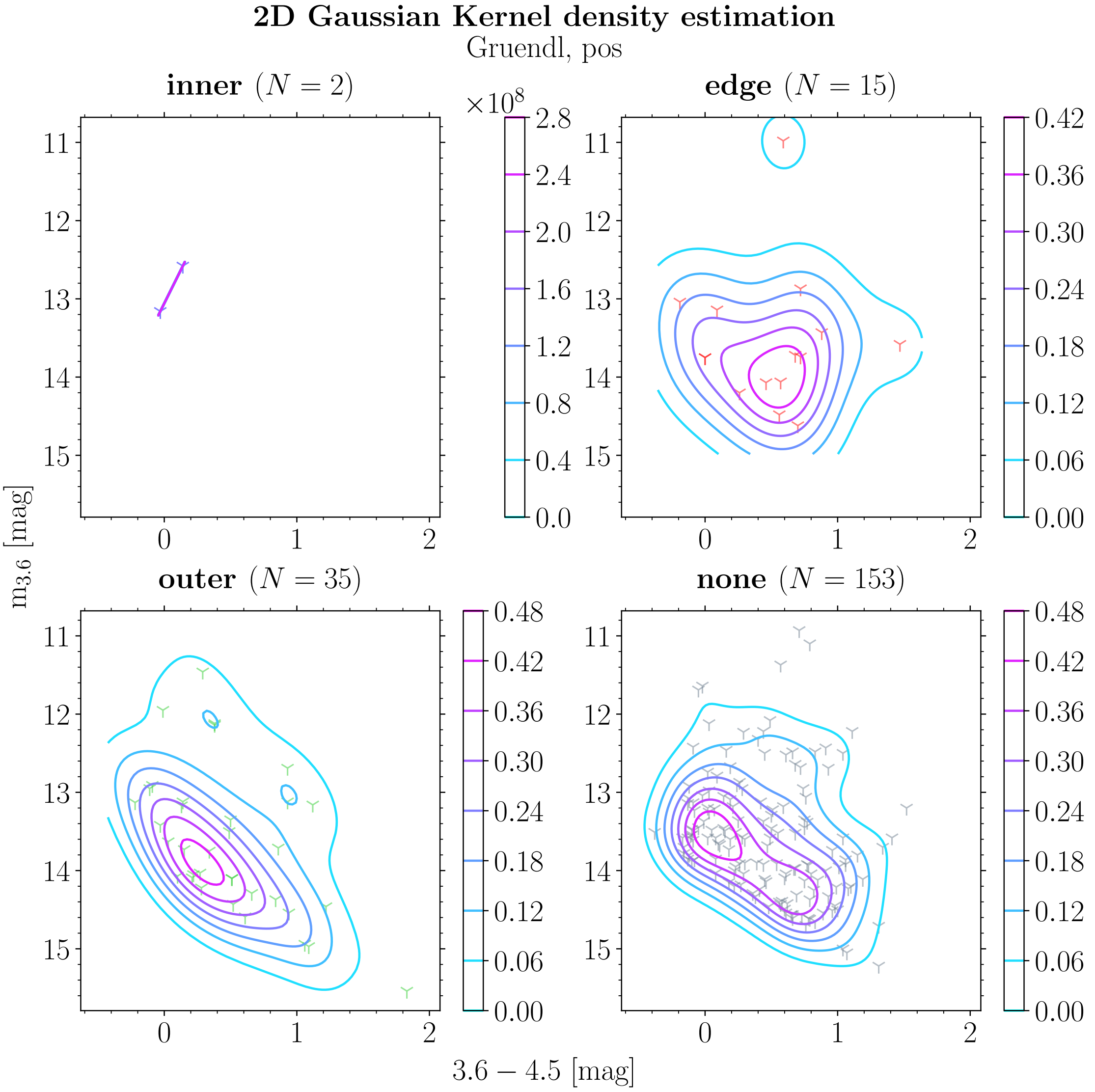

FIGURE A.26: The [3.6 – 4.5] vs [$m_{3.6}$] diagram for catalog 2 group *possible* YSOs (section 5.1.2) with contours indicating the distribution [Gruendl & Chu, 2009].

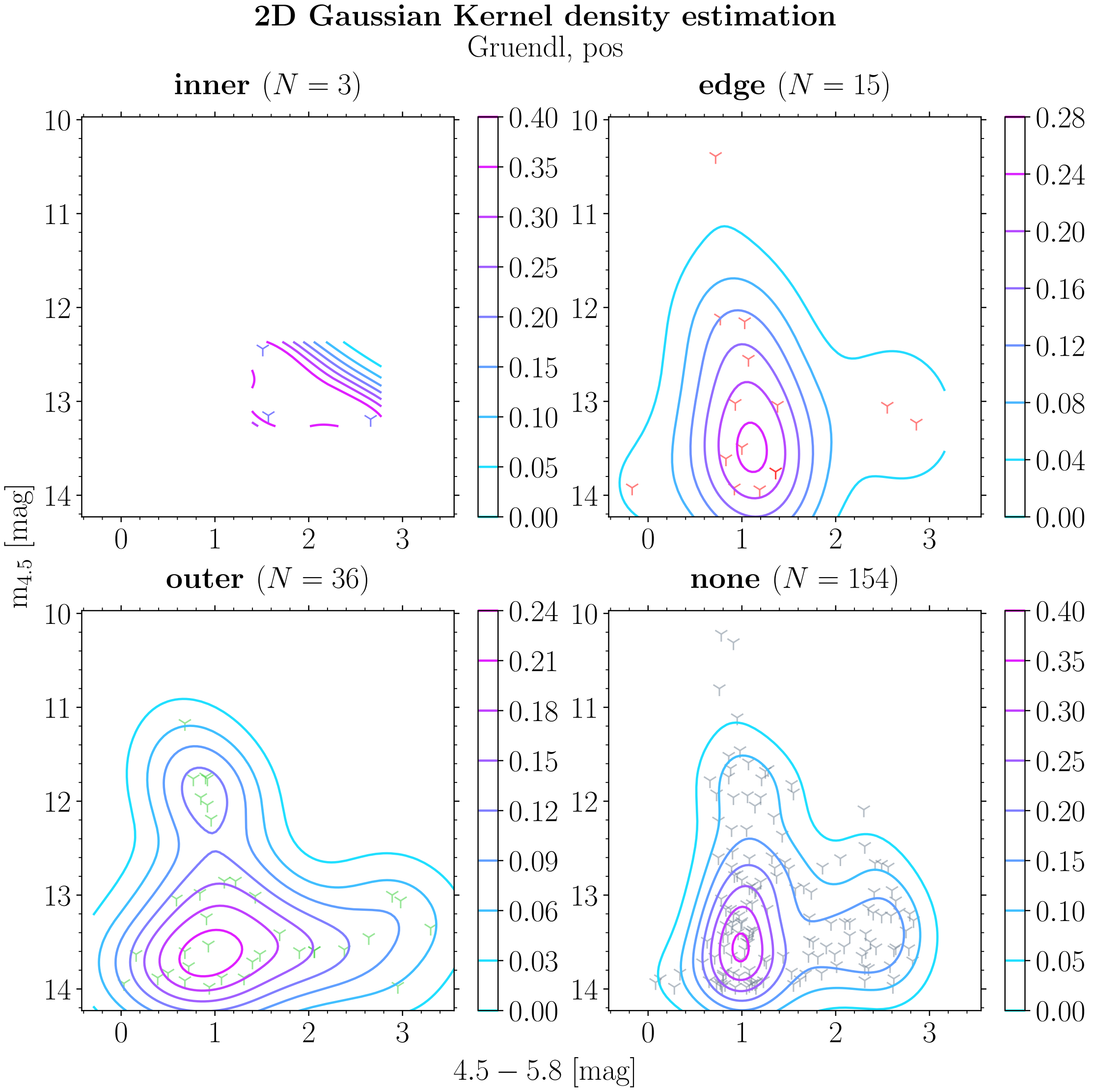

FIGURE A.27: The [4.5 – 5.8] vs [$m_{4.5}$] diagram for catalog 2 group *possible* YSOs (section 5.1.2) with contours indicating the distribution [Gruendl & Chu, 2009].

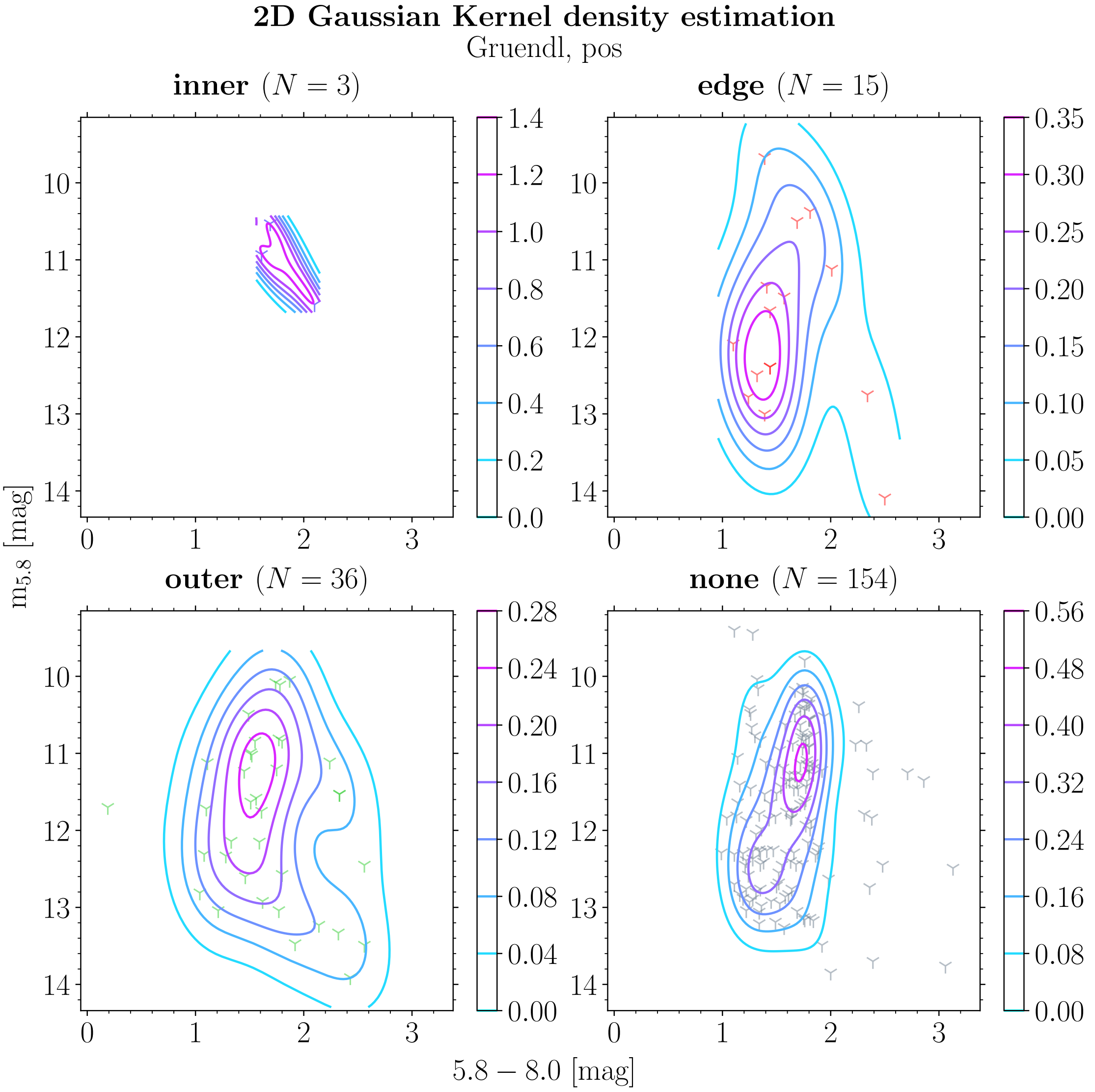

FIGURE A.28: The [5.8 – 8.0] vs [$m_{5.8}$] diagram for catalog 2 group *possible* YSOs (section 5.1.2) with contours indicating the distribution [Gruendl & Chu, 2009].

Color-Color Diagrams. The following figures document CCDs and their respective contour plots.It was not possible to generate contour diagrams for catalog 2 group *possible* YSOs. The algorithm encountered a mathematical error during the calculation. This matter was not investigated further, since it occurred for the data set which due to low sample size was excluded from the discussion.

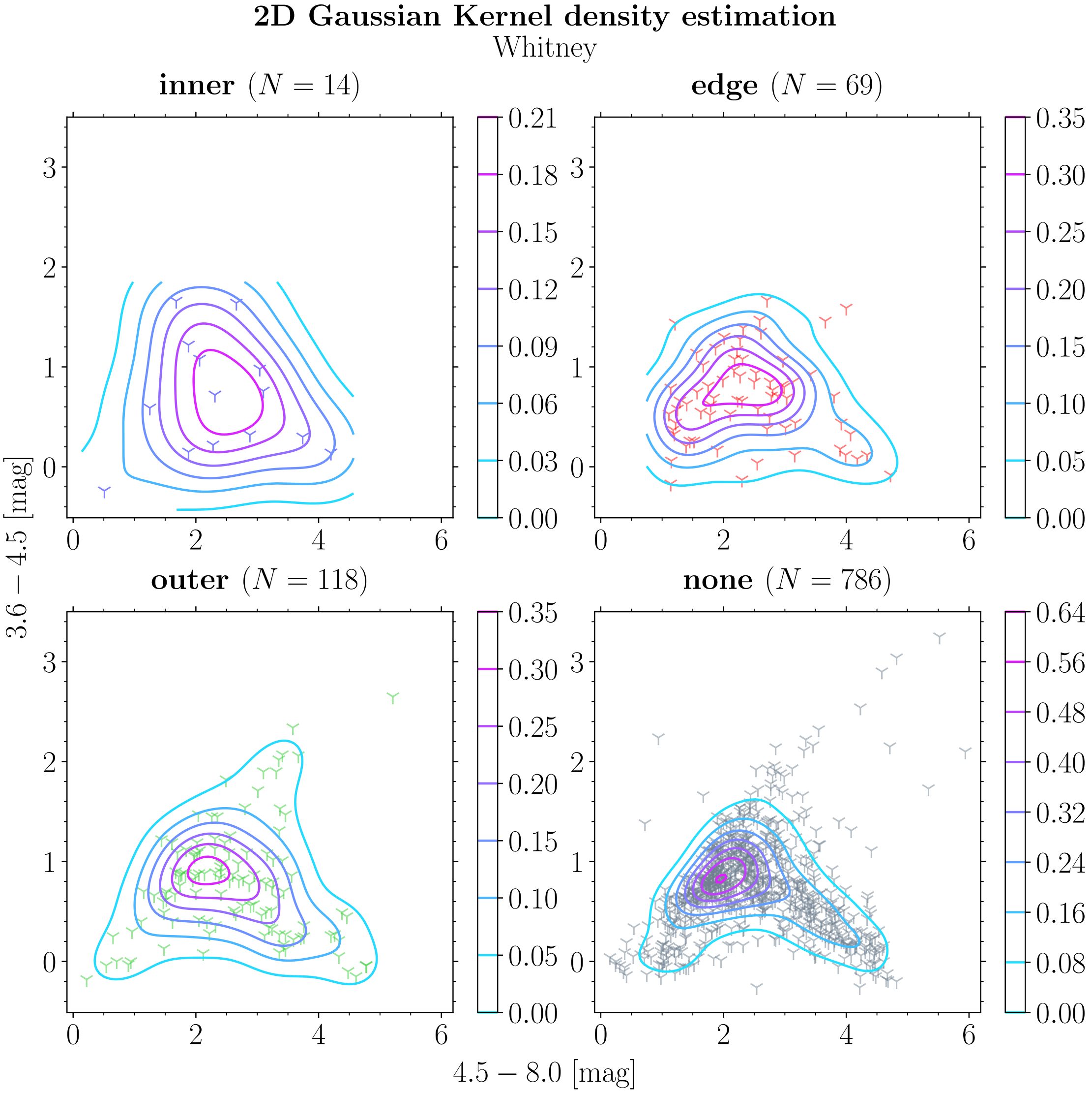

FIGURE A.30: [4.5 – 8.0] vs [3.6 – 4.5] CCD with contours for catalog 1 YSOs (section 5.1.1) [Whitney et al., 2008].

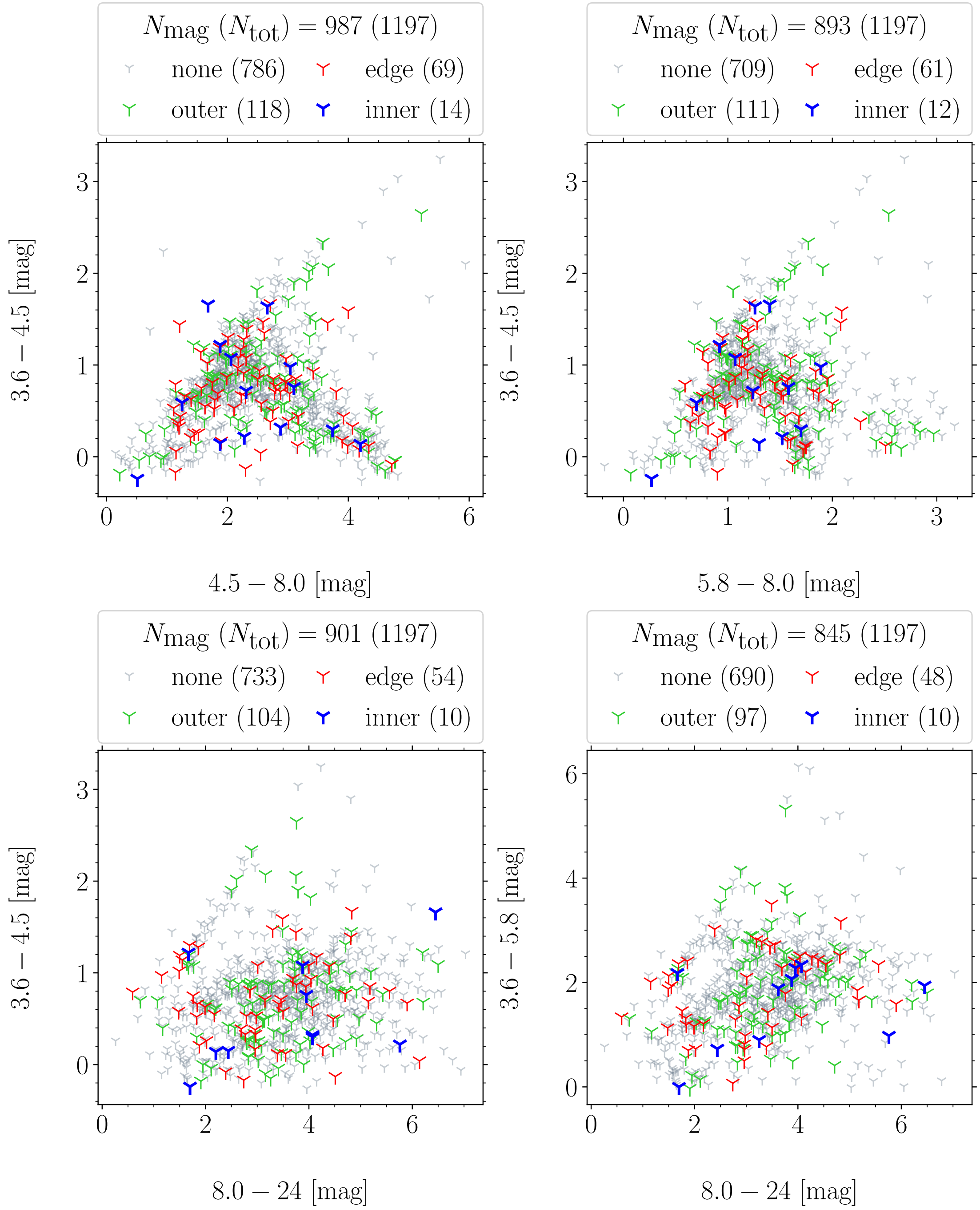

FIGURE A.29: CCDs for four magnitude combinations (section 6.2.2) for catalog 1 (section 5.1.1) [Whitney et al., 2008].

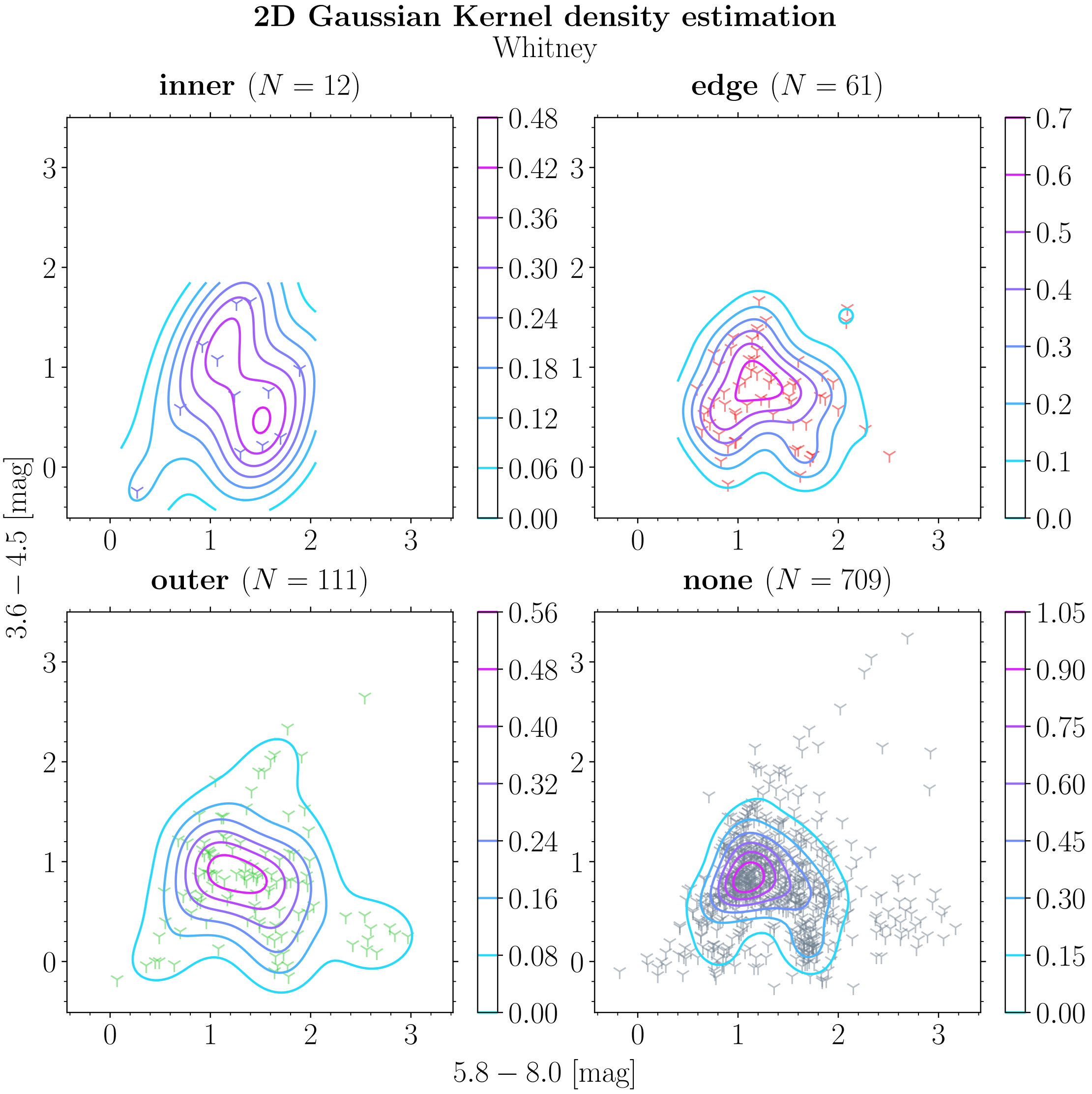

Figure A.31: [5.8 – 8.0] vs [3.6 – 4.5] CCD with contours for catalog 1 YSOs (section 5.1.1) [Whitney et al., 2008].

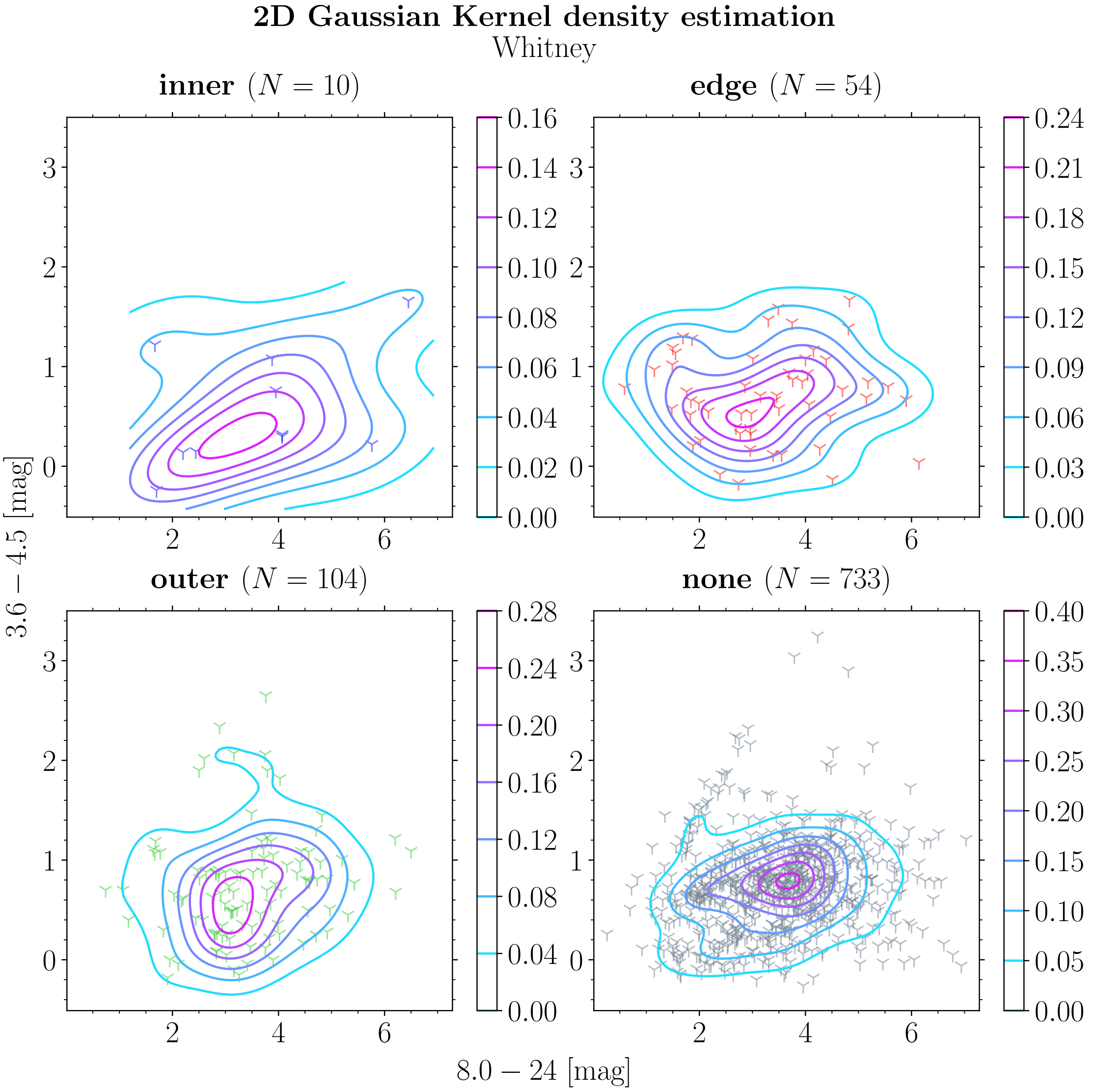

FIGURE A.32: [8.0 – 24] vs [3.6 – 4.5] CCD with contours for catalog 1 YSOs (section 5.1.1) [Whitney et al., 2008].

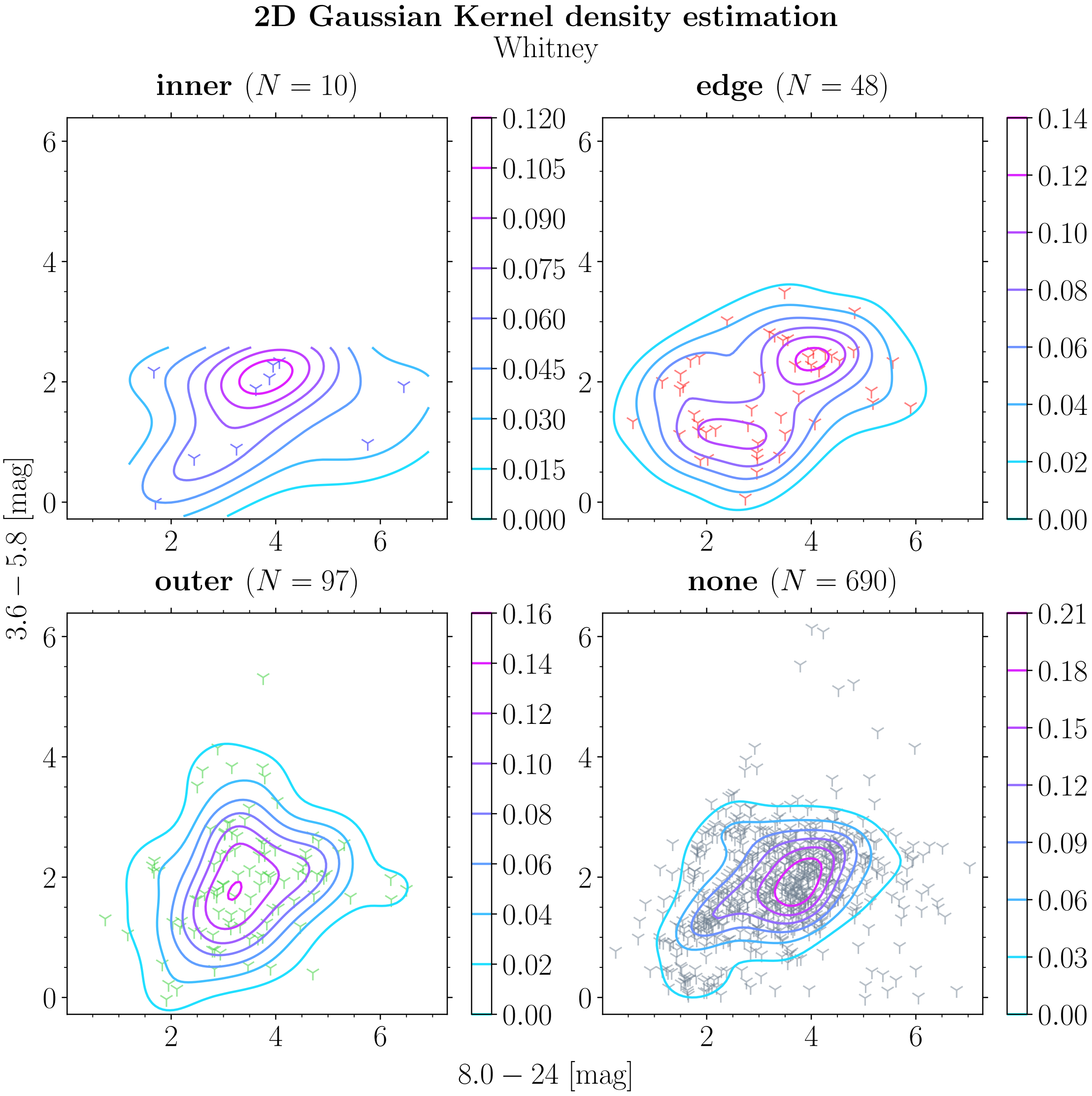

FIGURE A.33: [8.0 – 24] vs [3.6 – 5.8] CCD with contours for catalog 1 YSOs (section 5.1.1) [Whitney et al., 2008].

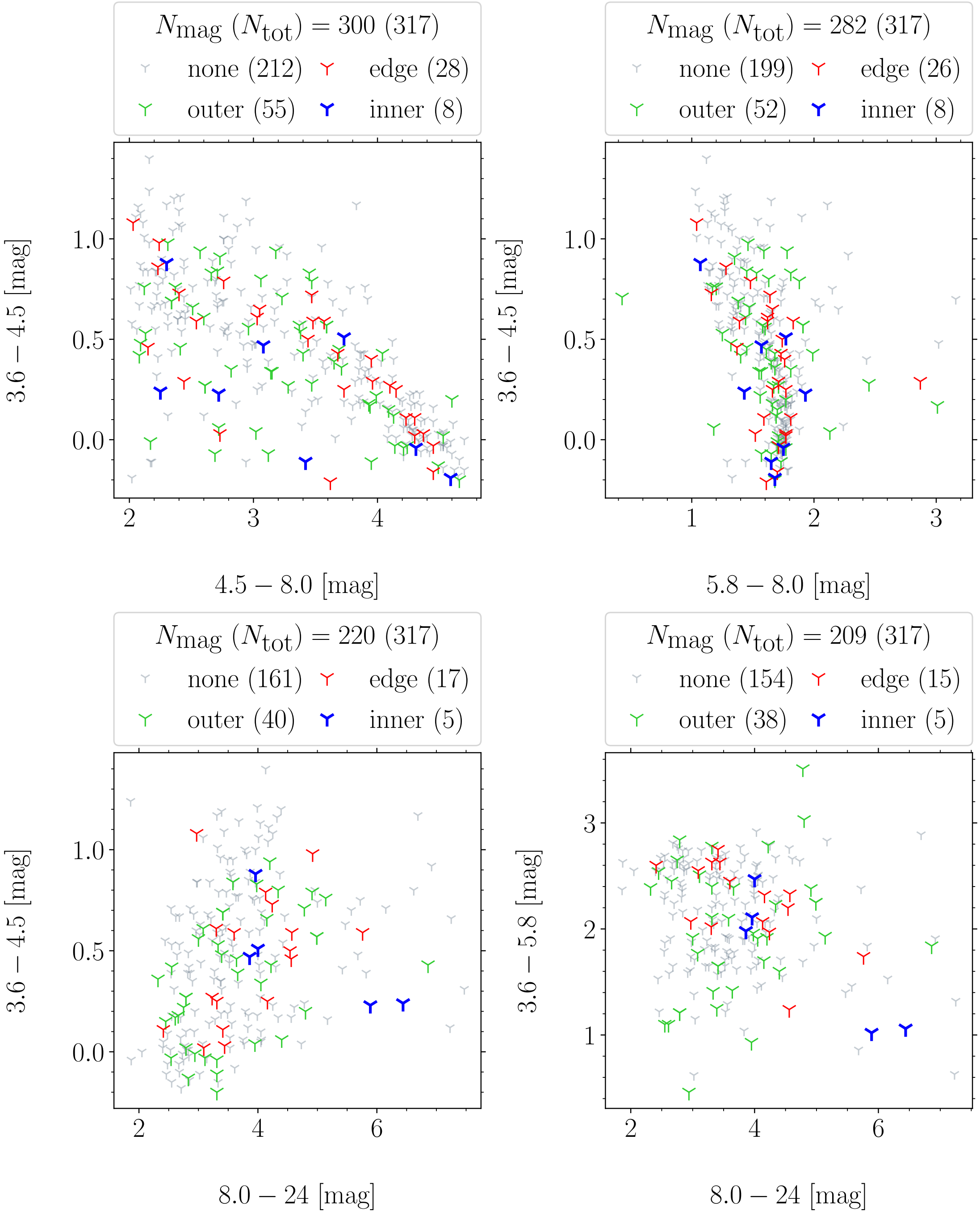

FIGURE A.34: CCDs for four magnitude combinations (section 6.2.2) for catalog 2 group *probable* YSOs (section 5.1.2) [Gruendl & Chu, 2009].

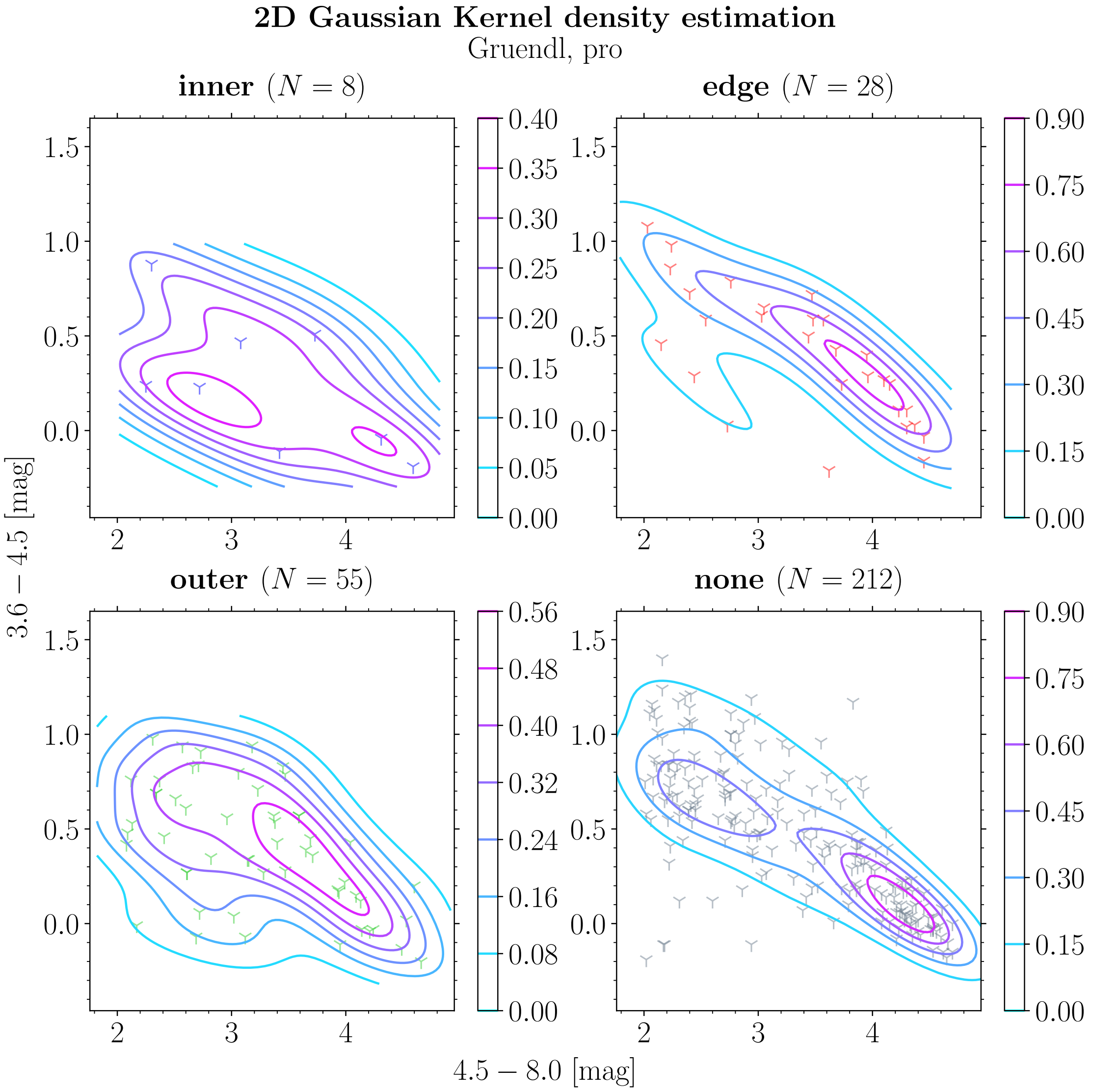

FIGURE A.35: [4.5 – 8.0] vs [3.6 – 4.5] CCD with contours for catalog 2 group *probable* YSOs (section 5.1.2) [Gruendl & Chu, 2009].

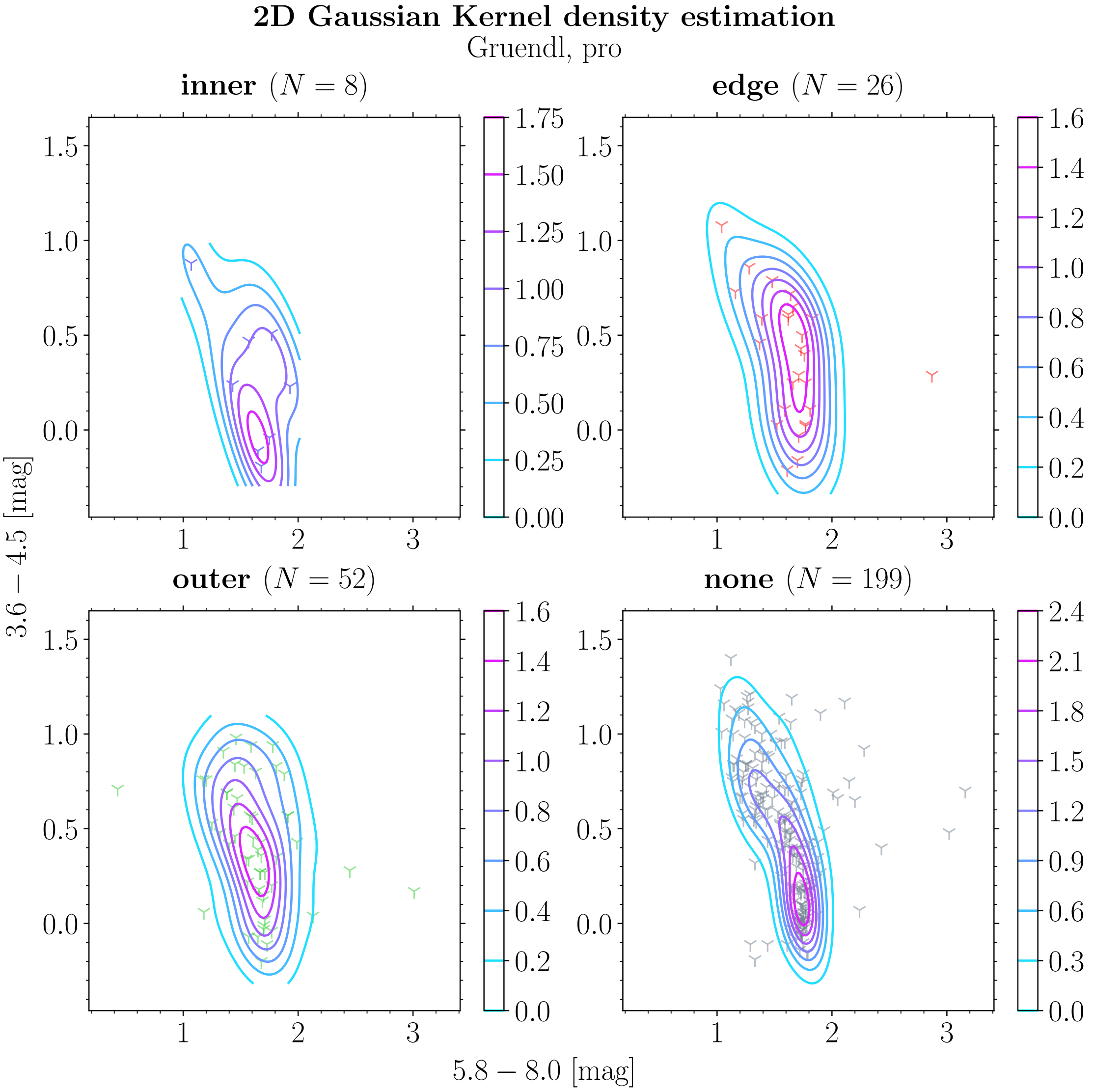

FIGURE A.36: [5.8 – 8.0] vs [3.6 – 4.5] CCD with contours for catalog 2 group *probable* YSOs (section 5.1.2) [Gruendl & Chu, 2009].

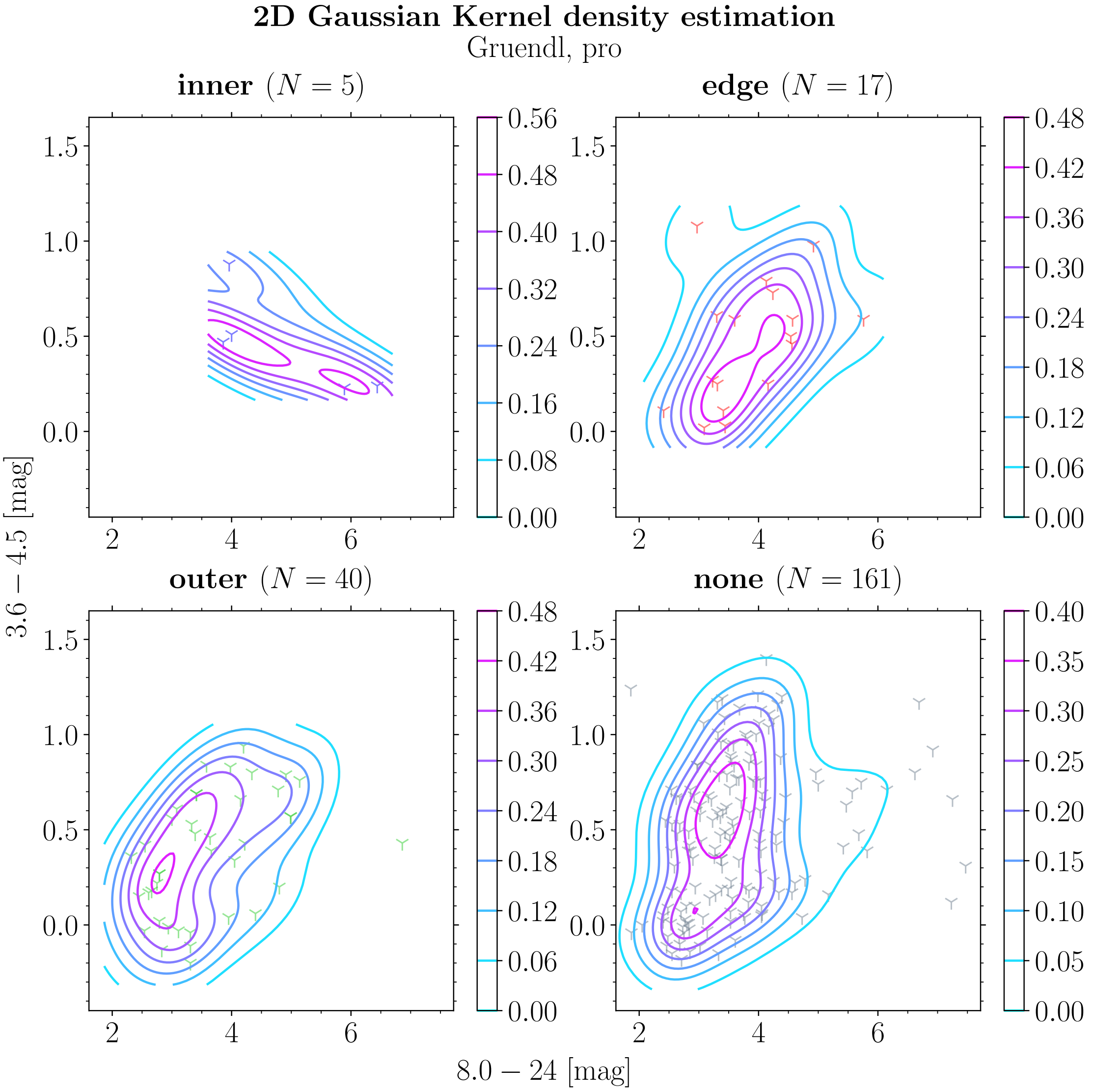

FIGURE A.37: [8.0 – 24] vs [3.6 – 4.5] CCD with contours for catalog 2 group *probable* YSOs (section 5.1.2) [Gruendl & Chu, 2009].

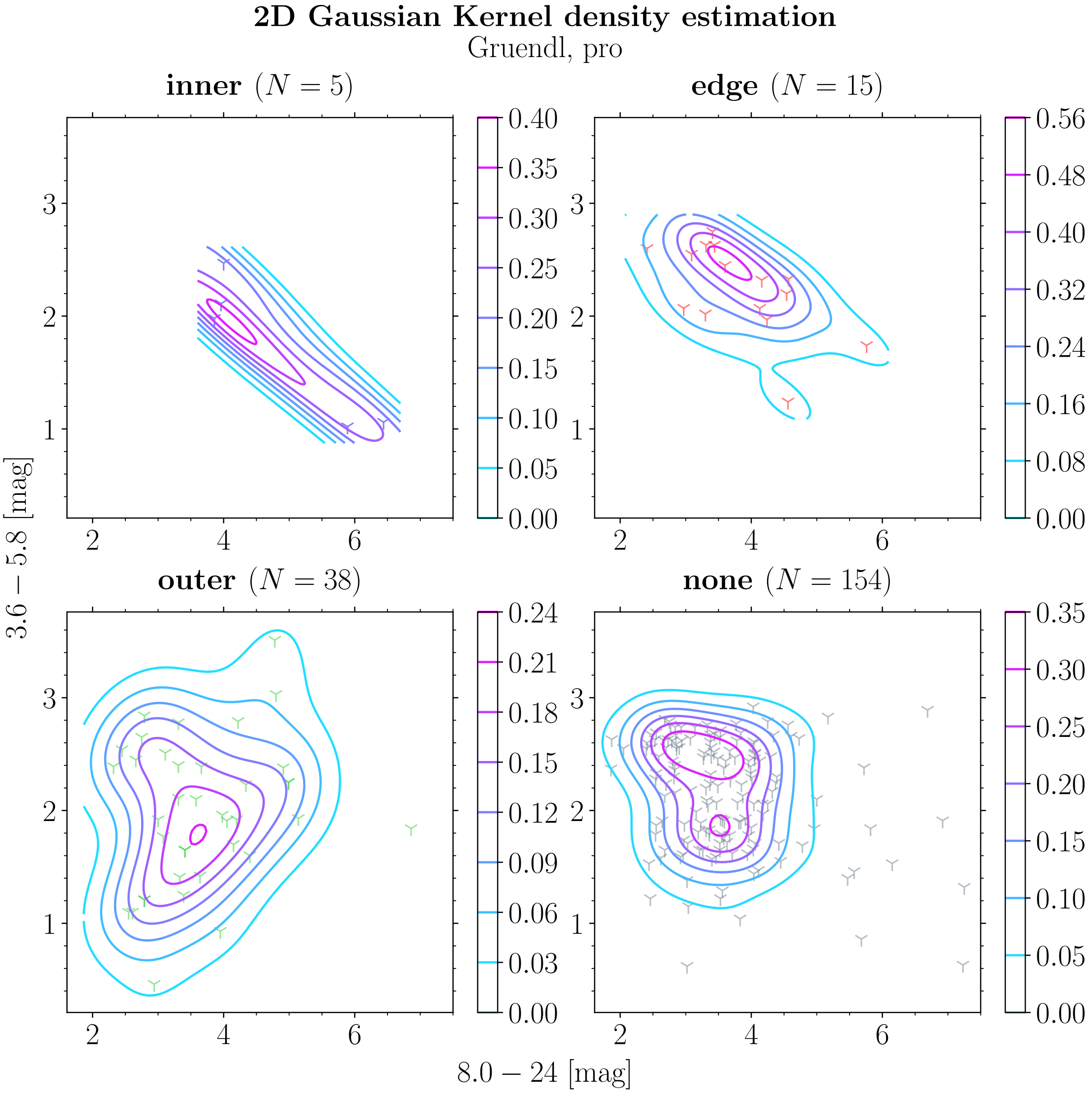

FIGURE A.38: [8.0 – 24] vs [3.6 – 5.8] CCD with contours for catalog 2 group *probable* YSOs (section 5.1.2) [Gruendl & Chu, 2009].

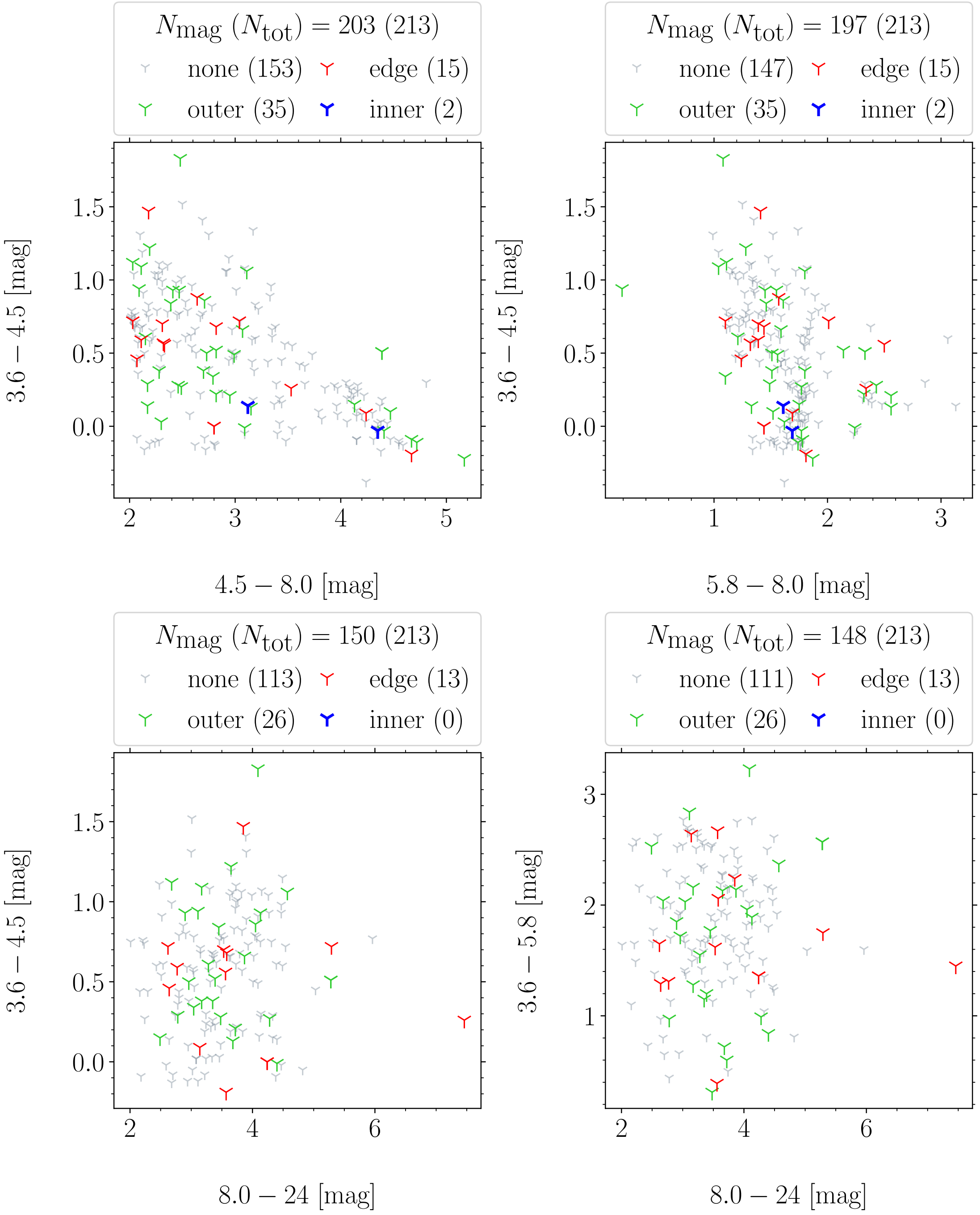

FIGURE A.39: CCDs for four magnitude combinations (section 6.2.2) for catalog 2 group *possible* YSOs (section 5.1.2) [Gruendl & Chu, 2009].

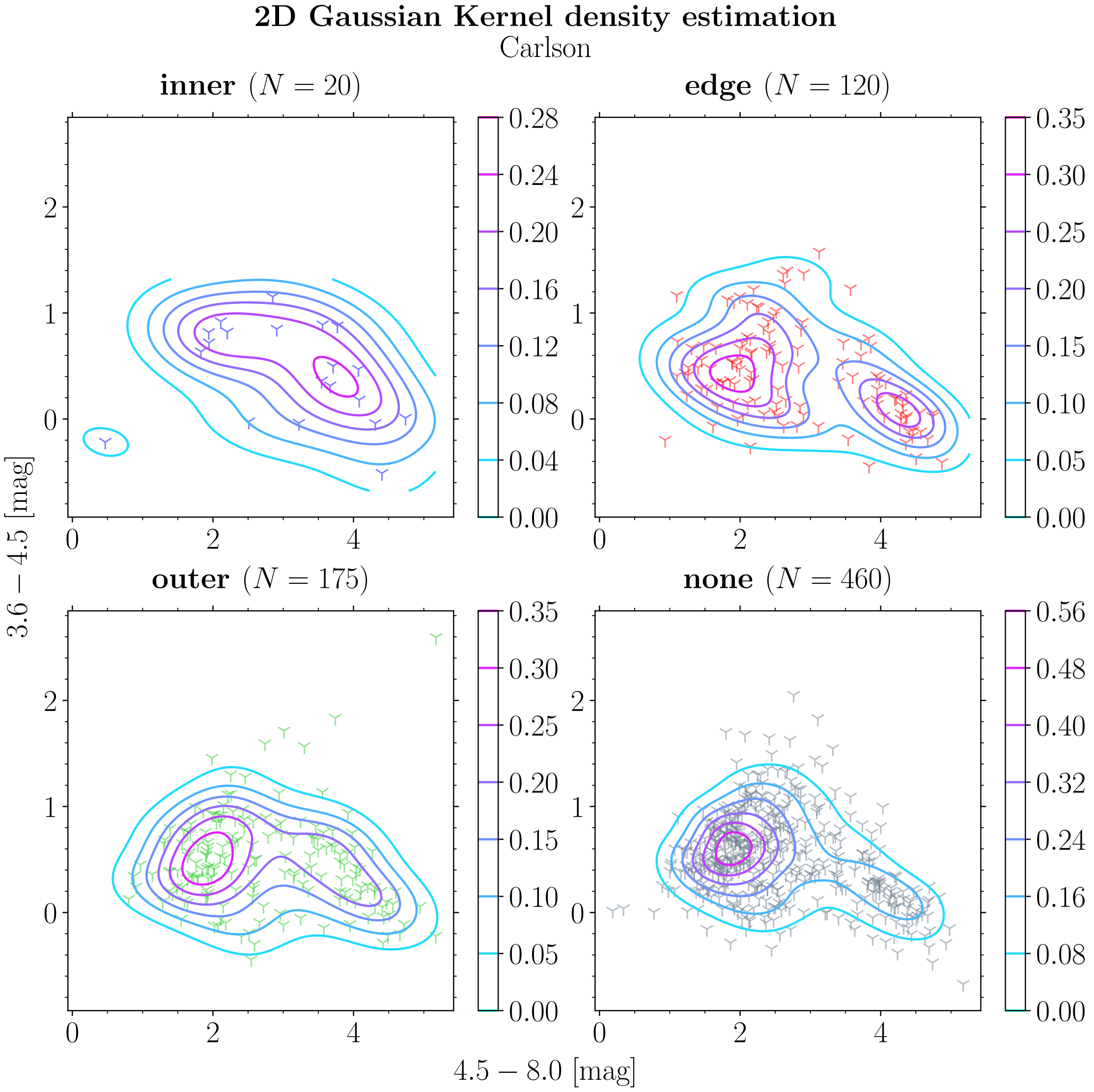

FIGURE A.40: [4.5 – 8.0] vs [3.6 – 4.5] CCD with contours for catalog 3 YSOs (section 5.1.3) [Carlson et al., 2012].

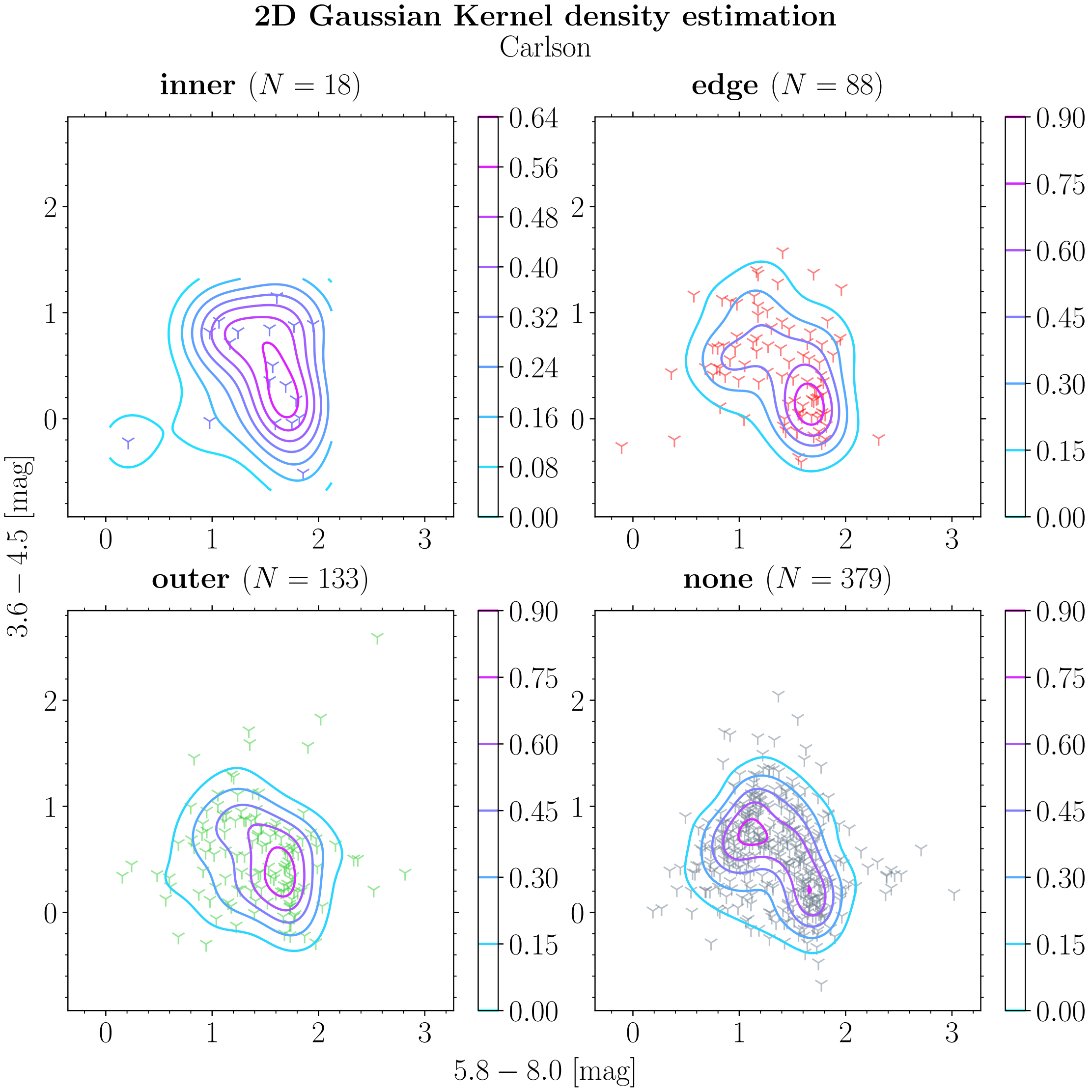

FIGURE A.41: [5.8 – 8.0] vs [3.6 – 4.5] CCD with contours for catalog 3 YSOs (section 5.1.3) [Carlson et al., 2012].

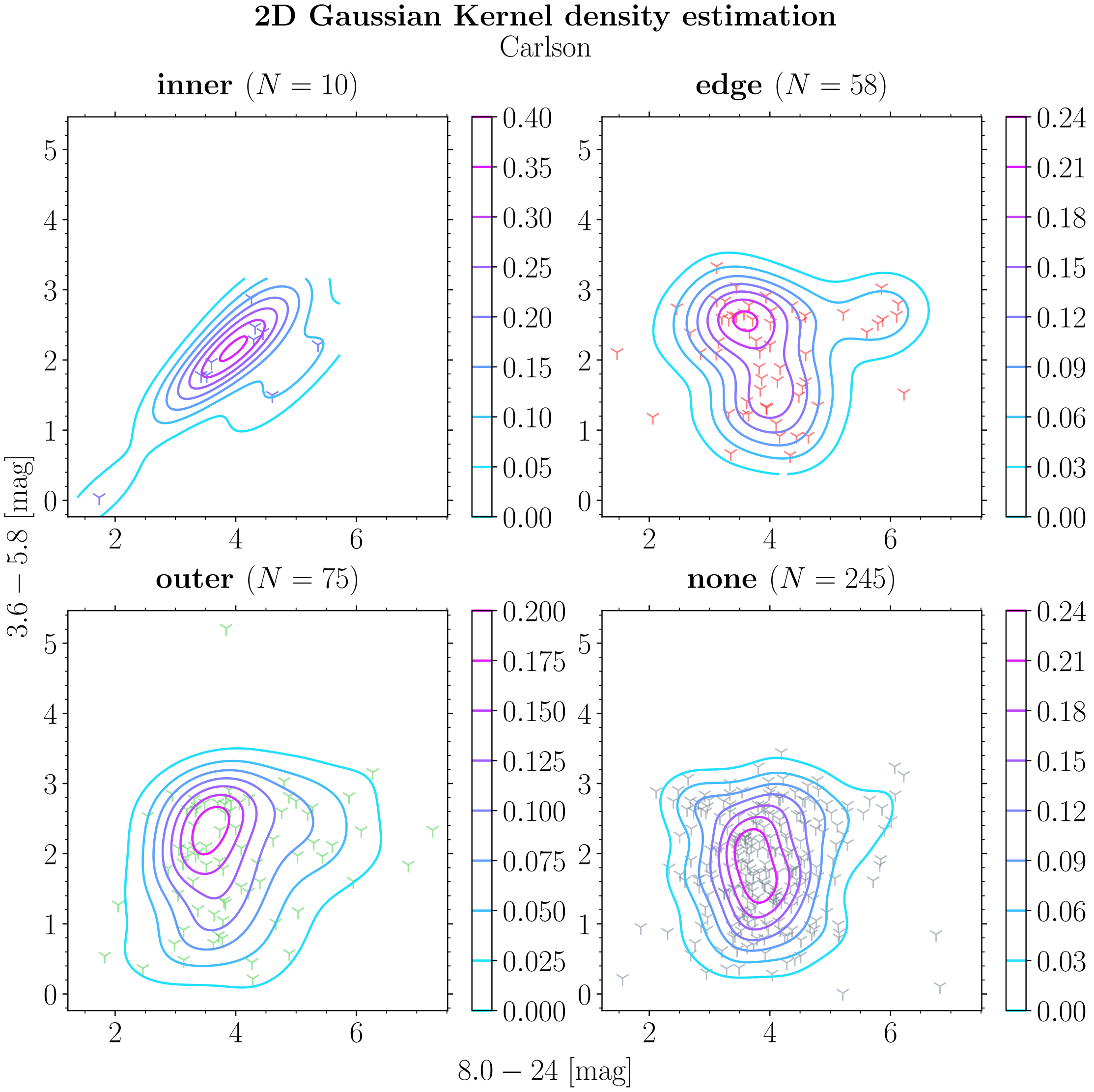

FIGURE A.42: [8.0 – 24] vs [3.6 – 5.8] CCD with contours for catalog 3 YSOs (section 5.1.3) [Carlson et al., 2012].

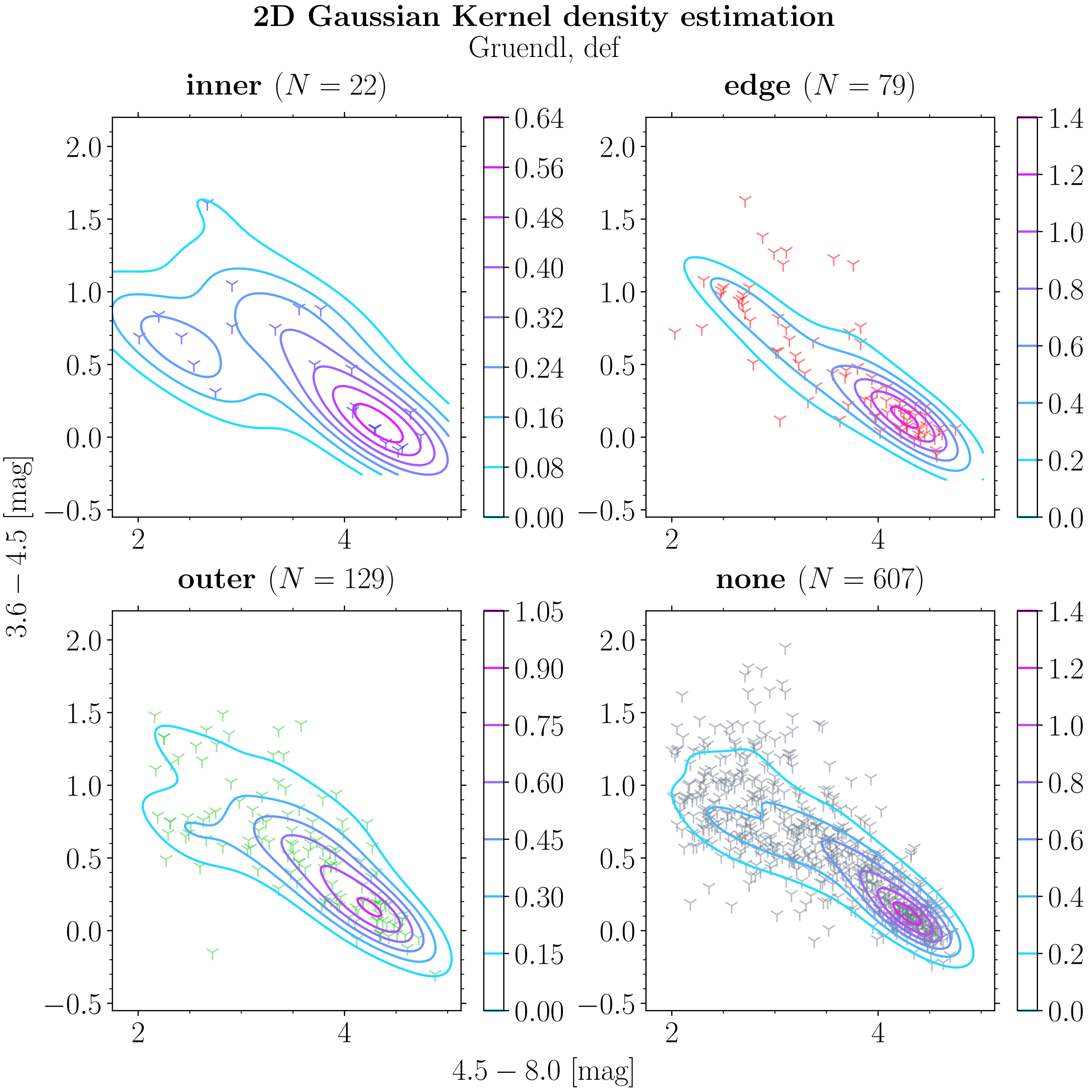

FIGURE A.43: [4.5 – 8.0] vs [3.6 – 4.5] CCD with contours for catalog 2 group *definite* YSOs (section 5.1.2) [Gruendl & Chu, 2009].

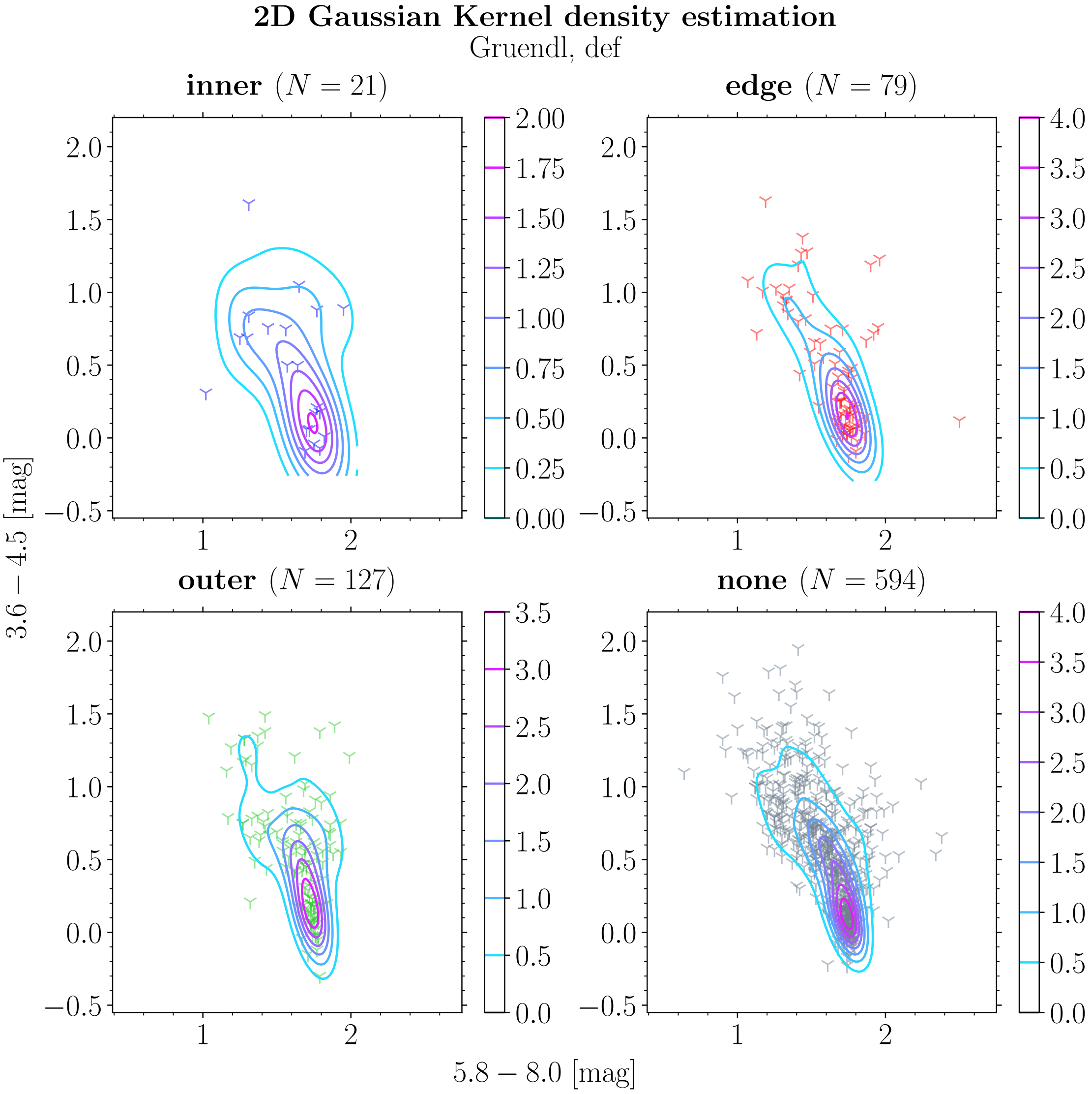

FIGURE A.44: [5.8 – 8.0] vs [3.6 – 4.5] CCD with contours for catalog 2 group *definite* YSOs (section 5.1.2) [Gruendl & Chu, 2009].

B Spectral Index

In their paper [Gruendl & Chu, 2009] (data catalog 2) only made the magnitudes m_λ of YSOs and not the flux densities F_λ available. To be able to calculate the spectral energy distribution (SED) and the spectral index α, it was necessary to convert the magnitudes to the flux densities. Usually observed flux densities F_ν are small, so instead of using the cgs-unit $[\mathrm{erg\,cm^{-2}\,s^{-1}\,Hz^{-1}}]$ a *Jansky* (Jy) as $10^{-23}\,\mathrm{erg\,cm^{-2}\,s^{-1}\,Hz^{-1}}$ is defined. The following formulae give insight into the calculations.

Conversion from magnitude to flux density. For this calculation the zero-point flux density $F_{0,\lambda}$ must be known. See table B.1 for the corresponding values for each wavelength λ.

Table B.1: Zero-point fluxes for the 2MASS bands and Spitzer IRAC and MIPS detectors [California Institute of Technology, 2022].

	2MASS			IRAC				MIPS	
λ [µm]	1.25 (J)	1.65 (H)	2.16 (K_s)	3.6	4.5	5.8	8.0	24	70
$F_{0,\lambda}$ [Jy]	1594	1024	666.7	277.5	197.5	116.6	63.1	7.14	0.775

The following equation results from the inversion of equation (2.7). The flux density F_λ is now a function of the magnitude m_λ:

$$F_\lambda = 10^{-23} \cdot F_{0,\lambda}\,[\mathrm{Jy}] \cdot 10^{m_\lambda/-2.5} \quad [\mathrm{erg\,cm^{-2}\,s^{-1}\,Hz^{-1}}] \tag{B.1}$$

The uncertainty on the flux density then becomes:

$$\delta F_\lambda = 10^{-23} \cdot F_{0,\lambda}\,[\mathrm{Jy}] \cdot \frac{\ln 10}{-2.5} \cdot 10^{m_\lambda/-2.5} \cdot \delta m_\lambda \quad [\mathrm{erg\,cm^{-2}\,s^{-1}\,Hz^{-1}}] \tag{B.2}$$

Calculation of spectral index. Following the choice of calculation for the spectral index in section 6.4 and substituting equation (B.1) into (6.1), one arrives at:

$$\alpha = \frac{\ln\left[(\nu \cdot 10^{-23} \cdot F_0 \cdot 10^{m/-2.5})_{\lambda_{\max}}\right] - \ln\left[(\nu \cdot 10^{-23} \cdot F_0 \cdot 10^{m/-2.5})_{\lambda_{\min}}\right]}{\ln \lambda_{\max}/\lambda_{\min}} \tag{B.3}$$

The variance of a function of a random variable can be approximated by second-order Taylor expansion:

$$\mathrm{Var}[f(X)] \approx f'(\mathrm{E}[X])^2 \cdot \mathrm{Var}[X] \tag{B.4}$$

Utilizing basic rules of error propagation and (B.4), the uncertainty on the spectral index α becomes:

$$\delta\alpha = \frac{1}{\ln \lambda_{\mathrm{max}}/\lambda_{\mathrm{min}}} \cdot \frac{\ln 10}{2.5} \cdot \sqrt{(\delta m)^2_{\lambda_{\mathrm{max}}} + (\delta m)^2_{\lambda_{\mathrm{min}}}} \tag{B.5}$$

C Images

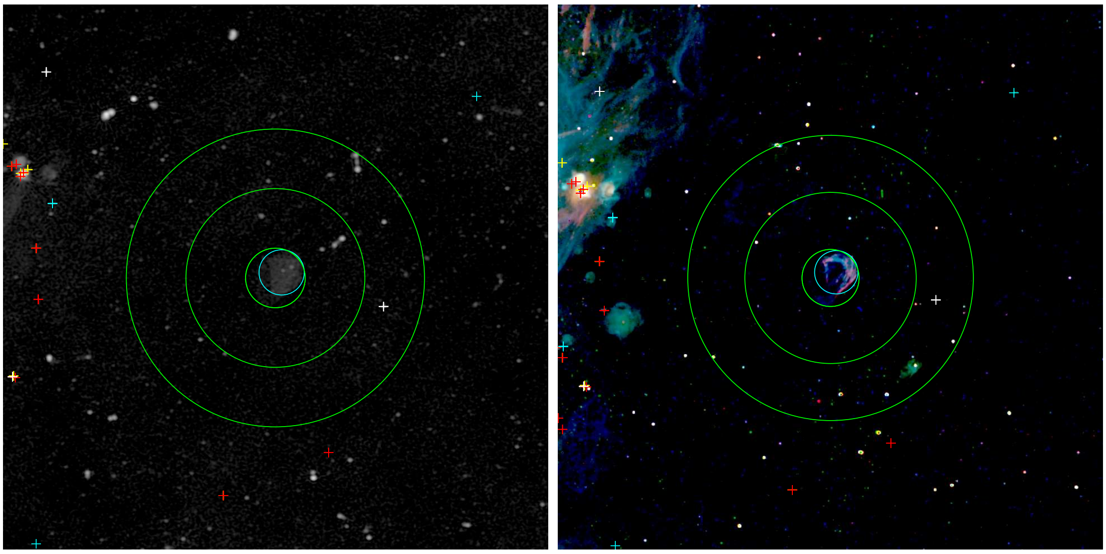

(a) Radio (b) Optical

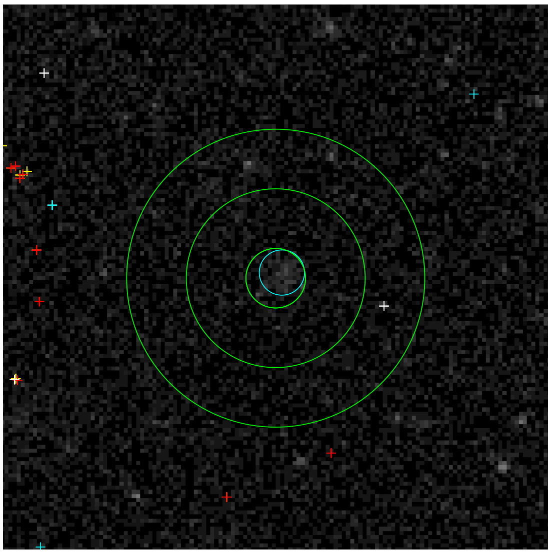

(c) X-ray

Figure C.1: MCSNR J0448−6700, [HP99] 460
ICRS coordinates (ep=J2000): 04:48:26.30 −67:00:24.0
$R = 145''$

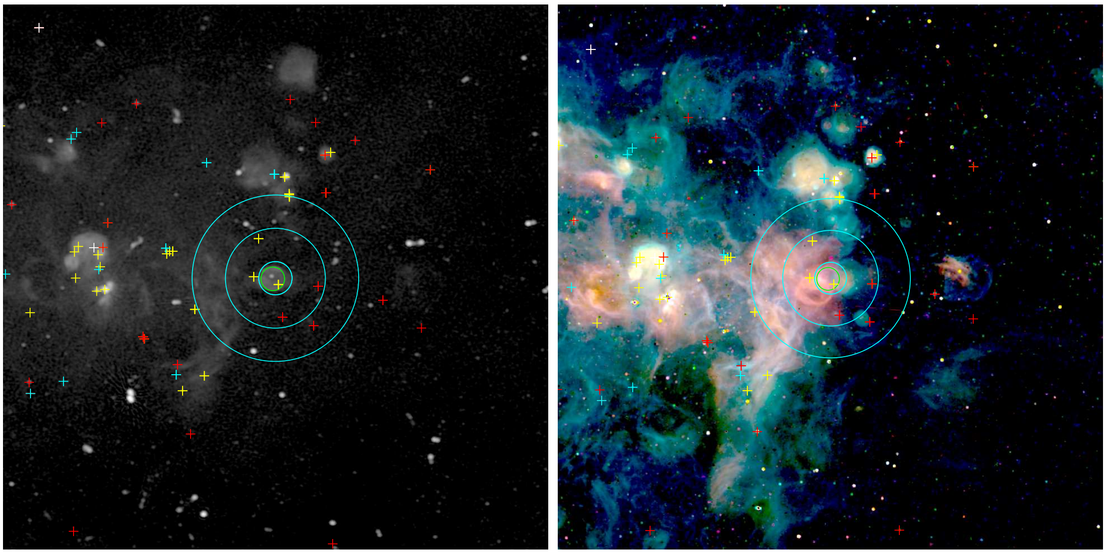

(A) Radio (B) Optical

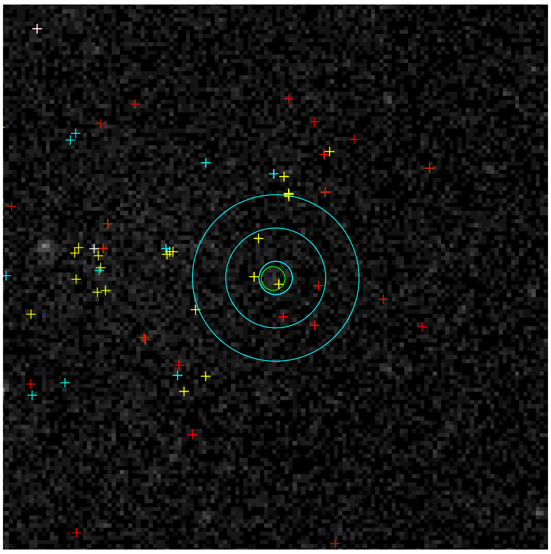

(C) X-ray

Figure C.2: MCSNR J0449−6920
ICRS coordinates (ep=J2000): R.A. = 04:49:20.0, Dec = −69:20:20.0
$R = 81''$

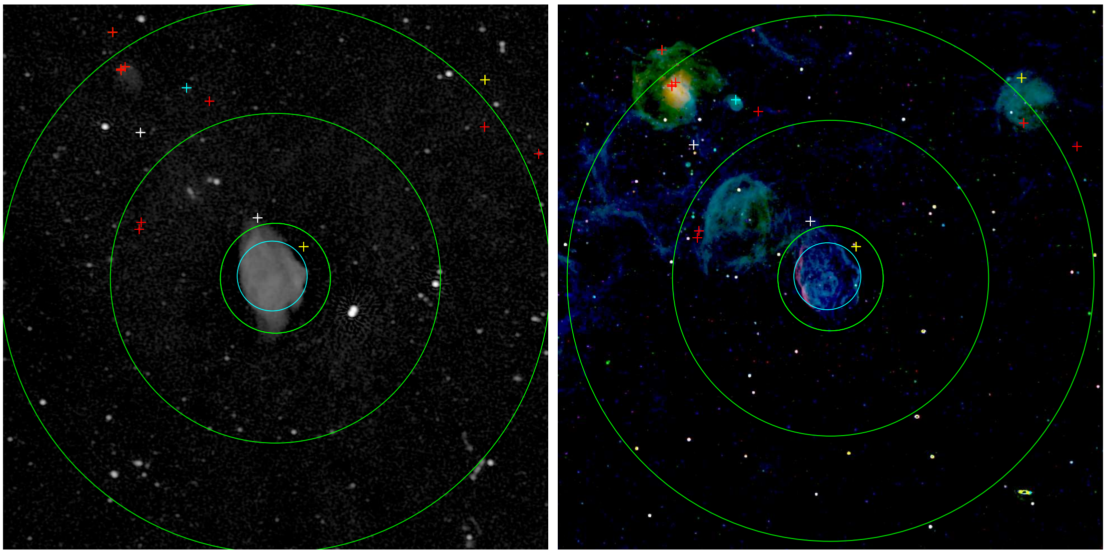

(A) Radio (B) Optical

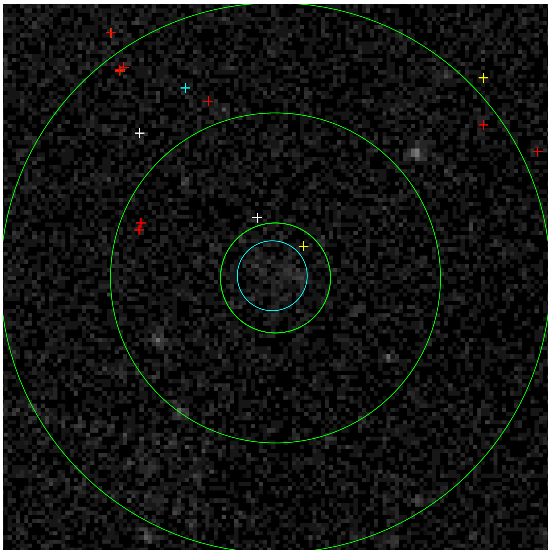

(C) X-ray

Figure C.3: MCSNR J0450−7050
ICRS coordinates (ep=J2000): R.A. = 04:50:23.5, Dec = −70:50:23.0
$R = 267.5''$

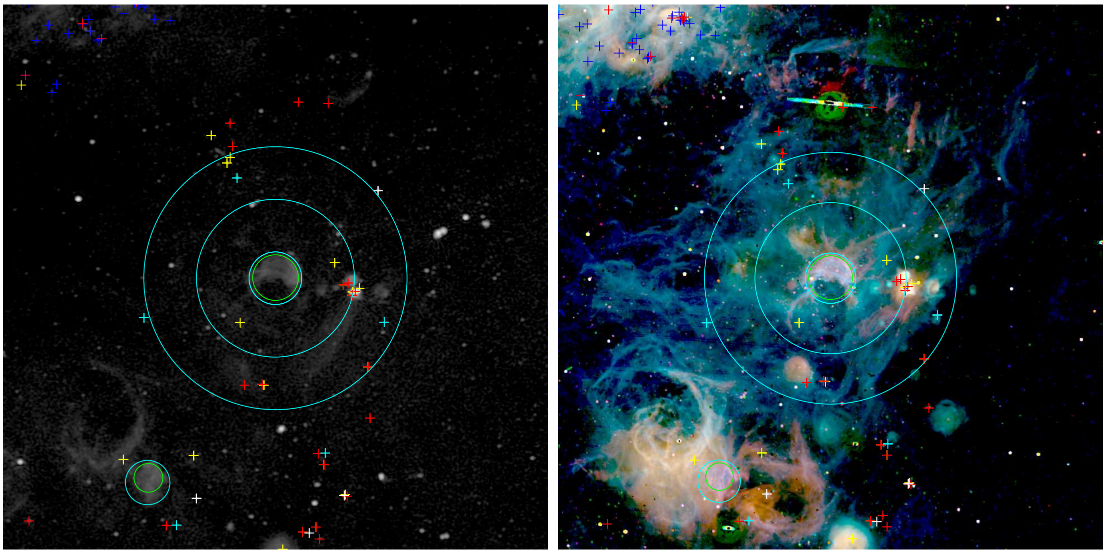

(a) Radio (b) Optical

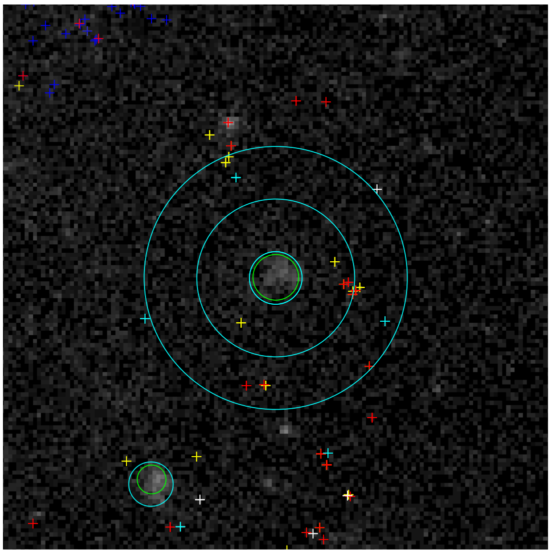

(c) X-ray

Figure C.4: MCSNR J0453−6655, N4
ICRS coordinates (ep=J2000): R.A. = 04:53:14.0, Dec = −66:55:13.0
$R = 128''$

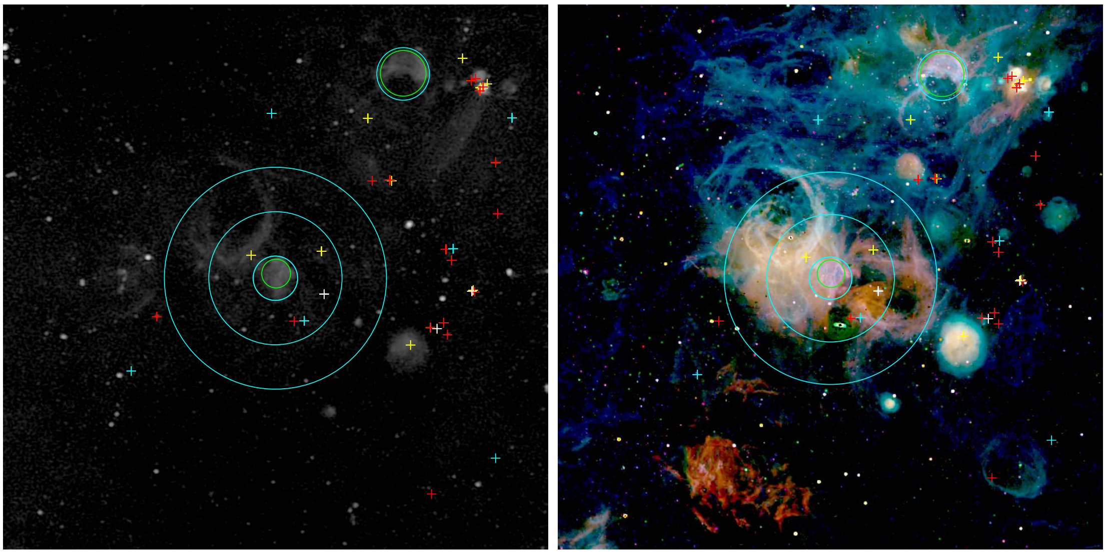

(A) Radio (B) Optical

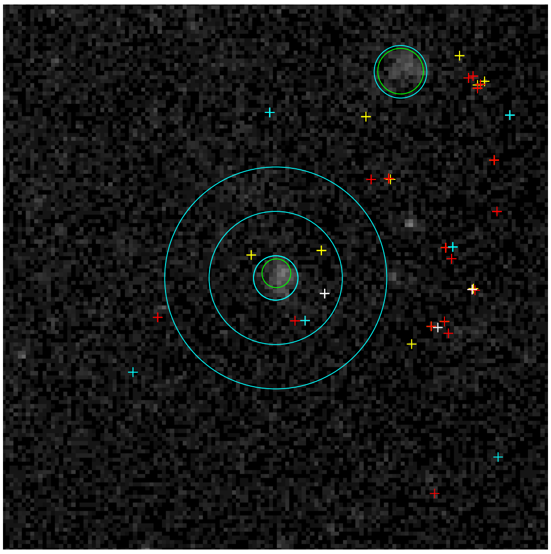

(C) X-ray

FIGURE C.5: MCSNR J0454−6713, N9
ICRS coordinates (ep=J2000): R.A. = 04:54:33.0, Dec = −67:13:13.0
$R = 108''$

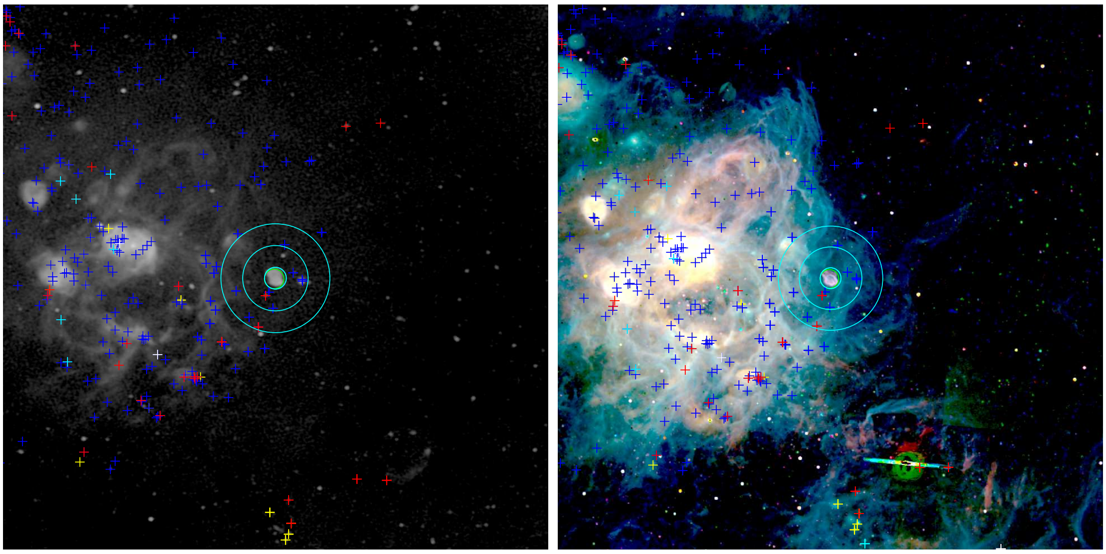

(A) Radio (B) Optical

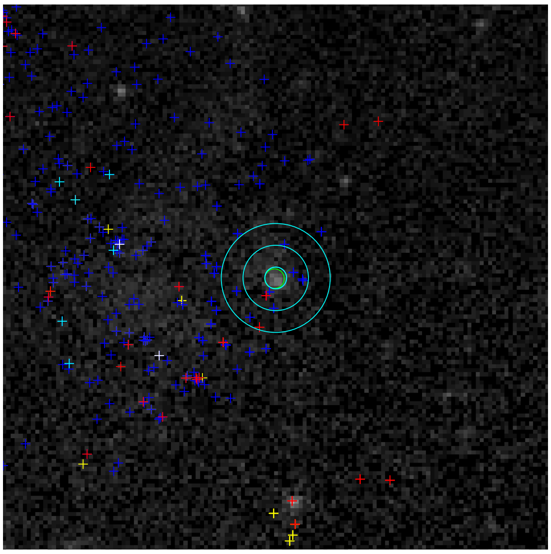

(C) X-ray

FIGURE C.6: MCSNR J0454−6626, N11L
ICRS coordinates (ep=J2000): R.A. = 04:54:49.0, Dec = −66:25:32.0
$R = 53''$

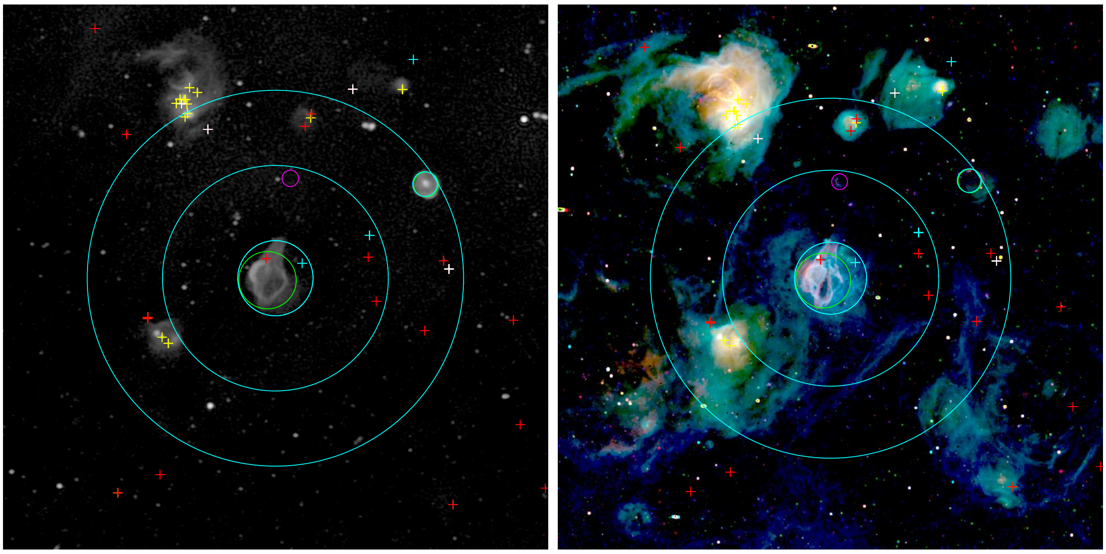

(A) Radio (B) Optical

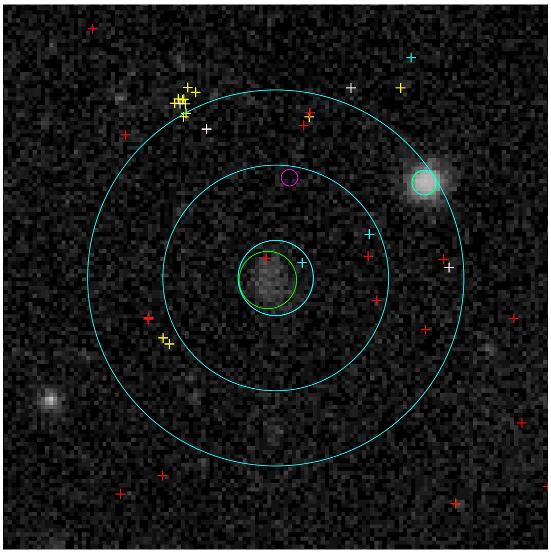

(C) X-ray

Figure C.7: MCSNR J0455−6839, N86
ICRS coordinates (ep=J2000): R.A. = 04:55:37.0, Dec = −68:38:47.0
$R = 183''$

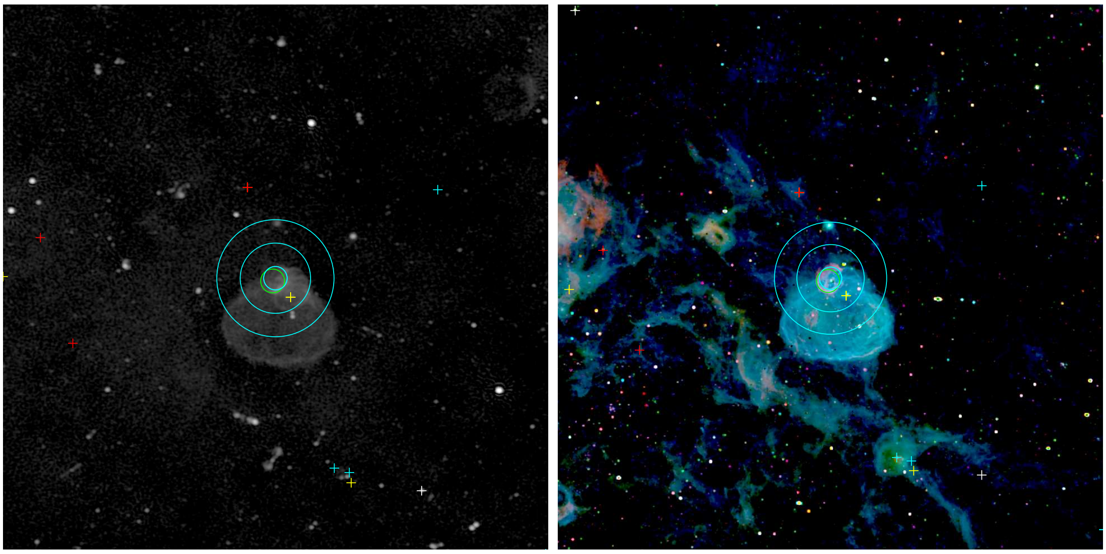

(A) Radio (B) Optical

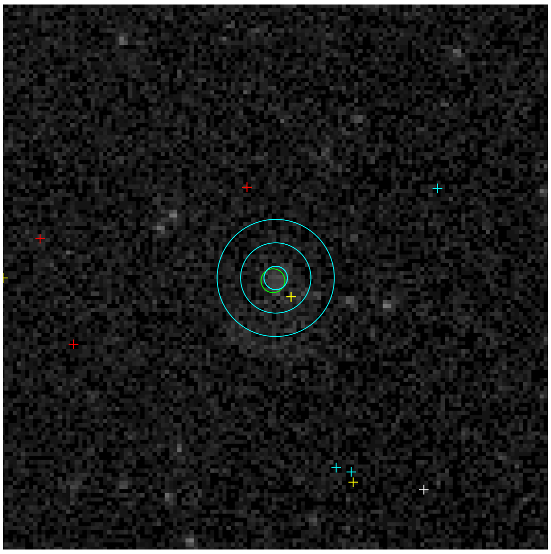

(C) X-ray

Figure C.8: MCSNR J0459−7008, N186D
ICRS coordinates (ep=J2000): R.A. = 04:59:55.0, Dec = −70:07:52.0
$R = 57''$

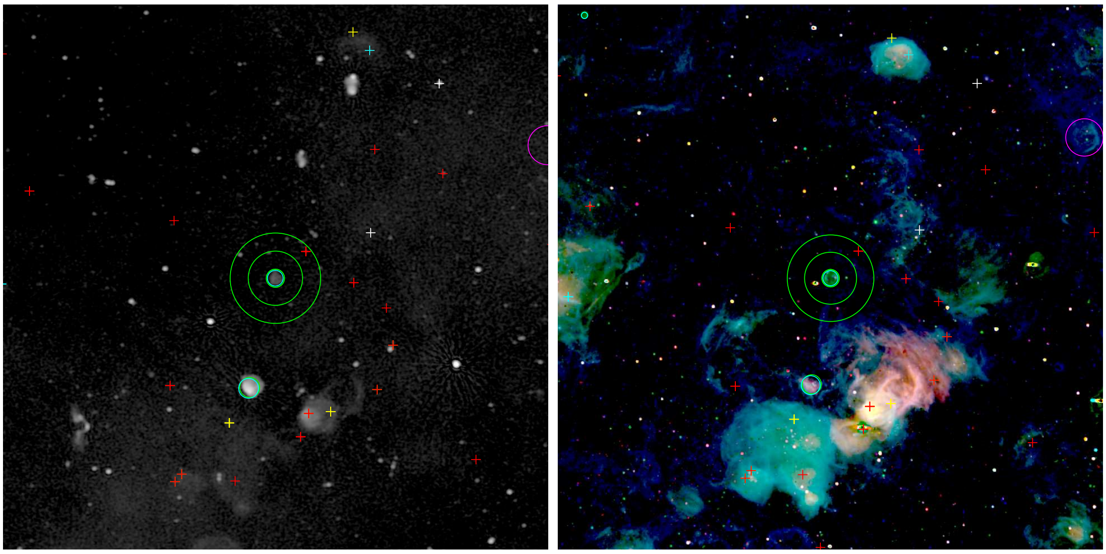

(A) Radio (B) Optical

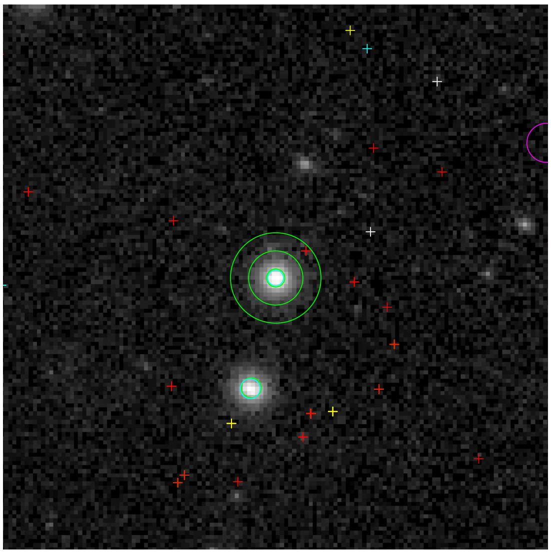

(C) X-ray

Figure C.9: MCSNR J0505−6752, DEM L71
ICRS coordinates (ep=J2000): R.A. = 05:05:41.9, Dec = −67:52:39.0
$R = 44''$

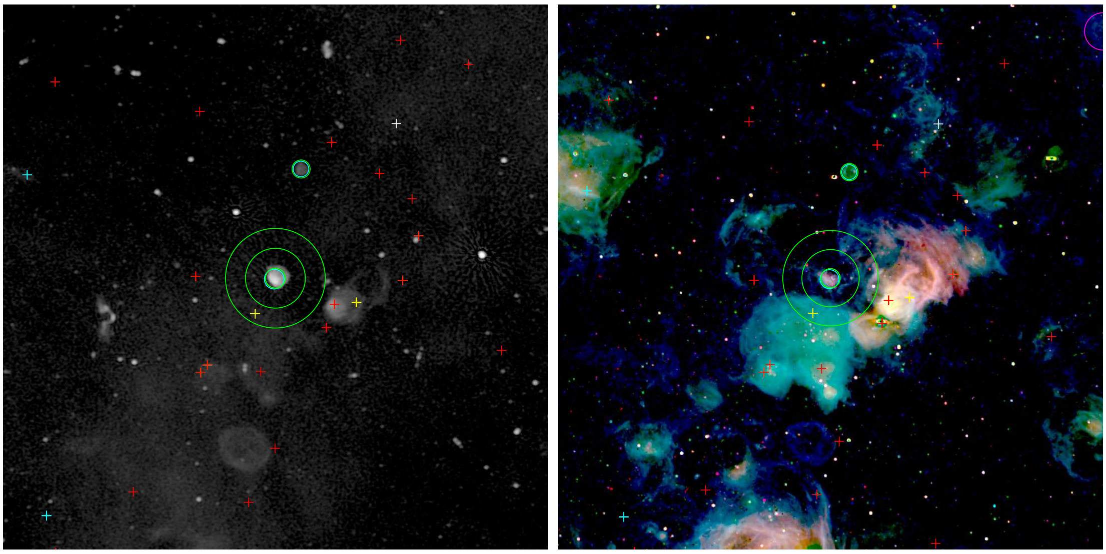

(A) Radio (B) Optical

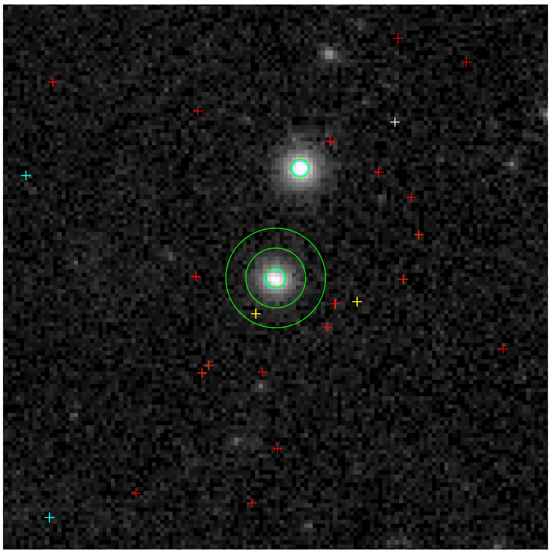

(C) X-ray

FIGURE C.10: MCSNR J0505−6801, N23
ICRS coordinates (ep=J2000): R.A. = 05:05:54.1, Dec = −68:01:42.0
$R = 48.5''$

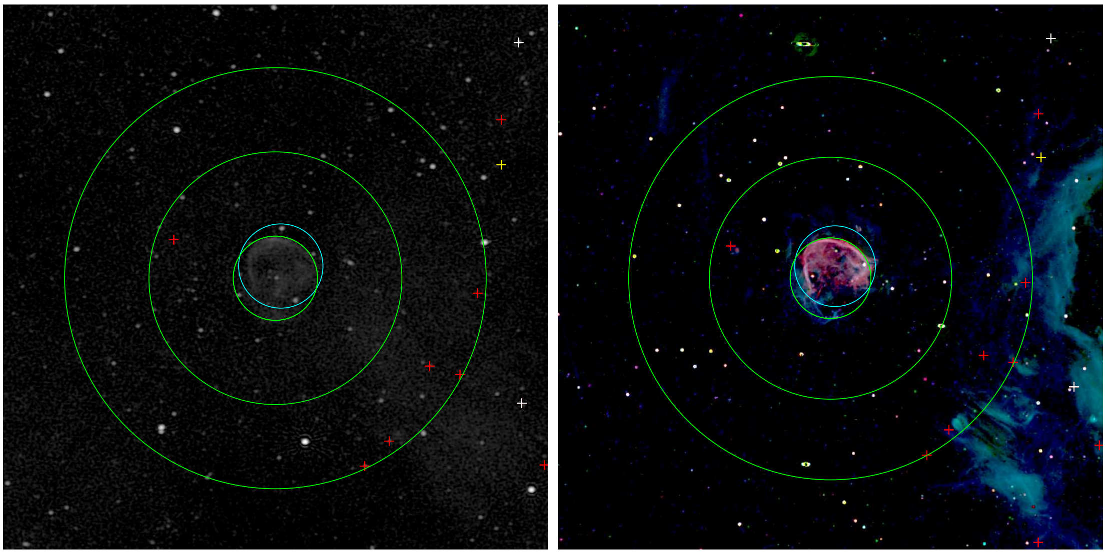

(A) Radio (B) Optical

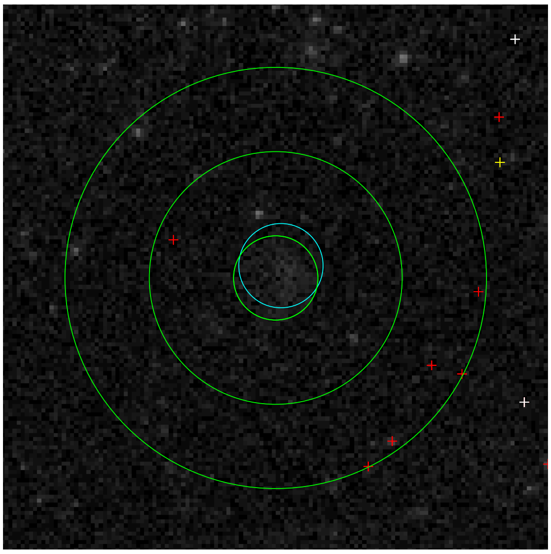

(C) X-ray

Figure C.11: MCSNR J0506−6542, DEM L72
ICRS coordinates (ep=J2000): R.A. = 05:06:08.2, Dec = −65:42:10.0
$R = 205''$

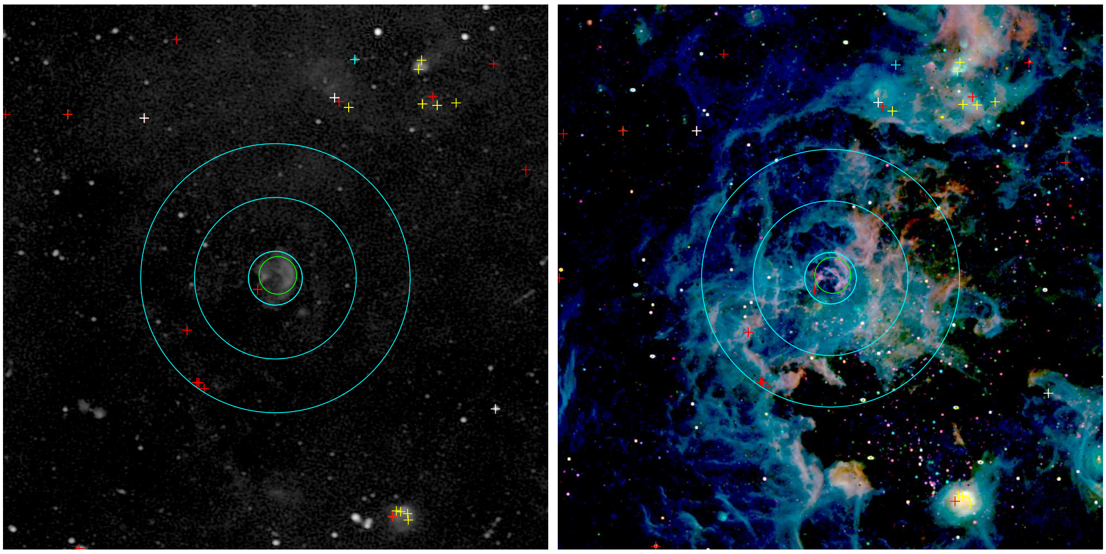

(A) Radio (B) Optical

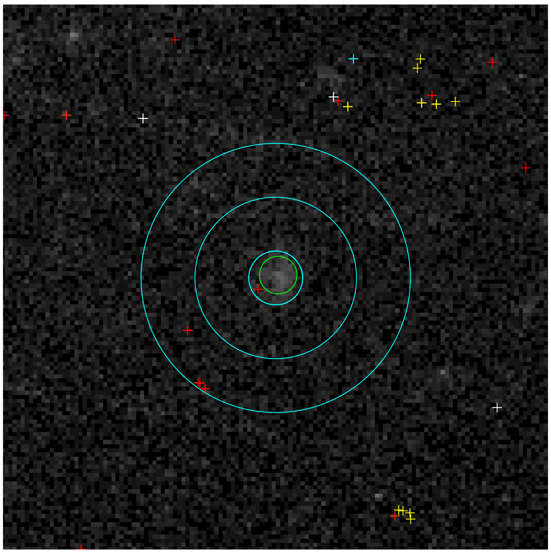

(C) X-ray

Figure C.12: MCSNR J0506−7026, [HP99] 1139
ICRS coordinates (ep=J2000): R.A. = 05:06:50.0, Dec = −70:25:53.0
$R = 131''$

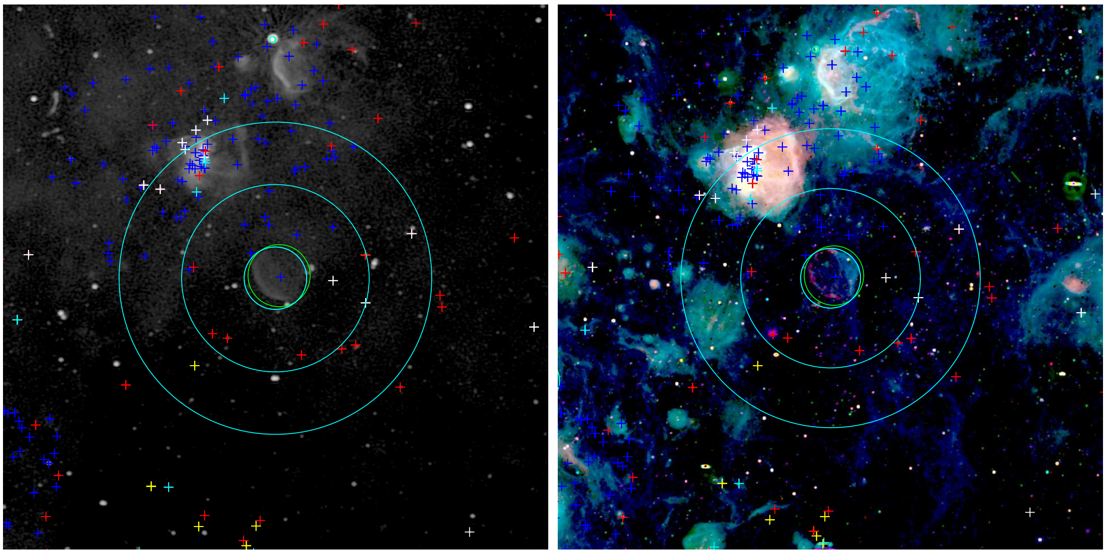

(A) Radio (B) Optical

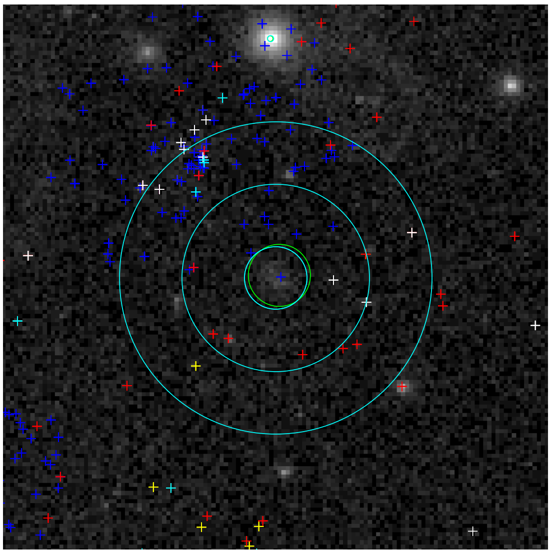

(C) X-ray

Figure C.13: MCSNR J0508–6902, [HP99] 791
ICRS coordinates (ep=J2000): R.A. = 05:08:37.0, Dec = –69:02:54.0
$R = 152''$

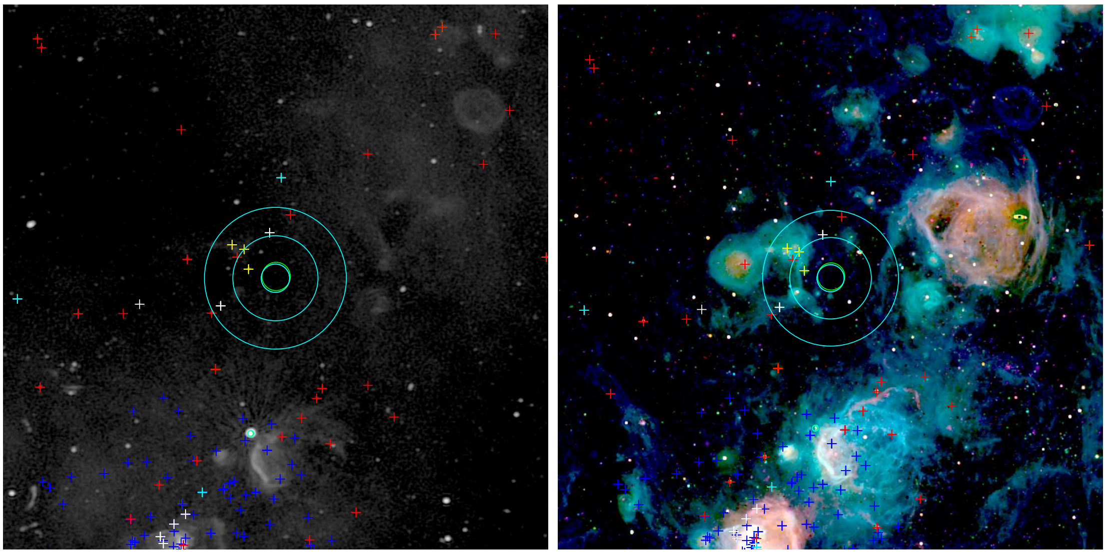

(A) Radio (B) Optical

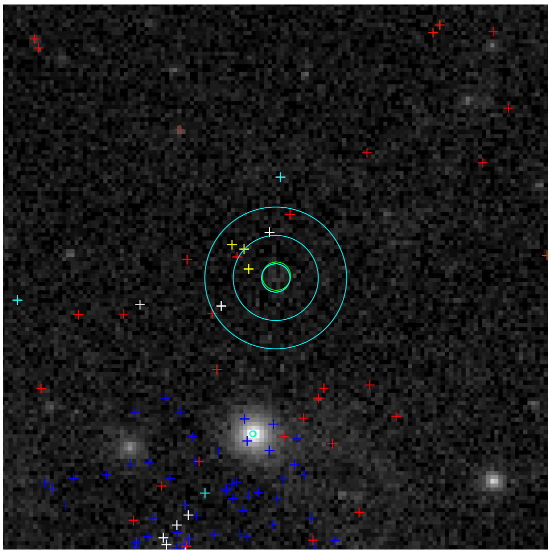

(C) X-ray

Figure C.14: MCSNR J0508−6830
ICRS coordinates (ep=J2000): R.A. = 05:08:50.0, Dec = −68:30:50.0
$R = 69''$

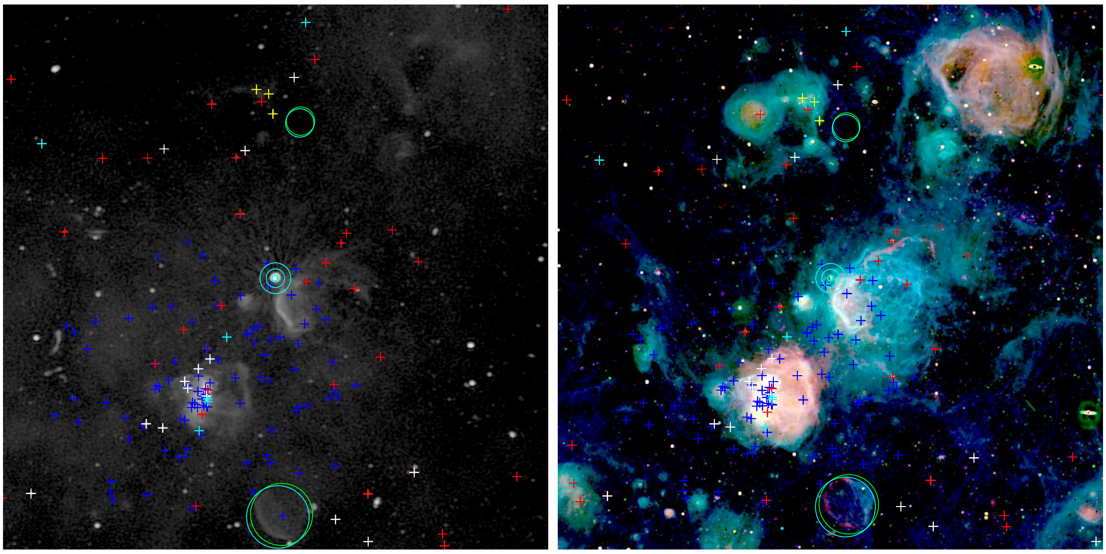

(A) Radio (B) Optical

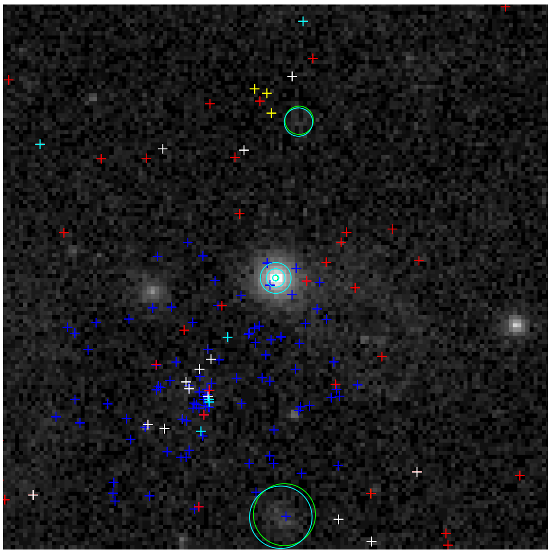

(C) X-ray

FIGURE C.15: MCSNR J0508−6843, N103B
ICRS coordinates (ep=J2000): R.A. = 05:08:59.0, Dec = −68:43:35.0
$R = 15''$

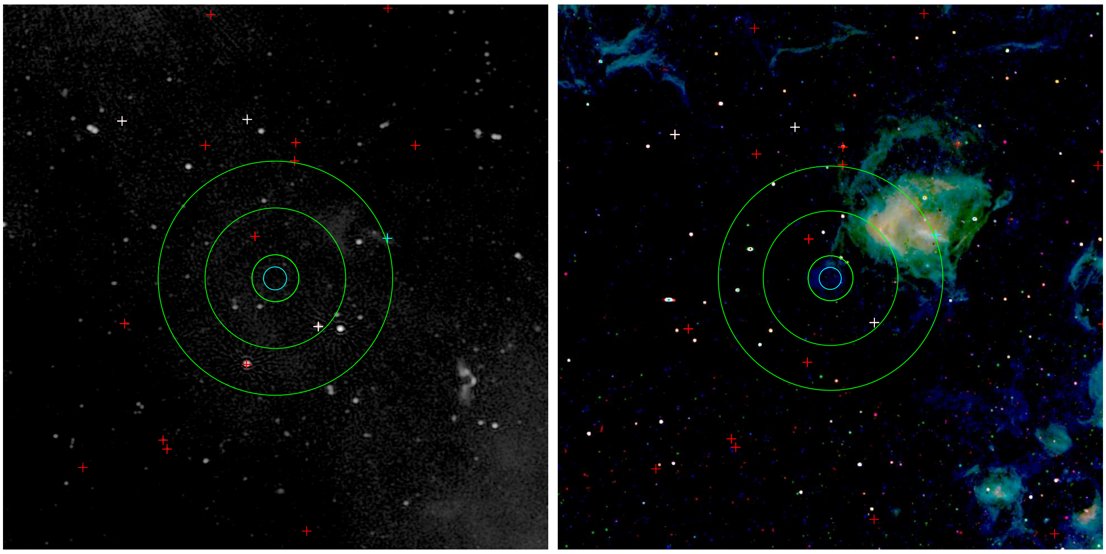

(A) Radio (B) Optical

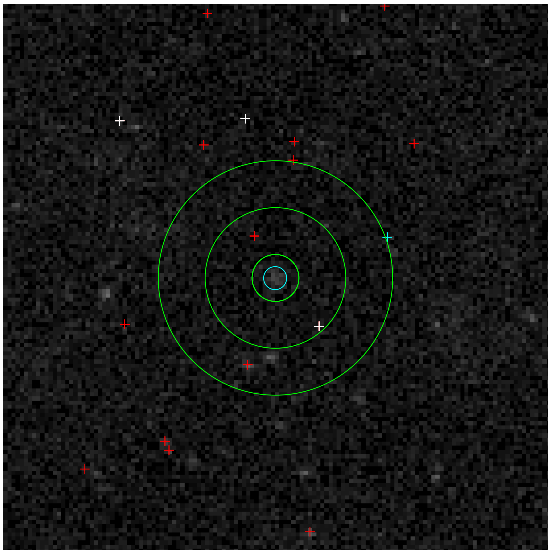

(C) X-ray

Figure C.16: MCSNR J0511−6759
ICRS coordinates (ep=J2000): R.A. = 05:11:10.7, Dec = −67:59:07.0
$R = 114''$

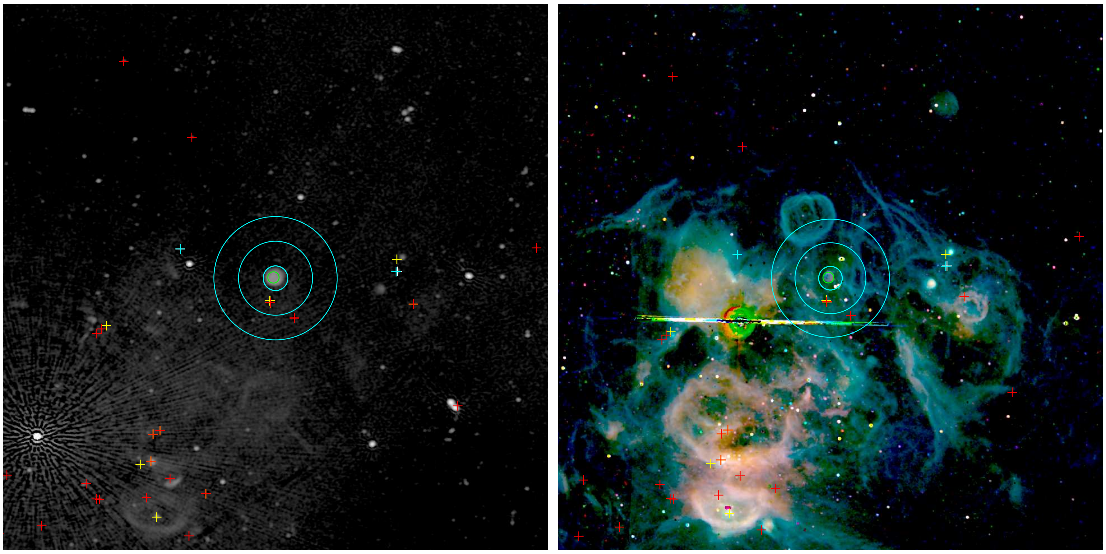

(A) Radio (B) Optical

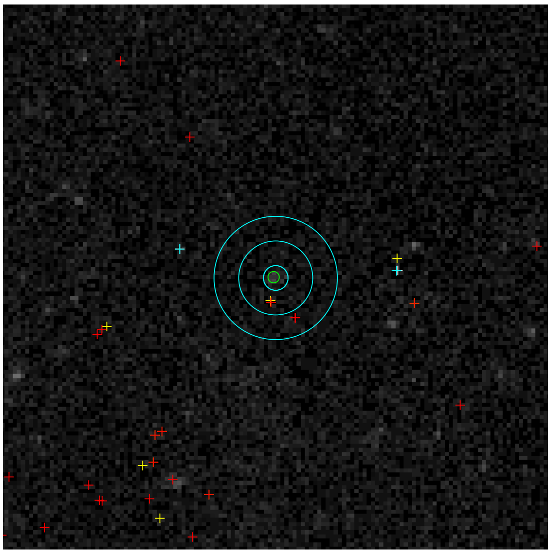

(C) X-ray

Figure C.17: MCSNR J0512–6707, [HP99] 483
ICRS coordinates (ep=J2000): R.A. = 05:12:27.0, Dec = –67:07:18.0
$R = 60''$

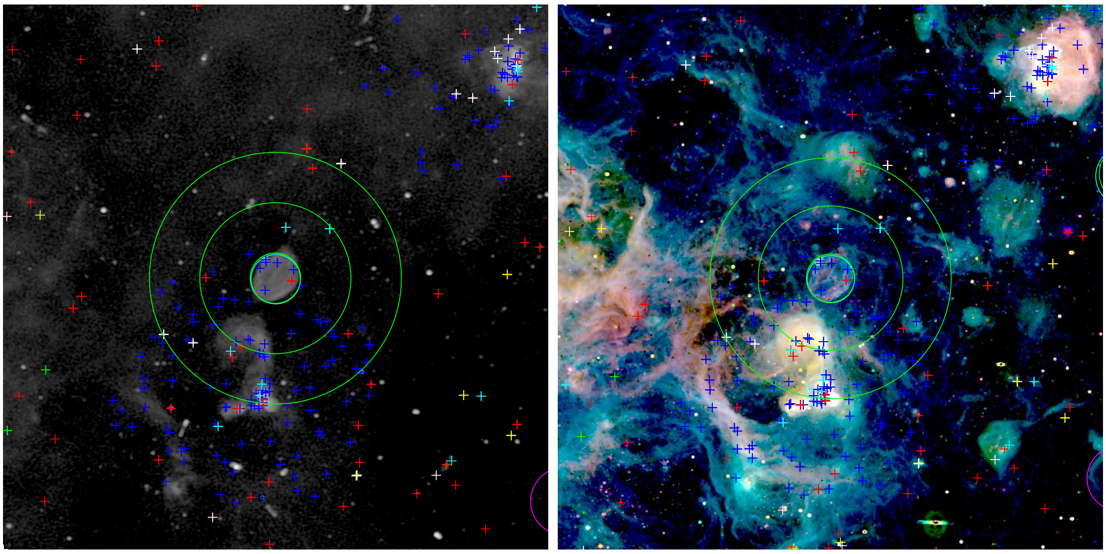

(A) Radio (B) Optical

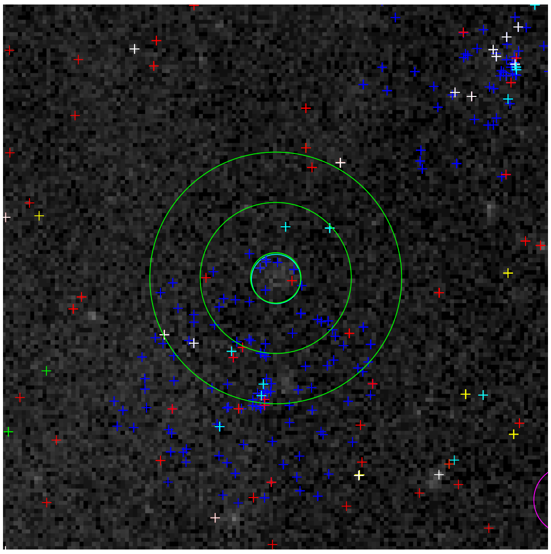

(C) X-ray

Figure C.18: MCSNR J0513−6912, N112
ICRS coordinates (ep=J2000): R.A. = 05:13:14.4, Dec = −69:12:15.0
$R = 122.5''$

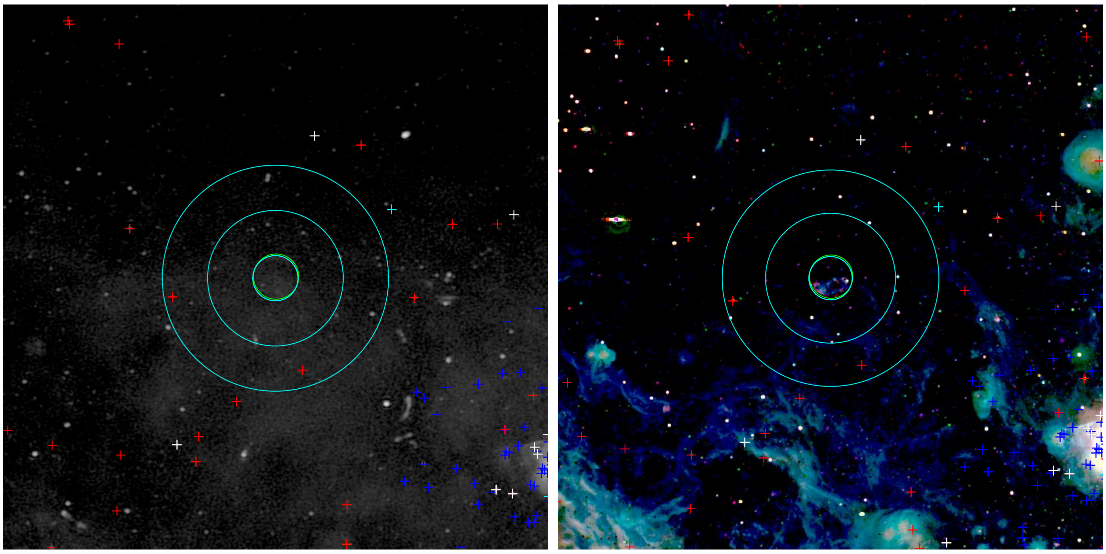

(A) Radio (B) Optical

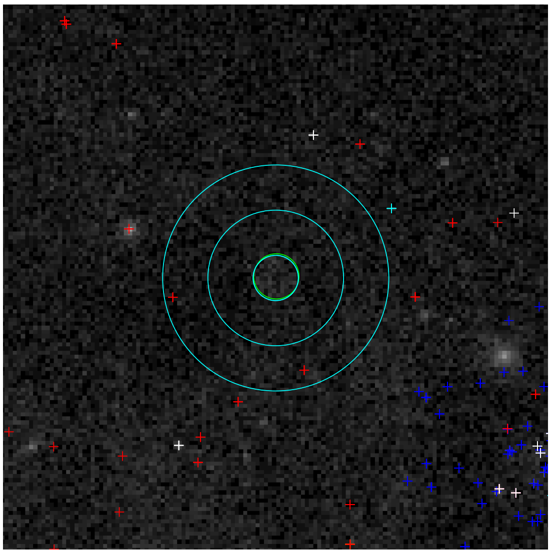

(C) X-ray

FIGURE C.19: MCSNR J0514−6840
ICRS coordinates (ep=J2000): R.A. = 05:14:16.0, Dec = −68:40:22.0
$R = 110''$

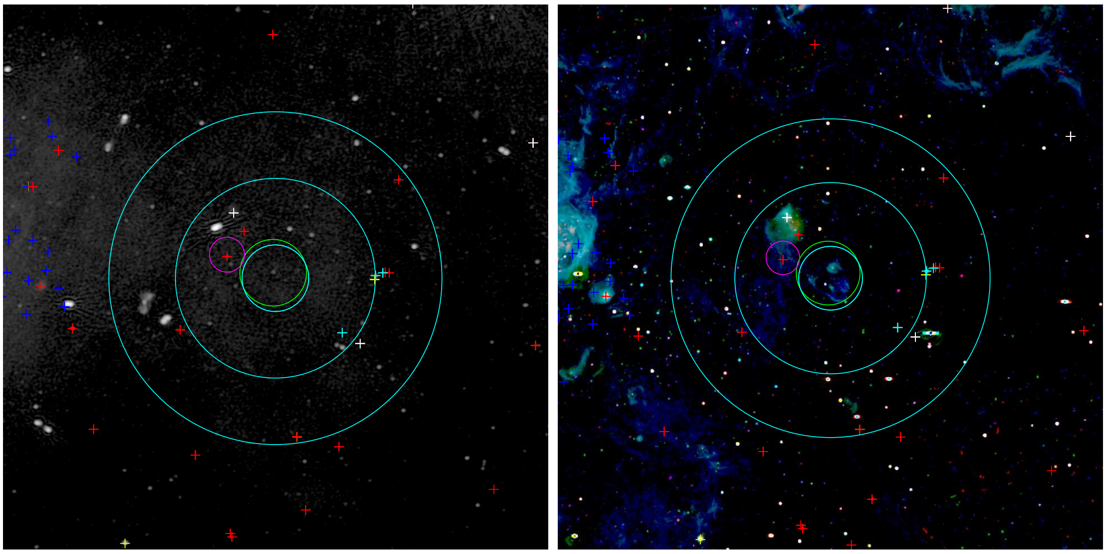

(A) Radio (B) Optical

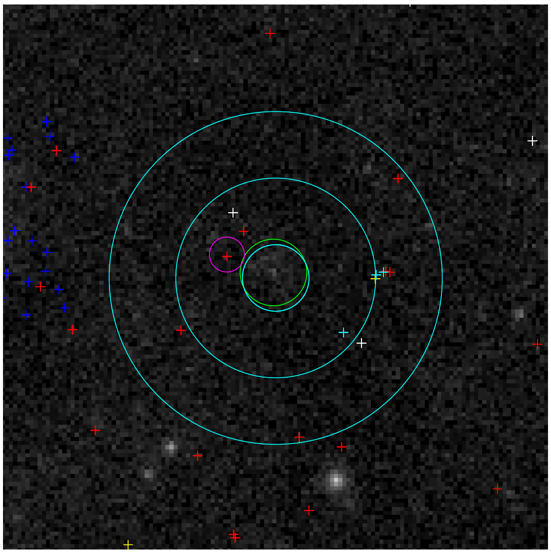

(C) X-ray

FIGURE C.20: MCSNR J0517−6759
ICRS coordinates (ep=J2000): R.A. = 05:17:08.0, Dec = −67:59:29.0
$R = 162''$

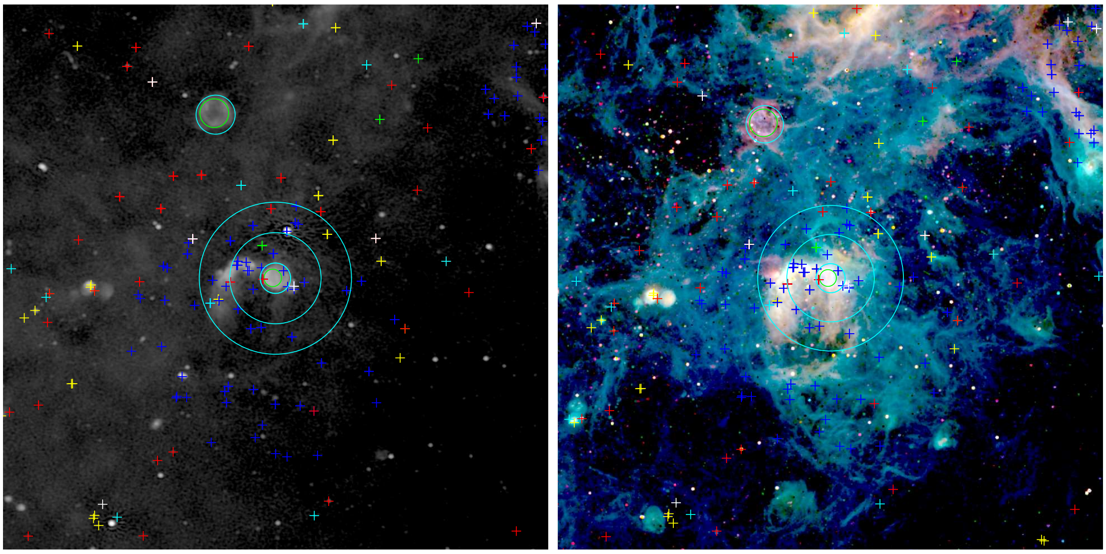

(A) Radio (B) Optical

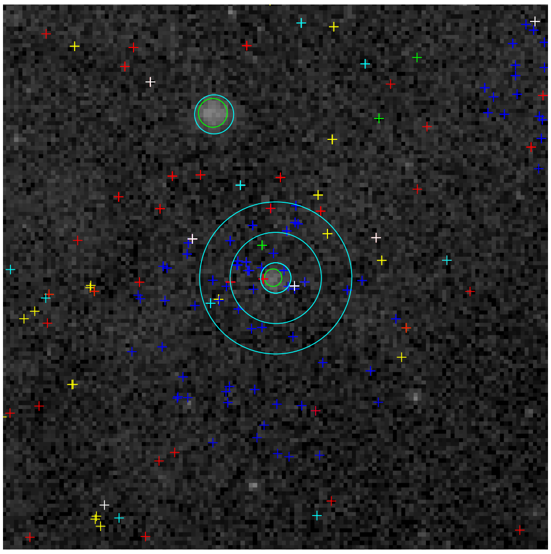

(C) X-ray

Figure C.21: MCSNR J0518−6939, N120
ICRS coordinates (ep=J2000): R.A. = 05:18:41.0, Dec = −69:39:12.0
$R = 74''$

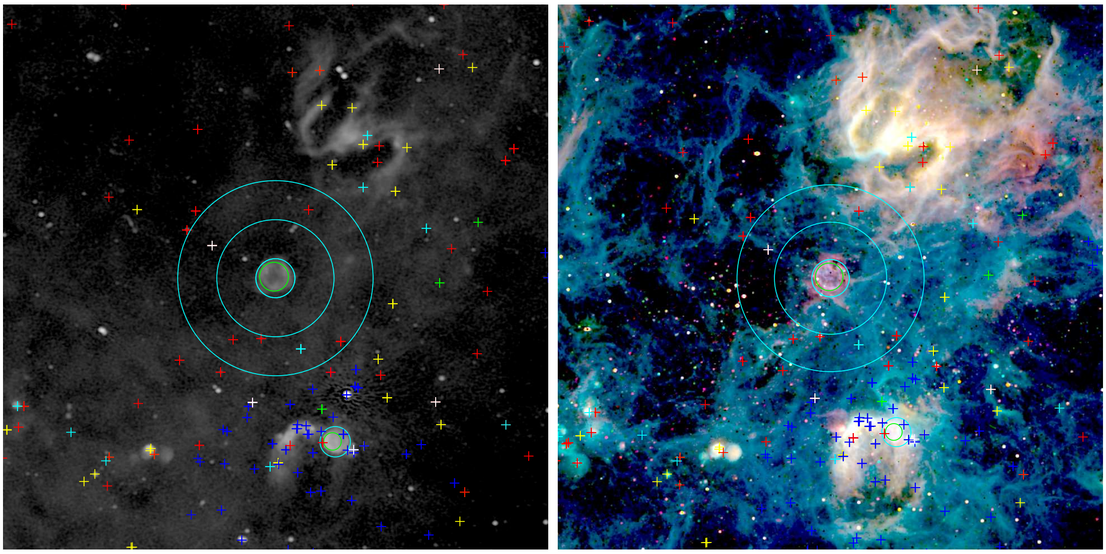

(A) Radio (B) Optical

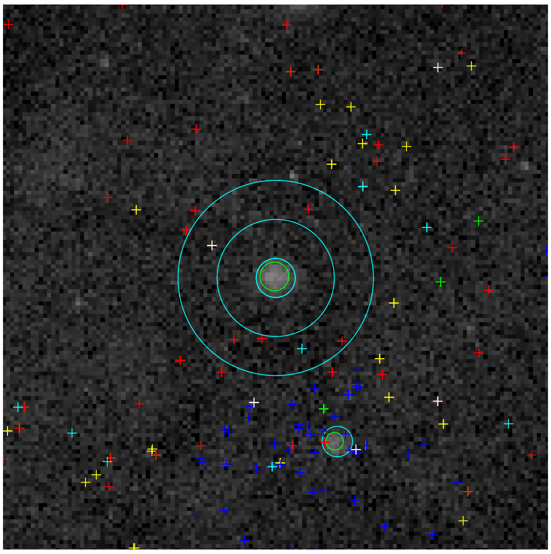

(C) X-ray

FIGURE C.22: MCSNR J0519−6902, B0519−690
ICRS coordinates (ep=J2000): R.A. = 05:19:44.0, Dec = −69:26:08.0
$R = 95''$

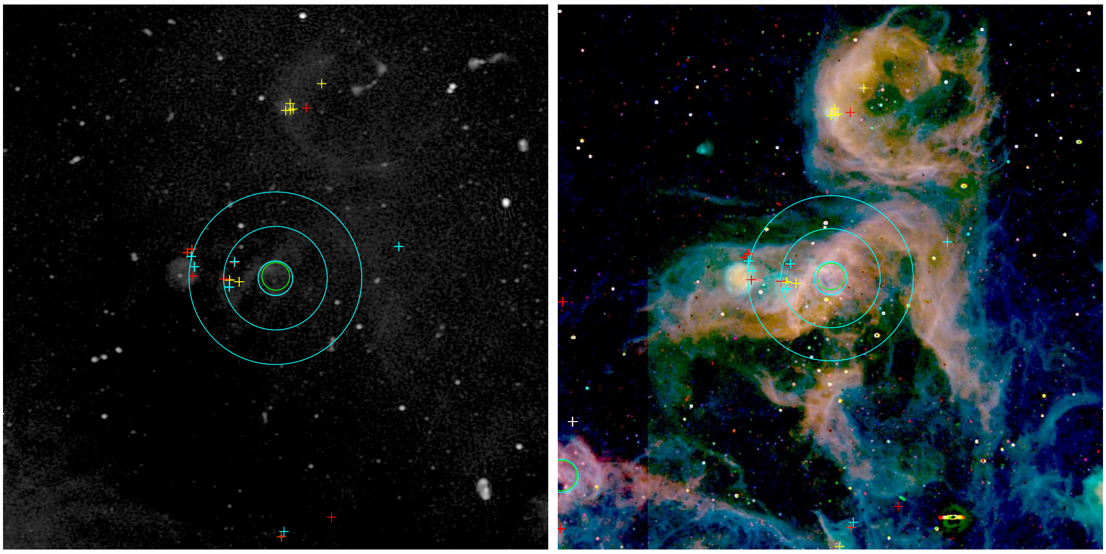

(A) Radio

(B) Optical

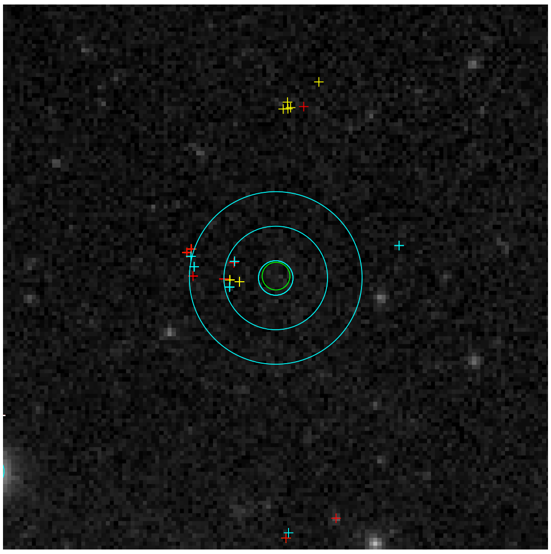

(C) X-ray

Figure C.23: MCSNR J0521−6543, DEM L142
ICRS coordinates (ep=J2000): R.A. = 05:21:39.0, Dec = −65:43:07.0
$R = 84''$

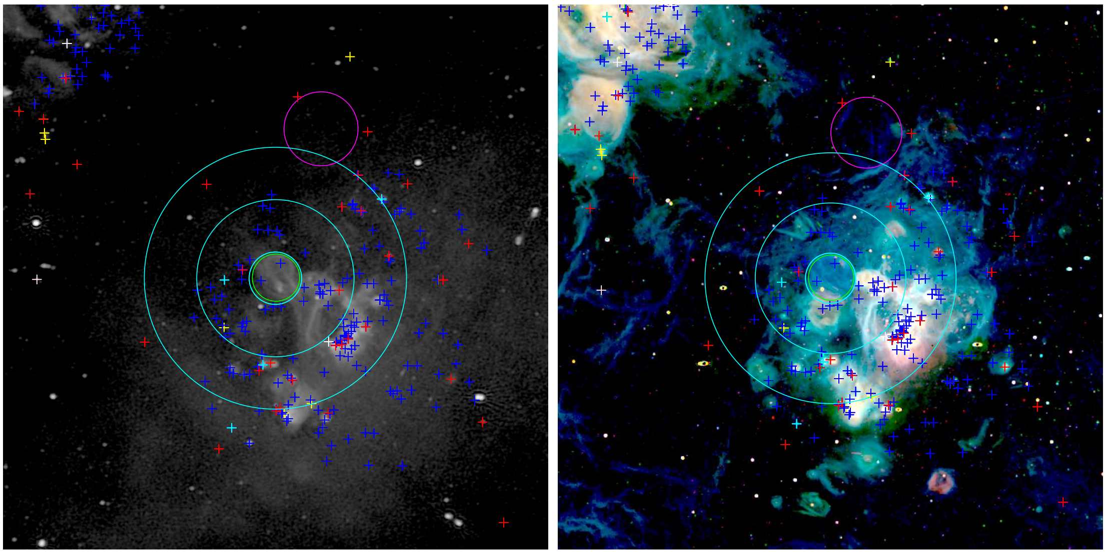

(a) Radio (b) Optical

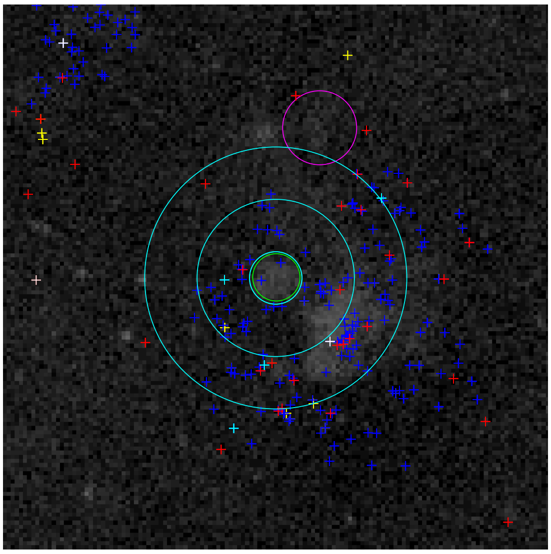

(c) X-ray

Figure C.24: MCSNR J0523−6753, N44
ICRS coordinates (ep=J2000): R.A. = 05:23:07.0, Dec = −67:53:12.0
$R = 127.5''$

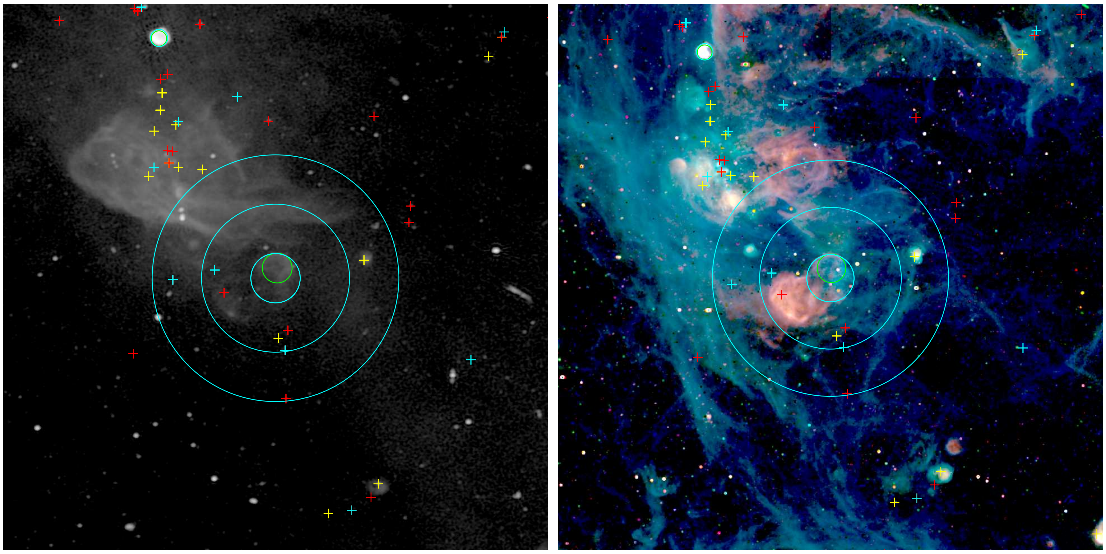

(A) Radio (B) Optical

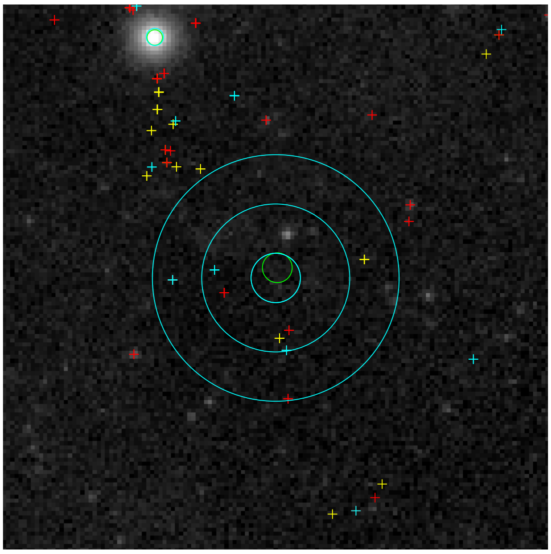

(C) X-ray

FIGURE C.25: MCSNR J0524–6624, DEM L175a
ICRS coordinates (ep=J2000): R.A. = 05:24:20.0, Dec = −66:24:23.0
$R = 120''$

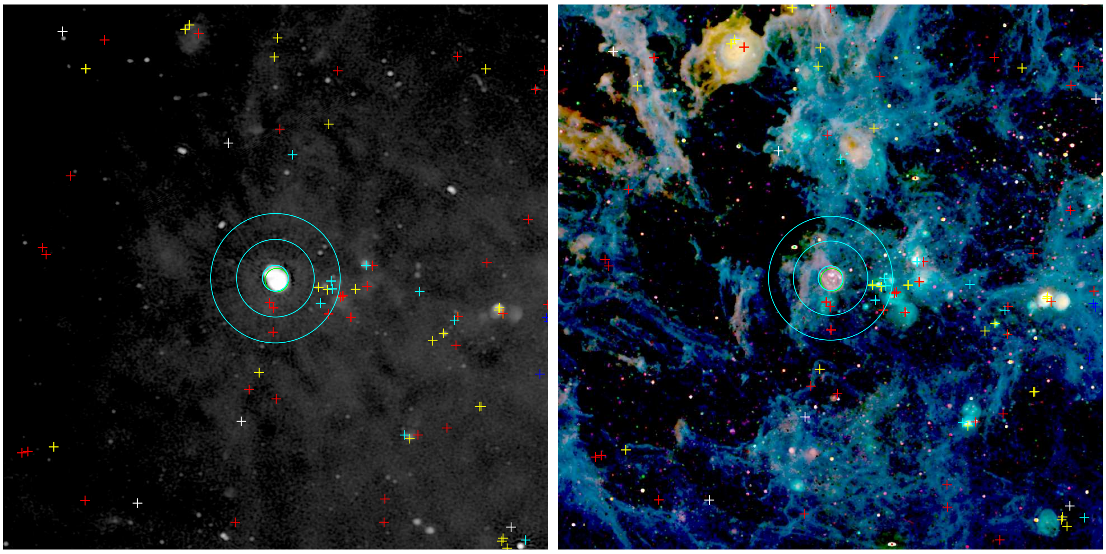

(A) Radio (B) Optical

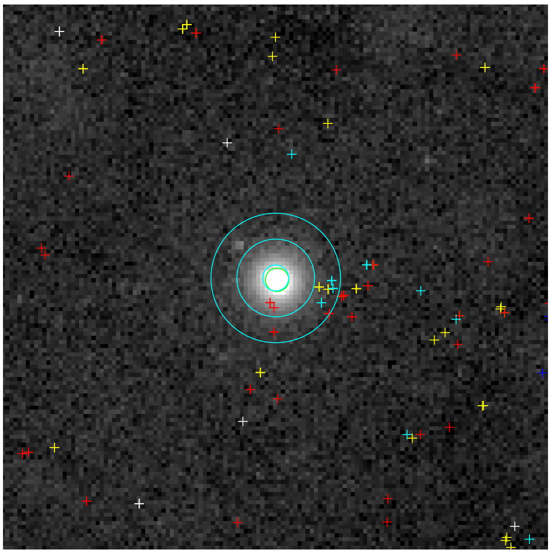

(C) X-ray

Figure C.26: MCSNR J0525−6938, N132D
ICRS coordinates (ep=J2000): R.A. = 05:25:04.0, Dec = −69:38:24.0
$R = 63''$

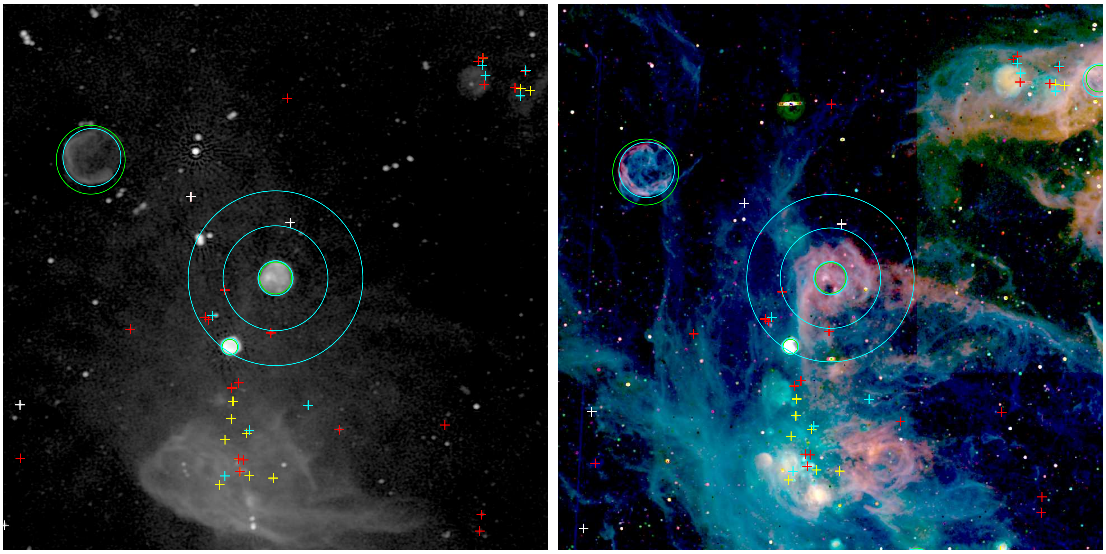

(A) Radio (B) Optical

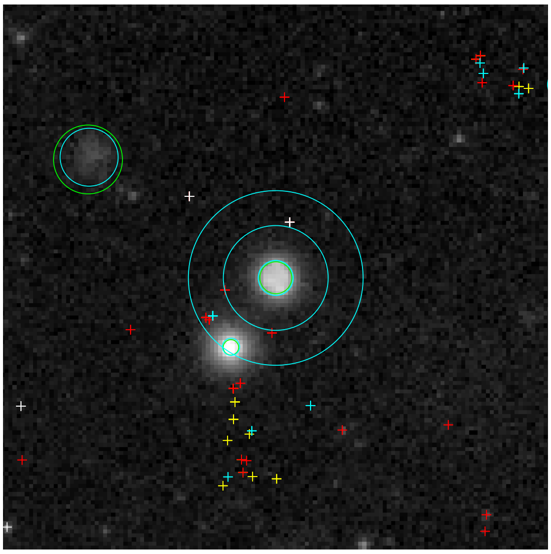

(C) X-ray

Figure C.27: MCSNR J0525–6559, N49B
ICRS coordinates (ep=J2000): R.A. = 05:25:25.0, Dec = –65:59:19.0
$R = 85''$

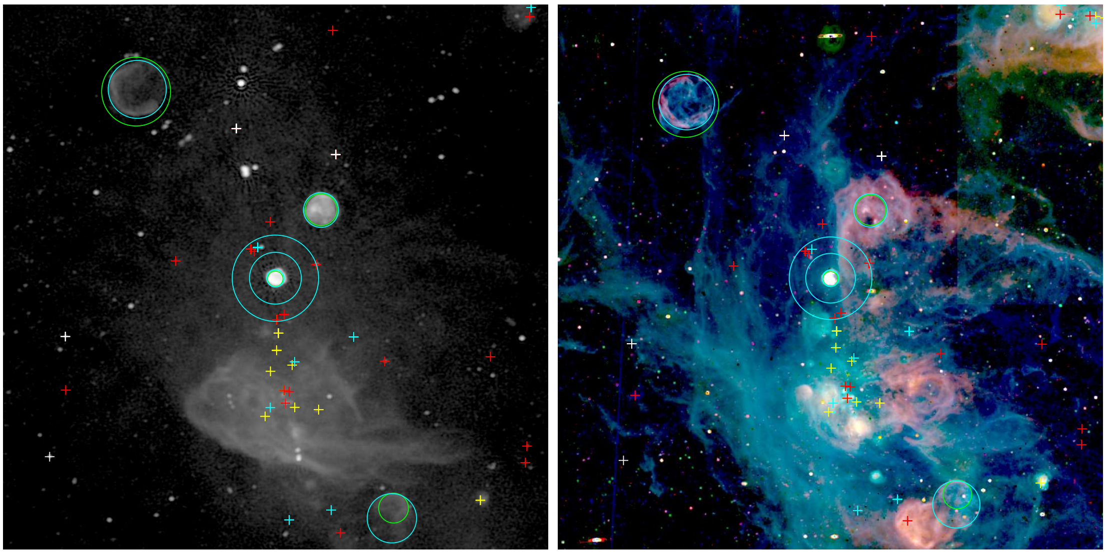

(A) Radio (B) Optical

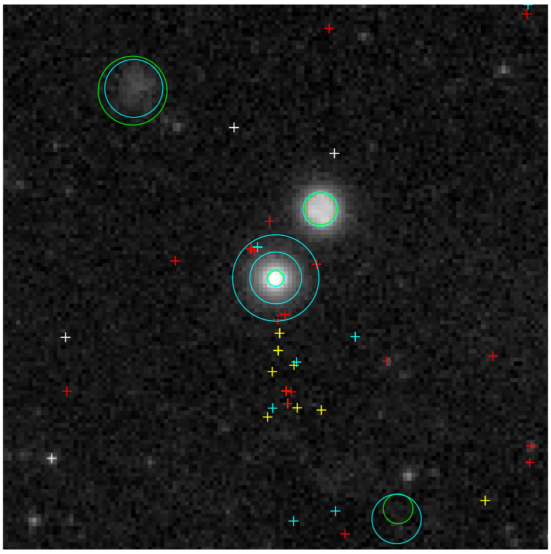

(C) X-ray

FIGURE C.28: MCSNR J0526−6605, N49
ICRS coordinates (ep=J2000): R.A. = 05:26:00.0, Dec = −66:04:57.0
$R = 42''$

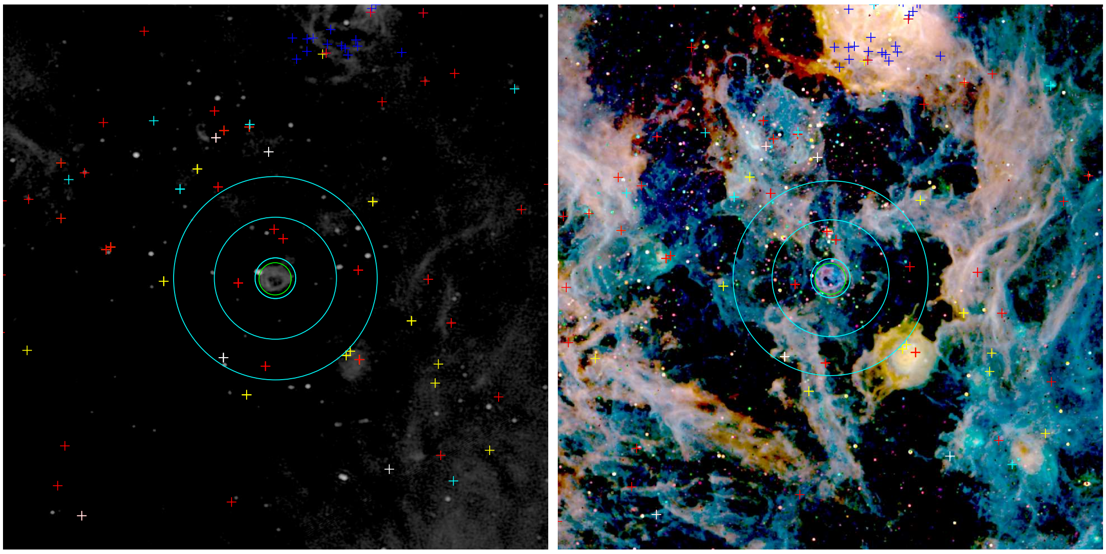

(a) Radio (b) Optical

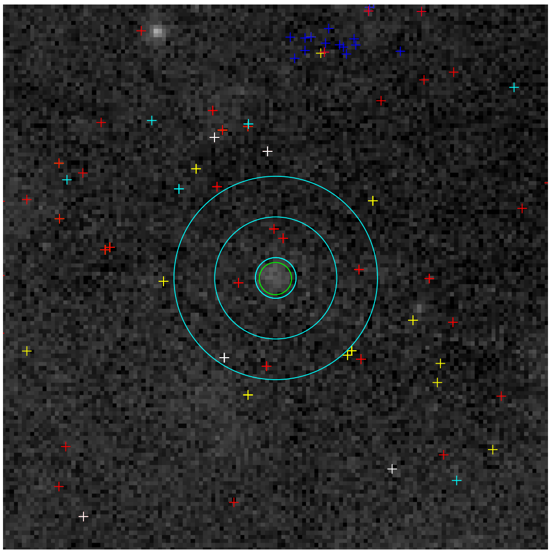

(c) X-ray

Figure C.29: MCSNR J0527−6912, B0528−692
ICRS coordinates (ep=J2000): R.A. = 05:27:39.0, Dec = −69:12:04.0
$R = 99''$

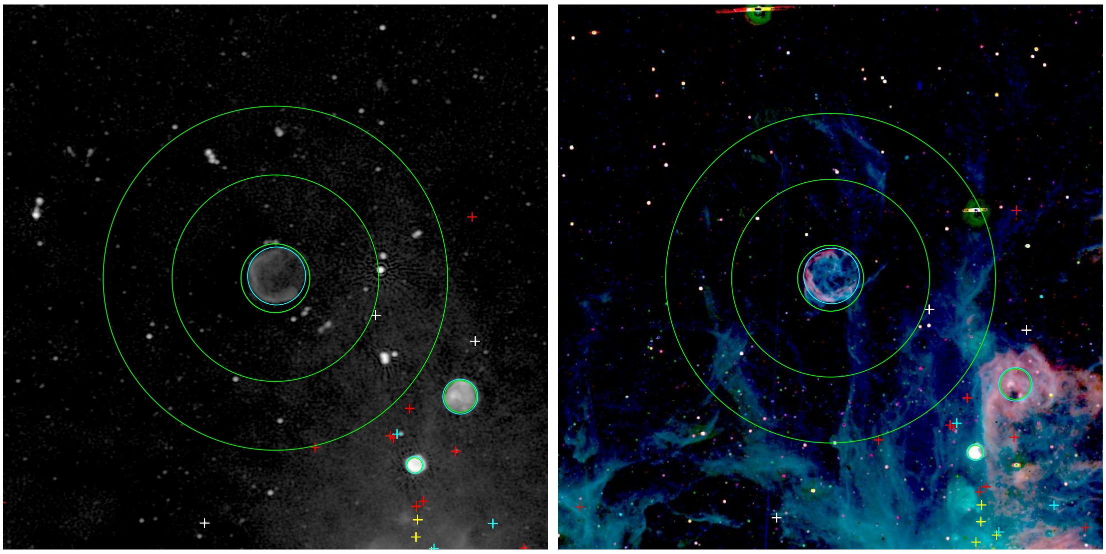

(A) Radio (B) Optical

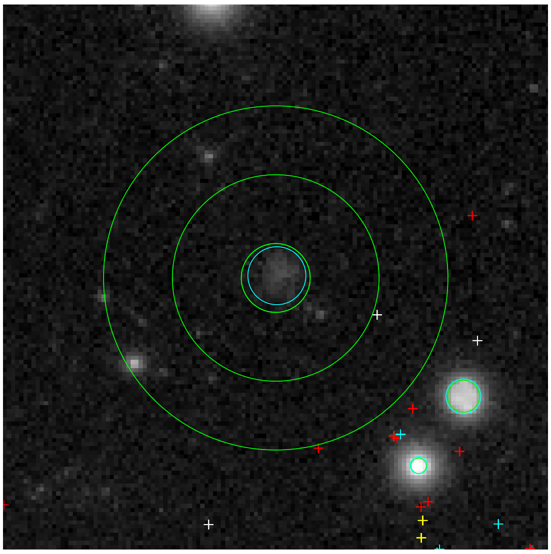

(C) X-ray

Figure C.30: MCSNR J0527–6549, DEM L204
ICRS coordinates (ep=J2000): R.A. = 05:27:54.9, Dec = –65:49:49.0
$R = 167.5''$

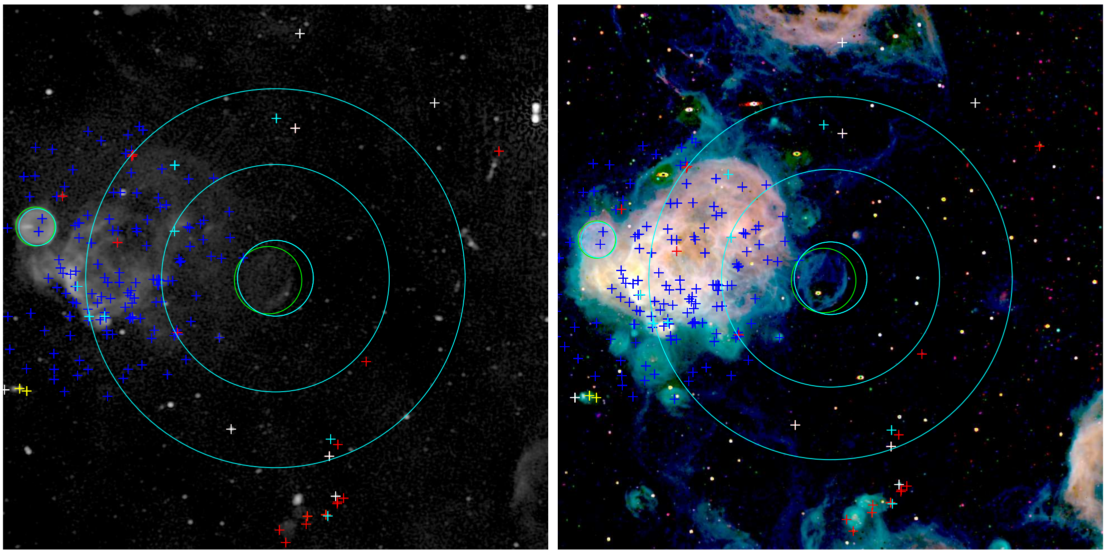

(A) Radio (B) Optical

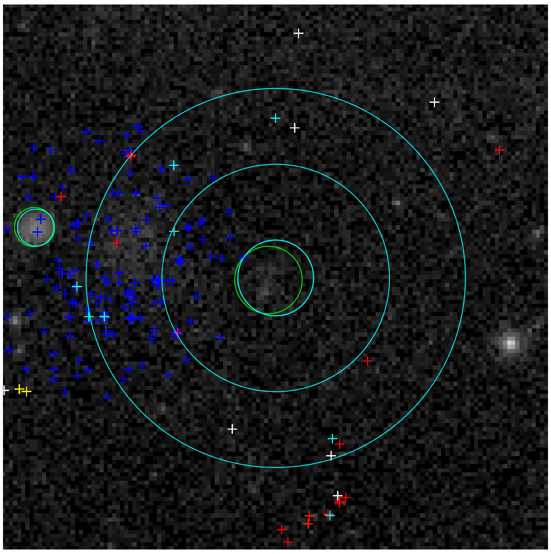

(C) X-ray

FIGURE C.31: MCSNR J0527−7104, [HP99] 1234
ICRS coordinates (ep=J2000): R.A. = 05:27:57.0, Dec = −71:04:30.0
$R = 184.5''$

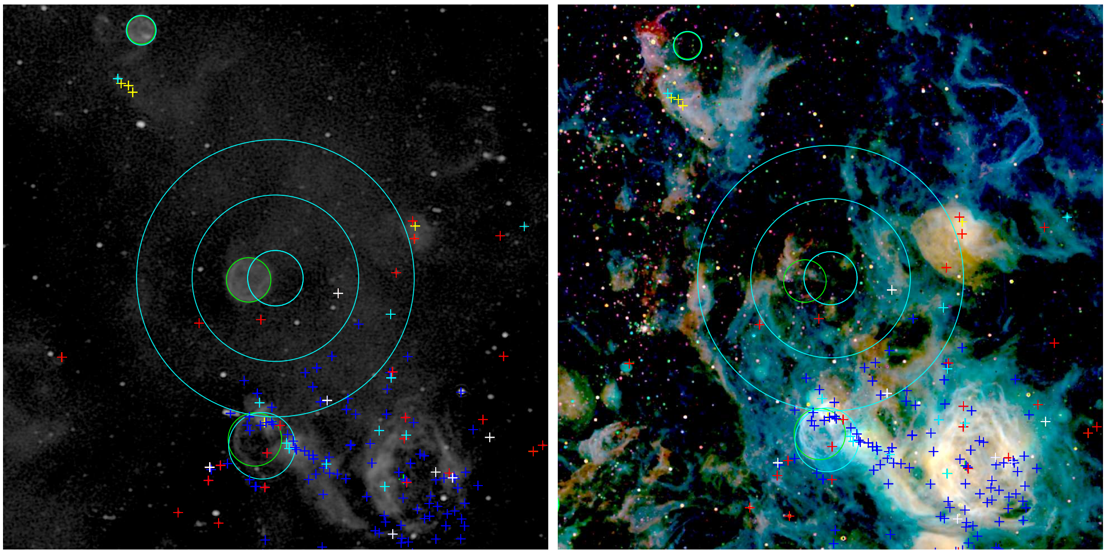

(A) Radio (B) Optical

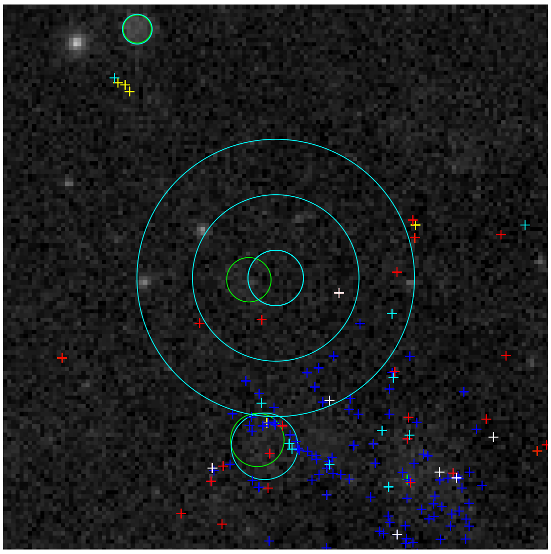

(C) X-ray

FIGURE C.32: MCSNR J0527−6714, B0528−6716
ICRS coordinates (ep=J2000): R.A. = 05:27:56.0, Dec = −67:13:40.0
$R = 135''$

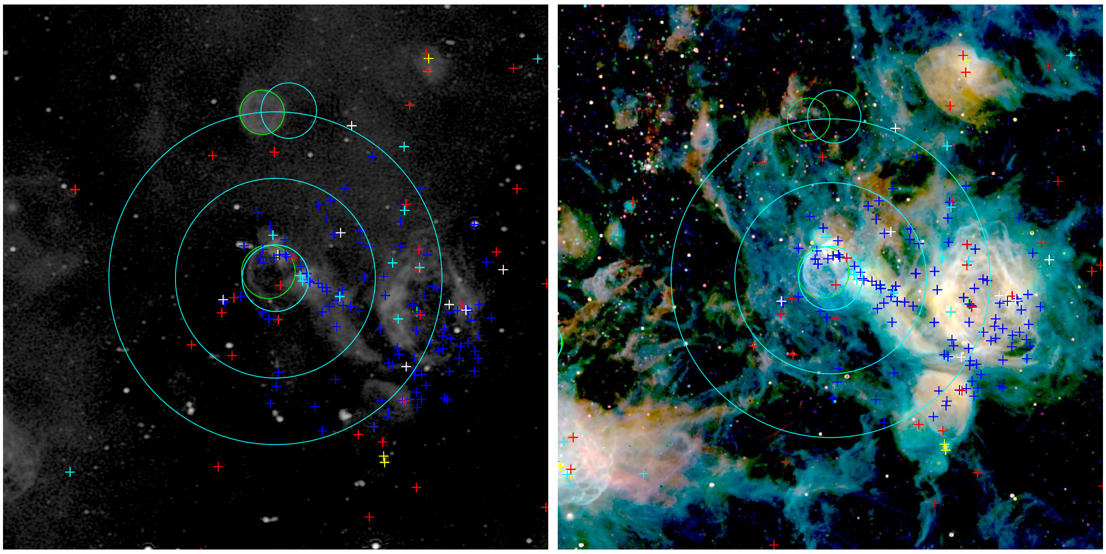

(A) Radio (B) Optical

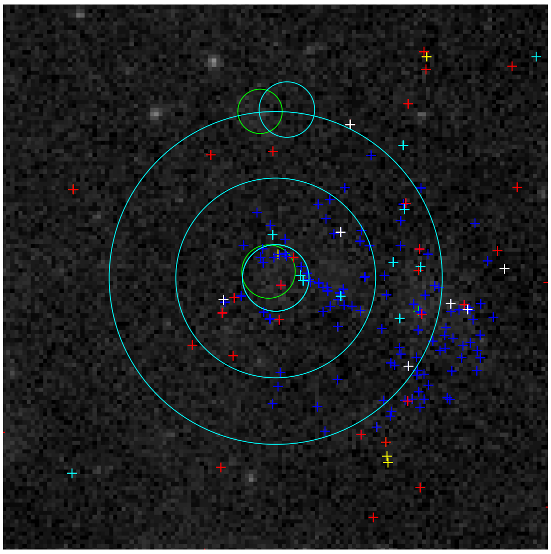

(C) X-ray

FIGURE C.33: MCSNR J0528–6727, DEM L205
ICRS coordinates (ep=J2000): R.A. = 05:28:05.0, Dec = –67:27:20.0
$R = 162''$

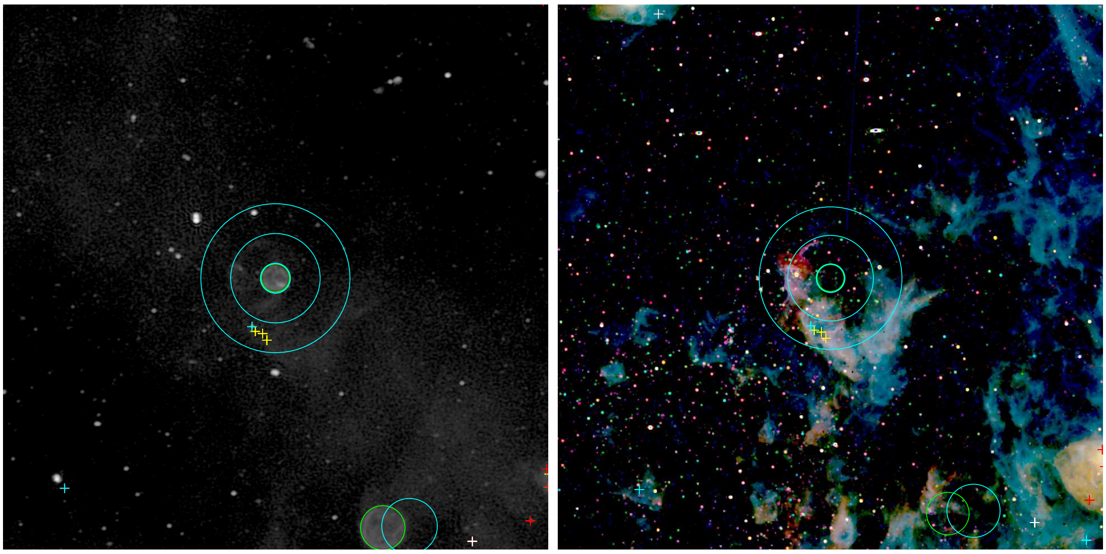

(A) Radio (B) Optical

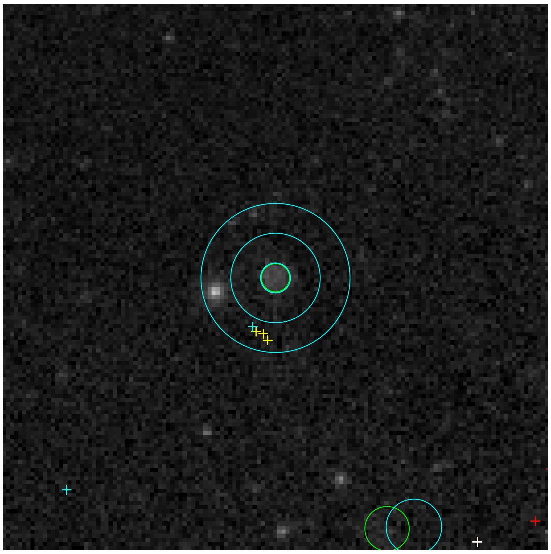

(C) X-ray

FIGURE C.34: MCSNR J0529−6653, DEM L214
ICRS coordinates (ep=J2000): R.A. = 05:29:51.0, Dec = −66:53:28.0
$R = 72.5''$

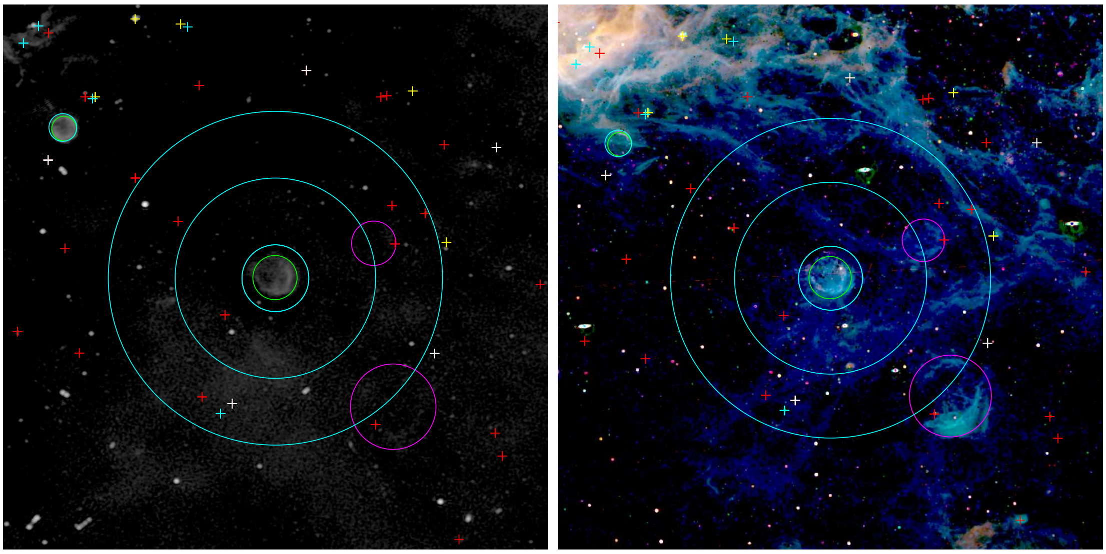

(A) Radio (B) Optical

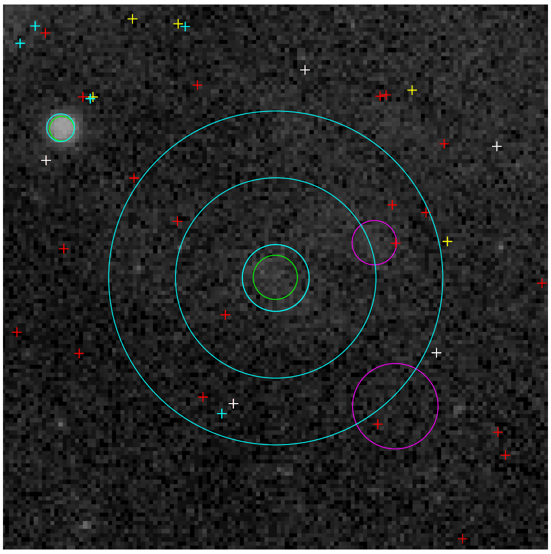

(C) X-ray

Figure C.35: MCSNR J0530−7008, DEM L218
ICRS coordinates (ep=J2000): R.A. = 05:30:40.0, Dec = −70:07:30.0
$R = 162.5''$

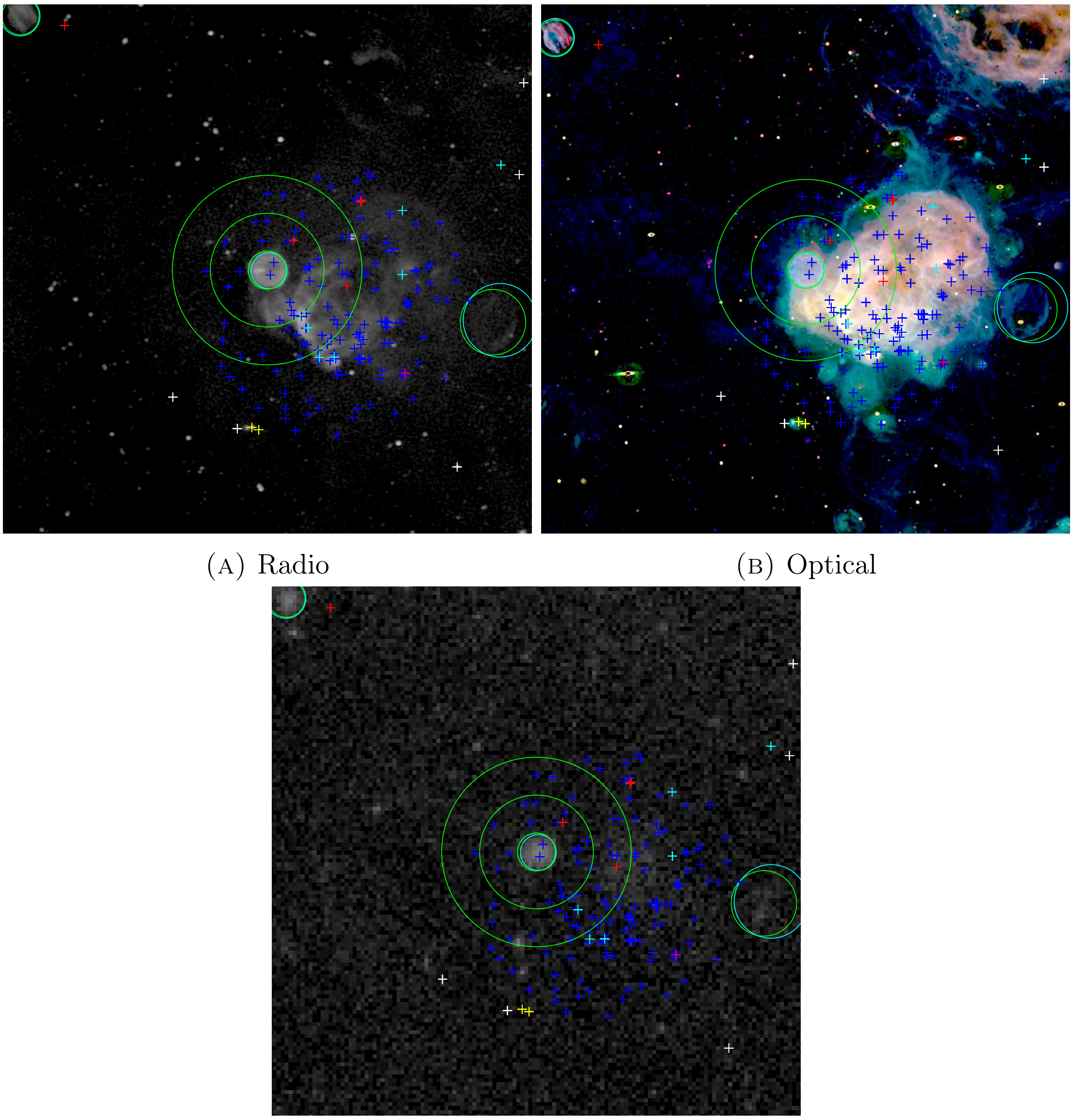

(A) Radio

(B) Optical

(C) X-ray

Figure C.36: MCSNR J0531−7100, N206
ICRS coordinates (ep=J2000): R.A. = 05:31:57.9, Dec = −71:00:16.0
$R = 95''$

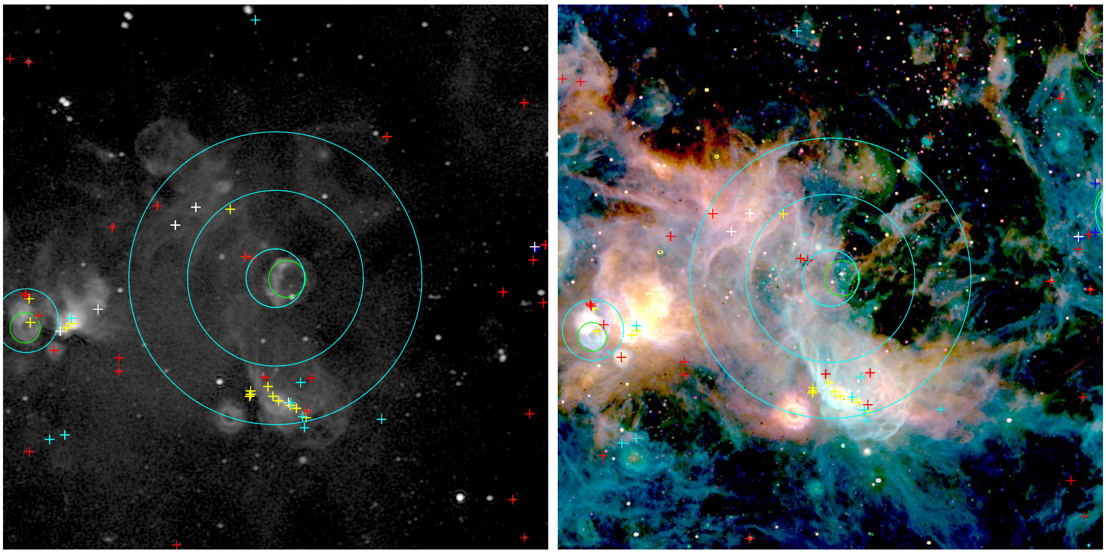

(A) Radio (B) Optical

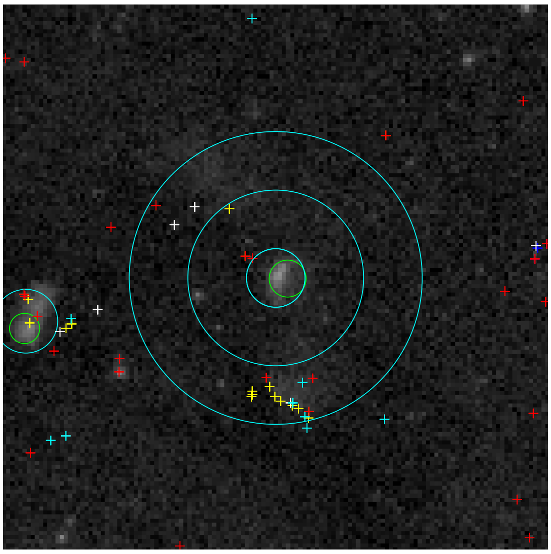

(C) X-ray

FIGURE C.37: MCSNR J0532−6732, B0532−675
ICRS coordinates (ep=J2000): R.A. = 05:32:30.0, Dec = −67:31:33.0
$R = 142.5''$

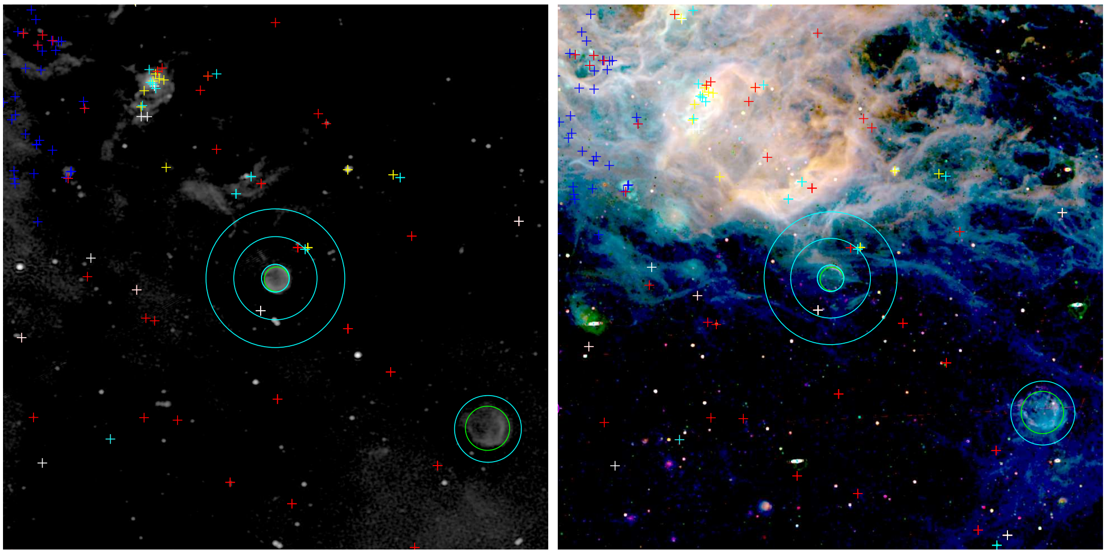

(A) Radio (B) Optical

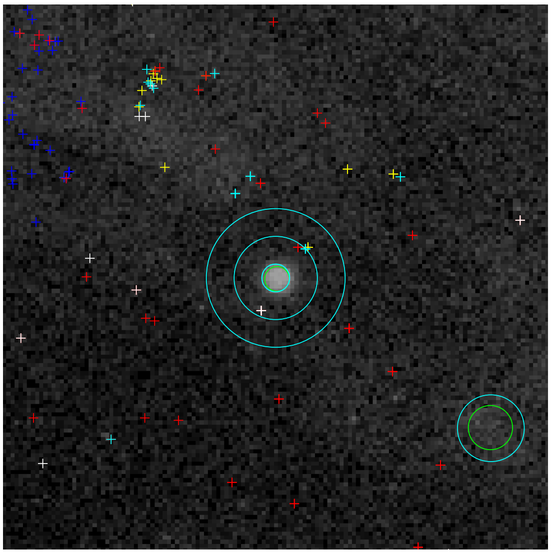

(C) X-ray

FIGURE C.38: MCSNR J0534−6955, B0534−699
ICRS coordinates (ep=J2000): R.A. = 05:34:02.0, Dec = −69:55:03.0
$R = 67.5''$

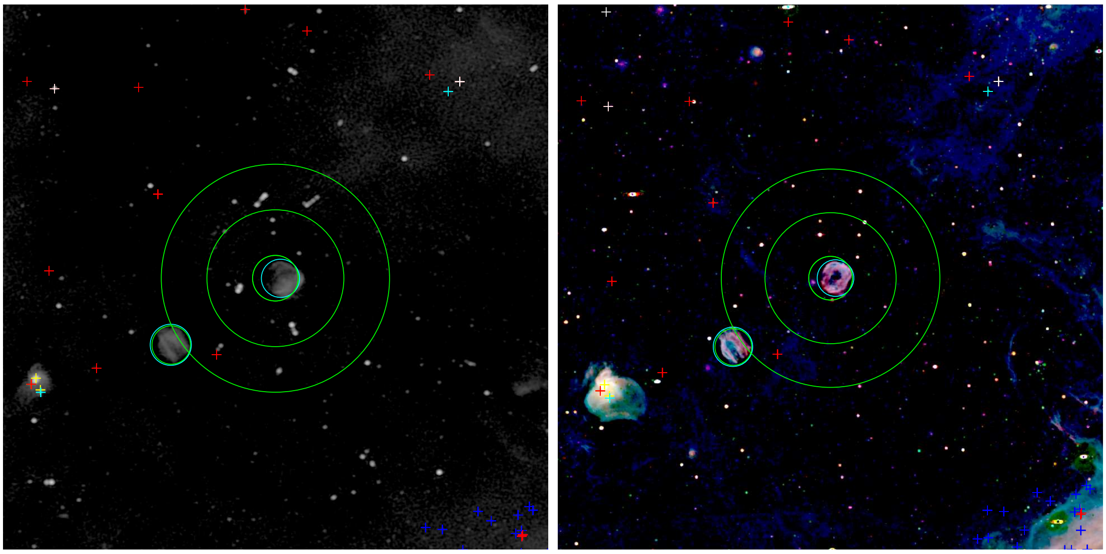

(A) Radio (B) Optical

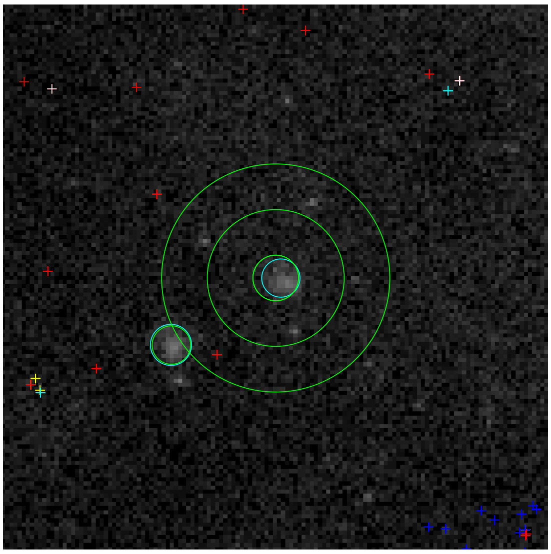

(C) X-ray

FIGURE C.39: MCSNR J0534−7033, DEM L238
ICRS coordinates (ep=J2000): R.A. = 05:34:23.0, Dec = −70:33:25.0
$R = 111''$

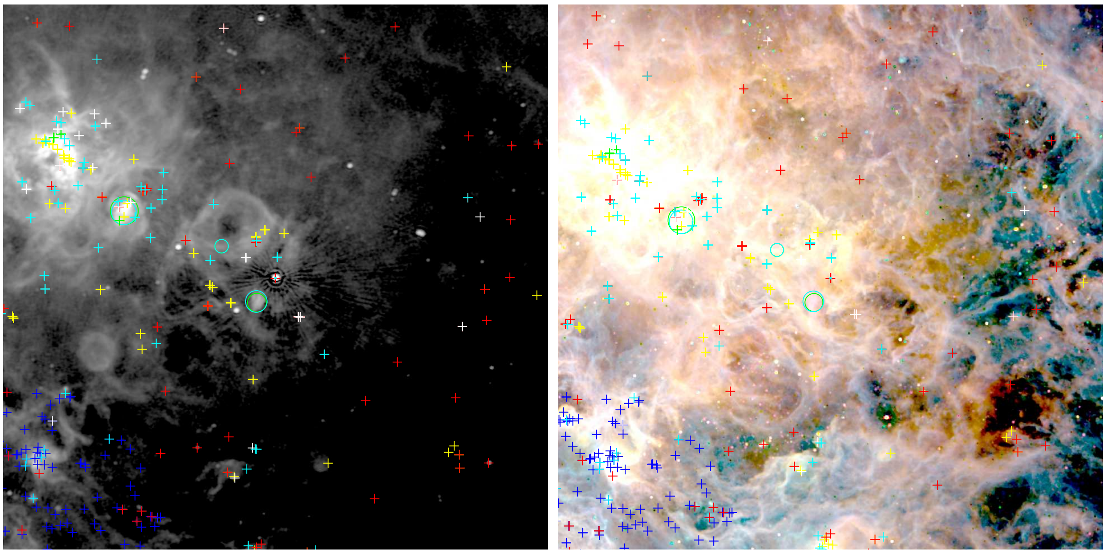

(A) Radio (B) Optical

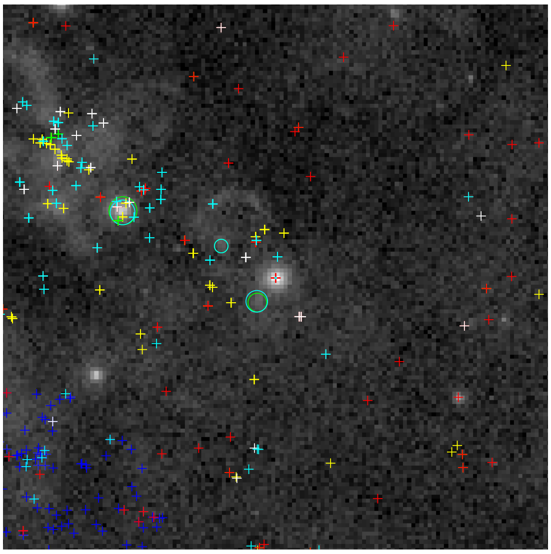

(C) X-ray

FIGURE C.40: MCSNR J0535−6916, SN1987A
ICRS coordinates (ep=J2000): R.A. = 05:35:28.0, Dec = −69:16:11.0
$R = 0.8''$

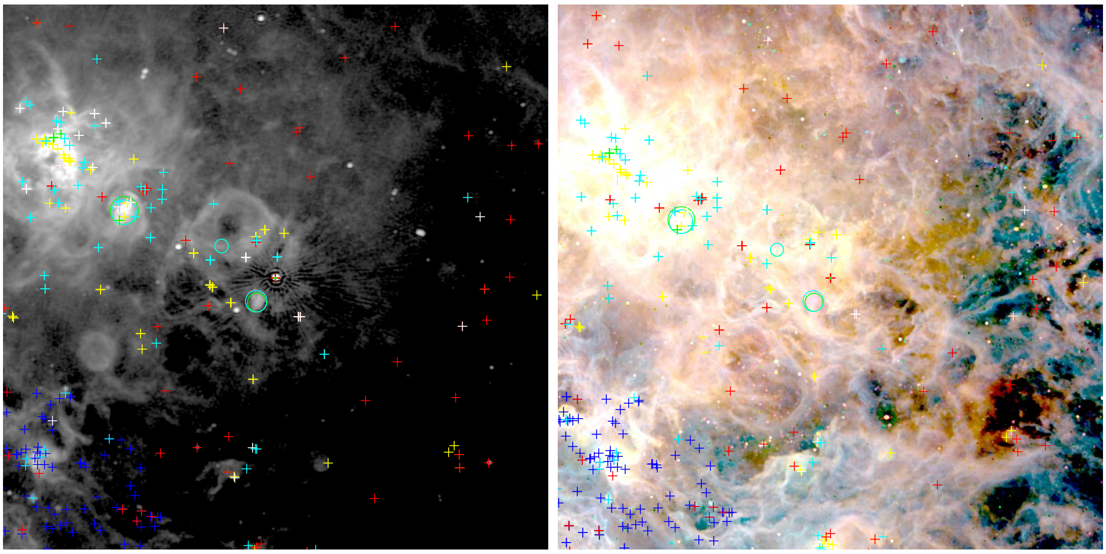

(A) Radio (B) Optical

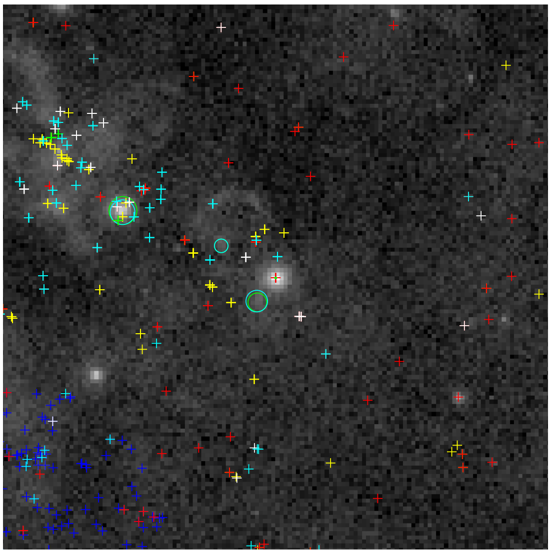

(C) X-ray

Figure C.41: MCSNR J0535−6602, N63A
ICRS coordinates (ep=J2000): R.A. = 05:35:28.0, Dec = −69:16:11.0
$R = 42''$

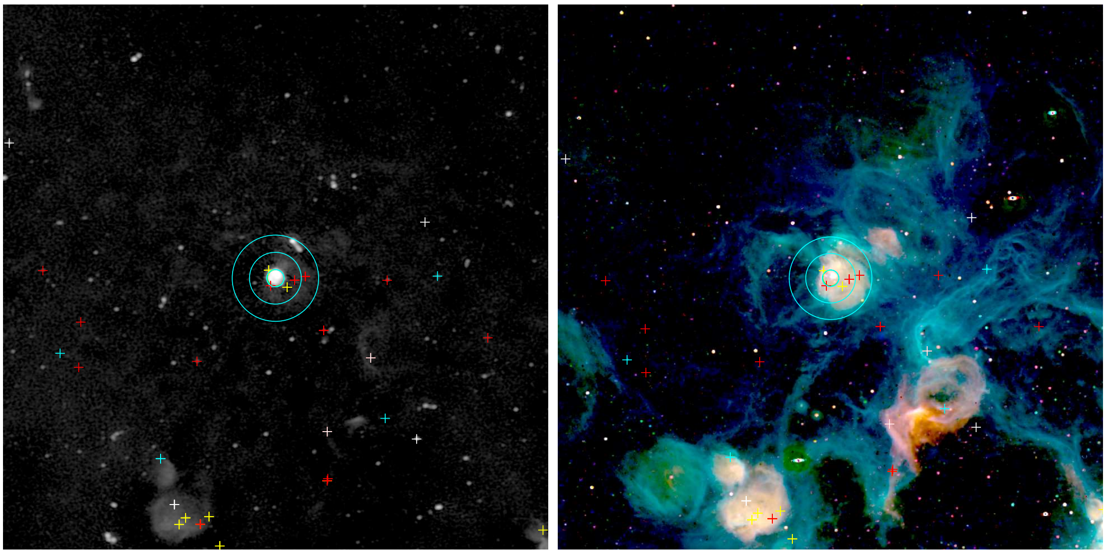

(A) Radio (B) Optical

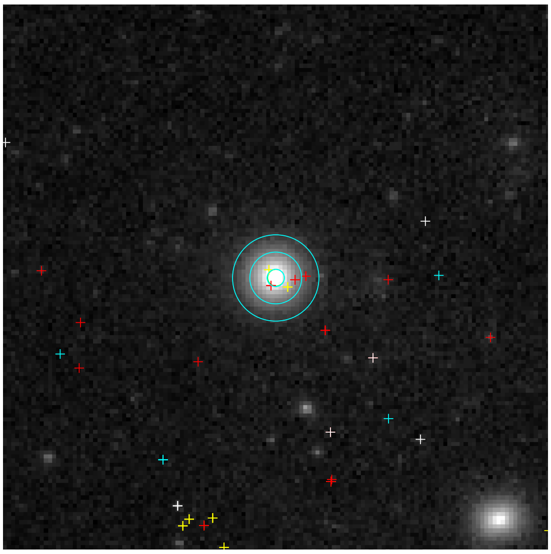

(C) X-ray

Figure C.42: MCSNR J0535−6918, Honeycomb
ICRS coordinates (ep=J2000): R.A. = 05:35:46.0, Dec = −69:18:02.0
$R = 52.5''$

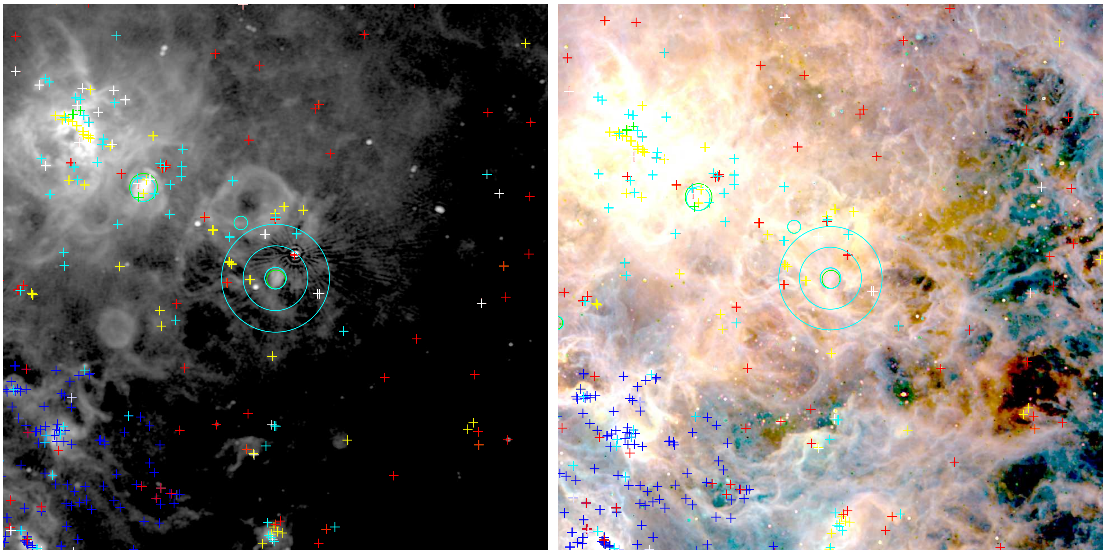

(A) Radio (B) Optical

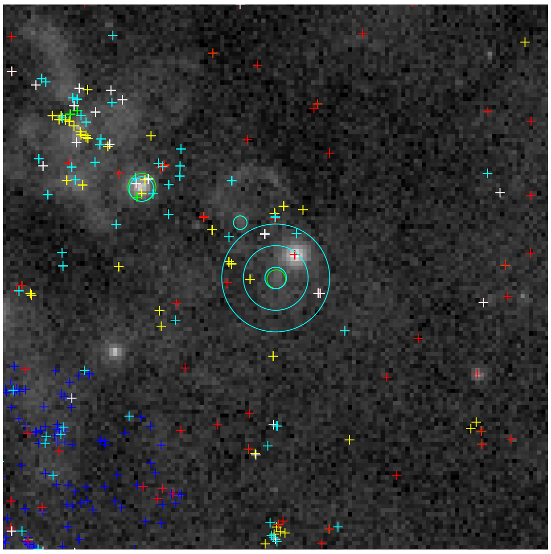

(C) X-ray

Figure C.43: MCSNR J0536−6735, DEM L241
ICRS coordinates (ep=J2000): R.A. = 05:36:03.0, Dec = −67:34:36.0
$R = 155''$

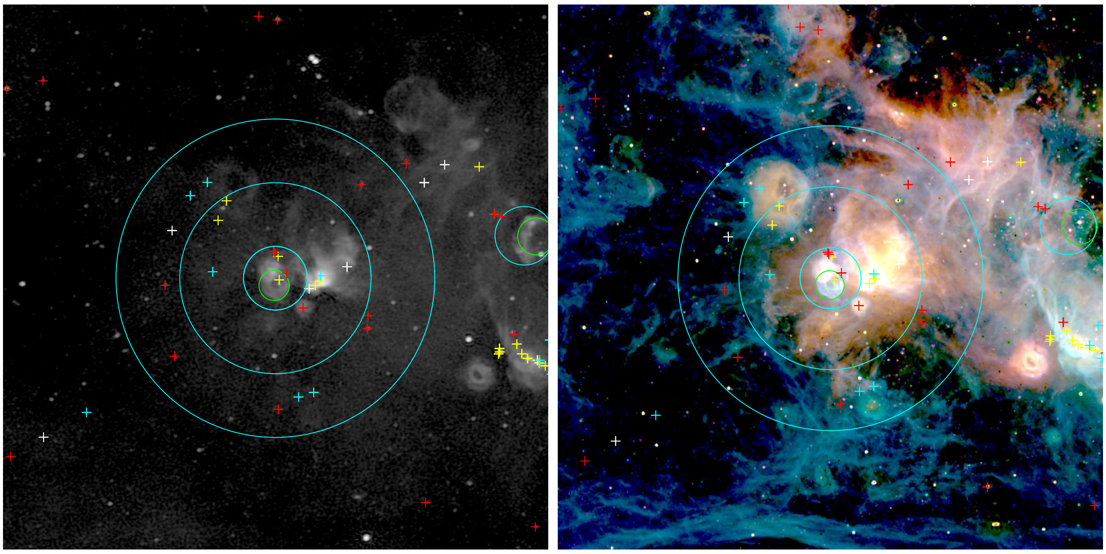

(A) Radio (B) Optical

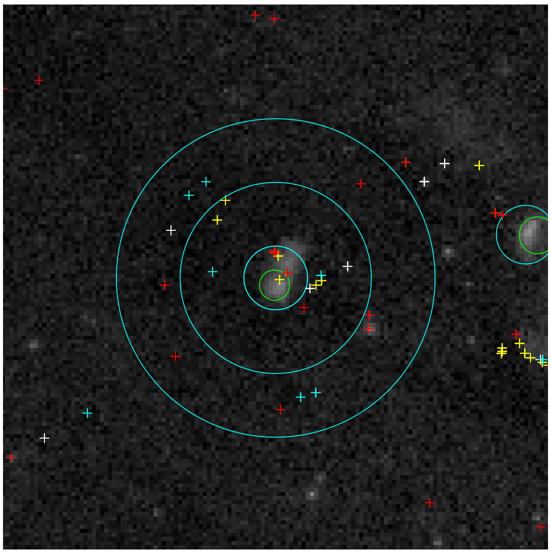

(C) X-ray

Figure C.44: MCSNR J0536−7039, DEM L249
ICRS coordinates (ep=J2000): R.A. = 05:36:07.0, Dec = −70:38:37.0
$R = 100''$

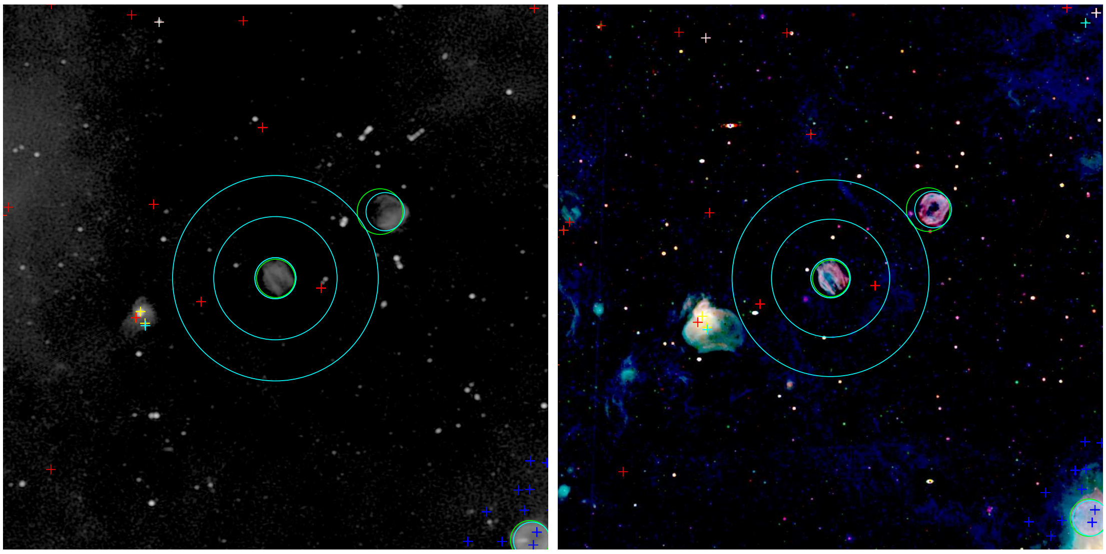

(A) Radio (B) Optical

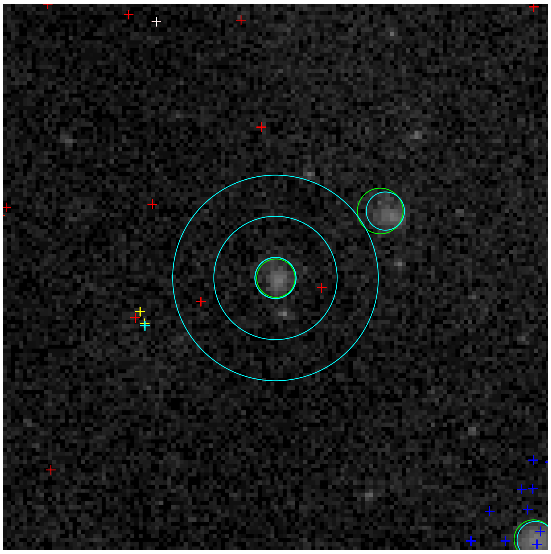

(C) X-ray

Figure C.45: MCSNR J0536−6913, B0536−6914
ICRS coordinates (ep=J2000): R.A. = 05:36:17.0, Dec = −69:13:28.0
$R = 33''$

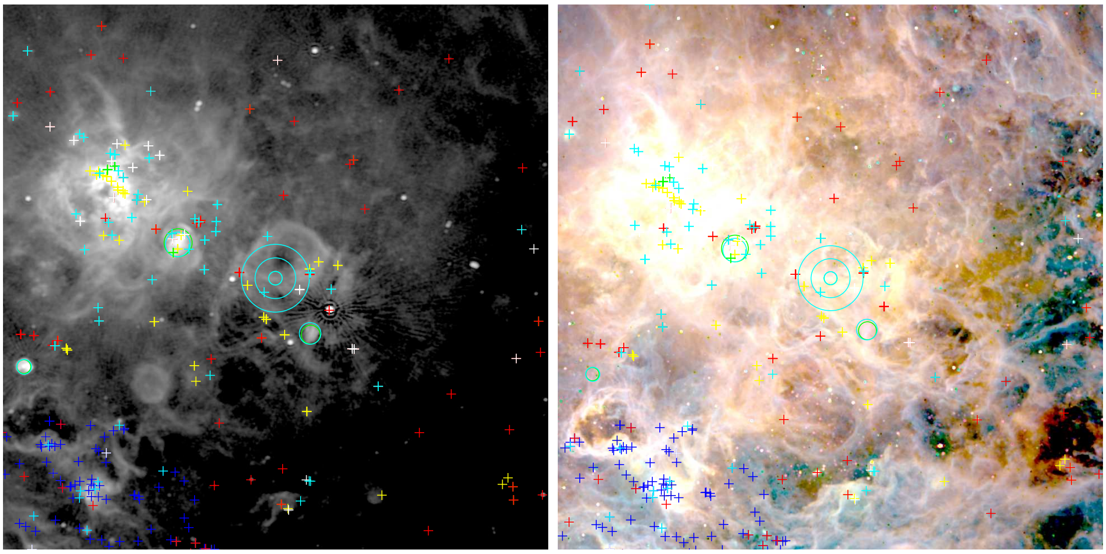

(A) Radio (B) Optical

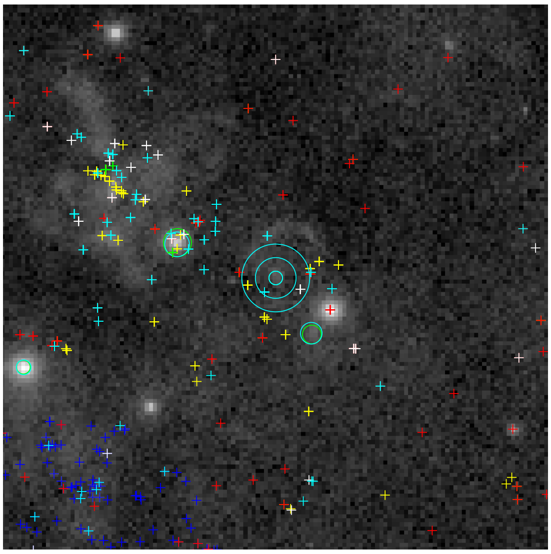

(C) X-ray

FIGURE C.46: MCSNR J0537−6628, DEM L256
ICRS coordinates (ep=J2000): R.A. = 05:37:27.0, Dec = −66:27:50.0
$R = 113.5''$

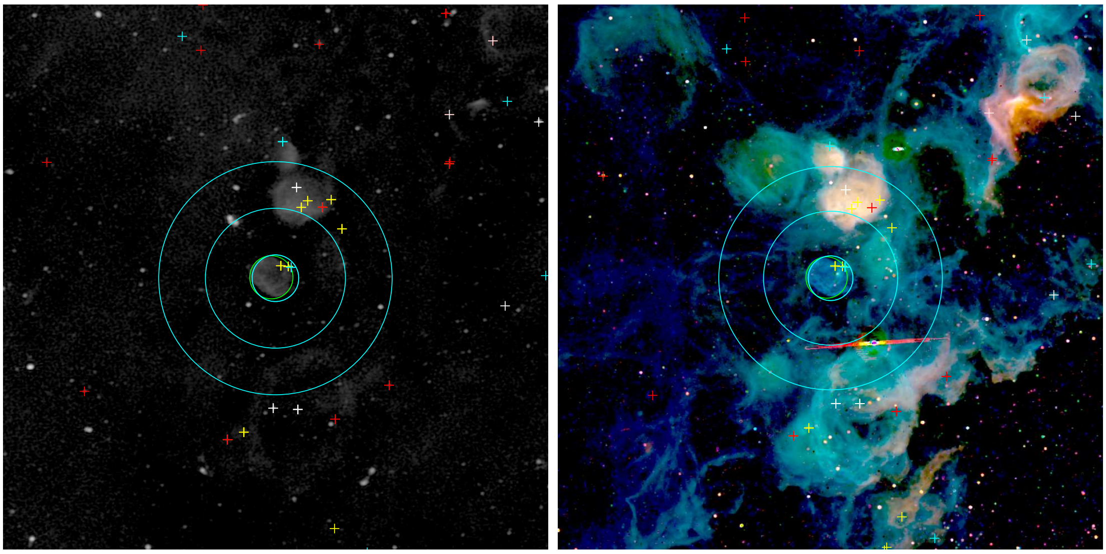

(A) Radio (B) Optical

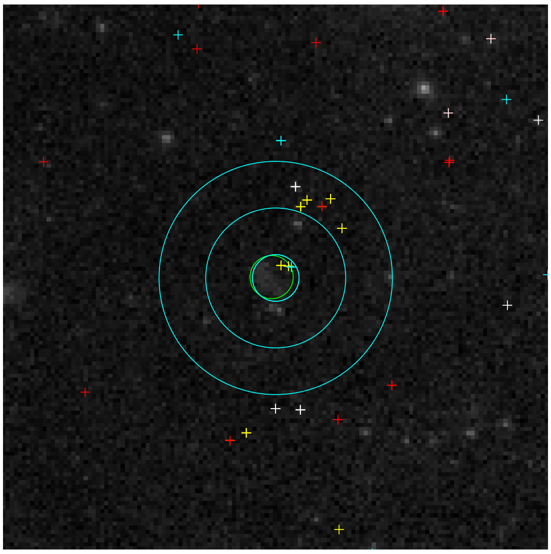

(C) X-ray

FIGURE C.47: MCSNR J0537−6910, 30 Dor B
ICRS coordinates (ep=J2000): R.A. = 05:37:45.6, Dec = −69:10:20.0
$R = 68''$

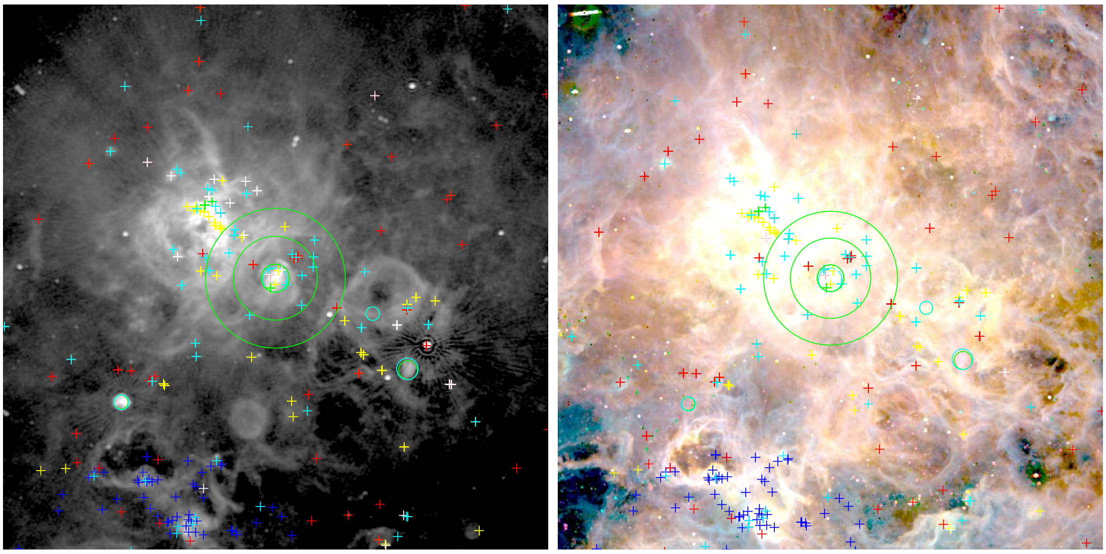

(A) Radio (B) Optical

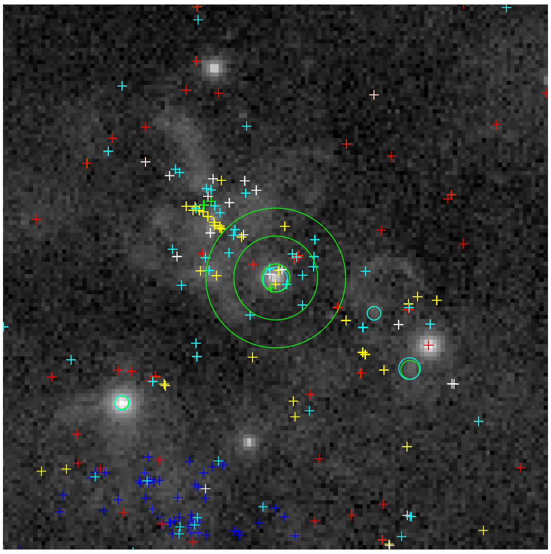

(C) X-ray

Figure C.48: MCSNR J0540−6944, N159
ICRS coordinates (ep=J2000): R.A. = 05:40:00.0, Dec = −69:44:06.0
$R = 60''$

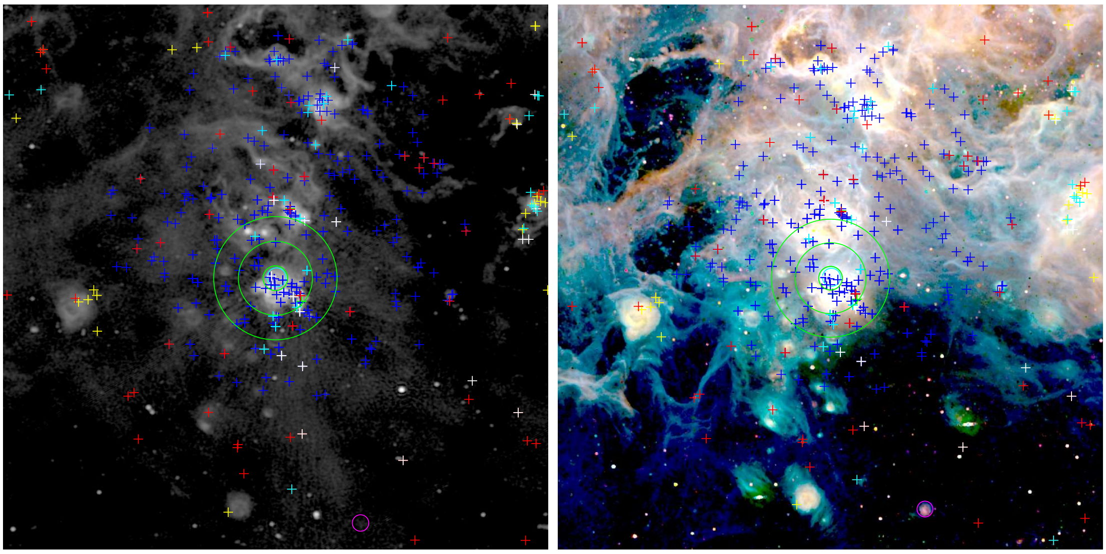

(A) Radio (B) Optical

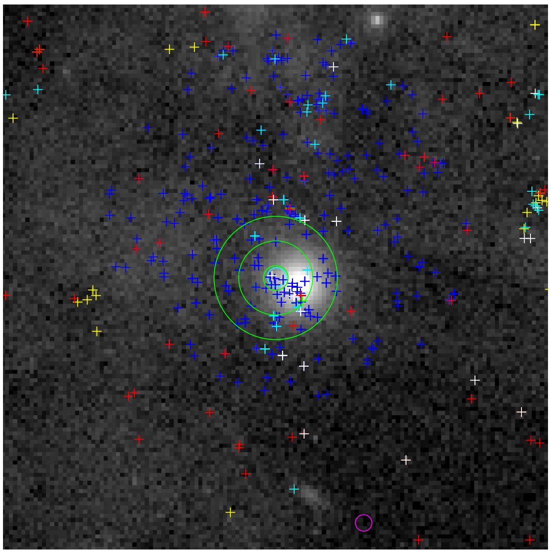

(C) X-ray

Figure C.49: MCSNR J0540−6920, B0540−693
ICRS coordinates (ep=J2000): R.A. = 05:40:11.0, Dec = −69:19:55.0
$R = 36''$

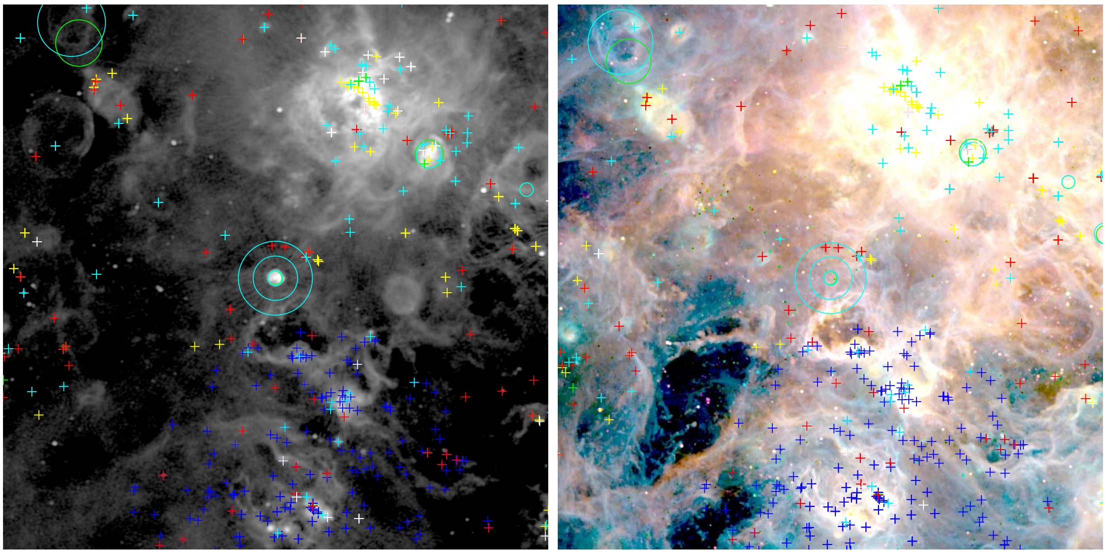

(A) Radio (B) Optical

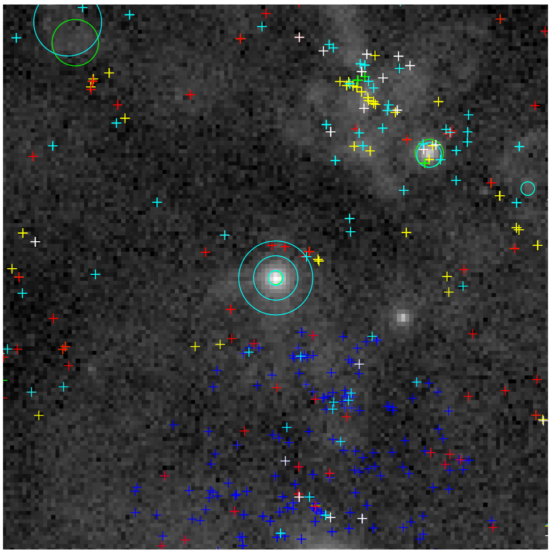

(C) X-ray

FIGURE C.50: MCSNR J0541−6659, [HP99] 456
ICRS coordinates (ep=J2000): R.A. = 05:41:51.0, Dec = −66:59:04.0
$R = 150''$

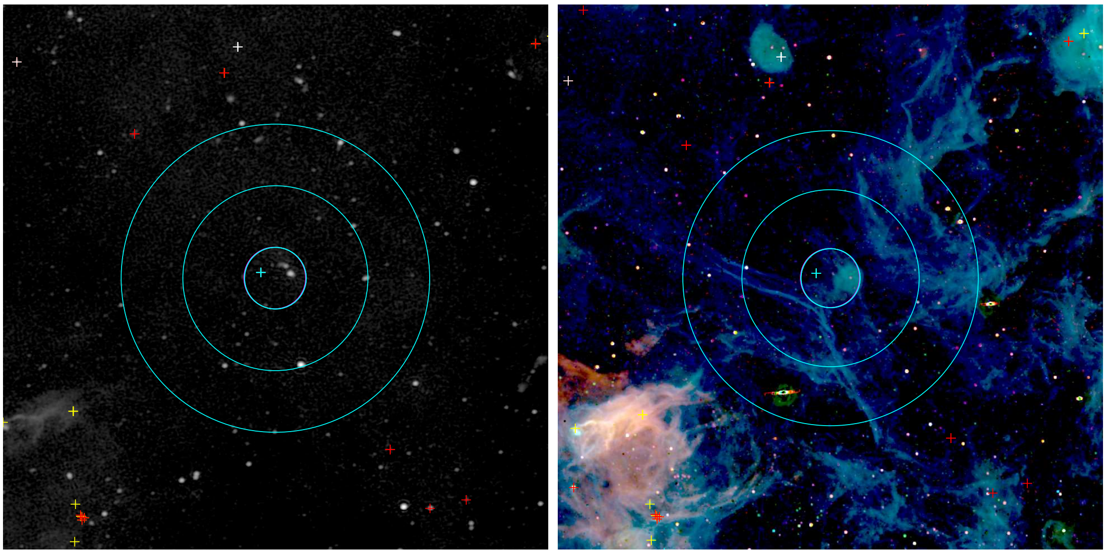

(A) Radio (B) Optical

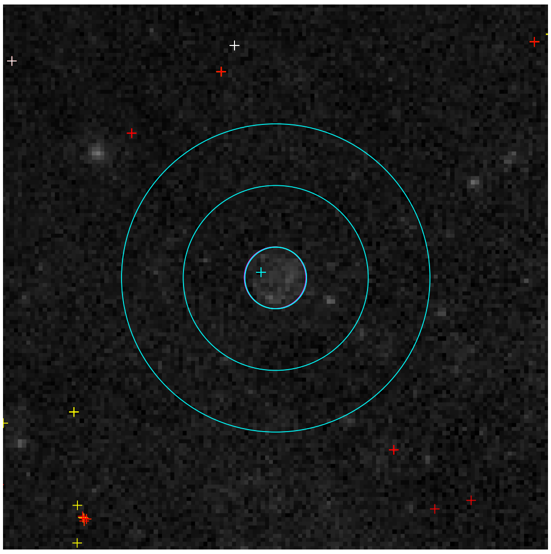

(C) X-ray

FIGURE C.51: MCSNR J0543−6858, DEM L299
ICRS coordinates (ep=J2000): R.A. = 05:43:08.0, Dec = −68:58:18.0
$R = 165''$

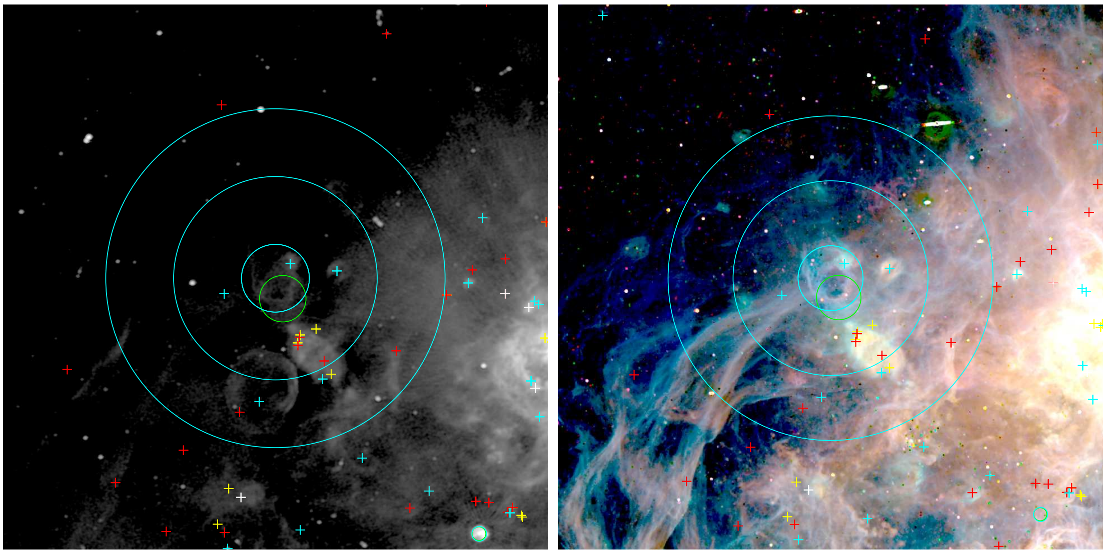

(A) Radio (B) Optical

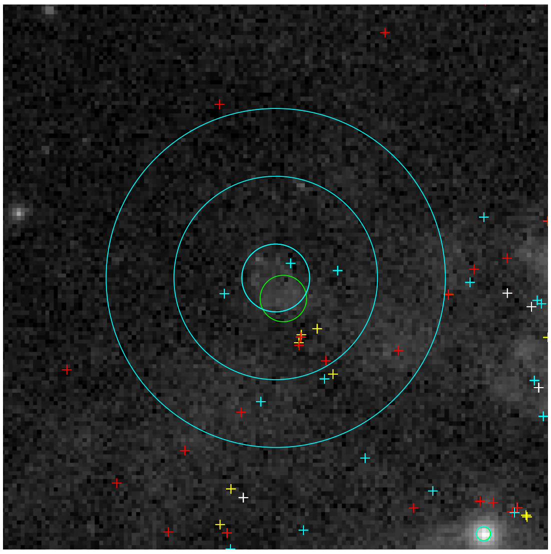

(C) X-ray

FIGURE C.52: MCSNR J0547−6942, DEM L316B
ICRS coordinates (ep=J2000): R.A. = 05:47:00.0, Dec = −69:42:50.0
$R = 100''$

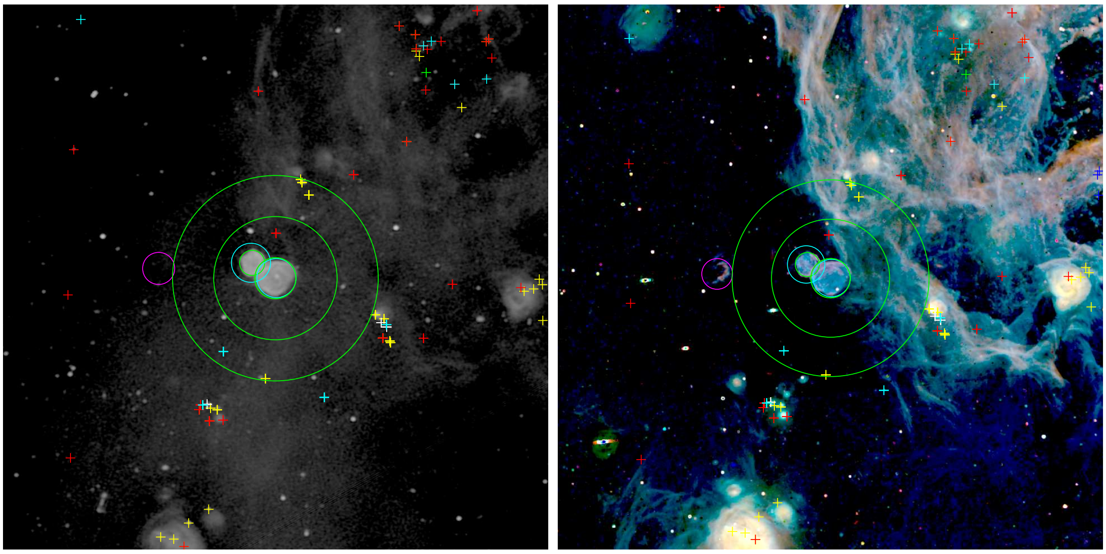

(a) Radio (b) Optical

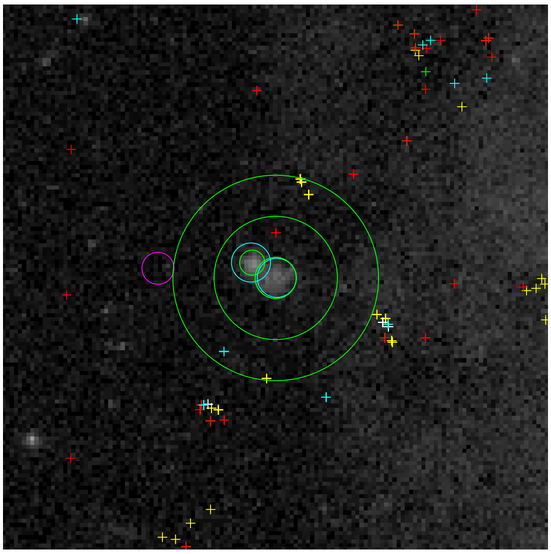

(c) X-ray

Figure C.53: MCSNR J0547−6941, DEM L316A
ICRS coordinates (ep=J2000): R.A. = 05:47:22.0, Dec = −69:41:26.0
$R = 95''$

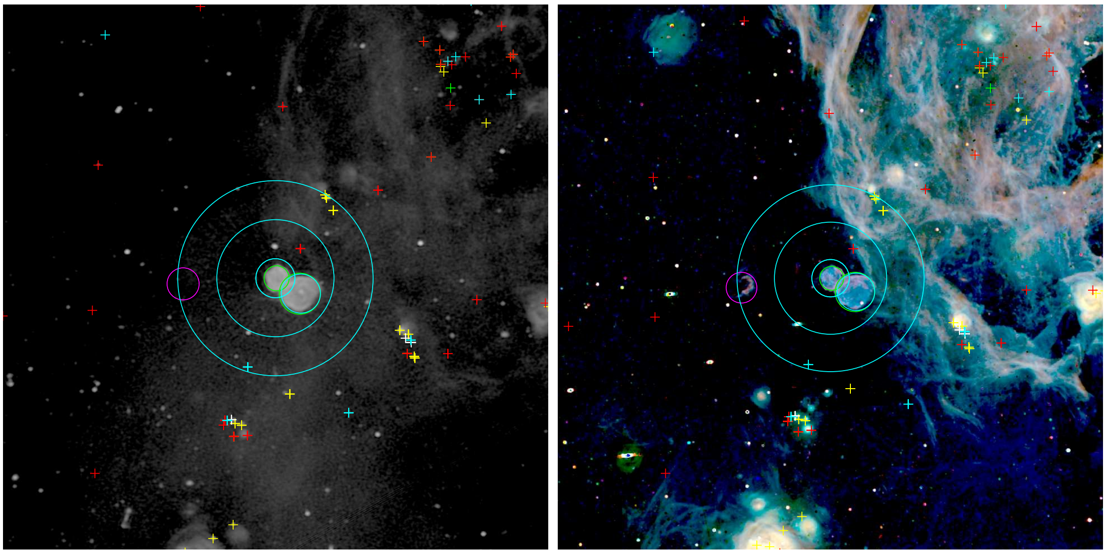

(A) Radio (B) Optical

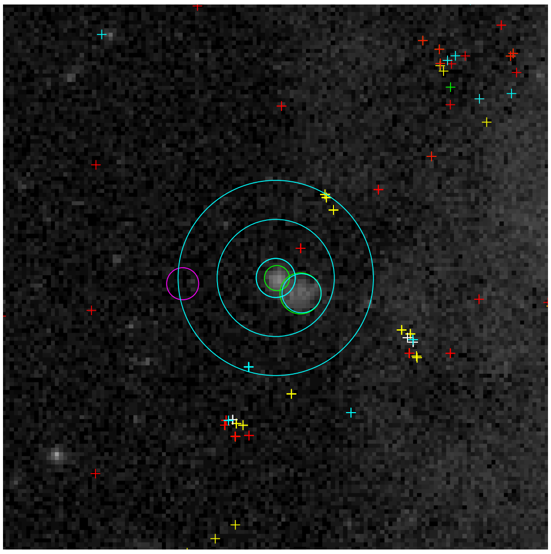

(C) X-ray

FIGURE C.54: MCSNR J0547−7024, LHG 89
ICRS coordinates (ep=J2000): R.A. = 05:47:48.8, Dec = −70:24:52.0
$R = 60''$

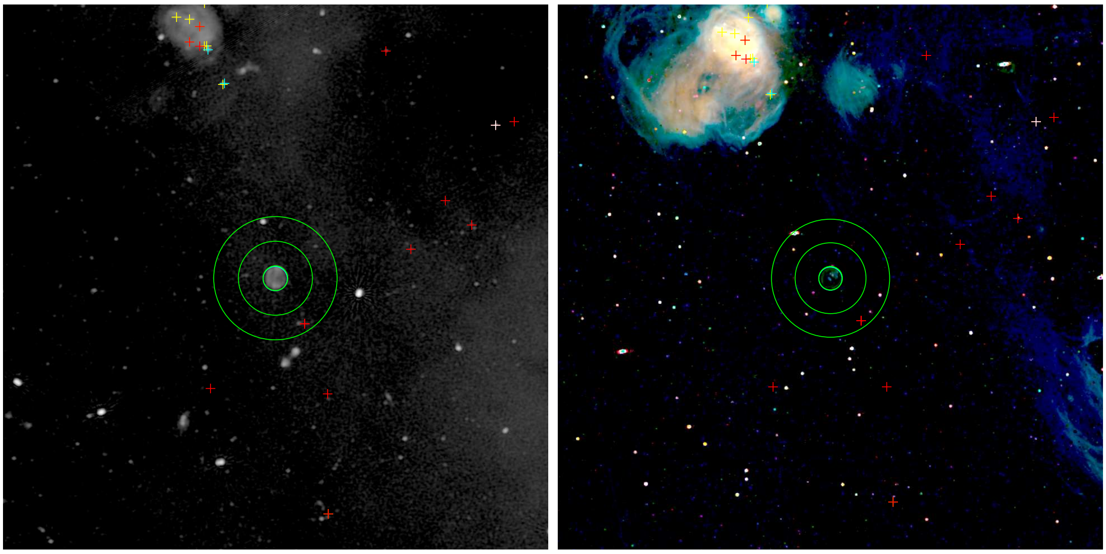

(A) Radio (B) Optical

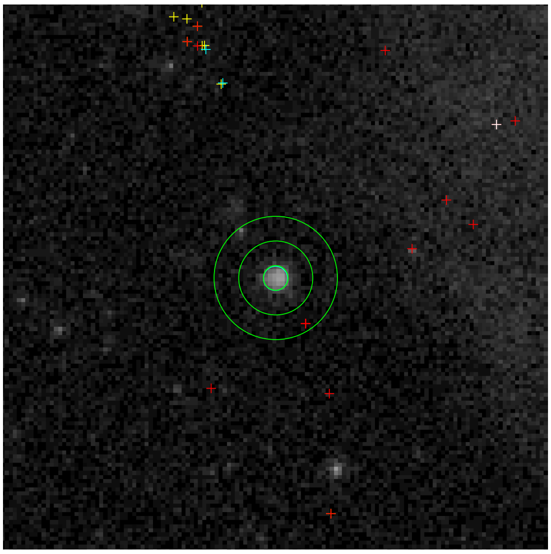

(C) X-ray

FIGURE C.55: MCSNR J0550−6823, DEM L328
ICRS coordinates (ep=J2000): R.A. = 05:50:30.7, Dec = −68:23:37.0
$R = 186.5''$

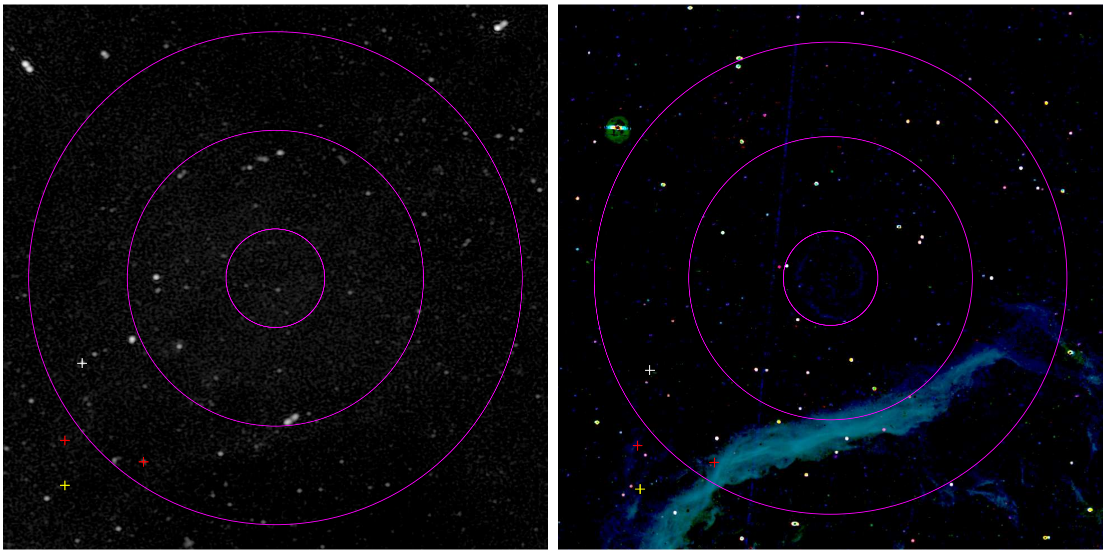

(A) Radio (B) Optical

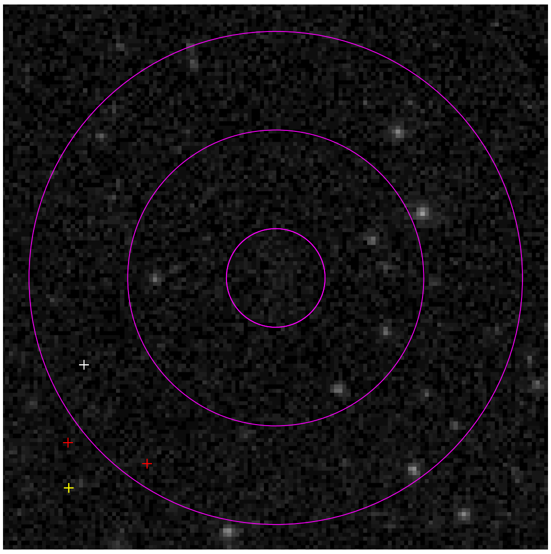

(C) X-ray

Figure C.56: MCSNR J0502–6739
ICRS coordinates (ep=J2000): R.A. = 05:02:02.5, Dec = −67:39:31.3
$R = 95''$

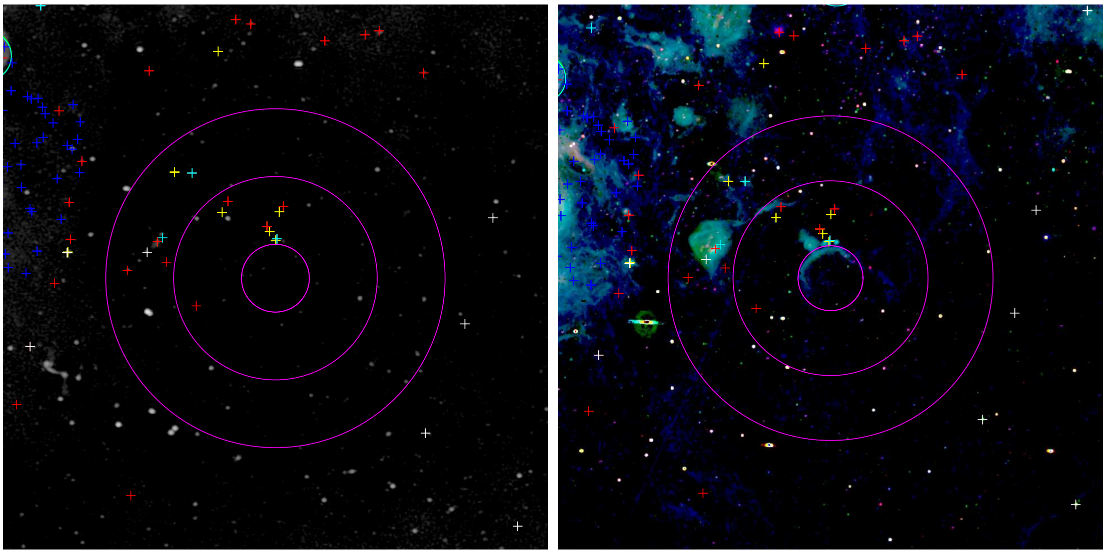

(A) Radio (B) Optical

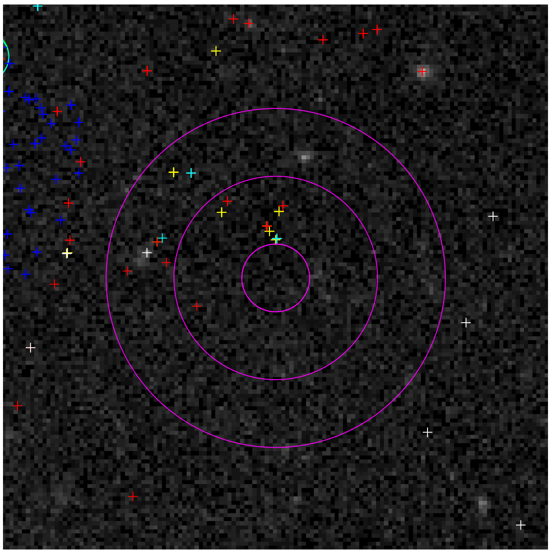

(C) X-ray

FIGURE C.57: MCSNR J0509−6402
ICRS coordinates (ep=J2000): R.A. = 05:09:16.1, Dec = −64:02:11.3
$R = 278''$

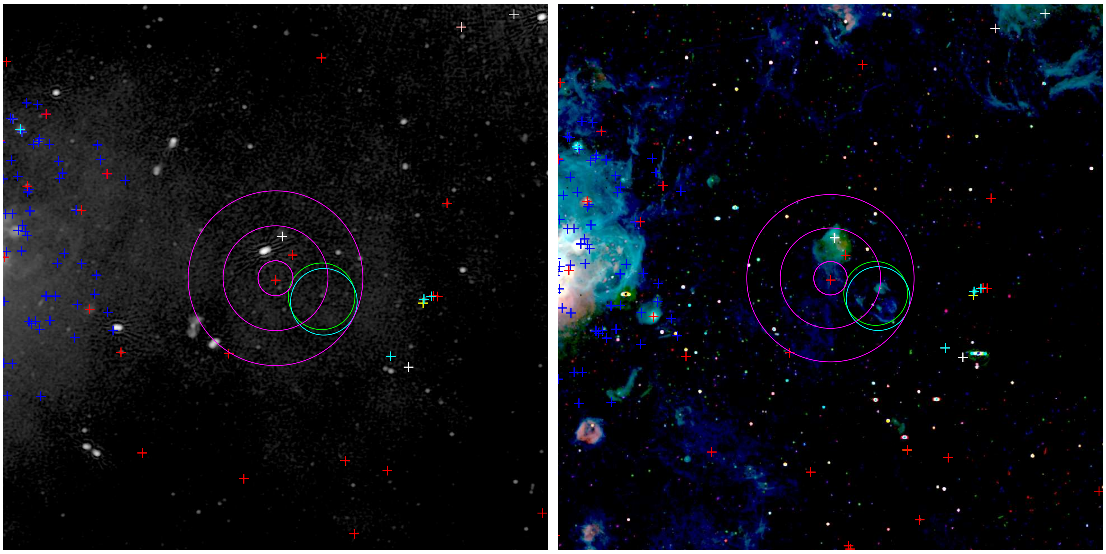

(A) Radio

(B) Optical

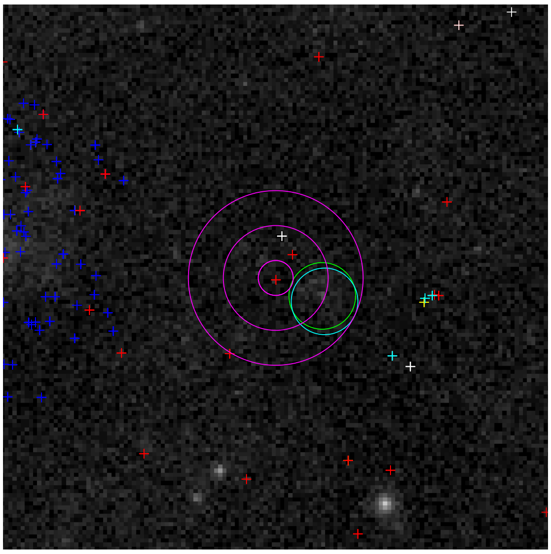

(C) X-ray

FIGURE C.58: MCSNR J0522−6740
ICRS coordinates (ep=J2000): R.A. = 05:22:32.4, Dec = −67:40:56.0
$R = 180''$

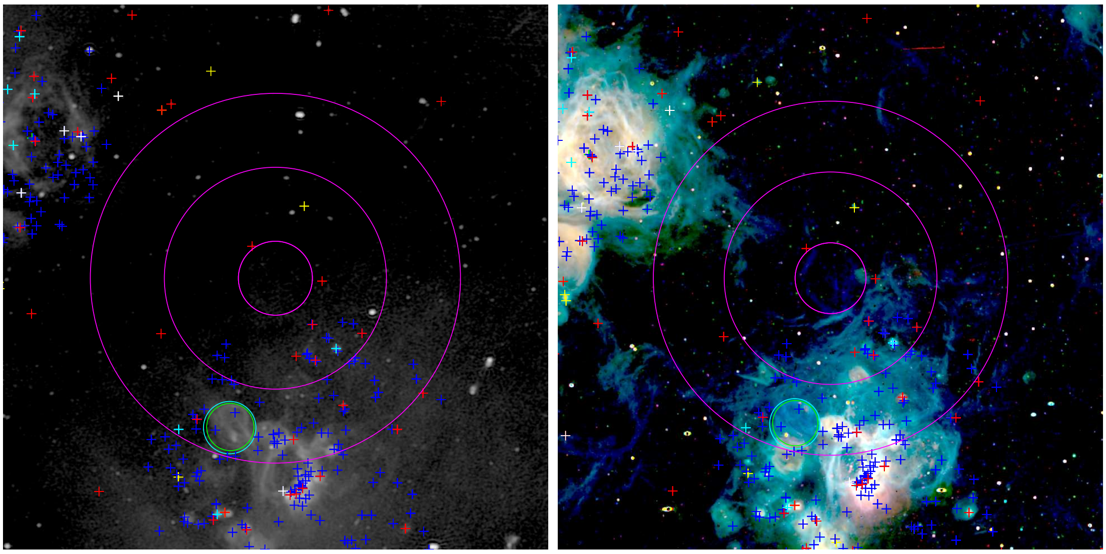

(A) Radio (B) Optical

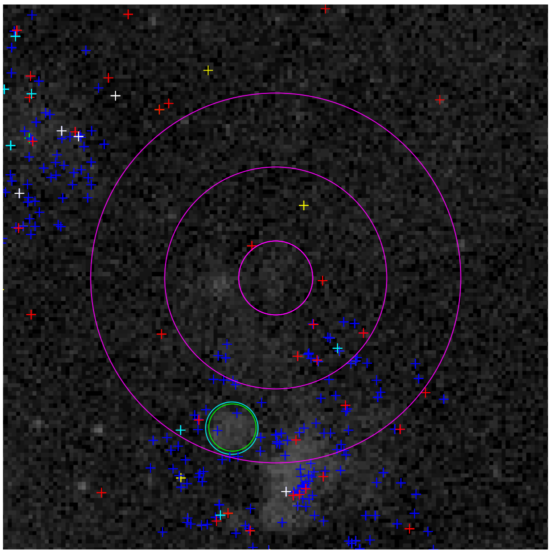

(C) X-ray

Figure C.59: MCSNR J0528−7017
ICRS coordinates (ep=J2000): R.A. = 05:28:46.0, Dec = −70:17:56.8
$R = 208''$

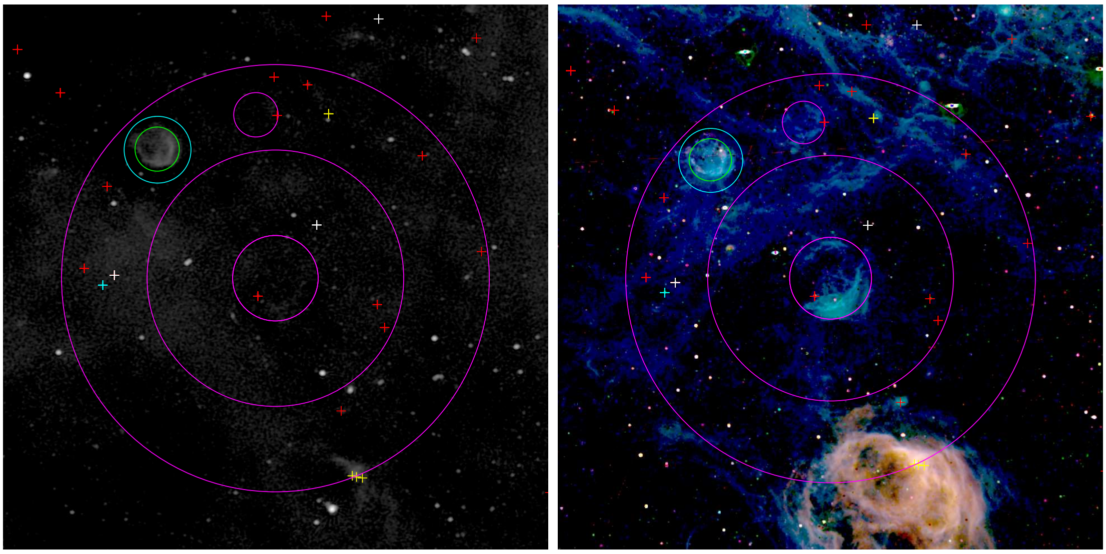

(A) Radio (B) Optical

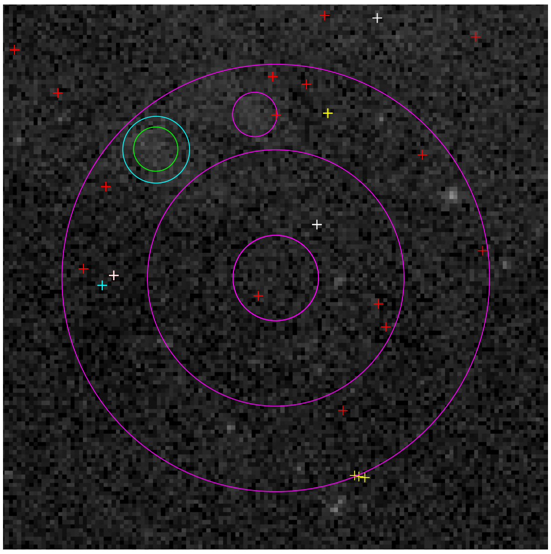

(C) X-ray

FIGURE C.60: MCSNR J0529−7004
ICRS coordinates (ep=J2000): R.A. = 05:29:05.9, Dec = −70:04:40.6
$R = 108''$

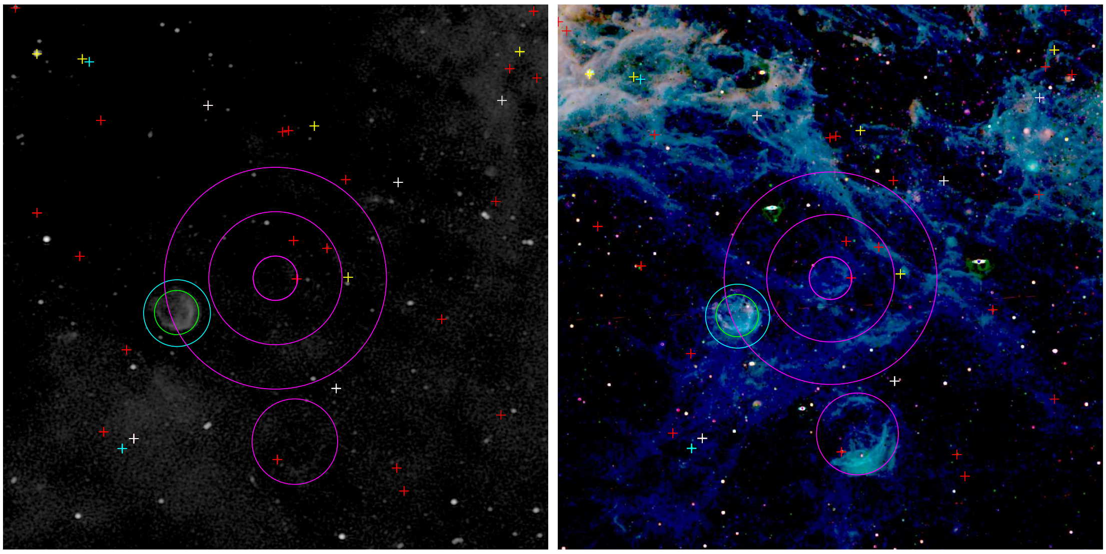

(A) Radio (B) Optical

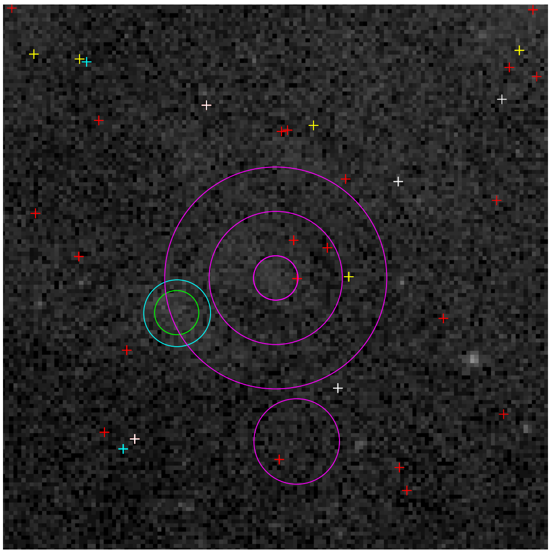

(C) X-ray

Figure C.61: MCSNR J0538−7004
ICRS coordinates (ep=J2000): R.A. = 05:38:47.2, Dec = −70:04:15.8
$R = 40''$

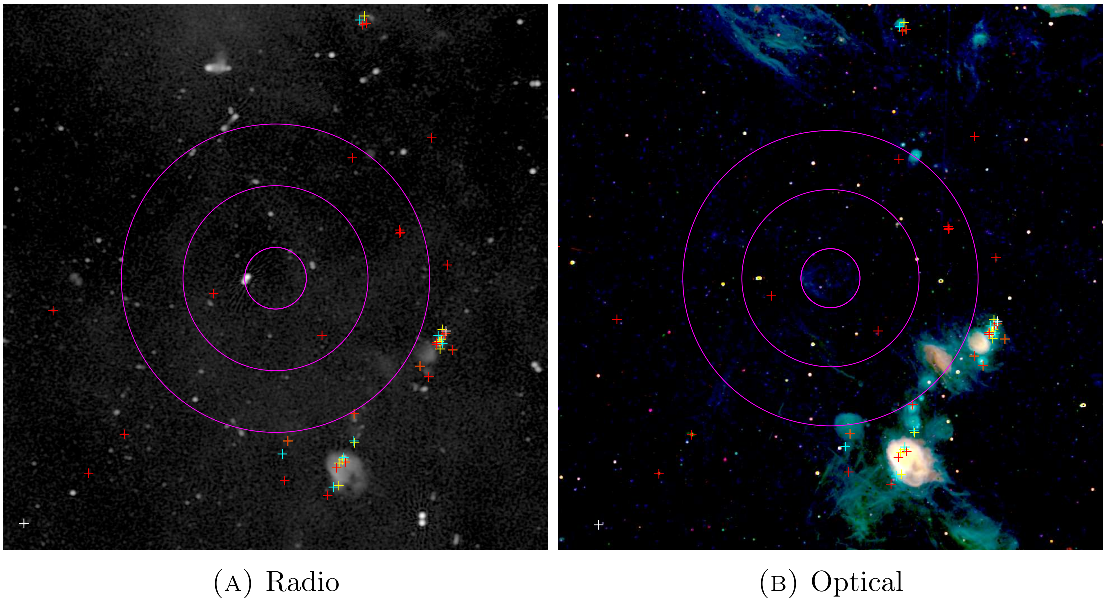

(A) Radio

(B) Optical

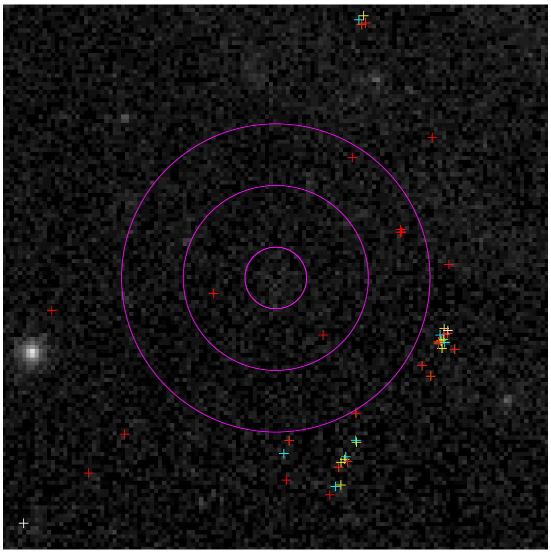

(C) X-ray

Figure C.62: MCSNR J0548−6941
ICRS coordinates (ep=J2000): R.A. = 05:48:49.1, Dec = −69:41:18.3
$R = 78''$